

Machining distortion prediction for aerospace structural components

TESIS DOCTORAL

presentada para optar al título de **Doctor**

María Aurrekoetxea Totorikaguena



DIRECTORES

Dr. Iñigo Llanos González de Durana

Prof. Dr. Luis Norberto López de Lacalle Marcaide

Bilbao, Octubre 2022



INGENIARITZA
MEKANIKOA
SAILA
DEPARTAMENTO
DE INGENIERÍA
MECÁNICA

Machining distortion prediction for aerospace structural components

by

Maria Aurrekoetxea Totorikaguena

directed by

Iñigo Llanos González de Durana

Luis Norberto López de Lacalle Marcaide

A thesis submitted in partial fulfillment for the
degree of Doctor of Philosophy

in the

Escuela de Ingeniería de Bilbao

Departamento de Ingeniería Mecánica

October 2022

Declaration of Authorship

I, Maria Aurrekoetxea Totorikaguena, declare that this thesis titled, ‘Machining distortion control for aerospace components’ and the work presented in it are my own. I confirm that:

- This work was done wholly or mainly while in candidature for a research degree at this University.
- Where any part of this thesis has previously been submitted for a degree or any other qualification at this University or any other institution, this has been clearly stated.
- Where I have consulted the published work of others, this is always clearly attributed.
- Where I have quoted from the work of others, the source is always given. With the exception of such quotations, this thesis is entirely my own work.
- I have acknowledged all main sources of help.
- Where the thesis is based on work done by myself jointly with others, I have made clear exactly what was done by others and what I have contributed myself.

Signed:

Date:

“Success is not final; failure is not fatal: It is the courage to continue that counts.”

Winston S. Churchill

Abstract

Machining distortion is a recurring issue when producing aerospace structural components, entailing high costs, and material and energy waste to the industry. It is currently confronted with long machining processes, including repeated unclamping, check, and correction sequences, which highly depend upon the experience of the skilled workers. The multiple sources of distortion, their interrelation, and variability make distortion a long-standing technical hitch, which remains unsolved despite the research efforts. This thesis addresses the understanding of machining distortion in aerostructures for the subsequent development of a procedure to determine residual stresses and calculate distortion in production lines.

In aerostructures the main distortion sources are residual stresses, both inherent to the machining blanks coming from the upstream manufacturing processes, and induced in the surfaces by machining due to the high thermal and mechanical loads. Distortion prediction in aerostructures often shows significant discrepancies with experimental results, related to inaccurate residual stress input data. Due to the variabilities between blanks, modeling cannot provide actual blank-initial residual stress data, while the measurement is complex, expensive, and limited to the laboratory. Moreover, as most used through-thickness stress measuring methods are destructive, blank-initial residual stress data cannot be measured in the blanks from which final parts are obtained. In the case of machining-induced residual stresses, the difficulties rely on the variabilities linked to machining conditions and the uncertainty linked to the measuring methods. For these reasons, the present project develops procedures for residual stress quantification in industrial environments and accurate distortion prediction.

First, a blank-initial residual stress characterization method is developed, which can be performed in real-size machining blanks at the shop-floor level, enabling to obtain the final parts from blanks with measured initial stresses. Besides, a good practice guide is defined for the blank-initial residual stress characterization through the on-machine Layer Removal method, and an uncertainty assessment procedure is presented, which enables identifying the range of application of the proposed method.

Secondly, more specific insight into machining-induced residual stresses and the measuring methods is provided. Measurements of the machining-induced stress profiles in aluminum and titanium alloys are performed, including a comparison between the Incremental Hole Drilling and the X-Ray Diffraction methods. Moreover, an empirical model for machining-induced stress prediction is developed and evaluated, showing fast and accurate results below the measuring uncertainty.

Thirdly, the applicability of the developments related to residual stress determination is evaluated through different studies linked to machining distortion prediction. On the one hand, experimental verification of the blank-initial residual stress characterization method is performed, demonstrating that accurate blank-initial residual stress characterization is possible using the ribbed on-machine Layer Removal method. On the other hand, a theoretical analysis of the potential of controlling distortion using the machining-induced residual stress empirical model is exposed displaying that it is possible to control the final distortion of titanium thin parts by generating customized machining-induced residual stresses in the surfaces.

Finally, the feasibility of the distortion prediction on a real part is evaluated using part geometry, material, residual stress, and process data. The obtained results show accurate machining distortion estimation, as well as an uncertainty range of this prediction, in a simple and fast form. In this way, a hybrid distortion model is presented for performing preliminary distortion studies during the process planning stage and the development of optimized manufacturing strategies while minimizing the final part distortion and facilitating engineering decision-making. This method enables avoiding typical layer-by-layer strategies, reducing the costs associated with long machining processes based on experimental trials. Moreover, a reduced on-machine Layer Removal and blank-initial residual stress estimation procedure speeds up the characterization and enables its implementation in production lines.

Resumen

La distorsión es un problema recurrente en la producción de componentes estructurales aeroespaciales, y conlleva altos costos y desperdicio de material y energía en la industria. Actualmente se resuelve mediante largos procesos de mecanizado, con secuencias repetitivas en las que se sueltan las piezas, se analiza la distorsión y se realizan correcciones, las cuales dependen en gran medida de la experiencia de los trabajadores cualificados. Las múltiples fuentes de distorsión, su interrelación y variabilidad hacen que la distorsión sea un problema técnico prolongado durante décadas, que sigue sin resolverse a pesar de los esfuerzos de investigación. Esta tesis aborda la comprensión de la distorsión tras el mecanizado de aeroestructuras con el objetivo de desarrollar un procedimiento capaz de determinar las tensiones residuales y calcular la distorsión en las líneas de producción.

En las aeroestructuras, las principales fuentes de distorsión son las tensiones residuales, tanto las procedentes de procesos de fabricación previos inherentes a los brutos, como las inducidas en las superficies por el mecanizado debido a las elevadas cargas térmicas y mecánicas. La predicción de distorsión en aeroestructuras a menudo muestra discrepancias significativas con respecto a resultados experimentales, las cuales se relacionan con imprecisiones en los datos de entrada de tensión residual. Debido a las variabilidades entre brutos, los modelos de simulación no proporcionan datos reales del estado inicial de tensiones residuales de cada bruto, y la medición de estas tensiones volumétricas es compleja, costosa y limitada al laboratorio. Además, dado que la mayoría de los métodos de medición de tensiones residuales volumétricas son destructivos, no se pueden obtener piezas finales a partir de brutos cuyas tensiones residuales iniciales hayan sido medidas. En el caso de las tensiones residuales superficiales inducidas por el mecanizado, las dificultades residen en las variabilidades vinculadas a las condiciones de mecanizado y en la incertidumbre vinculada a los métodos de medición. Por estas razones, el presente proyecto desarrolla procedimientos para la cuantificación de tensiones residuales en entornos industriales y la predicción precisa de distorsiones.

En primer lugar, se desarrolla un método de caracterización de tensiones residuales iniciales en los brutos de mecanizado, el cual se puede realizar en taller en brutos de tamaño real, permitiendo obtener piezas finales a partir de brutos con tensiones iniciales medidas. Además, se define una guía de buenas prácticas para la caracterización de tensiones residuales iniciales en brutos mediante el método de eliminación de capas en máquina (*on-machine Layer Removal*) y se presenta un procedimiento de evaluación de la incertidumbre que permite identificar el rango de aplicación del método propuesto.

En segundo lugar, se proporciona información específica sobre las tensiones residuales inducidas por el mecanizado y los métodos de medición. Se realizan mediciones de los perfiles de tensión inducidos por el mecanizado en aleaciones de aluminio y titanio, incluida una

comparación entre los métodos de perforación incremental (*incremental Hole Drilling*) y de difracción de rayos X (*X-ray diffraction*). Además, se desarrolla y evalúa un modelo empírico para la predicción de tensiones inducidas por el mecanizado, que muestra resultados rápidos y precisos por debajo de la incertidumbre de medida.

En tercer lugar, se evalúa la aplicabilidad de los desarrollos relacionados con la determinación de tensiones residuales a través de diferentes estudios vinculados a la predicción de distorsiones tras el mecanizado. Por un lado, se realiza la verificación experimental del método de caracterización de las tensiones residuales iniciales en brutos, que demuestra la capacidad del método presentado de cara a obtener datos de tensiones residual en brutos a partir de los cuales se pueden obtener piezas finales. Por otro lado, se expone un análisis teórico del potencial de control de la distorsión utilizando el modelo empírico de tensiones residuales inducidas por el mecanizado, el cual demuestra la posibilidad de controlar la distorsión final de las piezas esbeltas de titanio mediante la inducción de tensiones residuales de mecanizado customizadas en las superficies.

Finalmente, se evalúa la predicción de la distorsión tras el mecanizado en una pieza real utilizando la geometría de la pieza, el material, las tensiones residuales y los datos del proceso. Los resultados obtenidos de forma sencilla y rápida muestran una estimación de distorsión tras el mecanizado precisa, así como el rango de incertidumbre de dicha estimación. De esta forma, se presenta un modelo híbrido de predicción de distorsiones para realizar estudios preliminares durante la etapa de planificación del proceso y el desarrollo de estrategias de fabricación optimizadas minimizando la distorsión de la pieza final y facilitando la toma de decisiones. Este método permite evitar las actuales estrategias de mecanizado capa a capa, reduciendo los costes asociados a largos procesos de producción basados en ensayos experimentales. Además, se presenta un procedimiento reducido de eliminación de capas en la máquina (*reduced on-machine Layer removal*) y estimación de tensiones residuales iniciales en brutos, el cual acelera la caracterización y permite su implementación en las líneas de producción.

Acknowledgements

Esta tesis no hubiera sido posible sin el apoyo de varias personas e instituciones a las que quiero mostrar mi más sincero agradecimiento.

En primer lugar a Juan por su apoyo incondicional, incluso después de muchas noches sin dormir, y por darme fuerzas para seguir cuando no veía más opción que abandonar. También quiero agradecerle a Jon por la paciencia y buen humor con el que ha sido capaz de contagiarme incluso en los peores momentos. De la misma forma muchas gracias a mi madre, a mi tía, a mis hermanas Marta y Sofía y a mi aita, por apoyarme siempre sin exigir nada a cambio.

También me gustaría mencionar a algunos compañeros que han hecho de esta experiencia un recuerdo imborrable (Santi, Iker, Ainhoa, entre otros), y a aquellos que desde la distancia me habéis ayudado más que lo que se os puede agradecer con estas líneas (Klaus, Jose, Hostaizka, Adriana).

Por último, pero no menos importante, gracias a mis amigos, sin los cuales yo no sería nada. Gracias Ene y Mai por creer en mí y empujarme hacia adelante tanto mental como físicamente, y gracias al resto de la cuadrilla por esas cañas y conversaciones reconstituyentes (Amaia, Jani, Ruth, Bea, Sheila, Nagore, Nerea, Udane, Elena, Odile, Eneritz, Alaitz, Jera, Ane, Nekane). Gracias también a Silvia y Miren, por preocuparos siempre por mí y estar ahí pase lo que pase. Y gracias Alba por todos los abrazos (incluso por los que he esquivado).

Por último, gracias a mis directores de tesis y a Ideko por darme la oportunidad de realizar la tesis y guiarme a lo largo del proceso.

Contents

Declaration of Authorship	i
Abstract	iii
Resumen	v
Acknowledgements	vii
List of Figures	xii
List of Tables	xix
Abbreviations	xxi
Symbols	xxii
1 Introduction	1
1.1 Context	1
1.2 Necessity	3
1.3 Justification	3
1.4 Objective & scope	5
2 State of the Art	7
2.1 Materials for aerospace structural components	7
2.1.1 Aluminium	7
2.1.2 Titanium	9
2.1.3 Milling process	10
2.2 Machining distortion sources	12
2.2.1 Residual stresses (RS): Fundamental concepts	12
2.2.1.1 Bulk or Blank-Initial Residual stresses (BIRS)	13
2.2.1.2 Machining-Induced Residual Stresses (MIRS)	16
2.2.2 Cutting loads: Cutting forces and heat	18
2.2.3 Clamping loads	19
2.3 Distortion calculation and research	19
2.3.1 Classification upon modeling approach	20

2.3.1.1	Finite Element modeling (FEM)	20
2.3.1.2	Analytical	23
2.3.1.3	Other modeling approaches	28
2.3.2	Classification upon input data	29
2.3.2.1	Considering 1 Source of Distortion	30
2.3.2.2	Coupling 2 Sources of Distortion	31
2.3.2.3	Coupling Multiple Sources of Distortion	32
2.3.3	Discussion upon distortion calculation and research	33
2.4	Residual stress data acquisition	33
2.4.1	BIRS data acquisition	33
2.4.1.1	BIRS modeling	33
2.4.1.2	BIRS measurement	34
2.4.2	MIRS data acquisition	44
2.4.2.1	MIRS modeling	44
2.4.2.2	MIRS measurement	46
2.4.3	Discussion upon RS characterization	48
2.5	Distortion Control	49
2.5.1	Offline Methods	49
2.5.2	Online Methods	54
2.5.3	Discussion upon distortion control	55
2.6	Conclusions and research lines	57
3	Bulk or blank-initial residual stresses	59
3.1	Introduction	59
3.2	BIRS measurement by on-machine LR	62
3.2.1	Formulation	63
3.2.1.1	One dimensional (1D) formulation	63
3.2.1.2	Two dimensional (2D) formulation	65
3.2.2	Expansion of the on-machine LR formulation	66
3.2.2.1	Initial curvature consideration	66
3.2.2.2	MIRS consideration	68
3.2.2.3	Ribbed geometries: Semi-non-destructive method	70
3.2.2.4	Multicoupled formulation	77
3.3	Uncertainty assessment of the on-machine LR	78
3.3.1	Procedure for uncertainty assessment	79
3.3.1.1	Data treatment	80
3.3.1.2	Test-case definition	82
3.3.2	Preliminary analysis	83
3.3.2.1	<i>Mechanical properties (E, ν):</i>	83
3.3.2.2	<i>Geometry (b, e):</i>	85
3.3.2.3	<i>Probing (p):</i>	89
3.3.2.4	Preliminary study summary	90
3.3.3	Analysis of critical variables	90
3.3.3.1	Monte Carlo simulations	90
3.3.3.2	Data Filtering	95
3.3.3.3	Extension of the analysis to different geometries and BIRS profiles.	98

3.3.4	Conclusions of the uncertainty assessment	100
3.4	Summary and discussion	101
4	Machining-induced residual stresses	102
4.1	Introduction	102
4.2	Measurement methods	103
4.2.1	Hole Drilling (HD) method	103
4.2.2	X-Ray Diffraction (XRD) method	106
4.2.3	Discussion upon MIRS measurement methods	113
4.3	Aluminium MIRS measurement by iHD	115
4.3.1	Materials and procedure for machining test	115
4.3.2	iHD measurement procedure	116
4.3.3	iHD Results	117
4.4	Titanium MIRS measurement: uncertainty assessment	120
4.4.1	Materials and procedure for machining test	120
4.4.2	XRD Measuring Procedure	121
4.4.3	Repeatability and Reproducibility (RR) study of surface MIRS measured by XRD	126
4.4.4	Inter-method comparison for in-depth MIRS measurements: iHD vs. XRD	128
4.4.4.1	XRD measurements	129
4.4.4.2	iHD measurements	130
4.4.4.3	Comparison results analysis	131
4.5	MIRS modeling	133
4.5.1	Empirical models	133
4.5.2	Materials and procedure for MIRS data acquisition	135
4.5.3	Development of the MIRS empirical model	138
4.5.4	Model evaluation	142
4.5.5	Conclusions	148
4.6	Summary	149
5	Distortion prediction for aerospace structural components	152
5.1	Introduction	152
5.2	Experimental verification of BIRS characterization by on-machine LR	153
5.2.1	Test-case definition and experimental procedure	155
5.2.2	Results	156
5.2.3	Discussion	162
5.3	Analysis of distortion control through MIRS customization	163
5.3.1	Test definition	164
5.3.2	Results	166
5.3.3	Discussion	171
5.4	Prediction of final part distortion	171
5.4.1	Reduced LR measurement and BIRS estimation	172
5.4.2	Distortion prediction and uncertainty assessment	174
5.4.3	Test-case definition and experimental procedure	175
5.4.4	Results	181
5.4.5	Discussion	183
5.5	Summary and conclusions	184

6	Conclusions and future work	187
6.1	Accomplishments	187
6.2	Conclusions	189
6.3	Future work	190
6.4	Scientific contributions	191
6.4.1	Indexed articles	191
6.4.2	Scientific conferences	191
	 Bibliography	 193

List of Figures

1.1	Global gross domestic product (GDP) forecast to return to pre-crisis trend by mid-decade [1].	2
1.2	Machining distortion related to different geometries: a) Thin aluminium part [7], b) Bearing ring [8], c) Gear box [9].	4
2.1	Distribution of structural materials used on selected Boeing commercial aircrafts [10].	8
2.2	Trends and Forecast for the Global Titanium in the Global Aerospace Industry Market [13].	9
2.3	Orthogonal cutting process sketch with three main cutting zones [14].	10
2.4	Conventional milling (left) vs. Climb milling (right).	11
2.5	Classification of the machining distortion sources.	12
2.6	Distortion due to stress relaxation of a C-17 Cargo floor beam machined from die forging, with no stress relief [22].	15
2.7	Schematic of the MIRS formation in orthogonal cutting process with decomposed influence from different regions [43].	16
2.8	Classifications scheme of distortion prediction models.	20
2.9	FEM distortion modeling workflow diagram, including different modeling techniques.	21
2.10	Stress state, bending moment and deformed condition of the specimen when the initial stress balance of the specimen is broken due to material removal.	24
2.11	Sketch of the machining distortion process and energy release mechanism [107].	25
2.12	Flow chart for predicting machining distortion combining the bending moment and strain energy theories [38].	27
2.13	Measurement penetration vs. spatial resolution for various RS measurement methods [18].	37
2.14	Sketch of the crack compliance method for measuring BIRS showing the superposition principle used to calculate deformations from released stresses. [159].	37
2.15	Sketch of contour method for measuring BIRS showing the superposition principle, where stresses are plotted on one quarter of the original body [166].	38
2.16	Set-up for the Layer Removal Method using EDM and strain gauges [168].	39
2.17	Sketch of the on-machine LR in 1D, with measurements and material removal in opposite faces of the part [169].	39
2.18	Sketch of the deep hole contour method [173].	40
2.19	Plane plate with BIRS fulfilling the stress conditions for LR method: a) Initial state, no material is machined; b) in-process state indicating in grey color the layer to be removed.	43
2.20	HD commercial rig by HBM [189].	46

2.21	XRD commercial equipment by Stresstech [192].	47
2.22	Classification of distortion control strategies.	49
2.23	General workflow for offline distortion control.	50
2.24	Best-offset strategy for machining distortion control [135].	51
2.25	The material removal sequence vs. evolution of machining distortion [209].	52
2.26	MIRS profiles for different depths keeping constant the other machining conditions [53].	53
2.27	Control method based on the combination of enhancing equivalent stiffness and applying a interim step of stress relieve (setting parts freely for a time, aging or vibratory stress relieve [217].	54
3.1	BIRS measured in aluminium 7050: a) before stress relief, T74; b) after stress relief, T7451 [24].	60
3.2	BIRS profile example using polynomial functions to approximate experimental BIRS measurements in rolled plates. Only one half of the profiles is shown because of the symmetrical distribution assumption. [92].	61
3.3	BIRS measured in different sections of Al7449 blanks by neutron diffraction [112].	61
3.4	On-machine LR method procedure for BIRS measurement.	62
3.5	Discretization of the cross-section and mean stress σ_i^B of the layer i	64
3.6	Initial deformation of the machining blank in the unclamped form and, bending moment and stress applied by the clamping to flatten the initial curvature.	66
3.7	Discretization of the cross-section and stresses acting when the raw part with initial curvature is clamped.	67
3.8	MIRS on the surface, sub-layers after machining the three first layers and distances to the neutral plane of each of the affected layers.	69
3.9	Representation of the equivalent cross-sections in X and Y directions.	70
3.10	Discretization of the equivalent geometry cross-section for the ribbed LR.	71
3.11	Curvature progression due to ribbed LR simulation with the analytical formulation for the equivalent cross-section and the numerical model.	72
3.12	Workflow for equivalent bending stiffness calculation in ribbed part.	73
3.13	Diagrams for the BIRS characterization in ribbed geometries using the on-machine LR based on hybrid approach and I^{eq}	73
3.14	Representation of the FEM model of a quarter of a machining plate and detail of the sub-layers discretization (left); front and top views of the model including boundary conditions (right).	74
3.15	Remote displacement boundary conditions with deformable behaviour.	75
3.16	Element deactivation in FEM using the Birth and Death technique for the simulation of the full LR.	75
3.17	Curvature progression due to ribbed LR simulation with the the numerical model and analytical formulation using the equivalent bending stiffness I^{eq} .	76
3.18	Discretization of the cross-section and stresses considered in the multi-coupled formulation: a) Equivalent geometry discretization; b) Stresses throughout the cross-section BIRS, MIRS and stresses due to clamping forces to flatten the initial curvature.	77
3.19	Methodology used for uncertainty assessment of the on-machine LR method.	79
3.20	Options for assigning values of bulk stresses in the layers without curvature.	81
3.21	Geometry of the test-cases for the on-machine LR uncertainty assessment: a) Full LR; b) Ribbed LR.	82

3.22	BIRS profiles used for the uncertainty assessment in Al 7050-T7451: a) Preliminary study; b) Study of critical parameters.	83
3.23	Uncertainty assessment with a Young modulus E error of $\pm 2\%$ for the full LR 2D: a) curvatures (Phase 1), b) stresses (Phase 2) and, c) curvatures (Phase 3).	84
3.24	Uncertainty assessment with a Poisson coefficient ν error of $\pm 4\%$ for the full LR 2D: a) curvatures (Phase 1), b) stresses (Phase 2) and, c) curvatures (Phase 3).	85
3.25	Uncertainty assessment with a blank width b error of $\pm 2\%$ for the ribbed LR 1D: a) curvatures (Phase 1), b) stresses (Phase 2) and, c) curvatures (Phase 3).	86
3.26	Uncertainty assessment with a layer thickness e error of $\pm 0.05\text{mm}$ for the full LR 1D: a) curvatures (Ph. 1), b) stresses (Ph. 2) and, c) curvatures (Ph. 3).	86
3.27	Uncertainty assessment with a layer thickness e error of $\pm 0.05\text{mm}$, only in the second layer e_2 for the full LR 1D: a) curvatures (Phase 1), b) stresses (Phase 2) and, c) curvatures (Phase 3).	87
3.28	Uncertainty due to an input error of 0.2mm in the thickness of different layers “i”, e_i , in the stresses (Phase 2) and deformations (Phase 3, option 2) for the Full LR 1D.	87
3.29	Uncertainty assessment with a layer thickness e error of $\pm 0.05\text{mm}$, only in the second layer e_2 and compensated in the third layer e_3 for the full LR 1D: a) curvatures (Phase 1), b) stresses (Phase 2) and, c) curvatures (Phase 3).	88
3.30	Random probing error introduction on curvature calculations.	89
3.31	Uncertainty assessment with a random probing p error within a $\pm 0.010\text{mm}$ range for the full LR 1D: a) curvatures (Phase 1), b) stresses (Phase 2) and, c) curvatures (Phase 3).	90
3.32	Histogram for the curvatures obtained in machining step ‘j’ when introducing random probing errors for 2000 iterations.	91
3.33	Results for Monte Carlo simulations of layer thickness and probing random errors for a full LR in 1D: Phase 1 curvatures and Phase 2 stresses.	92
3.34	Results for Monte Carlo simulations of layer thickness and probing random errors for a ribbed LR in 1D: Phase 1 curvatures and Phase 2 stresses.	92
3.35	Results for Monte Carlo simulations of layer thickness and probing random errors for a full LR in 1D: Phase 3 curvatures, curvatures obtained using the different options from Figure 3.20.	93
3.36	Results for Monte Carlo simulations of layer thickness and probing random errors for a ribbed LR in 1D: Phase 3 curvatures, curvatures obtained using the different options from Figure 3.20.	93
3.37	Results for Monte Carlo simulations of random probing errors for a Ribbed geometry in 2D: a) Phase 1, curvatures; b) Phase 2, stresses.	94
3.38	Results for Monte Carlo simulations of random probing errors for a Ribbed geometry in 2D: Phase 3, curvatures obtained using the different options from Figure 3.20.	94
3.39	Weighting functions for data filtering by convolution: a) Gaussian; b) Triangular.	95

3.40	Different curvature filtering applied to Monte Carlo simulations of random probing errors for a Ribbed geometry in 1D: Phase 2, stresses, and Phase 3, curvatures, obtained using different filtering parameters and option 1 stress data treatment (Fig. 3.20).	96
3.41	Results with curvature filtering for Monte Carlo simulations of random probing errors for a Ribbed geometry in 2D: a) Phase 1, curvatures; b) Phase 2, stresses.	97
3.42	Results with curvature filtering for Monte Carlo simulations of random probing errors for a Ribbed geometry in 2D: Phase 3, curvatures obtained using the different options from Figure 3.20.	97
3.43	Results for Monte Carlo simulations of random probing errors for a Ribbed geometry in 1D with different geometries and BIRS profiles: Phase 2, stresses.	99
3.44	Results for Monte Carlo simulations of random probing errors for a Ribbed geometry in 1D with BIRS profiles of the same shape and different magnitude: Ph.2, stresses.	99
4.1	Schematic representation of MIRS profile in milling including parameters for a simplified description.	103
4.2	Typical design of strain gauges for HD, including principal stress directions of the type A strain gauge.	104
4.3	Hole and stress depths corresponding to coefficients \bar{a} [189].	106
4.4	Diffraction of X-rays by a crystal lattice, in which planes hkl are parallel to the surface [197].	107
4.5	Strain effect on the diffraction peaks [19].	108
4.6	Deformation measured by XRD at the sample coordinates [254].	109
4.7	Different scenarios of $d_{\phi\psi}$ vs. $\sin^2\psi$ curves: a) isotropic material, with a biaxial state of stress; b) material with large grain size; c) isotropic material, with triaxial stress state; d) material with steep stress gradient; e) material with preferential crystallographic texture [19].	112
4.8	Sample rotations possibilities for measuring stresses by XRD.	113
4.9	XRD measurement in Al7050-T7451 showing texture: a) Diffraction peaks of different intensities; b) $d_{\phi\psi}$ versus $\sin^2\psi$ graph showing the typical curved shape.	114
4.10	Face milling process, helical outwards strategy in up/down milling.	116
4.11	MIRS measuring points in the Al 7050-T7451 part.	117
4.12	MIRS measured in the Al 7050-T7451 part by iHD in four different locations.	118
4.13	Average MIRS measured in the Al 7050-T7451 part by iHD.	118
4.14	MIRS measuring points in the Al 7175-T7351 part.	119
4.15	MIRS measured in Al 7175-T7351 parts by iHD in six different locations.	119
4.16	Average MIRS measured in the Al 7175-T7351 parts by iHD.	120
4.17	Face milling process, Zig strategy.	121
4.18	XRD equipment: a) Diffractometer including goniometer and main unit; b) Electropolishing machine and electrolyte.	122
4.19	a) Electropolishing depth vs. time for a fixed set of variables; b) Electropolishing process.	123
4.20	Footprint after electropolishing at 0.12 mm depth after four iterations.	123
4.21	Detectors and collimator of the diffractometer.	124
4.22	Peak fit method settings using a Perason VII function.	125
4.23	Example of a corrected, 1A:0(C), and non-corrected, 1A:0, stress profile.	126

4.24	Measured points sketch for the RR study.	126
4.25	Variability of the measurements made at different points and by different operators.	128
4.26	Locations and directions for in-depth MIRS measurements by XRD and iHD methods: a) point locations; b) directions.	129
4.27	XRD measurement setup and electropolishing traced.	129
4.28	iHD in-depth MIRS measurement.	130
4.29	MIRS measured by XRD and iHD averaged for points P1, P2 and P3: a) Feed direction; b) Transverse direction.	132
4.30	Flow-diagram of the structure of empirical models.	134
4.31	Clamping of the part with vise for the machining test.	136
4.32	a) Edge naming in Tool T2; b) Tool wear on cutting edge 1 after cleaning machining.	136
4.33	Stress data acquisition process: a) XRD measurement; b) electropolishing.	137
4.34	MIRS empirical model as a function of v_c and f_z based on three regressions.	138
4.35	MIRS experimental values and obtained regression marked with dashed lines as a function of penetration depth ($v_c=60$ m/min and $f_z=0.02$ mm).	139
4.36	EDCF coefficient a_4 of R1 (dots) and regression R2 (dashed lines) as a function of the feed per tooth ($v_c=60$ m/min and $f_z=0.02$ mm, order 2 polynomial).	140
4.37	Coefficient of regression R2, a_{40} , (dots) and regression R3 (dashed lines) as a function of the cutting speed ($v_c=60$ m/min and $f_z=0.02$ mm, order 2 polynomial).	141
4.38	Pearson coefficient, r , values for the comparison of the different polynomial combinations against the experimental data used for building the model.	143
4.39	Mean error, \overline{er} , obtained for the comparison of the empirical model against the experimental data used for building the model.	143
4.40	3D representation of MIRS results obtained with the empirical model (surface) in comparison to experimental results (dots).	143
4.41	Pearson coefficient, r , values for the comparison of the model with different polynomial combinations against the experimental data used for validating the model.	144
4.42	Mean error, \overline{er} , values for the comparison of the model with different polynomial combinations against the experimental data used for validating the model.	145
4.43	Pearson coefficient, r , values of the MIRS profiles predicted with the model with different polynomial combinations against experimental data in the transverse direction.	146
4.44	Pearson coefficient, r , values of the MIRS profiles predicted with the model with different polynomial combinations against experimental data in the feed direction	147
4.45	Effects of the cutting speed and feed per tooth on MIRS profile characteristic parameters in transverse direction.	148
5.1	Process route for the experimental verification of the on-machine LR for BIRS characterization.	154
5.2	Geometry of the Al7050-T7451 aluminium part.	155
5.3	On-machine LR in a ribbed part for a 'j' layer: (a) Machining step; (b) Measuring step done by probing in the machining centre after the clamping is released.	156

5.4	Probing grid of the BIRS measurement by on-machine LR.	156
5.5	Curvature progressions obtained experimentally by on-machine LR in two parts (A and B), using: a) Raw probing data; b) Filtered probing data. . .	157
5.6	BIRS obtained experimentally by on-machine LR with the multi-coupled formulation in two parts (A and B), using: a) Raw probing data; b) Filtered probing data.	157
5.7	BIRS profiles completed using the four BIRS data treatment options in part A using filtered probing data.	158
5.8	Part A: Experimental curvatures measured by probing compared with the ones obtained from stresses in Phase 3, for different data treatment options, displaying the uncertainty range for a probing error of 0.010mm.	159
5.9	Part B: Experimental curvatures measured by probing compared with the ones obtained from stresses in Phase 3, for different data treatment options, displaying the uncertainty range for a probing error of 0.010mm.	160
5.10	BIRS measured experimentally by on-machine LR for parts A and B including the uncertainty ranges.	161
5.11	Distortion simulation including uncertainty range and experimental values for the two test parts A and B, using the BIRS measured by ribbed on-machine LR.	161
5.12	Geometries of the dist. analysis in Ti6Al4V upon MIRS customization. . .	164
5.13	MIRS profiles used for building different case combinations for the distortion analysis on Ti6Al4V upon MIRS customization.	165
5.14	Sketch of the upper and lower surfaces in which MIRS loads are applied for the geometry S1.	165
5.15	Curvatures obtained under different MIRS variations in the part geometry S1 of Ti6Al4V.	166
5.16	Different distortion shapes as a result of the curvatures combinations for the cases 5, 7, 8, 9, 13 and 14 in the part geometry S1.	167
5.17	Curvatures obtained under different MIRS variations in the part geometry S3 of Ti6Al4V.	168
5.18	Curvatures obtained under different MIRS variations in the part geometry A1 of Ti6Al4V.	168
5.19	Curvatures obtained under different MIRS variations in the part geometry A2 of Ti6Al4V.	169
5.20	Analysis of the influence of wall height on the study of distortion control through MIRS customization.	170
5.21	Normalized BIRS profiles in different blanks fulfilling the hypothesis analogous stress profile shape.	172
5.22	Procedure of reduced LR and BIRS estimation.	173
5.23	Workflow for final part distortion prediction, including uncertainty.	175
5.24	Simplified part geometry of Al7175-T7351 for the machining distortion analysis.	176
5.25	Dimensions of the simplified Al7175-T7351 part in millimeters.	176
5.26	Recurring distortion shape in the machining of the Al7175-T7351 aerostructure.	176
5.27	Part location within the blank and offset in each of the sides.	177
5.28	BIRS measured in a machining Al7175-T7351 blank of 130x700x80mm by on-machine Full LR.	178

5.29	a) Setup 1: open pocket side machining; b) Setup 2: Triangle-ribbed side machining; c) Setup 3: small lateral side machining; d) Setup 4: large lateral side machining.	178
5.30	Reduced on-machine LR in Setup 1, open pocket side: a) machining of a layer 'j'; b) probing.	179
5.31	Machining of the two parts (<i>a</i> and <i>b</i>) in Setup 1, open pocket side, and Setup 2, triangle-ribbed side.	179
5.32	a) Final part machined; b) Measurements in a CMM.	180
5.33	Final part probing in Part <i>a</i> : a) Grid 3x9; b) Sweeping the open pocket side.	180
5.34	Data obtained in the reduced LR method: experimental and simulation curvatures of the reduced LR method.	181
5.35	BIRS obtained by full LR in one sacrificial blank (σ_{full}^B) and estimated BIRS for the blanks <i>a</i> (σ_a^B) and <i>b</i> (σ_b^B), from which final parts were obtained. . .	181
5.36	BIRS estimated with uncertainty ranges including measuring uncertainty due to probing errors: a) Part <i>a</i> ; b) Part <i>b</i>	182
5.37	Distortion FEM simulation for obtaining the final part equivalent bending stiffness of parts <i>a</i> and <i>b</i> , displayed in two different orientations.	182
5.38	Distortion simulation using estimated BIRS, including uncertainty range and experimental values for the two test cases: a) Lowest offset; b) Same offset in both sides, upper and lower sides.	183

List of Tables

2.1	Major attributes of aerospace aluminum alloys [11]	8
2.2	Main origins of residual stress resulting from different manufacturing processes [20].	14
2.3	Advantages, disadvantages and application scope of most common RS measuring methods.	36
2.4	Principles, capabilities and limitations of modeling approaches.	45
2.5	Review of machining distortion control research.	56
3.1	Uncertainty sources of the on-machine LR method.	79
3.2	Parameter definition for the analysis of the main uncertainty sources in the on-machine LR.	83
3.3	Summary of the cases studied in the preliminary analysis.	84
3.4	Cases studied in the analysis of critical variables.	91
3.5	Parameters used in the filtering analysis.	95
3.6	Quantification of the confidence interval (3σ) for the raw and filtered data of the probing uncertainty assessment.	98
3.7	Different geometries analyzed in the extension of the uncertainty assessment due to probing p errors.	98
4.1	Uncertainty ranges for the iHD in Al-alloy and Ti-alloy, calculated according to [189].	114
4.2	Chemical composition of Al-alloys 7050-T7451 and 7175-T7351.	115
4.3	Mechanical properties of Al-alloys 7050-T7451 and 7175-T7351.	115
4.4	Tools used for inducing the MIRS in the aluminium parts.	116
4.5	Cutting parameters used with Tool A1 and Tool A2.	116
4.6	Chemical composition of Ti6Al4V alloy.	120
4.7	Mechanical properties of Ti6Al4V alloy.	120
4.8	Tools used for inducing the MIRS at different cutting conditions.	121
4.9	Cutting parameters used with tool T1.	121
4.10	XRD equipment features: diffractometer and electropolishing machine.	122
4.11	Comparison between the experimental results and nominal values of the titanium high-stress titanium reference.	124
4.12	XRD measuring parameters used for the RR study.	127
4.13	MIRS measured at 3 different locations (P1, P2, P3) by 2 operators.	127
4.14	XRD MIRS measurements for the comparison between methods.	130
4.15	iHD measuring parameters.	130
4.16	iHD MIRS measurements for the comparison between measuring methods.	131
4.17	Tool used for inducing the MIRS at different cutting conditions.	135
4.18	Recommended cutting parameters for the tool T2.	135

4.19	Cutting conditions used in machining test for the MIRS empirical model. .	137
4.20	Regression combinations used for the construction of the MIRS empirical model, where the numbers 1 and 2 are the order of the polynomials of R2 and R3 respectively.	138
4.21	Regression combinations and coefficients for Eq. 4.26.	141
4.22	Pearson coefficient and mean error of the MIRS empirical model against the experimental data.	142
4.23	Pearson coefficient, r , and mean error, $\bar{e}r$, values for the comparison of the model against experimental data not used for building the model.	144
4.24	Pearson coefficient, r , values of the MIRS profiles predicted with the model with different polynomial combinations against experimental data in the transverse direction.	145
4.25	Pearson coefficient, r , values of the MIRS profiles predicted with the model with different polynomial combinations against experimental data in the feed direction	146
4.26	Coefficients of the model constructed with 1st grade polynomials	149
5.1	Machining conditions used for the experimental test	155
5.2	Distortion results as deformations in Z direction (δ_z).	162
5.3	Case combinations analyzed regarding MIRS magnitude and direction variations.	166
5.4	Maximum and minimum deformations in Z direction, δ_z , for the curvatures of parts S1, S3, A1, and A2 under different combinations of MIRS.	169
5.5	Cases grouped according to the results similarity in magnitude and trend. .	170
5.6	Machining conditions used for the experimental test.	179
5.7	Distortion results as deformations in Z direction (δ_z) of the parts a and b . .	183

Abbreviations

BIRS	Bulk or B lank- I nitial R esidual S tresses
CAD	Computer- A ided D esign
CAM	Computer- A ided M anufacturing
CMM	Coordinate M easuring M achine
CNC	Computer N umerical C ontrol
DHC	Deep H ole C ontour
DHD	Deep H ole D rilling
EDCF	Exponential D ecay C osine F unction
EDM	Electrical D ischarge M achining
FCM	Finite C ell M ethod
FDM	Finite D ifference M ethod
FEM	Finite E lement M odeling
FWHM	Full W idth at H alf M aximum
HD	Hole D rilling
iHD	incremental H ole D rilling
LR	Layer R emoval
MIRS	Machining- I nduced R esidual S tresses
MC	Monte C arlo
MPE	Minimum P otential E nergy
MRR	Material R emoval R ate
OEM	Original E quipment M anufacturer
RR	Repeatability and R eproducibility study
RS	Residual S tresses
STL	Stereolithography
XRD	X - R ay D iffraction

Symbols

a_e	Width of cut	mm
a_i	Area of the layer i	mm ²
a_p	Depth of cut	mm
\bar{a}, \bar{b}	Tabulated calibration constants of HD method	-
A, B, ... F	Second order surface coefficients	-
\bar{A}, \bar{B}	Calibration constants of HD method	MPa
Ak	Matrix of areas and leverages	mm ³
b	Blank width	mm
c	Mean extrapolation coefficient	-
c^{MC}	Cloud of extrapolation coefficients from Monte Carlo simulation	-
C_0	Amplitude of the EDCF	MPa
d	Inter-planar distance	nm
d_0	Inter-planar distance under stress free conditions	nm
$d_{\phi\psi}$	Inter-planar distance as function of the angles ϕ and ψ	nm
D	Diameter	mm
e	Layer thickness	mm
\bar{e}_r	Mean error	MPa
e^M	Sub-layer thickness	mm
E	Young modulus	MPa
f_z	Feed per tooth	mm
G_{ij}	Kernel function	mm/N
$h_{\phi\psi}$	Unit vector in the direction of $\epsilon_{\phi\psi}$	-
H	Thickness of the plate	mm
i	Layer number	-
I	Second moment of area of the cross-section	mm ⁴

I^{eq}	Equivalent stiffness of cross-section	mm ⁴
I_{B2}^{eq}	Eq. stiff. of cross-section corresp. to reduced LR (blank 2)	mm ⁴
$I_{B2,F}^{eq}$	Eq. stiff. of cross-section corresp. to the final part (blank 2)	mm ⁴
I^{geo}	Second moment of area of the equivalent geometry	mm ⁴
j	Machining step number	-
k_{ij}	Leverage from layer i to the parts' neutral plane at j step	mm
k_{ij}^s	Leverage from sub-layer s to the parts' neutral plane at j step	mm
m	Total number of machining steps	-
M	Slope of the strain measured on the graph $\epsilon_{\phi\psi}^{hkl} - \sin^2\psi$	-
Mb	Bending moment	Nmm
Mb^0	Bending moment due to flattening the blank's initial curvature	Nmm
Mb^B	Bending moment due to BIRS	mm
Mb^M	Bending moment due to MIRS	mm
n	Total number of layers	-
np	Distance to the neutral plane from the bottom of the part	mm
N	Reflection order of Braggs' Law	-
p	Probing or deformation measurements in LR test	mm
P	Mean pressure of RS of Hole Drilling method calculation	MPa
Q	Tangential stress component of the HD method calculation	MPa
r	Pearson coefficient	-
$R1, R2, R3$	First, second and third regression	-
s	Sub-layer number	-
S	Total number of sub-layers in MIRS affected zone	-
$S1, S2, S3$	Sample coordinates in XRD	-
$S_1^{hkl}, \frac{1}{2}S_2^{hkl}$	Elastic constants of the X-rays for the lattice plane	MPa
T	Tangential stress component in iHD	MPa
v_c	Cutting speed	m/min
v_f	Feedrate	mm/min
VB	Average flank wear	mm
w	Unmachined blank width fraction	mm
x	Depth below the machined surface	mm
$x_{C,max}$	Location of the maximum compressive MIRS from the surface	mm
x_{sta}	Response depth from the surface at which MIRS stabilize	mm
XEI	Vector of curvatures and stiffness	Nmm

z	Number of cutting edges	-
β	Angle of the principal direction	rad
δ_z	Deformation in Z direction	mm
δ_z^{exp}	Experimental deformation in Z direction	mm
δ_z^{sim}	Simulation deformation in Z direction	mm
ΔI^+	Electropolishing intentisty	A
Δm	Mass of material removed by electropolishing	kg
Δt	Electropolishing time	s
ϵ	Strain	-
$\epsilon_{\phi\psi}$	Strain measured as function of the angles ϕ and ψ	-
$\epsilon_{\phi\psi}^{hkl}$	Strain measured as function of ϕ , ψ of crystal plane {hkl}	-
ζ	Damping coefficient of the EDCF	-
θ	Diffraction angle	$^\circ$
θ_0	Position of the diffraction peak without stresses	$^\circ$
λ	Wavelength on the incident radiation	nm
σ	Residual stress	MPa
$\bar{\sigma}$	Average measured stress	MPa
$\hat{\sigma}$	Predicted stress	MPa
$\bar{\hat{\sigma}}$	Average predicted stresses	MPa
σ_1	Stress measured in Direction 1	MPa
σ_3	Stress measured in Direction 3	MPa
σ_{max}	Maximum principal stress	MPa
σ_{min}	Minimum principal stress	MPa
σ_ϕ	Normal stress in the coordinates of the sample	MPa
σ^0	Stresses due to flattening the initial curvature	MPa
σ^B	Bulk or Blank-Initial Residual stresses, BIRS	MPa
σ_{full}^B	BIRS measured by full LR test	MPa
σ_{B1}	BIRS of blank 1	MPa
σ_{B2}	BIRS of blank 2	MPa
σ_{B1}^{exp}	BIRS obtained from experimental curvatures of LR test (blank 1)	MPa
σ_{B1}^{MC}	Cloud of BIRS from Monte Carlo simulations (blank 1)	MPa
σ_{B2}^{MC}	Cloud of BIRS estimated with c^{MC} (blank 2)	MPa
σ^M	Machining-Induced Residual Stresses, MIRS	MPa

$\sigma_{C,max}^M$	Maximum compressive MIRS	MPa
σ_{Sur}^M	MIRS profile parameter, Peak RS at the surface	MPa
3σ	Confidence interval of 99.7% (three standard deviations)	MPa
τ_{13}	Shear stress measured in direction 13	MPa
τ_ϕ	Shear stress in the coordinates of the sample (S1,S2,S3)	MPa
ν	Poisson ratio	-
ϕ	Rotation angle in XRD	$^\circ$
φ	Phase angle of the EDCF	$^\circ$
χ	Curvature	mm^{-1}
χ_0	Initial curvature of the machining blanks	mm^{-1}
χ^{an}	Curvatures with analytical formulation & equivalent geometry	mm^{-1}
χ^{exp}	Experimental curvature	mm^{-1}
χ_{B1}^{exp}	Experimental curvatures of full LR test (blank 1)	mm^{-1}
χ_{B2}^{exp}	Experimental curvatures of reduced LR (blank 2)	mm^{-1}
χ^{FEM}	Curvature with FEM model and real geometry	mm^{-1}
$\chi_{B2,F}^{MC}$	Curvatures cloud of final part simulation (input σ_{B2}^{MC})	mm^{-1}
χ^{sim}	Simulation curvatures	mm^{-1}
χ_{B2}^{sim}	Calculated curvatures of reduced LR simulation (blank 2)	mm^{-1}
$\chi_{B2}^{sim,MC}$	Curvatures cloud of reduced LR simulation (input σ_{B1}^{MC})	mm^{-1}
ψ	Inclination angle in XRD	$^\circ$
ω_d	Damping frequency of the EDCF	rad/s

*To Juan and my family, whose love, encouragement and support made it
all possible.*

Chapter 1

Introduction

Machining distortion is a common challenge when producing aerostructures. The purpose of this work is the understanding of machining distortion in aerostructures for the subsequent development of a procedure to determine residual stresses and calculate distortion in production lines.

1.1 Context

Machining blanks undergo large strains and temperature gradients due to primary processes (forging, casting, quenching...) that result in residual stresses. Moreover, the machining process itself also causes additional residual stresses in the surface due the high temperatures and plastic deformations reached. All these stresses together with machining process loads, such as clamping and cutting forces, result in deviations from the nominal geometry and dimensions when the part is released from the clamping, known as machining distortions.

Machining processes play a key role in the manufacturing of precision components such as aerostructures. The capabilities of these processes concerning geometrical accuracy and surface quality, as well as their high productivity, make the use of these processes extensive in the aerospace sector. In fact, although immensely affected by the outbreak of the COVID-19 pandemic, the aerospace sector has proved to be more resilient than what it was expected, reaching pre-pandemic levels much faster than predicted and forecasting a continuous growth in the upcoming years (Fig. 1.1) [1].

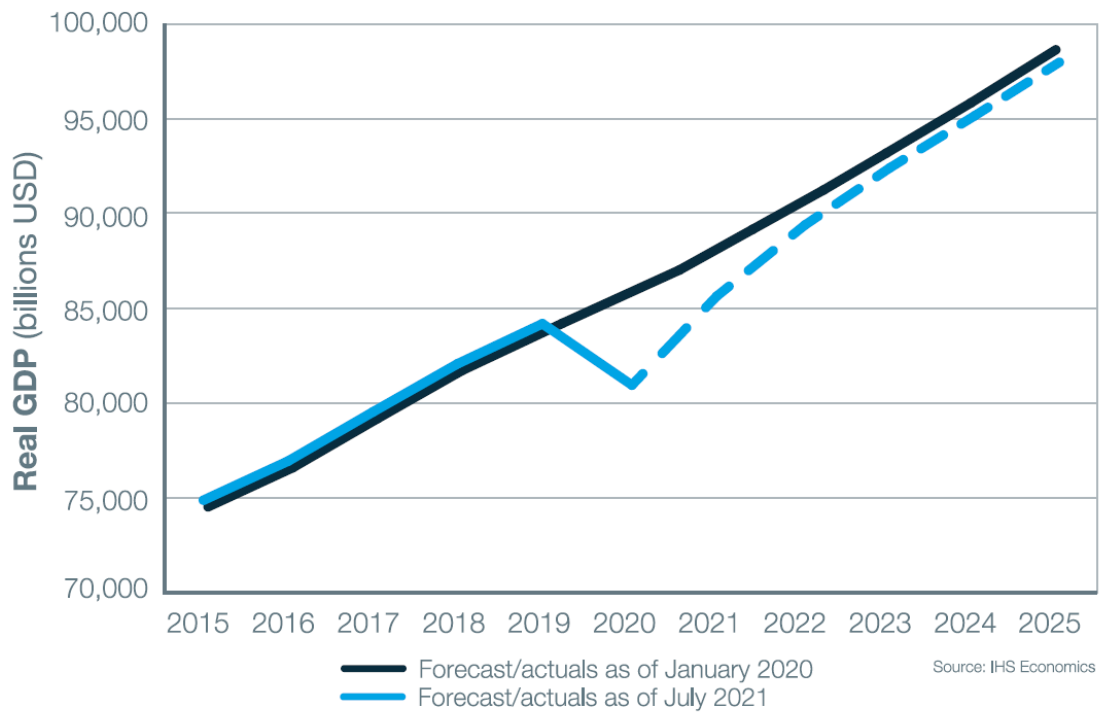


FIGURE 1.1: Global gross domestic product (GDP) forecast to return to pre-crisis trend by mid-decade [1].

According to Boeing Commercial Outlook 2021-2040 [1], the fundamentals that have driven air travel the past five decades and doubled air traffic over the past 20 years remain intact. Medium-term production prospects for aerospace are still promising, assuming global air travel recovers over the next couple of years. In fact, the expected growth of the air traffic is a 4% in the next 20 years, forecasting a global demand of more than 43000 new deliveries. In terms of production, the high demand of aircrafts translates in a high demand of aerostructures for the their fabrication.

Moreover, the rise in ecological aspirations and the increase of fuel price is boosting the efforts of the aerospace sector on reducing the weight of the aircraft structural components. At the same time, the growing safety requirements due to passenger security increases the complexity of aerostructures machining. In addition to the competitiveness of the air transport compared to other transportation means, the economic margins are squeezed leaving Tier 1 & 2 manufacturers for OEMs in a hard position. In a way to overcome this situation and push forward industry, investment in R&D has boosted the Zero Defect Manufacturing (ZDM) concept, which aims at eliminating defects and process errors, such as machining distortion, while improving the process efficiency and product quality.

1.2 Necessity

As mentioned, aerospace components are bonded to the concepts of passenger security and weight reduction. For this reason, machining aerostructures implies high accuracy and quality demands difficult to fulfill. The appearance of uncontrolled defects or non-conformities in the machined parts can reduce significantly the productivity and overall efficiency of the process. An important category of these non-conformities is machining distortion, which entails the discrepancies between the nominal geometry and dimensions aimed at the process planning stage, and the actual ones after the machining process is executed.

The appearance of machining distortions is a recurring concern at a costly price in the precision manufacturing industry. A study by the aircraft company Boeing estimated the rework and scrap cost due to part distortions to be over 290 million dollars for four aircraft programs, while revealed that thin-walled aerospace parts stand a 47% chance for geometrical or dimensional non-conformities after machining [2]. In other sectors producing high precision parts, distortions are considered a great concern, as it was estimated a yearly economic loss of 850 million euros for the German automotive, machine tool and power transmission industries [3]. In the specific case of bearings, a leader manufacturer estimated that the rework costs can amount to 30-40% of the total component cost depending on the size of the component, due to the expensive technologies required for the job, such as hard grinding [4].

Even in cases where means are put into reducing or correcting distortions, it is not uncommon to result in component rejection [3]. Some other issues related to machining distortions are linked to assembly, as it is the downstream phase of product development and it is highly influenced by machining distortion. In best cases, where discrepancies are not excessive and the component is just within tolerances, assembly often requires costly additional time. Other followed approaches consist of straightening or bending the components into the desired shape, which involves long processing times and is not always possible, particularly with complex geometries. Moreover, the effect of distortions on the component performance and lifetime can be significant when pre-stressed assembly states occur. These states may affect negatively the product functionality, increasing stress concentration in key areas and reducing fatigue life [5].

1.3 Justification

Even if machining distortion is a longstanding technical hitch, it is not yet solved and keeps preventing process optimization and lead time reduction. Furthermore, as distortion

appears at the final phase of production chain, right before assembly, component rejection implies the high costs related to the upstream manufacturing processes, material, energy and time.

The multiple sources of distortion (residual stresses, thermo-mechanical machining loads, clamping loads) and their interrelation make machining distortion an issue which is currently confronted by long processes, including repeated unclamping, check and correction sequences, which highly depend upon the experience of the skilled workers.

One of the main reasons for this lack of repeatability and randomness are residual stresses. Indeed, residual stresses play a key role in the dimensional instability as they are inherent to manufacturing processes. Their creation and development is spread over the entire manufacturing chain and, even though they can be reduced by thermal and mechanical treatments, the unbalance produced by the elimination of material through machining breaks the initial force and momentum balance. The understanding of residual stresses and their relation with dimensional instabilities is key for the control and minimization of distortions.

The final part geometry has also a big influence on machining distortion because its implications in the distortion sources, like bulk stresses prior to machining or the clamping strategy required. Besides, the amount of material that will be removed or the asymmetry of the final geometry also play a key role, to the point that even mathematical correlation can be calculated between part geometry and distortion [6]. In this way, classifications of part geometries together with the typical distortion issues linked to them can be performed. For instance, slender asymmetric geometries imply different predominant distortion source from axisymmetric geometries or other complex shape components, as depicted in Figure 1.2.

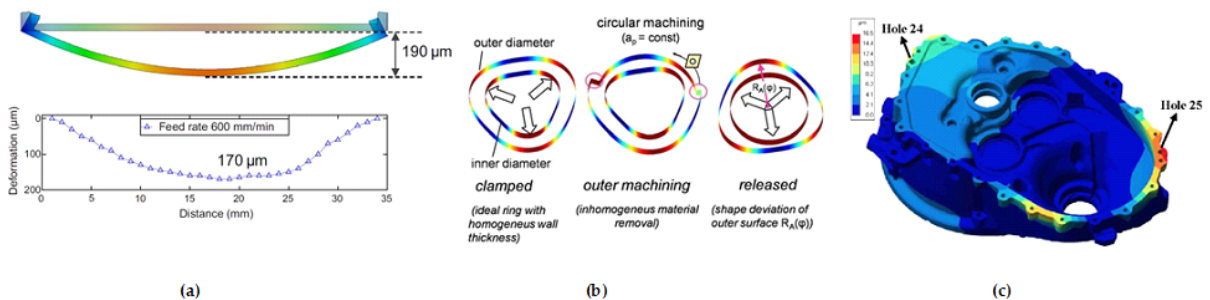


FIGURE 1.2: Machining distortion related to different geometries: a) Thin aluminium part [7], b) Bearing ring [8], c) Gear box [9].

In the case of aerostructures, a number of particular conditions are favourable to part distortion: high material removal ratios, asymmetric geometries, low stiffness due to the

thinness of the features, rigorous tolerance requirements and high productivity demands resulting in aggressive machining conditions. All these circumstances mixed together, make the manufacturing of aerostructures a challenging task with a wide rejection probability.

Up to date there is no solution enabling the quantitative identification of the contribution of each cause to the final distortion, neither which provides guidelines based on source measurement and distortion calculation tools that can be implemented in production lines. In this way, machining distortion is a common and recursive problem depending on human experience which is lacking a method to approach new components by different operators and conditions.

1.4 Objective & scope

In order to provide a solution to the above described problem, the objective of this research is to understand machining distortion in metallic aerostructures and its main sources, and the development of procedures for their quantification in industrial environments and subsequent distortion calculation. This way, production time, scrap cost and energy consumption could be reduced. And, at the same time, new opportunities could be brought to improve the present processes and develop new strategies resulting in a competitive advantage for aerospace manufacturers.

This research, focuses on the study of machining distortion and its relationship with residual stresses in aerostructures with a high material removal ratio. The scope of this work is establishing the basis for the development of residual stress characterization procedures, and building prediction tools focusing not only in the accuracy but also in the capacity to be implemented in industrial environments.

Therefore, this dissertation deals with the problem raised during this introduction, “how can be machining distortion confronted by machining companies with industrially implementable solutions”.

The dissertation is organized as follows:

In the first phase of this study, Chapter 2, the theoretical concepts related to distortion are introduced and critically discussed, including the state-of-the-art investigations in relation to residual stresses, measuring methods, distortion calculation tools and control strategies in aerostructures.

In the second phase of this study, covered in Chapter 3, a measuring method of volumetric stresses of machining blanks in industrial environments is developed and its uncertainty

analyzed. Afterward, Chapter 4, explores superficial residual stresses induced by machining processes and develops an empirical model to predict stresses upon machining conditions.

The third part of the study, Chapter 5, evaluates the practicality of the developments of chapters 3 and 4 through different case-studies. This way, the experimental verification of the bulk or blank-initial residual stresses measuring method in industrial environments is performed; the possibility of controlling distortion through the induction of customized machining-induced residual stresses in the machined surfaces is analyzed; and a fast procedure for BIRS characterization in production lines is presented and experimentally verified. The effects of residual stresses on distortion are determined combining analytical and numerical models.

Finally, Chapter 6 gathers the conclusions of the study and states of future work lines.

Chapter 2

State of the Art

This chapter introduces the sources of machining distortion in aerostructures, and reviews the works on distortion calculation by two different classifications. Afterward, the methods for gathering the residual stress data for distortion calculation are discussed, and the strategies to control distortion developed by academia are analyzed. The chapter finishes with some additional brief concepts on materials of aerostructures, milling processes and residual stress measurements.

2.1 Materials for aerospace structural components

To obtain a continuous performance increase, engineers are constantly seeking for lighter, stronger and more durable components. Due to this, the two materials mainly used in the fabrication of aerostructures are aluminium and titanium.

2.1.1 Aluminium

Aluminium, due to its distinctive advantages, is established as an asset in the manufacturing of structural aeronautic parts. Since the early-1920s, airframes have been built largely out of aluminum. And, even with the increase in the composites use, aluminium remains being the preferred choice particularly in commercial aircrafts. The dominance of aluminum alloys for airframe applications is shown in Figure 2.1 [10]. In current aircrafts, aluminium is found in the fuselage, the wing panes, the rudder, the exhaust pipes, the door and floors, the seats, the engine turbines, and the cockpit instrumentation.

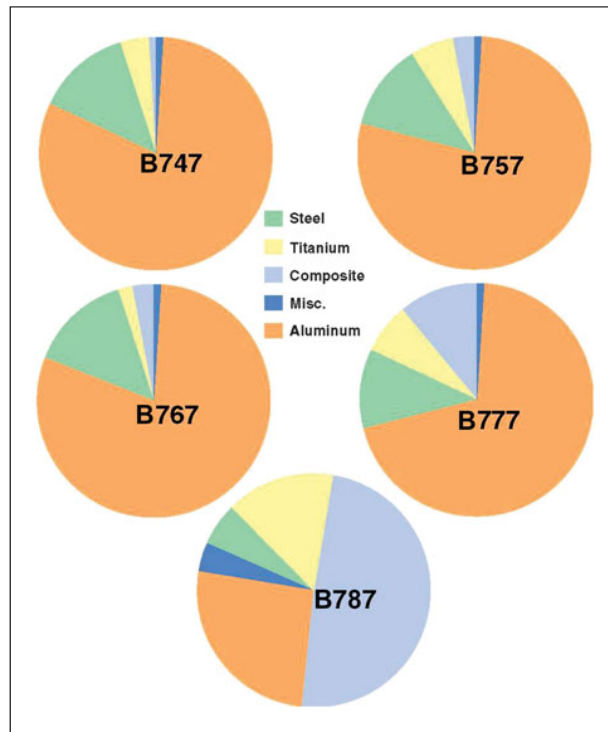


FIGURE 2.1: Distribution of structural materials used on selected Boeing commercial aircrafts [10].

The reasons for the extended use of aluminium are its low cost, high strength-to-weight ratio, heat treatment capability, good cryogenic properties avoiding embrittlement and ease of fabrication. The most used alloys in the aerospace sector are the aluminium–copper (2XXX series), aluminium–magnesium–silicon alloys (6xxx series), and aluminium–zinc (7XXX series). Some of the important properties of each of these alloy series are given in Table 2.1 [11].

TABLE 2.1: Major attributes of aerospace aluminum alloys [11]

2XXX: Al–Cu Alloys	Heat treatable High strength at room and elevated temperatures Typical ultimate tensile strength range: 186–427 MPa Usually joined mechanically but some alloys are weldable
6XXX: Al–Mg–Si Alloys	Heat treatable High corrosion resistance Moderate strength Typical ultimate tensile strength range: 124–400 MPa Readily welded by GMAW and GTAW methods Outstanding extrudability
7XXX: Al–Zn Alloys	Heat treatable Very high strength; special high toughness versions Typical ultimate tensile strength range: 220–606 MPa Mechanically joined

These alloy series are heat-treatable, through which different combinations of mechanical and corrosion resistance properties are inferred. The heat treatments are typically a combination of a solution stage and quenching, followed by natural and artificial aging. For instance, aerospace alloys of the 7XXX family typically have T6 T7 tempers. While T6 treatment would induce excellent mechanical strength but a correspondingly lower corrosion resistance of the alloy, it is for products that do not undergo cold working after solution treatment. Alternatively, intermediate conditions can be attained using suitable variants of the T7 temper, including stress relieve treatments by stretching codenamed by T51 [12].

This work focuses in currently most used aluminium alloys for aerostructures, i.e. Al7050-T7451 and Al7175-T7351.

2.1.2 Titanium

While aluminum still covers the greatest portion of the aircraft, titanium represents also a big share of the material used to build airframes (Fig. 2.1), with a growing trend as depicted in Figure 2.2. In cases where higher strength, outstanding resistance to fatigue and corrosion, or when temperature capabilities need improvement, titanium alloys become the preferred choice. Although titanium is about two-thirds heavier than aluminum, its higher strength results in lesser material (weight) requirement for the same performance. For this reason, titanium is also used to save space in specific cases. As drawbacks, even though it is an abundant material, its high melting point and extreme reactivity makes titanium an expensive material.

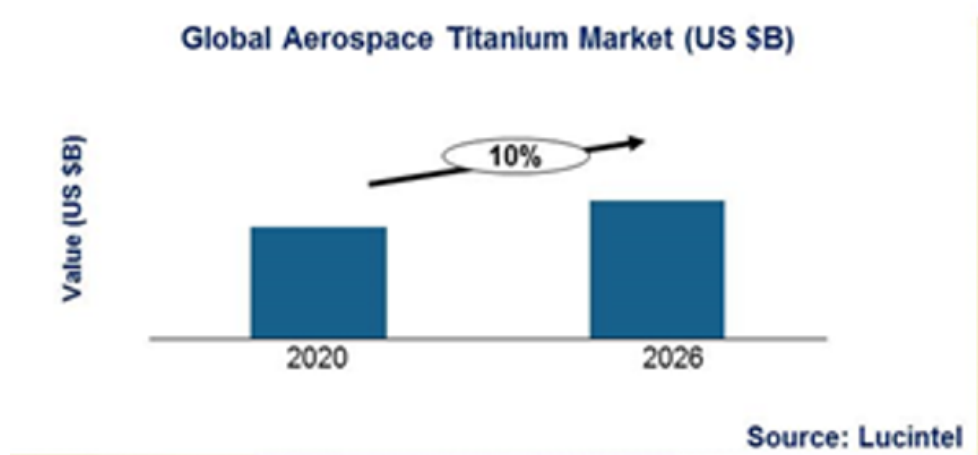


FIGURE 2.2: Trends and Forecast for the Global Titanium in the Global Aerospace Industry Market [13].

Titanium alloys are classified according to the amount of α and β phases retained in their structures at room temperature. The $\alpha + \beta$ alloys, which include Ti-6Al-4V, Ti-6Al-6V-2Sn, and Ti-6Al-2Sn-4Zr-6Mo, have high strengths and a good combination of mechanical properties, rather wide processing windows, and can be used in the range of 315–400°C. In fact, Ti-6Al-4V was one of the first titanium alloys developed and still remains the predominant titanium alloy in the aerospace industry, because of its balanced and robust property set. For this reason, this work focuses in Ti6Al4V.

2.1.3 Milling process

The milling process is the main machining process used for the manufacture of aerospace structural components.

Machining are production processes based on material removal, so that a work-piece can be transformed into a desired size and shape. Conventional machining processes are classified in turning, milling, drilling, grinding, broaching, reaming and boring operations.

The cutting action is produced by shear deformation, in which the material is separated from the work-piece in the form of chips. The cutting edge of the cutter penetrates the workpiece and the material is plastically deformed in the primary shear deformation zone, as depicted in Figure 2.3. This chip, as it passes along the rake face of the tool, undergoes a secondary deformation. These two deformation processes are mutually dependent because the material that rubs the rake face has been previously heated and plastically deformed as it passes through the primary deformation zone. At the same time, the deformation in the rake face determines the heating and deformation of the chip. The friction area, where the flank of the tool rubs the newly machined surface, is called the tertiary zone. These plastic deformations and heat exchange influence the surface integrity of the machined surface.

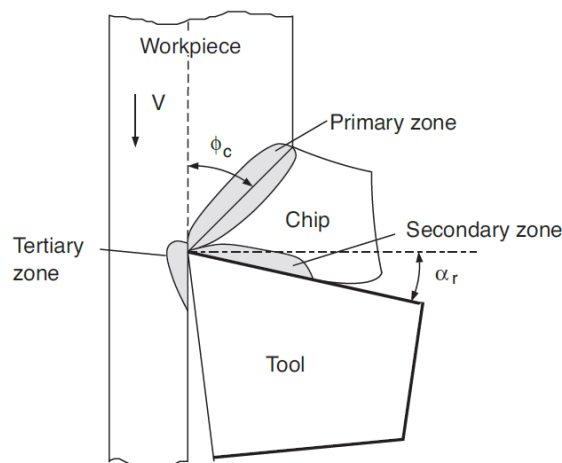


FIGURE 2.3: Orthogonal cutting process sketch with three main cutting zones [14].

When dealing with aerostructures, milling operations are the preferred option. This is because milling offers many degrees of freedom enabling to obtain almost any geometry, which is essential to manufacture any non-axisymmetric geometry. Milling implies interrupted cutting, meaning that non-constant chip thickness influences the process in terms of dynamic process stability and continuous thermal and mechanical cycles.

Milling processes are governed by four parameters, namely, cutting speed (v_c , in m/min), feed per tooth (f_z , in mm/tooth), axial depth of cut (a_p , in mm) and radial depth of cut (a_e , in mm). The selection of the values for these parameters is based on the combination of work-piece and tool materials, work-piece and tool geometries and machining strategy. This way, the productivity of a machining process is determined by the material removal rate (MRR , in cm^3/min), where N being the spindle speed (in rpm), D the tool diameter (in mm), v_f feed rate in (mm/min) and z the number of teeth or cutting edges in the tool. In general, the higher the MRR , the higher the power required for the operation, as well as, the heat and forces generated.

$$N = \frac{1000 \times v_c}{\pi \times D}; v_f = f_z \times z \times N; MRR = \frac{v_f \times a_p \times a_e}{1000} \quad (2.1)$$

The two major types of milling operations are face milling, in which the cutting action occurs primarily at the end corners of the milling cutter; and peripheral milling, in which the cutting action occurs primarily along the circumference of the cutter. At the same time, the tool rotation with respect to the feed direction distinguishes two operation possibilities: conventional (also called up milling) in which the feed direction of the cutting tool is opposite to its rotation, and climb milling (also called down milling) in which the cutting tool is fed in the direction of rotation (Figure 2.4).

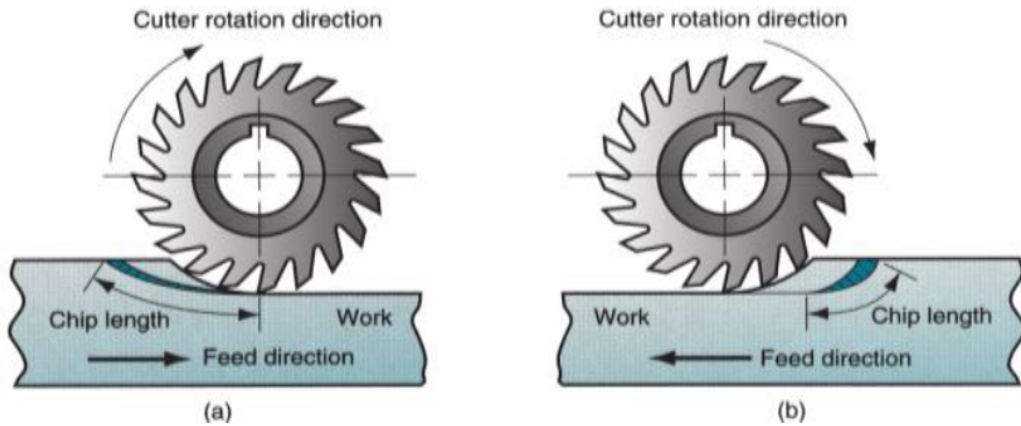


FIGURE 2.4: Conventional milling (left) vs. Climb milling (right).

2.2 Machining distortion sources

There are three main distortion sources in machining processes (Fig.2.5), namely, residual stresses (RS), thermal-mechanical cutting loads and clamping loads. RS are divided into two categories: superficial RS inherent to the machining process itself (Machining-Induced Residual Stresses, MIRS) and volumetric RS prior to the machining process (Bulk or Blank-Initial Residual Stresses, BIRS). Hence, the events inherent to the machining process are covered by MIRS and process thermal-mechanical loads. On the other hand, external but related to machining, BIRS gathers the RS state resulting from the upstream manufacturing chain and clamping loads represent the loads required to fix the part during the process.

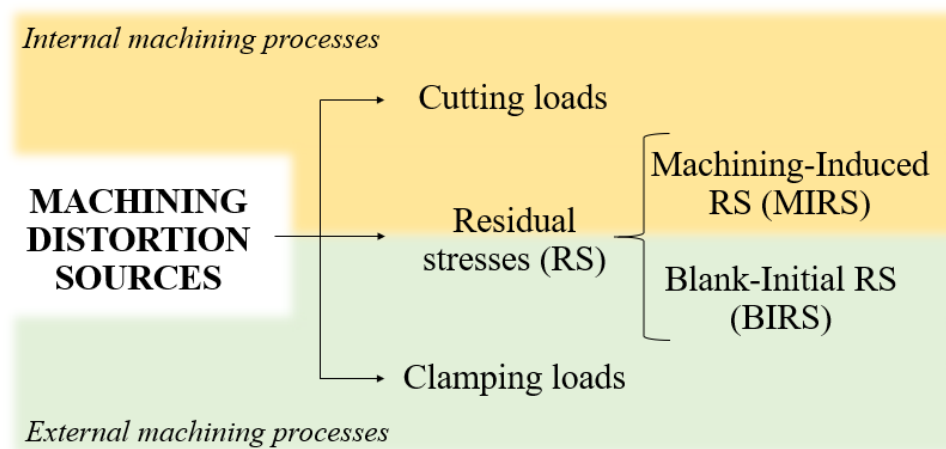


FIGURE 2.5: Classification of the machining distortion sources.

This classification is also followed in other works because its potential for industrial implementation, as it simplifies the complex problem of RS [15]. Next each of these distortion sources is described in detail.

2.2.1 Residual stresses (RS): Fundamental concepts

Residual stresses (RS) can be defined as the stress state that remains in the material when external forces or other stress sources are not applied [16]. These stresses are the elastic response to a non-homogeneous distribution of strain within the material, and they self-equilibrate globally within the component. This implies that if an analysis of the system considered is performed, both resultant force and resultant momentum will be zero.

Although this study focuses on the impact of RS on dimensional stability and distortions, RS are often known by other detrimental ways they affect material properties, namely fatigue life, tensile strength, brittle fracture, stress corrosion and coating adhesion [17, 18].

Consequently, it cannot be denied that RS play a very important role in the manufacturing of metallic components.

RS can be classified by different criteria, being the classification according to the scale over which they self-equilibrate, l_0 , the most extended. Hence, the Macro-stresses or Type-I, vary continuously over large distances l_0^I (in mm); and any change in their equilibrium results in a change of macroscopic dimensions. Contrarily, the Inter-granular stresses, also known as Type-II or micro-stresses, vary over the grain scale l_0^{II} (in μm) and exist in poly crystalline materials simply because the properties between neighboring grains are different. Finally, the Sub-micron-stresses or Type-III, vary at atomic scale l_0^{III} (in \AA) and correspond to crystalline defects (vacancies, dislocations, etc.). These three types coexist in processed metal work-pieces [18, 19].

If RS are classified according to their cause or origin, three different categories can be found:

- Mechanical, due to non-homogeneous plastic deformation produced by external mechanical loads;
- Thermal, which include expansions and contractions due to non-homogeneous temperature distributions;
- Chemical or metallurgical, because of the phase transformations induced by materials processing, resulting in volume and properties changes of the crystal structure.

However, a separation of these three causes is mainly conceptual or theoretical, as the three phenomena are of often interrelated, and depend much on the manufacturing process leading to them (Table 2.2). Furthermore, to produce a component usually several different processes are combined.

Similarly, RS are also classified into two categories depending on their penetration depth. This way, superficial RS are typically measured by non-destructive or semi-destructive methods, often reaching ranges in the order of millimeters or below. However, volumetric or through-thickness stresses are mainly measured with destructive methods (Section 2.4.1.2), and reaching ranges on the order of tenths to hundredths of millimeters.

2.2.1.1 Bulk or Blank-Initial Residual stresses (BIRS)

Blank-initial residual stresses (BIRS) are the volumetric or through thickness RS inherent to the bulk material result of its processing history.

TABLE 2.2: Main origins of residual stress resulting from different manufacturing processes [20].

	Origin	Mechanical	Thermal	Chemical
Manufacturing Process	Casting	-	TG	PC
	Shot/Hammer-peening	HPD	TG ^a	PC ^b
	Roller burnishing			
	Shock laser treatment			
	Bending			
	Rolling			
	Forging			
	Straightening			
	Extrusion			
	Grinding	PD	TG	PC ^b
	Turning			
	Milling			
	Drilling			
	Boring			
	Quenching	-	TG ^c	PC ^d
	Case-hardening			
	Nitriding	-	TI ^e	LCV
	Welding	-	TG	MC
	Brazing	MI	TI	PC at interface
PVD, CVD	MI	MI	PC	

MI: Mechanical Incompatibility

PD: Plastic Deformation

TI: Thermal Incompatibility

TG: Temperature Gradient

PC: Phase-change

MC: Micro structural-change

HPD: Heterogeneous plastic deformation between part core and surface

LCV: Local changes of volume

^a if the process is performed at non-constant sufficiently high temperatures

^b if the the process is performed at sufficiently high temperatures

^c during cooling

^d depending on composition and cooling

^e conductivity gaps

As explained, they are self-equilibrated as long as no changes occur. However, this is an unstable situation that can be broken by any subsequent material removal processing, e.g. machining operation. When bulk material is removed, the mechanical equilibrium of the part is broken, which makes the body react by deformations (Fig. 2.6), generating a redistribution of the BIRS. This phenomenon is known as Stress Relaxation, and it can be a serious problem in the manufacturing of aerostructures because of the high ratios of removed material, often asymmetrically. In this sense, D'Alvise et al. [21] considered the

final geometry of the aerostructure (in terms of asymmetry due to the removed material) a crucial factor in machining distortion.



FIGURE 2.6: Distortion due to stress relaxation of a C-17 Cargo floor beam machined from die forging, with no stress relief [22].

Even if BIRS are a source which greatly impacts machining distortion, they are also very difficult to control as an input variable to machining. Indeed, variation in bulk stress profiles can occur easily for many reasons, such as the position of a part within the whole batch [6]. Even repeating the process in detail, variation in BIRS are most likely to happen [23]. These variabilities between BIRS make that, even in cases where the blank manufacturing process is controlled, machining distortion remains as an unpredictable phenomenon. In most cases machining blanks undergo stress relieve treatments for lowering BIRS, reaching values within the measurement uncertainty range [24]. Nevertheless, even under this premise of lowered BIRS, stress relaxation is found the predominant distortion source [25].

In order to avoid distortion problems generated by the coupling of asymmetrical slender geometries and BIRS, the most used machining strategy is based on incrementally removing material from both sides of the part, so the distortions can be identified and compensated gradually as they appear [26]. This strategy comprises several set-up and machining sequences which is very time-consuming and requires a lot of highly skilled manual labour. In cases where chemical clamping is required to avoid damage, set-up times can be even doubled [27]. In any case, the optimal machining strategy varies upon components that are obtained from thick plates, pre-forms, etc. and their corresponding previous processing [28].

BIRS are acknowledged as the main distortion source in several investigations [29–38] (Section 2.3), but the variabilities on bulk residual stresses and the related difficulties for getting reliable data for them hinders accurate distortion predictions and control [39].

2.2.1.2 Machining-Induced Residual Stresses (MIRS)

The high temperatures, forces, strain and stress fields that occur in the cutting zone generate thermal and mechanical strains, or even metallurgical transformations, in the machined surface that lead to RS, namely MIRS. They alter the stress state of the component introducing a bending moment, which may cause macroscopic distortion when the part is released from the clamping. In general terms, the MIRS penetration is on the order of tenths to hundredths of millimeters, but for cases when components have very thin floors/walls, of the order of a couple of millimeters, this penetration might have proportionally a considerable weight, becoming a significant distortion source [40, 41].

The final MIRS distribution results from the combination of different stress profiles (Fig. 2.7, Profiles 1, 2 and 3), coming from the inhomogeneous plastic deformation induced by the cutting forces, thermal stresses, and volume changes caused by phase transformations [42, 43]. Depending on the magnitude of the mechanical, thermal and metallurgical effects, the penetration and shape of the stress profiles vary. As thermal effects have limited penetration and higher magnitude than mechanical effects, tensile stresses in the surface can often appear [40].

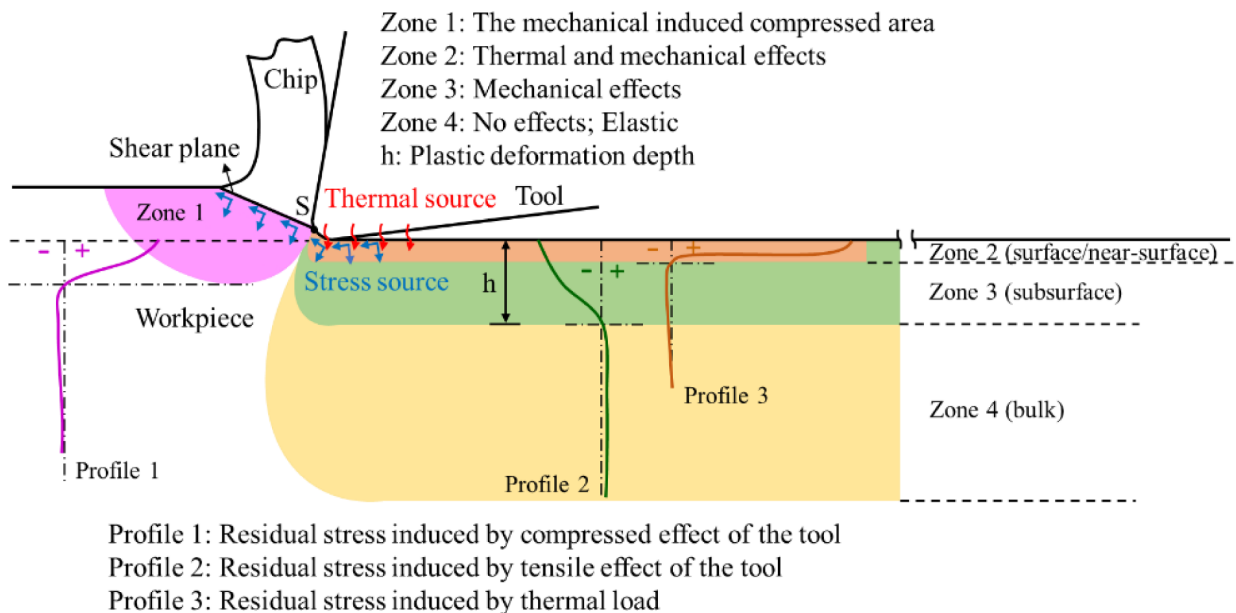


FIGURE 2.7: Schematic of the MIRS formation in orthogonal cutting process with decomposed influence from different regions [43].

At the same time, the amount of heat, forces and plastic deformation depend on the combination of many process conditions, and so the shape and magnitude of the MIRS. These process conditions can be divided into three categories: Physical-chemical properties of the work-piece material; geometry and physical-chemical properties of the tool material; and machining conditions. All these conditions interact during the process and are responsible for the final stress state of the machined surface.

According to bibliography, the basic relationships can be found between MIRS profiles and the cutting conditions:

- **Cutting speed (v_c):** Theoretically, increasing v_c increases the thermal effect and, in this way, the tensile stresses on the surface [43]. Particularly in aluminium alloys, some authors found no change or slight change on MIRS with the increase of v_c , while other found a significant impact on the MIRS [44, 45]. These contradictory results can be also found in titanium alloys. While some authors reported that increasing the v_c decreased MIRS [46, 47], others found the opposite [48].
- **Feed per tooth (f_z):** In general, a feed increase results in an increase of cutting forces and thus, MIRS become more pronounced in terms of penetration and depth at which the stress stabilize. In aluminum alloys, increasing f_z increases the penetration depth [44] and also the amplitude [45, 49], while it has been found not having effect in superficial MIRS [50]. In titanium, high f_z implies that superficial MIRS tend to be less compressive or to a zero value, while the maximum compressive residual stress significantly increases [51]. Others did not find a clear correlation between f_z and MIRS change [52].
- **Depth of cut (a_p):** Analogously, to the feed, the increase on a_p implies an increase in cutting forces and therefore MIRS theoretically compressive MIRS increase in amplitude and penetration depth. In aluminium, some authors found this correlation [53], while others reported that increasing a_p reduces compressive stresses [45]. In titanium, also, the increase of a_p is found to increase compressive MIRS [47].
- **Tool wear:** Flank wear and edge radius increase the cutting forces, as well as, the temperature at the cutting zone. For these reasons both the mechanical effect and the thermal effect on the machined surface increase. This way, an increase of flank wear increases tensile stresses on the surface and also their penetration depth [43]. This premise was found positive aluminium [54] and in titanium [55], which also found a deeper penetration depth of the compressive stresses.
- **Coolant:** The use of coolant affects the temperature field of the cutting zone. Theoretically, dry cutting leads to more tensile stresses on the surface. In titanium, apart from finding this premise positive, also was found that the dry cutting leads to

more shallow MIRS, that oil lubrication reduces MIRS providing a deeper and more compressive MIRS profile than dry cutting; and that cryogenic cooling significantly increases compressive stresses and their penetration due to the increase in forces [56].

- **Tool geometry:** All studies agree on that tool geometry has a significant impact on MIRS. However, the wide variety of tools, which upgrade constantly, makes it difficult to compare different studies and find clear conclusions. However, some general outcomes are that higher edge radius increases temperatures and thus, tensile MIRS on the surface [43]. The effect of rake angle is not that straightforward, as both the thermal and the mechanical effect increase when this changes from positive to negative angle. The final surface stress depends on which of the effects has more influence. In fact, in some cases this change implies a decrease in surface tensile stresses [43]. However, in general higher rake angles reduce MIRS [41].
- **Milling strategy:** Theoretically, up milling generates more tensile stresses because when the cutting edge leaves the surface this is at its maximum temperature; while in down milling cold plastic deformations are more present, which leads to more compressive stresses [57]. However, contradictory results are reported [47].

Due to the complex interactions between cutting conditions and MIRS, researchers put a big effort in building simulation models to predict MIRS (Section 2.4.2.1). However, experimental results do not always obey these general trends. Even keeping constant the machining conditions, the repeatability of MIRS is a factor to be considered [58].

2.2.2 Cutting loads: Cutting forces and heat

Besides MIRS, the cutting loads (forces and heat) generated in the cutting process are distortion sources too, as they may vary the part geometry or even the actual position of the cutting tool with respect to the nominal one. An investigation performed together with 75 industrial companies (from Europe and Asia) proves that thermal issues are an important source of distortion [59].

On the one hand, from a static point of view, the cutting forces produce elastic deformations that can affect the final part [60]. This type of distortion is often called force-induced error or surface-form error. In this way, not only the tool can be subject of deflection, but also the machined component [52, 61]. In components with thin floors and walls (included free-form surfaces, for which this subject is widely studied [62]), the mechanical stiffness is position-dependant, making the analysis of the distortion a cumbersome task [63, 64]. Moreover, even the choice of the cutter size might be an important distortion factor because of the increase in cutting forces, even if feed, speed, depth of cut and material removal rates are kept constant [65].

On the other hand, during the machining process or shortly afterwards, thermal influences can cause further deformations. Temperature gradients and thermal expansion stresses are generated, resulting in additional deformation which, however, diminishes after temperature stabilization [40]. In long slender components, where the heat is introduced asymmetrically, this phenomenon might become more significant. Moreover, trends in machining which seek the reduction or elimination of cutting fluids lead to increased part heating and greater thermal distortions [66].

When comparing the influence of force and temperature on distortion, Masoudi et al. [67] found that, although the direct correlation for both phenomena with part distortion, in the case of thin-walled cylindrical components the force effect was predominant.

2.2.3 Clamping loads

In a similar way that cutting forces can cause deflections on the work-piece, clamping forces can also cause elastic deformations that become dimensional and form errors, especially in thin-walled components [68, 69]. Designing, analyzing, and adjusting the work-piece-fixture system is a key subject to improve machining accuracy. Placing locators and clamps in optimal positions can minimize the elastic deformation of the components and, hence, the distortion due to clamping loads [70]. Besides, the mechanical behaviour of the work-piece during machining due to inherent BIRS is not usually considered during the fixture design [71], resulting in undesired clamping force values when stress relaxation occurs.

2.3 Distortion calculation and research

Accurate simulations of the machining processes are necessary to solve scientific, technical and economic issues in the manufacturing industry. They are key enablers for the scrap and rework cost reduction, decreasing the traditional trial and error procedures. Predictive models also enable subsequent generation of control or optimization solutions, and in some cases even boost the development of new processes. According to a study done by Volk et al. [72], using the appropriate validated model can save a manufacturing company up to 54% of the cost incurred.

The various sources of distortion together with the different modeling approaches multiply the possibilities of overcoming this task. The choice of a particular model depends on the geometry of the component, material, machining operation, information requested, accuracy of this information, available time and computational resources, amongst others. Next sections introduce two different classifications, one regarding the modeling approach

and the other one targeting the number of distortion sources considered as input for the simulation model, as depicted in Figure 2.8.

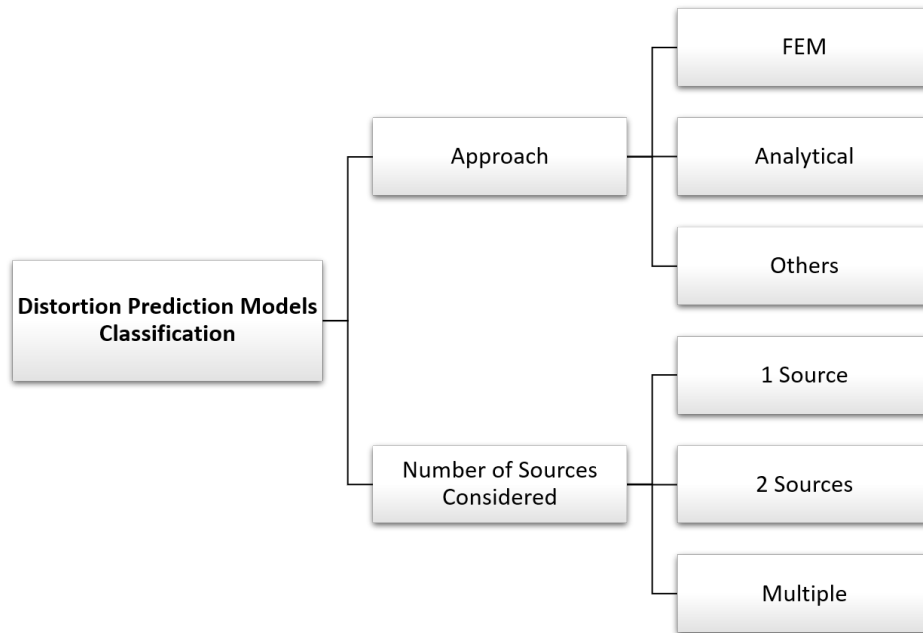


FIGURE 2.8: Classifications scheme of distortion prediction models.

2.3.1 Classification upon modeling approach

2.3.1.1 Finite Element modeling (FEM)

In the last two decades the relevance of modeling and simulation of manufacturing processes has significantly risen, boosted mainly by the improvement of computation capabilities.

Finite element modeling (FEM) is a numerical method which divides a large continuum into small elements, constructing a mesh with a finite number of nodes. The connection of these elements results in a set of simultaneous algebraic equations that, minimizing an associated error function, approximates the solution.

FEM allows the simulation of complex geometries while the complete understanding of the underlying physical mechanisms is not required, remaining still as a “plug and play” solution. If the loads generating distortions are known (BIRS, MIRS, cutting forces, thermal loads...), they can be introduced in a macro-scale model, avoiding the computational effort required to include the thermal-mechanical interaction between tool and work-piece in a micro model. The main shortcomings of this approach though, are the difficulties in modeling properly loads and boundary conditions, and the high computational time. In fact, Ma et al. [39] compared 2D with 3D models revealing that for the same mid-size component, simulation takes from a couple of hours to over a couple of days.

Amongst the most popular software solutions for distortion prediction using FEM, ABAQUS, ANSYS, MSC Marc, DEFORM, CalculiX, FORGE can be found, even though the use of open source software is gaining relevance [73, 74].

The main factors that influence the accuracy of a FEM model are:

- Element type: the two main element types for the 3D modeling of machining distortion are hexahedral and tetrahedral [75–78]. For the same number of nodes, hexahedral mesh was proved better than tetrahedral [39], as well as for material data (BIRS, MIRS, temperatures and forces) interpolation onto the mesh (specially if high gradients are present) [79]. However, for simple bending moment calculations, both types provide acceptable results [80], being tetrahedral often chosen for its lower computational cost [81]. Moreover, in some cases higher node amount tetrahedral element mesh provided closer results to experimental than hexahedral mesh [82]. Concerning interpolation, linear (one integration point) was found best for machining distortion simulation [83].
- Mesh generation: the accuracy of the model is highly dependant on the mesh quality [75], and different meshes can change the accuracy significantly [84]. Therefore, generating initially a correct mesh is vital for guaranteeing the accuracy of the model. Moreover, an additional concern comes from the significant increase in calculation requirements when the model requires a mesh change, as it happens when the geometry of the part changes along the simulation (e. g. some machining sequence simulations).
- Modeling procedure: three different procedure can be distinguished (Fig.2.9) [39]:

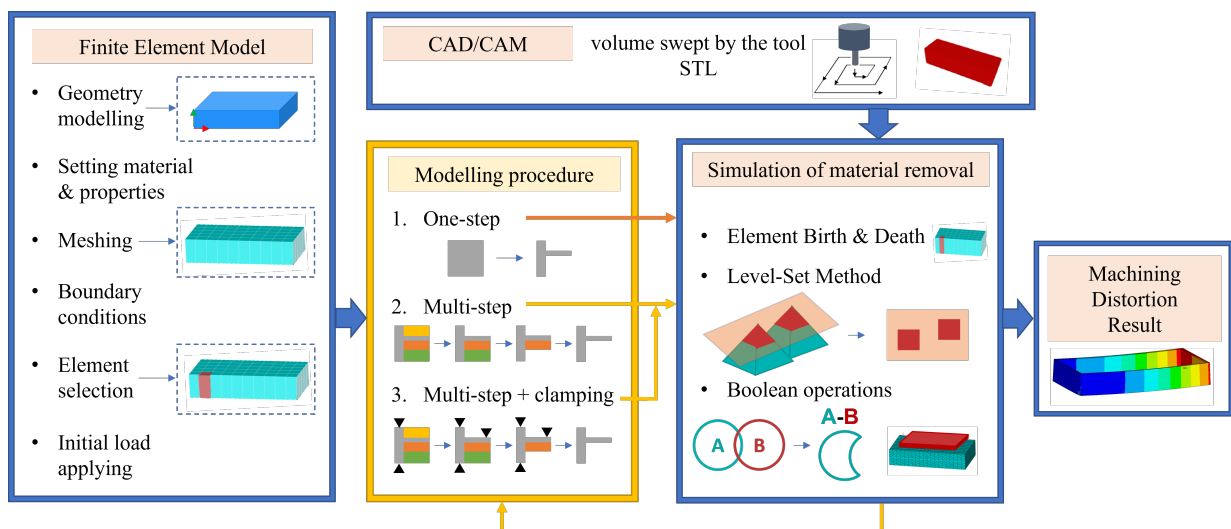


FIGURE 2.9: FEM distortion modeling workflow diagram, including different modeling techniques.

The first one is named *One-Step procedure*, and introduces the loads directly onto the final machined geometry. It is a fast procedure which avoids changing the mesh, although it comes with an accuracy penalty [75, 77].

Secondly, the *Multi-Step procedure based on pre-defined machining paths*. To simulate the removal of the material happening in machining operations, some elements are deactivated. This is performed by setting their stiffness to zero using the “Element Birth and Death” method or “Boolean Operations”, which deactivate larger volumes. The first one is mature and a convenient tool for calculation, but it is as well difficult to use when complex parts are to be simulated. Besides, if changes in the machining path occur, the model needs to be remeshed from the beginning. Nevertheless, it is an extended practice in distortion prediction [85–87]. Boolean operations instead, are gaining relevance due to their potential in industrial environments [88], especially if they are combined with CAD/CAM systems providing the volume swept by the tool in an STL file format [81]. An alternative for element deactivation, which is less extended but efficient for remeshing is the “Level-Set Method” [21, 89]. This one enables defining cutting paths independently of the work-piece mesh by defining a signed distance function at the nodes. As a disadvantage, the level-set function has to be recomputed on the updated configuration after each machining step [75].

Finally, a *Multi-Step procedure with path dependant material removal*. It is performed integrating, apart from the machining paths, also the fixture interactions, which result in a model performing closer to experimental trials [79].

- Boundary conditions: The choice of boundary conditions significantly affects the distortion prediction [90], as well as the convergence of the model [91]. For this reason selecting the right set of boundary conditions is crucial for the accuracy of the model. Furthermore, it may happen that in the material removal simulation the elements to which the boundary conditions are associated result removed, and the model becomes unconstrained. For these cases some software solutions, such as DEFORM, can automatically apply boundary conditions ensuring that the model is not left unconstrained [79].
- Simulation of material removal: If *Element Birth and Death* technique is used, the model becomes a non-linear system. Solving an analysis with non-linearities requires the convergence of an iterative solution procedure. In this regard, the Newton-Raphson method transforms a non-linear problem into a series of linear problems [75] and, being an iterative method, generally converges in fewer iterations than the other available methods [79]. Apart from the iterative solution procedure, the convergence of the model may require the load to be applied gradually with solutions carried out at intermediate load values. These intermediate solution points within a

step are known as substeps. Essentially a substep is an increment of load within a step at which a solution is carried out.

- **Loads:** the RS loads can be applied directly as constant stresses in each point (one integration point) of previously selected elements, or with a specific script to compute RS profiles on a mesh using the coefficients of polynomial functions which approximate the experimental profiles [92]. If elements with multiple integration points are considered in the prediction of part distortion, Gauss points coordinates for each element are calculated using the shape functions, and RS values are assigned to each Gauss point according to a predefined function [83]. Thermomechanical loads instead, are applied to the corresponding nodes of previously defined feed-step element elements [93].

Last but not least, FEM simulation models need to be validated, and typically adjusted, with experimental results (similar machining conditions) or models of different approaches [72, 94]. However, the variations in input data are inevitable (BIRS non-repetitive between blanks, experimental measurement uncertainties, factors that cannot be controlled in machining test, etc.). While for simple geometries machining simulations differ from experimental results in a range of 19%-40%, for complex aerospace parts errors of 50% are commonly seen [95]. In order to reduce these errors, one strategy followed is validating the model at each incremental step to isolate the shortcomings of the model. Another one is enlarging on purpose input data magnitudes, and by that output variables, so that noise and errors in experimental measurement diminish [39].

Although the wide research and development of these models, the penalty of computational time hinders its implementation in industrial environments [39].

2.3.1.2 Analytical

As an alternative to overcome the problem of requiring long computational times, analytical models for distortion prediction are being developed. Analytical models have a closed form solution, meaning that the solution to the equations which describe the changes of a system is expressed as a set of mathematical equations.

The main advantage of analytical models is that they can run simulations faster than numerical models, which enables in-process industrial application. Besides, in comparison with numerical models, they have reduced license fees, which is especially attractive for small and medium-size companies [96]. On the other hand, their development is not straightforward, as machining distortion is a coupled non-linear problem. It requires a deeper understanding of the physics and material constitutive relationships, which are

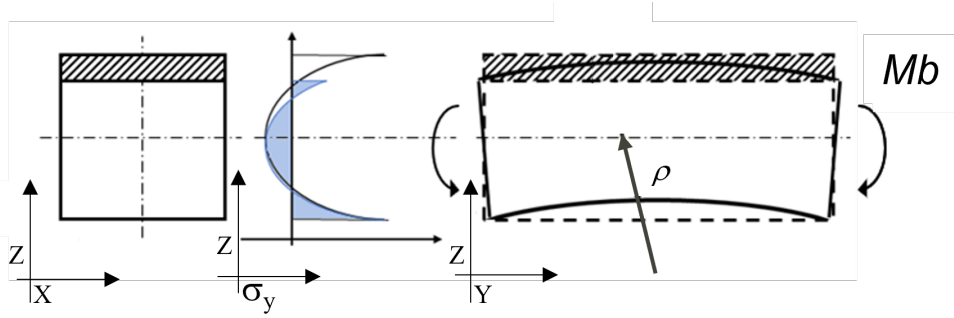


FIGURE 2.10: Stress state, bending moment and deformed condition of the specimen when the initial stress balance of the specimen is broken due to material removal.

very complex and not explicit due to the plastic deformation history of materials. For this reason, broad assumptions are taken in analytical modeling. Probably the most recurring one is considering the material linear-elastic and isotropic, even though some exceptions can be found [97].

The analytical models are typically implemented through programming languages as Matlab, C++, Python and Visual Basic. Concerning the modeling techniques, three different groups can be distinguished: the models based on the beam/plate bending moment theory, those based on the strain energy density relaxation theory, and other less extended analytical models.

Bending moment theory

The bending moment theory for distortion prediction due to BIRS relaxation (Section 2.2.1.1) was the pioneering work in analytical modeling [98], which was presented by Shin in the early 1990's.

According to this method, when the material is taken away, the initial force (F) and momentum (M) balance (Eq. 2.2) breaks, provoking a bending moment (Fig. 2.10). As a result, the work-piece bends and the BIRS redistribute to reach a new state of equilibrium. Discretizing the section in layers, the bending moment is calculated as the integral of the average stress (σ) multiplied by the area (A) and the leverage to the neutral axis or plane (k).

$$\int_V dF = 0, \quad \int_V dMb = 0 \quad Mb = \int_V \sigma k dA \quad (2.2)$$

The Equation 2.3 illustrates the curvature relation of the work-piece before and after a layer of material is removed, where i is the number of the layer being removed, ρ_i and ρ_{i+1} are the curvature radius before and after the layer removal (in mm^{-1}), t is the thickness of the layer (in mm), e_i and e_{i+1} are the section thicknesses before and after the layers

removal (in mm), σ_j is the stress of the removed layer (in MPa), and E is the elasticity modulus (in MPa).

$$\frac{1}{\rho_i} - \frac{1}{\rho_{i+1}} = \frac{6te_i\sigma_j}{E(e_{i+1})^3} \quad (2.3)$$

Distortion by stress relaxation is calculated in these models as pure bending using the Euler–Bernoulli beam theory when uniaxial stresses are considered, and by the Timoshenko plate bending theory if biaxial BIRS are considered [99, 100].

When it comes to complex geometries, analytical models present limitations, as they are suitable for simple and regular parts due to their broad assumptions [101–103].

In regards of modeling analytically the effects of MIRS using the bending moment theory, distortion is calculated analogously [104]. The main difference relies on the geometric aspect, as MIRS only affect to a limited superficial depth (typically below a millimeter), and they should be considered only for the machined surface.

Strain energy density relaxation

An alternative method for distortion calculation is through energy considerations, more specifically considering the bending strain energy as an evaluation index of the bending distortion risk. This approach is also known as the minimum potential energy (MPE) consideration. The concept of strain energy per unit length for a beam, which is proportional to the square of its curvature, was first introduced by Euler in 1744 [105]. From the total potential energy of a solid body, the strain energy stored in the material is an elastic energy resulting from the deformation of the body due to externally applied loads [38, 106].

Figure 2.11 shows an schematic diagram of the machining distortion process considering strain energy.

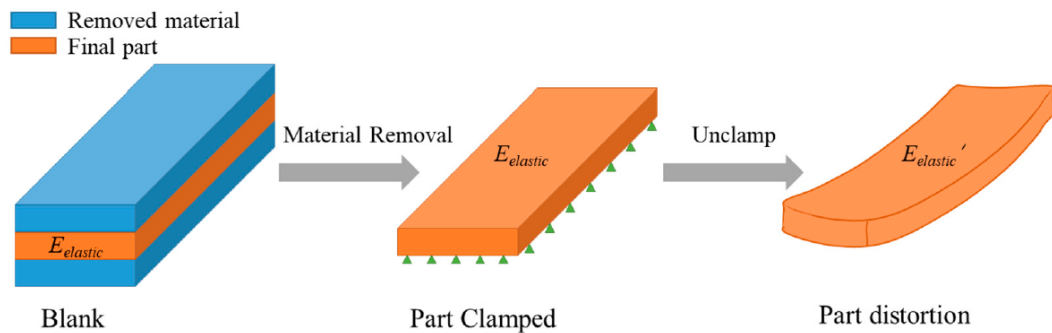


FIGURE 2.11: Sketch of the machining distortion process and energy release mechanism [107].

When material is removed, the unreleased elastic deformation stored in the work-piece as an elastic strain energy $E_{elastic}$ is still under clamped state. When it is released from the clamping, part of his energy is released causing a strain redistribution and part distortion, until an equilibrium is reached when the part is at its minimum potential energy state (principle of the minimum potential energy). The released elastic energy consists of bending strain energy E_{bent} , stretching strain energy $E_{stretch}$, twisting strain energy E_{twist} , and shearing strain energy E_{shear} , respectively.

The elastic strain energy U is calculated in its general form through Equation 2.4, where \bar{U} is the strain energy density (in kJ/m^3); σ_x , σ_y and σ_z are the respective stresses in the X, Y and Z directions (in MPa); τ_{xy} , τ_{yz} and τ_{xz} are shear stresses on the XY, YZ and XZ planes (in MPa); V is the volume of the part (in m^3); E is the elasticity modulus (in MPa); G is the shear modulus (in MPa); and ν the Poisson ratio.

$$U = \int_V \bar{U} dV = \int_V \left(\frac{1}{2E} (\sigma_x^2 + \sigma_y^2 + \sigma_z^2) - \frac{\mu}{E} (\sigma_x \sigma_y + \sigma_y \sigma_z + \sigma_x \sigma_z) + \frac{1}{2G} (\tau_{xy}^2 + \tau_{yz}^2 + \tau_{xz}^2) \right) dV \quad (2.4)$$

For the case of plates with a 1D symmetric stress distribution, the simplified strain energy is often used (Eq. 2.5) [108], where t is the thickness of the plate (in mm).

$$\bar{U} = \frac{1}{t} \int_0^{t/2} \frac{\sigma(z)^2}{E} dz \quad (2.5)$$

It is important to remark that there is no convention for the naming of strain energy, and one can find different works referring to strain energy by different symbols.

Heymes [109], pioneer in the use of this technique for distortion calculation of plates, found that strain energy density values lower than 1 kJ/m^3 provided no significant distortion, while a risk of significant distortion resulted with values larger than 2 kJ/m^3 and large distortion could be observed with values over 4 kJ/m^3 . Others stated that the distortion is proportional to the strain energy density [110] and stress range [108]; and showed through numerical simulations that the magnitude of machining distortion strongly relates to the square root of strain energy density and stress range [111]. These findings however, do not agree with results from other studies based on strain energy relaxation [109, 112]. More recently, Fan et al. [107] demonstrated the capabilities of this rapid method comparing the analytical distortion results with numerical simulation and experimental results, achieving average errors of 3% and 23% respectively.

Although, this technique is good for providing quick indication of machining distortion and enables direct comparison of complex stress distributions, it has some limitations. On the one hand, this approach assumes (like the Bending Moment Theory) that the material is linearly elastic and remains this way throughout the machining process. Besides, it does not consider the RS distribution, the final part geometry, neither the location of the final part within the blank. For these reasons, recent works attempt to incorporate the benefits of different techniques, combining the bending moment and strain energy methods, as depicted in Figure 2.12 [38].

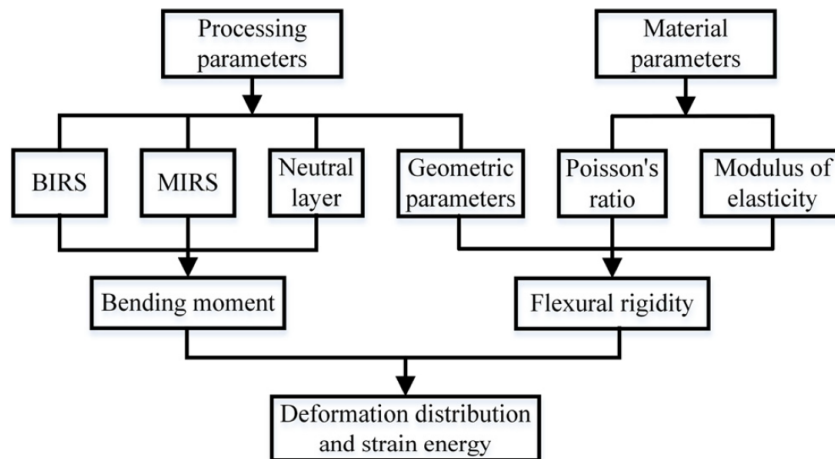


FIGURE 2.12: Flow chart for predicting machining distortion combining the bending moment and strain energy theories [38].

Other analytical models

This third group gathers the analytical distortion models which are based on other formulations different from the two explained above.

Under the assumption of linear elasticity throughout the machining process, Nervi et al. [94] formulated an analytical distortion prediction model using the *Navier-Lame equations* [113]. This was performed by a differential formulation for the analysis of the equilibrium of an elementary volume. Based on the principle of superposition, it gave proof to the following theorem: In any given configuration of the elastic body, the stress distribution depends on BIRS tensor, σ_{ij}^0 , defined on the initial Ω_0 and the current $\Omega_k (k = 1, 2, \dots, n)$ configurations, but not on the intervening configurations. Being λ the first Lamé constant and G the shear elastic modulus (in GPa), the model could be formulated with Equation 2.6.

$$\int_{\Omega} (\lambda \epsilon_{kk}^{(u)} \epsilon_{ii}^{(v)} + 2G \epsilon_{ij}^{(u)} \epsilon_{ij}^{(v)}) dV = - \int_{\Omega} \sigma_{ij}^0 \epsilon_{ij}^{(v)} dV \quad (2.6)$$

The disadvantages of this technique are that the effect of MIRS is not considered, neither the effect of the clamping loads. Furthermore, it requires that the constraints are placed in such way that mechanical contact is not altered during the machining process.

Also, a model based on the *Virtual Work Principle* recently developed by Zhu et al. [97] can be found. This, physics-based model states that the excessive deformation of a body with RS should be attributed to the work of an external force on the object with RS. Thus, considering MIRS, the geometrically non-linear strain and gravity, it calculates the deformation when the RS reduce to zero. An advantage of this approach is that it does not require special dimensions of an object. However, its accuracy is limited as it does not consider BIRS.

2.3.1.3 Other modeling approaches

This category comprises distortion prediction models under less extended approaches.

Finite difference method (FDM)

The finite difference method (FDM) is another type of numerical technique for solving differential equations by approximating derivatives with finite differences. These finite difference approximations are algebraic in form, and the solutions are related to grid points. Compared with FEM, FDM is a fast and efficient method and, because of that, it is applied to many engineering fields for establishing prediction models. However, its use in distortion prediction is not that extended. This might be because its application in different geometries requires reworking the formulation from the scratch. In this way, Guang-yao and Han-bin [114] proposed a finite difference method at irregular meshes for bending of plates with variable thickness. Wu et al. [26] predicted distortion due to cutting loads by FDM, obtaining low errors when comparing with FEM and experimental results. Inversely, Zhu et al. [97] used FDM to validate the accuracy of a general analytical model.

Finite cell method (FCM)

The Finite Cell Method (FCM) combines the fictitious domain concept with high-order functions and it is highly suited for complex model geometries and/or continuously changing material interfaces [115]. It represents an alternative to overcome re-meshing problems linked to FEM, reducing complexity. In the context of machining simulation, FCM presents the major advantage of decoupling the computational mesh and the (in-process) work-piece

geometry. Although its clear advantage, the use of this method is only recently been applied, combined with voxel models, for the simulation of machining distortion [81, 116].

Machine Learning or Artificial Intelligent models

Machine learning methods and algorithms provide flexible multi-order non-linear modeling, which is valid when the assumptions of linear domain and the superposition principles are not valid. This way, an increase of distortion models combining enrichment AI strategies can be seen. Amongst these AI strategies, neural networks [117, 118] and deep learning-based prediction [119] can be highlighted. Although these models represent a promising alternative, it is unforeseeable which model enrichment AI strategy yields better results. Besides, they require a high number of data and expertise to be developed.

Hybrid models

Hybrid models are the combination of different modeling approaches, with the purpose of merging strengths and bypass limitations. By definition, hybrid models can be of different kinds. One example is the hybrid model developed by Gulpak et al. [120], which consisted of 3 sub-models with a regression model and FEM simulation. Regression models were used to calculate specific boundary conditions for the FEM simulations. Alternatively, Izamhah et al. [78] integrated FEM and statistical analysis in one framework, so the agility and flexibility were kept. More recently, Li et al. [121, 122] worked on a semi-analytical model, in which the analytical part reduced the computational time and the equivalent bending stiffness for complex geometries with different ribs layouts was obtained by numerical simulation.

Looking briefly at the possibilities of distortion simulation according to the modeling approach, although FEM is the most extended, the agility of analytical modeling makes it still an eligible choice for industrial application.

2.3.2 Classification upon input data

Simulation models try to replicate the behaviour of real environments in virtual systems to provide insights that enable their solution. The models can achieve this when the focus is reduced by taking assumptions and simplifications, such as the isolation of the different inputs and their choice according to their sensitivity on the output. The following section gathers machining distortion simulation models of aerostructures according to the input variables or distortion sources they consider.

2.3.2.1 Considering 1 Source of Distortion

BIRS

For the case of aerostructures with high ratios of material removed, this is probably the most extended approach, reaching one third of the total distortion modeling. As long as the effects of other distortion sources are negligible [32, 35, 37, 38], these models offer the advantages of being simple to perform and understand, requiring less computational time (in the case of numerical models). Nonetheless, this is a daring premise because many studies demonstrate that the main source of distortions may vary upon work-piece material [87], machining parameters [41] and other variables [123–125].

Amongst all research in this line, some findings are of special interest. In particular, Gao et al. [101] found through the so-called coefficients of stresses in each layer that, eliminating stresses in the upper part of the blank is contributing more to controlling deformation. Yang et al. [23] introduced the concept of deformation evaluation index and analyzed the effect of the web-deformation and side-wall deformation on the whole part distortion. Fan et al. [107] analyzed quantitatively the influence of BIRS fluctuation on part distortion for different positions of the final part within the blank.

MIRS

Contrarily to the previous case, distortion prediction models considering only the MIRS are very seldom. The bending moment caused due to induced surface stresses leads to deformations and, depending on the magnitude of the introduced stresses and the stiffness of the part (which is low in the case of thin walls or floors), this effect can become significant [126] and even predominant over others [41, 58, 87, 94]. Due to their increased efficiency, these models are capable of handling large-scale parts with complex curved surface geometries with a reduction in computational time [127].

However, considering just the MIRS as distortion source can only be reasonable when the amount of material to be removed is very little (near-net-shapes) and the stress profiles induced by machining are significant in comparison to the stiffness of the component [128, 129]. In fact, these models acknowledge that ignoring BIRS may be responsible for the discrepancies with experimental results [96, 97].

In any case, they can be beneficial for developing knowledge on the redistribution of MIRS upon machining strategy. For instance, the investigation performed by Jiang et al. [130] studied the effect of overlap rate of cutting tool path on distortion; and the study by Chighizola et al. [49] evaluated the effect of the MIRS measuring method on the machining distortion prediction accuracy.

Other single source: cutting forces, thermal loads or clamping loads

Considering aerostructures, distortion modeling upon just one of these sources is considerably more reduced. In the case of cutting force, distortion models which predict the deviation between the theoretical machining paths and the actual ones as a consequence of cutting forces, the main focus are work-pieces with shapes of single walls or blades [61, 63, 131], instead of aerostructures. Nevertheless, along with the machining process, the change in stiffness in slender geometries (such as aerostructures) is a factor to consider. In fact, the complex machining deformation modeling becomes not only position-dependant [64], but also time-dependant [63].

Even more reduced are the models of machining distortion induced only by thermal loads, and mostly focus in components different from aerostructures [66, 86, 132].

Regarding the models that only consider clamping force, the premise only true to a certain extent, as the clamping forces are linked to the cutting forces generated in the machining process, as well as to the changes experienced by the work-piece due to the stress relaxation when the material is removed. However, by convention, models considering clamping forces as input differ themselves from others which simulate the tool and/or work-piece deflection, focusing on the deflection of the work-piece because of the clamping forces. In this way, different combinations can be found, namely, of work-piece and clamping flexibility [133] or clamping and milling forces combined [134].

2.3.2.2 Coupling 2 Sources of Distortion

BIRS and MIRS

In recent years, the combination of BIRS and MIRS in distortion prediction is gaining relevance [35, 102, 104, 121, 123–125, 135]. This might be because several studies proved that assuming one of these two inputs negligible leads to errors [125]. In this regard, Weber et al. [136] studied the scale effects of each RS type and their combined effects for analogous parts of different wall thickness.

This group represents the second most recurring when simulating complete part distortion of final components. Some of the most relevant outcomes of these investigations are the analysis of the effect of different machining paths and machining sequences on distortion [104], the relationships between potential energy and distortion [125], or the effect of different stiffening rib layouts on the final part distortion [121, 122]. Moreover, Yang et al. [87] demonstrated that, while BIRS were the main distortion source for aluminium alloy monolithic components, the effects due to MIRS were predominant for titanium alloy monolithic components.

Other combinations of two distortion sources

Cutting loads, forces and heat, standalone consideration is used for the evaluation of transient thermal-mechanical loading conditions on distortion. Not being a very extended modeling approach, the influences of thermal-induced deflections from the force-induced deviations have been analyzed [137], as well as the final part distortion in floors and walls, applying thermal-mechanical loads [93].

An investigation of BIRS and cutting forces combined, showed that for that specific case the effect of the machining path could be neglected [138], which contradicts other studies [135]. Alternatively, the models using BIRS and clamping forces as input could be used to conduct clamping experiments with different clamping forces, sequences and positions, enabling to systematically improve the assembly for aerostructures [139].

In regards of the models coupling BIRS and thermal loads, Gulpak et al. [120] superimposed the effects of BIRS and thermal loads, which were simulated as a moving heat source representing the thermal input of the machining process. The calculation method allowed the inclusion of torsion source stresses responsible for the twist of the machined work-pieces, as well as the bending source stresses in two directions.

2.3.2.3 Coupling Multiple Sources of Distortion

Multifactor coupling refers to those prediction models which consider more than two distortion sources as input variables. Under this category, there are fewer works, but which investigate distortion more comprehensively. For instance, BIRS, fixture layout, operation sequence, tool path, cutting loads and cutting variables were merged in a model representing a 3D machining environment [69]. Jayanti et al. [140] developed a model accounting for the effects of BIRS, MIRS and tool deflection due to dynamic cutting forces along tool-path. Alternatively, Tang et al. [141] coupled BIRS, MIRS, cutting loads (mechanical and thermal) and clamping loads, in a distortion prediction model.

On the other hand, works on multifactor distortion prediction are evolving to new and different perspectives. For example, apart from the effects of MIRS, the geometrically non-linear strain and gravity were considered by Zhu et al. [97]. Another example are online distortion prediction intelligent models, which combine the initial process information with work-piece state and process monitoring data and historical or simulation data (for model training), avoiding RS data acquisition (which is always challenging and a significant error source) and achieving this way accurate prediction results [119].

The advantage of these multiple source models is that, theoretically, and if the input data is accurate, they should represent precisely the solution. However, having accurate input

data is not an easy task, especially in the case of RS. Moreover, they are in general more complex to develop and understand, require more computational time and resources, and thus, are more difficult to be implemented in industry.

2.3.3 Discussion upon distortion calculation and research

Along this section, several distortion models and investigations are reviewed. Considering published research outcomes, it can be concluded that the main distortion sources in aerostructures are RS, BIRS and MIRS, and thus, most distortion models use as input only these sources (as single inputs or combined). Besides, numerical models are more extended than analytical models, which are mostly based on the Bending Moment Theory. However, analytical models are only applicable to very simple geometries, and numerical still require long computational times for representing a real solution for industrial implementation. This way, hybrid modeling solutions are gaining relevance, as they can combine the advantages of both approaches, agility and accuracy.

Moreover, distortion calculation in aerostructures often shows significant discrepancies with experimental results, which are considered in a great extent the consequences of the inaccurate RS input data.

2.4 Residual stress data acquisition

For the acquisition of RS data, simulation models or measuring methods can be employed, which are presented and discussed hereafter.

2.4.1 BIRS data acquisition

This section is divided into BIRS estimation through upstream processes modeling, and BIRS measurement using different destructive and non-destructive techniques.

2.4.1.1 BIRS modeling

BIRS distributions are complex to determine because of the multiple sources and their interactions. One of the approaches followed to estimate the distribution of BIRS is the simulation of the metal forming process to obtain the machining blank, which has the advantage of providing, not only the bulk stresses, but also the strain history of the material [22]. However, metal forming process simulation encounters difficulties due to their physical complexity and the lack of data for the material constitutive laws [142].

In fact, there is a reduced number of analytical models for predicting RS of upstream manufacturing processes [143]. Due to the highly coupled non-linear nature of the problem, most recurring solution relies on FEM models, which are highly influenced by the material models frictional behaviour, the heat transfer coefficient, the boundary conditions and the mesh generation [39, 144, 145].

Although simulations for almost all upstream processes can be found, most are linked to blanks obtained by forging or quenching [92, 146–149]. Moreover, in the last years commercial software solutions have improved significantly. Amongst them can be found, FORGE, SIMUFACT or DEFORM for forming; and ADDSTEFAN, MAGMA, SIMTEC for casting. Alternatively, due to the increasing interest in additive manufacturing processes, works on process modeling for determination of the RS generated by additive manufacturing processes can be found too [150, 151].

Due to the expense and difficulties in getting reliable BIRS data, for which often destructive measurement methods are often used, as explained in next section, many works use modeling for obtaining the input data BIRS necessary in distortion prediction [104, 124].

However, model verification and validation tasks are very challenging, as BIRS result from the combination of a number of different processes and their measurement is often performed by destructive methods (Section 2.4.1.2). Besides, BIRS are subject to substantial statistical variation, as they are very sensitive to part position within the batch and other external conditions that cannot be controlled [6]. On top of that, the high degree of expertise and costly licenses, hinder their application for distortion control at production companies.

Finally, the quality of the modeling is strongly governed by the accuracy on the inputs (e.g. material behaviour) [71]. In some occasions, in order to perform accurate BIRS simulations, additional experimental trials are required. For instance, quenching models require to obtain the heat transfer coefficient experimentally [79].

2.4.1.2 BIRS measurement

Experimental measurements are critical not only for the acquisition of input data for distortion prediction models, but also for the construction and validation of BIRS modeling tools.

In general, all stress measurements require an indirect measurement of strain or displacement to be measured, from which stresses are subsequently calculated [18]. For this reason, researchers refer to measuring, determining or even characterizing RS equally. Obtaining accurate and reliable RS data is not an easy task. This is because RS measurement methods

obtain stresses from a typically small measure of displacement or strain [18], whose error has a significant effect on the calculated stresses. Table 2.3 summarizes the characteristics of various RS measurement methods for different practices and applications.

Non-destructive methods rely on the measurement of some property affected by strain, for example the distance between atomic planes for diffraction methods. On the other hand, destructive methods, also named mechanical or relaxation methods, obtain stresses by measuring the deformations after the material is cut in some way. These methods are known and have been used for many years [152], and the different versions offer a wide range of geometries, materials and applications.

Apart from the classification regarding the method of analysis meaning destructive or non-destructive, RS measuring methods can also be distinguished by measurement penetration, measurement resolution and cost of analysis, as depicted in Figure 2.13.

Some of these methods (ultrasonic, magnetic and eddy current, etc.) just provide qualitative information of stresses, thus not being able to quantify RS for their use as input data in distortion models. For this reason, these methods are not considered hereafter.

Measuring through-thickness stresses (BIRS) is more challenging than measuring stresses in the surface (MIRS), regardless the measuring method used. The most used methods in distortion research of aerostructures are: amongst non-destructive methods, neutron scattering and synchrotron X-ray diffraction; and amongst destructive methods, crack-compliance, contour method, layer removal and hybrid methods. Next paragraphs describe briefly these methods.

The non-destructive neutron scattering is an effective method for measuring three-dimensional stress fields at large depths, and for this reason is used in some machining distortion investigations to obtain BIRS input data [30, 79, 153, 154]. Also in the non-destructive category, synchrotron X-ray diffraction can be used for BIRS characterization [155, 156]. These two methods are of special interest when pre-form geometries are complex or stress profiles are expected to be randomly distributed. However, they require very expensive equipment with limited availability, take long times to be performed and involve health and environmental hazards under prolonged exposure times, even leaving parts radioactive for months in the case of medium-large sized parts.

While destructive methods seem less attractive than non-destructive methods because of the damage on the specimen, these are very frequently the preferred choice in distortion modeling because of their versatility and reliability [157, 158]. Besides, recently developed computational tools and high precision machining and measuring processes are expanding the scope of these methods [18].

TABLE 2.3: Advantages, disadvantages and application scope of most common RS measuring methods.

RS measuring methods				Non-destructive methods				
Destructive methods				Non-destructive methods				
Hole Drilling	Contour method	Layer Removal	Crack-compliance	Deep hole drilling	X-ray diffraction	Synchrotron X-ray diffraction	Neutron scattering	Ultrasonic method
<i>Advantages</i>								
-Simple	-High spatial resolution	-Simple	-High spatial resolution	-Big measurement depth	-Convenient	-High penetration	-High spatial resolution	-Fast
-Fast	-Common machining tools	-Common machining tools	-RS in cross section	-Common	-Fast	-Can be used for preformed parts	-High penetration	-Low cost
-Standardized	-Extended use	-Can be integrated in CNC	-RS in cross section		-High spatial resolution		-High penetration	-Big measurement depth
-Field use					-Field use		-3D stress fields	
<i>Disadvantages</i>								
-Partially destructive (drilled hole of small diameter)	-Seriously destructive	-Seriously destructive	-Destructive	-Partially destructive	-High cost	-Very high cost	-Very high cost	-Limited spatial resolution
-Low spatial resolution with depth parts increasing	-Cannot be used for simple geometries of plates and cylinders	-Only used for simple geometries of plates and cylinders	-Not as extended as other destructive methods	-Limited sensitivity and spatial resolution	-High quality surface needed	-Used for laboratory usually	-Slow access to data	-Only qualitative
					-Low damage (if electropolishing)		-Used for laboratory usually	
<i>Application scope</i>								
-Macrostress	-Macrostress	-Macrostress	-Macrostress	-Macrostress	-Microstress	-Microstress & macrostress	-Macrostress	-Macrostress
-MIRS	-BIRS	-BIRS	-BIRS	-BIRS	-MIRS	-BIRS & MIRS	-BIRS	-BIRS
-From μm to cm	-From μm to 1m	-From μm to 1m	-From μm to hundreds of mm	-From μm to 1m	-Depth below $50\mu\text{m}$ (with electropolishing up to mm)	-From μm to mm	-Depth up to hundreds of mm	-Depth up to 10cm

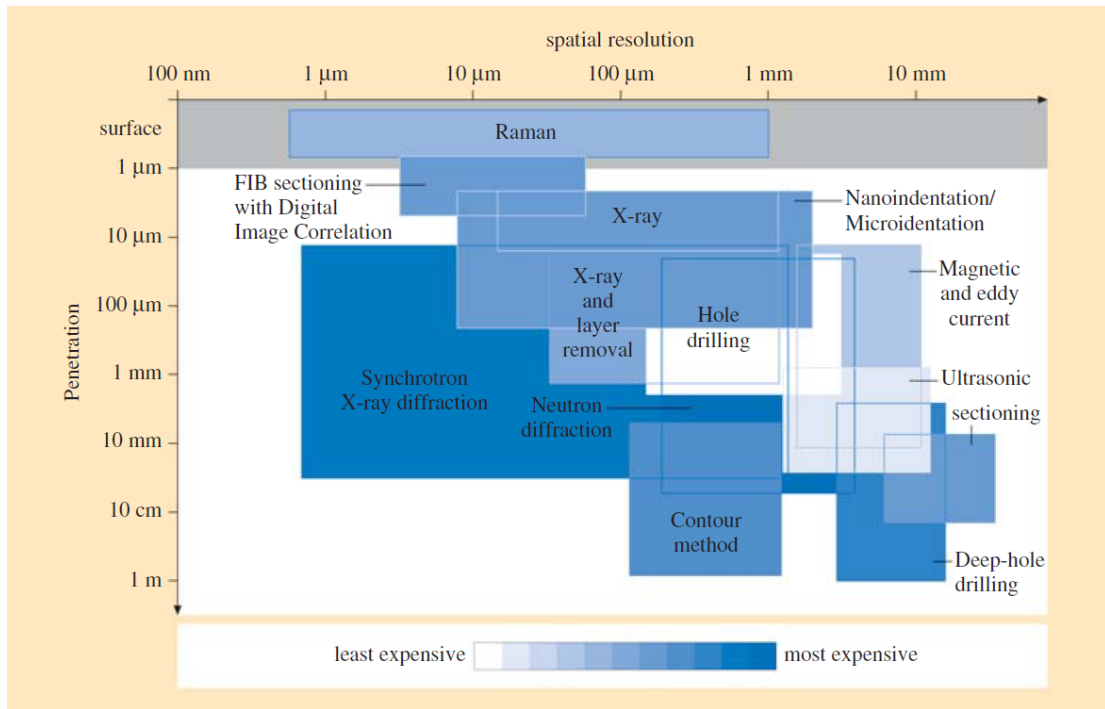


FIGURE 2.13: Measurement penetration vs. spatial resolution for various RS measurement methods [18].

The crack-compliance method (Figure 2.14) consists of determining the stress profile by successive extension of a slot and measuring the resulting strains or displacements [159].

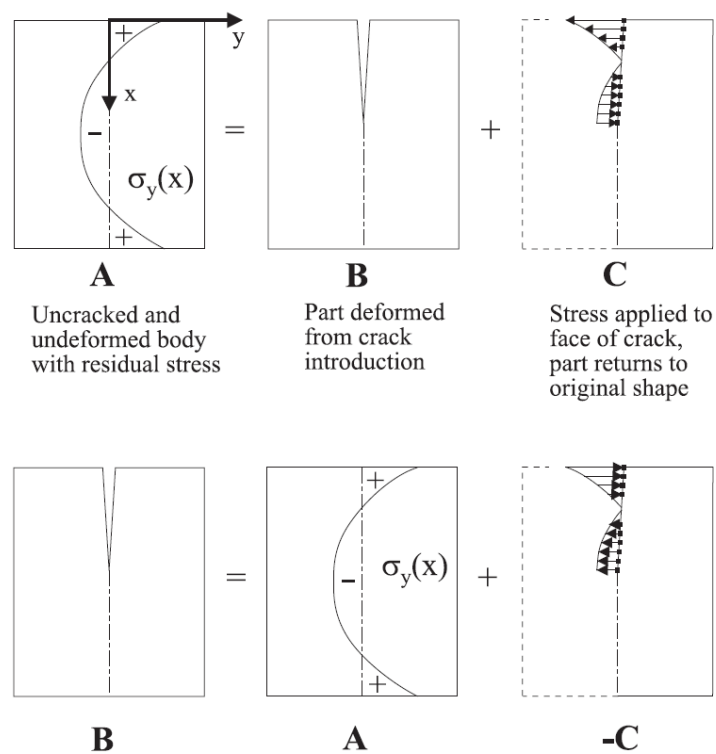


FIGURE 2.14: Sketch of the crack compliance method for measuring BIRS showing the superposition principle used to calculate deformations from released stresses. [159].

Extensive work can be found for assessing the accuracy, uncertainty and repeatability of the crack-compliance method [24, 159–161]. For this reason, a big part of the distortion studies used crack compliance for BIRS characterization [23, 35, 107, 141]. Even variants of the method for improving its accuracy by piecewise calculation are explored [162].

Other extended technique is the contour method, which provides cross-sectional stress fields (2D), as depicted in Figure 2.15. It involves cutting through the specimen cross-section using a wire EDM, and measuring the surface height profiles of the cut surfaces using a coordinate measuring machine or a laser profilometer. The originally existing BIRS normal to the cut can be evaluated from finite element calculations by determining the stresses required to return the deformed surface shape to a flat plane [18]. This method is useful for measuring BIRS in forgings [163], and welded parts [164]. Regarding machining distortion, a big share of the studies use the contour method for obtaining BIRS data [123, 165].

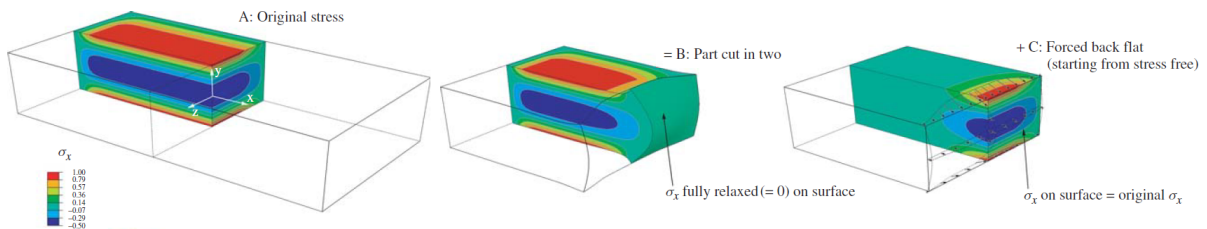


FIGURE 2.15: Sketch of contour method for measuring BIRS showing the superposition principle, where stresses are plotted on one quarter of the original body [166].

Following a similar idea, but with the difference of a diagonal cut, the slope or wedge method can be found [38, 167].

The layer removal (LR) method can be also used for BIRS measurement in cylindrical or plane parts with stresses only varying in depth but being parallel to the surface. Its main feature is that the material is removed in successive uniform layers from the surface of the part, and the deformations due to stress relaxation are measured, from which stresses are calculated.

The traditional LR method has to be performed in laboratory environments and parts of limited size, because the material is removed by EDM (not to introduce additional stresses), and the measurements are made using strain gauges in the opposite face of the part where the layers are removed, requiring gluing and removing operations, as depicted in Figure 2.16) [168].

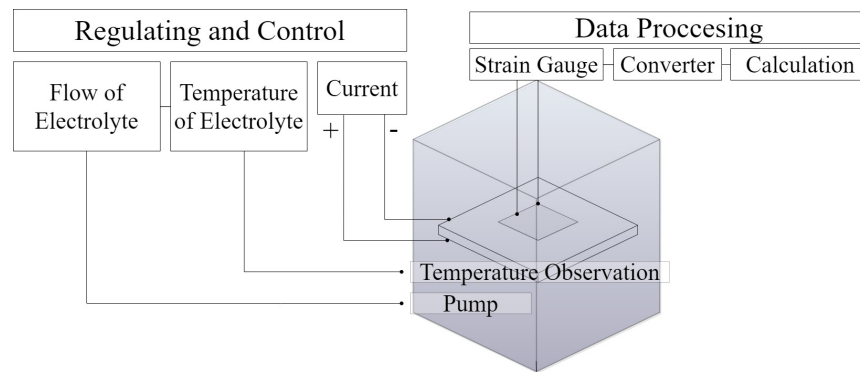


FIGURE 2.16: Set-up for the Layer Removal Method using EDM and strain gauges [168].

Its recent variant, the on-machine LR, also labelled as modified LR, is based on the idea of performing the LR in a conventional machining centre. Although the traditional LR shares the basic concept with the on-machine LR, in operational terms this method is effectively novel. This measuring method was introduced for first time by Chantzis et al. [73], who used a high resolution linear transducer to measure the displacements, and a specially designed jig to ease the measurement procedure. A year later, Dreier and Denkena [169] presented also a method derived from the traditional LR which used a machine-tool and a standard touch-probe (Fig. 2.17), reducing considerably implementation time. In comparison with other displacement measuring solutions, the touch-probe offers full automation of the measuring task, higher resolution than linear transducers and easier data acquisition.

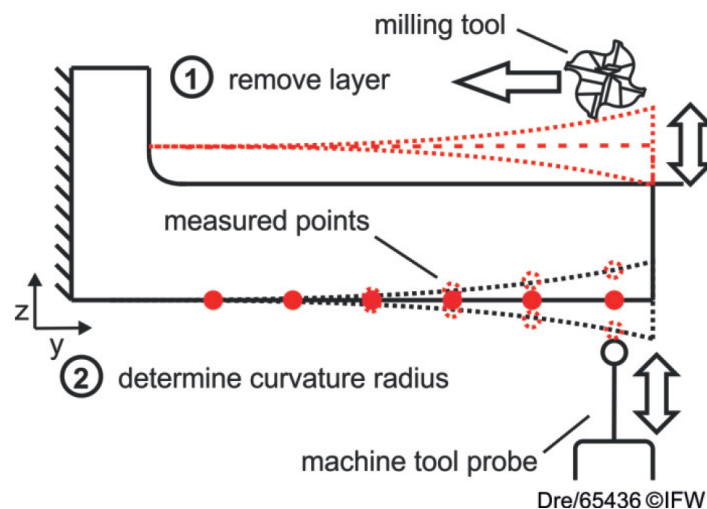


FIGURE 2.17: Sketch of the on-machine LR in 1D, with measurements and material removal in opposite faces of the part [169].

The main advantages of the on-machine LR method is that it can be performed in industrial environments by untrained staff, becoming this way an appropriate solution for measuring BIRS in rolled aluminium blanks for the aerospace structural parts manufacturing. For

these reasons the on-machine LR is used in many distortion-related investigations [25, 32, 101, 170–172]. Nevertheless, this method only attains BIRS, thus does not consider other circumstances involved while the measurement is performed. For instance, the modification of the stress state due to the material removal by machining. Furthermore, even appearing straightforward in concept, the on-machine LR has subtle details that require increased conceptual understanding and must be learned from practical experience to achieve the most refined results.

The Deep Hole Drilling (DHD) method is useful for determining the BIRS within the deep interior of large specimens. The method involves drilling a deep hole into the part and measuring the change in diameter as the surrounding material is overcored [18]. While results from the DHD method are confined to a line distribution, 3D distributions of BIRS can be derived with the aim of FEM. Nevertheless, distortion investigations assessing BIRS input data through DHD were not found. The same applies to the Deep Hole Contour (DHC) method depicted in Figure 2.18, which achieves a reduced degree of damage on the part and does not require the application of strain gauges, trepanning, or complete sectioning of the tested specimen [173].

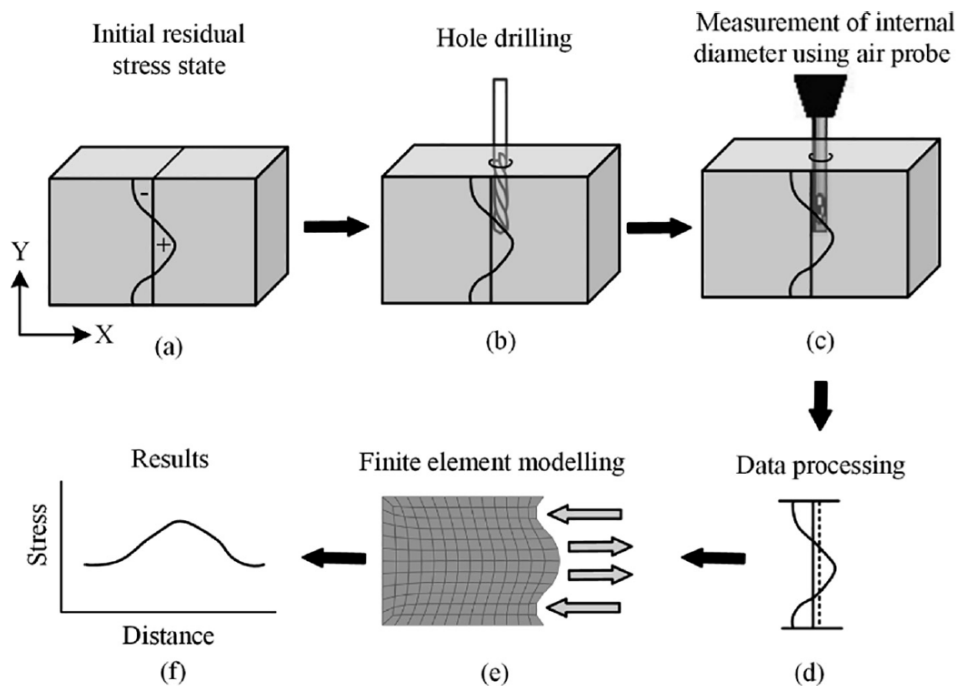


FIGURE 2.18: Sketch of the deep hole contour method [173].

There are few studies comparing non-destructive against destructive methods, demonstrating that comparable through thickness RS profiles can be obtained [174–176]. However, as the formulation used for the BIRS calculation responds to certain hypothesis and the

particular procedures related to each measurement method (interpolation and extrapolation functions, filtering methods, etc.), there is a high probability of obtaining different RS measurement results.

Finally, in relation with the use of the measured BIRS data for distortion calculation, often local measurements extrapolate to whole blanks [164], even though there can be variation of BIRS within the part [112, 177], which can be an additional source of error.

Formulation behind RS measurement by destructive methods

There are differences between the destructive or mechanical methods regarding the material removal geometry and the way deformations or strains are measured. However, even if each method seems to have its own specific calculation formulae, there is a mathematical commonality to all destructive methods. To begin with, the relationship between measured deformations and stresses is given most commonly by a Volterra integral equation of first kind (Eq. 2.7) [157].

$$d(l) = \int_{l_0}^l g(L, l) \sigma(L) dL \quad (2.7)$$

Where, $d(l)$ is the deformation (displacement or strain) measured when the depth of the removed material equals l ; l_0 is the initial depth; and $\sigma(L)$ are the stresses originally present at all depths L within the removed material. The kernel function $g(L, l)$ describes the deformation sensitivity to a stress at depth L within removed material of depth l .

It is an inverse problem, meaning that the evaluation of the unknown quantity, stress, requires a solution from left to right. This comes from the fact that the calculated stress corresponds to the removed material, while the measurements are taken in the adjacent material to the removed one. Furthermore, the measured deformation depends on all stresses of the removed material. This way, the relationship between stresses and deformation is not one to one, coming in the form of an integral equation. The choice of this integral equation influences significantly the solution. A frequent choice is a unit pulse function due to its simplicity and direct physical interpretation.

However, solving the inverse problem results complicated because the stress term is within the integral. An alternative way of fulfilling the task, expresses the unknown stress function $\sigma(l)$ as the sum of basic functions, $u_i(L)$, multiplied by coefficients c_i (Eq. 2.8).

$$\sigma(l) = \sum c_i \cdot u_i(L) \quad (2.8)$$

It is important to note that the functions must be linearly independent and that their combination should represent the solution properly. Again, unit pulses offer a conceptually and algebraically straightforward choice. The width of each pulse corresponds to successive increments in material removal depth, which are not necessarily all equal. For unit pulses, the coefficients c_i in Equation 2.8 correspond to the stresses within each material increment, σ_i . Substituting unit pulse functions into equations 2.7 and 2.8 yields the matrix equation (Eq. 2.9).

$$[G] \cdot \{\sigma\} = \{d\} \quad (2.9)$$

In this, the left side represents the solution containing the unknown vector σ , meaning the stress at each of the increments. The right side contains the vector with deformation measurement data, d , after each material removal increment. These data differ depending on the BIRS measuring method. Likewise, the coefficients G , are particular to the stress measurement method, and correspond to the deformation caused by a stress within increment “ j ”, of a cut that is “ i ” increments deep. Because the deformations are sensitive only to stresses within the removed material, zero values of G occur only when $j > i$. Thus, G is a lower triangular matrix.

Layer Removal (LR) method

Considering the significance of the LR method within this work, next paragraphs briefly introduce its basic concepts.

The pioneer work which, established the relationship between stresses and curvatures of thin metallic films was performed by Stoney in 1909 [178]. Years later, Treuting and Read [152] developed the LR method for stress measurement in sheet materials. Its main feature was that the material is removed in successive uniform layers from the surface of the part. The deformations due to stress relaxation (Fig. 2.10) are measured and, from these measurements the stresses are obtained.

It is suited to parts with stresses only varying in depth but being parallel to the surface (Fig. 2.19). This way, two components of stresses are considered, which match with the curvature directions. The geometries in which LR can be performed can be cylindrical and plane plates.

As previously mentioned, in a free part the BIRS are balanced, satisfying the force and momentum equilibrium equations (Eq.2.10) [100], where, H is the height of the part, σ_x is the stress in X direction, and z is the distance in the plate thickness direction. An analogous expression with σ_y corresponds to the perpendicular section.

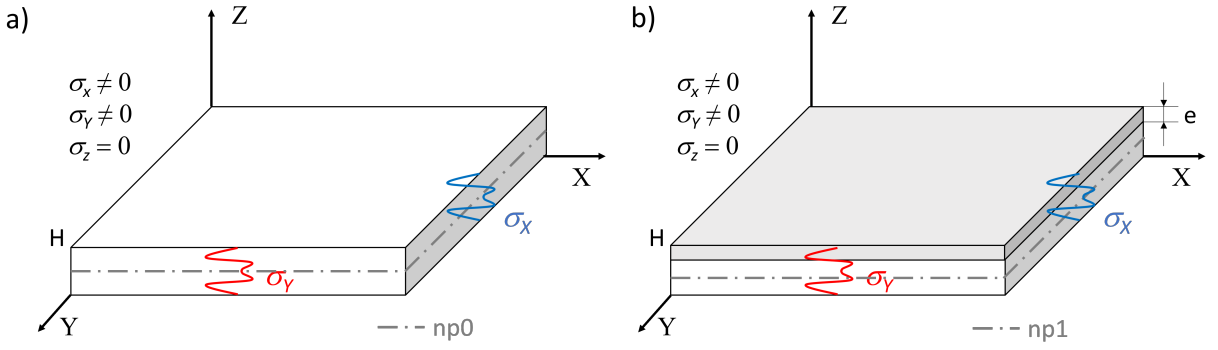


FIGURE 2.19: Plane plate with BIRS fulfilling the stress conditions for LR method: a) Initial state, no material is machined; b) in-process state indicating in grey color the layer to be removed.

$$\int_0^H \sigma_x(z) dz = \int_0^H \sigma_x(z) z dz = 0 \quad (2.10)$$

The method works under three additional assumptions. First, the part must be linear in pure bending, over the range of curvatures involved. Second, the part must be isotropic, thus, the elastic constants are the same throughout the material. Finally, the removal of the layers should not disturb the stress in the remaining material.

Under these premises a layer of material is removed (Fig. 2.19b), removing at the same time a part of the BIRS distribution and leaving an unbalanced distribution of internal loads (Eq. 2.11 and 2.12, with similar expressions for the Y direction). It must be noted that the neutral plane of the portion also moves as the material of the plate is removed.

$$F = \int_0^{H-e} \sigma_x(z) dz \quad (2.11)$$

$$Mb = \int_0^{H-e} \sigma_x(z) \cdot \left[z - \frac{e}{2} \right] dz \quad (2.12)$$

At this point, the clamping constrains the deformation of the part with external forces and moments equal to the ones result of the BIRS unbalance. When the clamping is released, the part deforms such as to introduce additional stresses and restore internal equilibrium. Thus, the forces and moments associated with the deformation are equal and opposite to those of the BIRS. The forces due to the additional stress introduced by deformation are given by the elongation, and the moments by the curvature. The measured curvatures $\chi_x(z)$ and $\chi_y(z)$ and bending moments for pure bending of semi-infinite flat plates [99]

relate using Equation 2.13, where E is Young modulus, ν is Poisson ratio, and the negative sign is due to the curvature occurring on removal of the applied moment.

$$M_b = \frac{-E \cdot (H - e)^3}{12(1 - \nu^2)} \cdot (\chi_x(z) + \nu \cdot \chi_y(z)) \quad (2.13)$$

Analogous expressions apply to Y direction.

The desired relation between measured curvatures and unknown stresses is given by substituting Equation 2.13 into 2.12. In order to obtain the complete through-thickness BIRS profile, layers of material are removed iteratively.

2.4.2 MIRS data acquisition

In comparison to BIRS, MIRS characterization is more extended, both by modeling and measuring. However, as MIRS vary upon machining conditions, it is difficult to anticipate their effects in machining distortion. Moreover, contradictions between published results regarding cause-effect relationships of MIRS can be easily found, which are directly related to the uncertainty of MIRS characterization, both by modeling and measurement.

2.4.2.1 MIRS modeling

In the last decades, the improvement of computation capabilities has boosted machining process modeling, rising the number of investigations. The need for investigating the effects of cutting conditions, tool geometry, cooling conditions and MIRS has emerged with a significant research effort being made by the international research community [179]. For this reason, studies compiling the state-of-the-art in predicting machining performance, which summarize the MIRS modeling works, can be easily found. This way, Arrazola et al. [180] summarized the advances in modeling of metal machining since 1998; Ulutan and Ozel [181], as well as, Wang and Liu [182] focused on machining modeling for titanium and nickel alloys; and Wang et al. [183] focused on general MIRS modeling. Moreover, there are commercial solutions specifically designed for machining process simulation and MIRS prediction, such as MACHPro, AdvanEdge, DEFORM and VERICUT. However, their use is quite complex and would require highly qualified and trained workers.

Different model approaches can be defined, which are divided into four main categories, empirical, analytical, numerical and hybrid. Table 2.4 depicts them, as well as, their basic principles, capabilities and limitations.

TABLE 2.4: Principles, capabilities and limitations of modeling approaches.

<i>Modeling approach</i>	Empirical	Analytical	Numerical	Hybrid
<i>Principle</i>	<ul style="list-style-type: none"> -Statistically established -Based on experimental test -Data curve fitting -Minimum error principle 	<ul style="list-style-type: none"> -Slip-line theory or minimum energy principle -Based on metal elasto-plastic theory and cutting conditions -Kinematic and energy equations 	<ul style="list-style-type: none"> -Continuum mechanics using FEM, FDM & meshless FEM -A function to minimize the functional and discretization 	<ul style="list-style-type: none"> -Combine different approaches -Meta-models for a family of models to be integrated
<i>Capabilities & Advantages</i>	<ul style="list-style-type: none"> -Earliest prediction method -Applicable to most mach operations -Industry relevant parameters** -Very efficient -Practical -Fast 	<ul style="list-style-type: none"> -Study the mechanism and principles of MIRS generation -High academic value -Promote development in mechanical science -Fundamental Variables * -Fast 	<ul style="list-style-type: none"> -Commonly used -Reflect the whole machining -Less experimental work -Industry relevant parameters** and some Fundamental Variables* -Versatile -Simple modeling (2D) 	<ul style="list-style-type: none"> -Overcome limitations of single approaches -Improves capabilities and accuracies of base models (speed, cost and accuracy) -Increased robustness
<i>Limitations & Disadvantages</i>	<ul style="list-style-type: none"> -Established under certain conditions -Limited application range -Extensive experimentation -Accuracy depend of math. function 	<ul style="list-style-type: none"> -Unique to each problem -Complex for industrial relevant parameters -Accuracy limited to assumptions -Regarded as difficult to perform or formulate -Usually limited to 2D 	<ul style="list-style-type: none"> -Focused on calibrating material constitutive model or flow-stress data -Low efficiency (3D) -Time-consuming -May require submodels to capture complex phenomena (e.g. phase transformation) 	<ul style="list-style-type: none"> -Not fully implemented -Limited to the strength of the base model -Need for extensive data from experiments and/or simulation

*Fundamental variables: cutting and feed forces, tool-chip contact length, chip thickness, temperatures, stresses, hydrostatic pressure, strains, strain rates, chip speed, plastic and friction energies...

**Industry relevant parameters: Tool life, surface roughness, accuracy, residual stresses (surface integrity), stability, chip form/breakability, burrs...

In analytical MIRS models, the different assumptions (such as plain strain or plain stress conditions) which are employed for performing the calculations using physical equations, represent the ideal conditions of events and usually are not practically applicable [184, 185]. FEM models usually provide a good understanding, but also they involve many assumptions and require experimental validation without which they can lack the capability of prediction [43, 186]. Besides, the computation cost can be too high to account for their use in industry. Empirical models, being based on experimental data provide fast and applicable results, although they are only applicable for the case and range for which they are built [187].

The repeatability and accuracy of measuring methods with which the models are built is rarely addressed on available research which, lowers the evaluation robustness of the MIRS models. Finally, MIRS modeling is mostly established for orthogonal cutting, while actual turning or milling operations are not that studied, neither solid milling tools [182, 183].

2.4.2.2 MIRS measurement

As the penetration depth decreases to superficial range, measuring RS becomes easier. Besides, due to the implications of the MIRS on the functional performance of the parts, and boosted by the lower cost of the measuring in comparison to through-thickness RS (Table 2.3, Fig. 2.13), MIRS measuring methods are well-established within industry as quality control techniques. The two main methods for MIRS measurement are X-ray diffraction (XRD) and hole drilling (HD).

Briefly explained, the HD is a destructive method based on stress relaxation. A small hole is drilled in the surface of the component, where a strain gauge previously glued to the surface measures the generated strains [188]. Figure 2.20 shows a typical commercial hole drilling rig, by HBM [189].



FIGURE 2.20: HD commercial rig by HBM [189].

The XRD method is based on measuring the inter-planar distance of the crystal lattice, which represents the deformation generated in the material. From this value the stress is calculated with the elastic constant, assuming a linear elastic distortion of the corresponding lattice plane [190, 191]. Although the XRD is within the non-destructive category, the electropolishing required for in-depth measuring to acquire complete MIRS profiles makes this method destructive too. Figure 2.21 shows a XRD commercial equipment by Stresstech.



FIGURE 2.21: XRD commercial equipment by Stresstech [192].

Both methods are used equally in distortion research and have their variants. Some works emphasize the overall necessity to combine destructive and non-destructive methods in order to improve the accuracy and efficiency of the measurements [193, 194]. Due to the high uncertainty of the MIRS measurements, some researchers recommend using two independent techniques for the measurement of a part to make a measurement reliable [79, 195]. On this basis, although quantitative comparisons between different measuring methods are reported, [49, 196, 197], big differences in results obtained by different methods are common, so that just qualitative comparisons are performed [198, 199]. In fact, investigations evaluating which MIRS measuring method provides best results for distortion calculations are very seldom [49].

Moreover, the high stress gradient typical of machining process (3000 MPa/mm from the surface to about 0.1 mm in depth [18]), makes the spatial resolution and thickness of the measurement volume an important consideration. Furthermore, balance must be found between measurement accuracy and spatial resolution, as a greater spatial resolution comes often at the cost of reduced precision, and vice versa. In this regard, XRD being a non-destructive method enables the repetition and averaging of measurements, which typically improves accuracy.

2.4.3 Discussion upon RS characterization

In summary, the acquisition of reliable RS data is complex and costly. The inability to determine accurately RS, BIRS and MIRS, is a major cause for inaccurate distortion calculations. Experimental measurements are not only critical for the acquisition of input data for distortion prediction models, but also for the construction and validation of the distortion source estimation tools.

Regarding BIRS, modeling is not capable of providing data reflecting the variabilities between machining blanks. Considering that the materials used for aerospace manufacturing often undergo stress relief treatments (low the magnitude stresses), the BIRS variabilities can represent a significant difference in subsequent distortion calculation. Moreover, manufacturing process models for BIRS estimation require also experimental trials, not providing a significant advantage from direct BIRS measurement.

Alternatively, almost all BIRS measurement methods were originally developed as laboratory techniques, and require carefully controlled conditions only possible in a laboratory environments. Besides, they are limited to small and simple test-piece geometries. In this regard, the incipient on-machine LR techniques offers new possibilities, although it does not consider the MIRS induced in the surface by the machining process and it is a destructive method.

In this way, considering the unavoidable BIRS variabilities between blanks, destructive methods cannot measure BIRS in blanks from which final parts are obtained. Thus, by definition, it is impossible to perform accurate distortion calculations with inaccurate input BIRS data. Non-destructive methods though, are very costly and require long times until the blanks can be machined due to radioactivity kept in the blanks, thus are not applicable for their industrial implementation.

Concerning MIRS, the measuring uncertainty is also an issue, which is combined with the fact that different measuring methods often provide different results and with the variation of MIRS upon the machining conditions.

In order to foresee the MIRS profiles induced in the parts by a set of machining conditions modeling is used. Considering the wide range of materials, tools, machining conditions, etc. there is a wide variability of MIRS models in literature. However, when companies perform the machining of an aerospace susceptible of having distortion issues, the models available in literature are not directly applicable. On the one hand, because analytical models are complex and require expertise. And, on the other hand, because numerical models have costly licenses and often do not match with experimental results unless calibrated with experimental trials.

2.5 Distortion Control

Distortion control of aerostructures is a recurring topic in literature [15, 28, 200]. This section reviews the strategies proposed by scientific literature for distortion control, which are classified into offline and online methods, according to Figure 2.22.

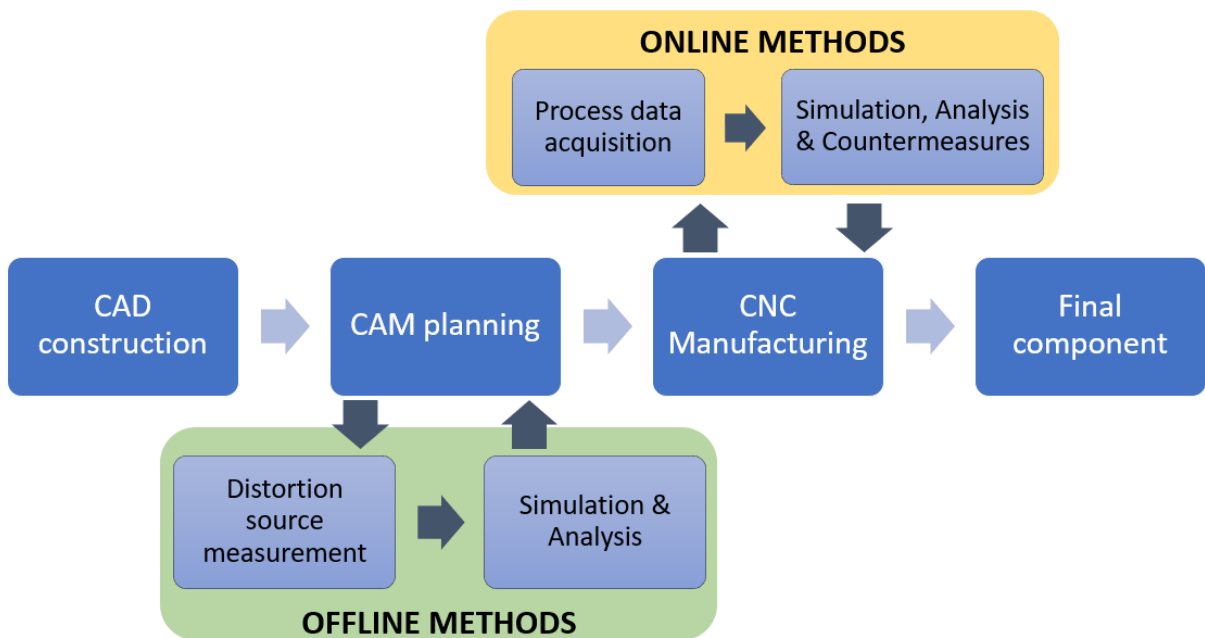


FIGURE 2.22: Classification of distortion control strategies.

The methods for post-machining correction (e.g. peen-forming [201], laser-peening [202], age forming [203]) and the methods for stress relieving (e.g. vibratory stress relieve - VSR [204], cryogenic stress-relief [205]) are not herein considered.

2.5.1 Offline Methods

Offline or process planning methods refer to those approaches which include preparatory steps based on measuring and modeling techniques, determining the tactics that would lead to minimum distortion. These tactics are often focused on finding the optimal offset or part location within the machining blank, defining the most appropriate machining sequence, tool path, and machining conditions, and acting through the geometry and stiffness variation of the part (Fig. 2.23).

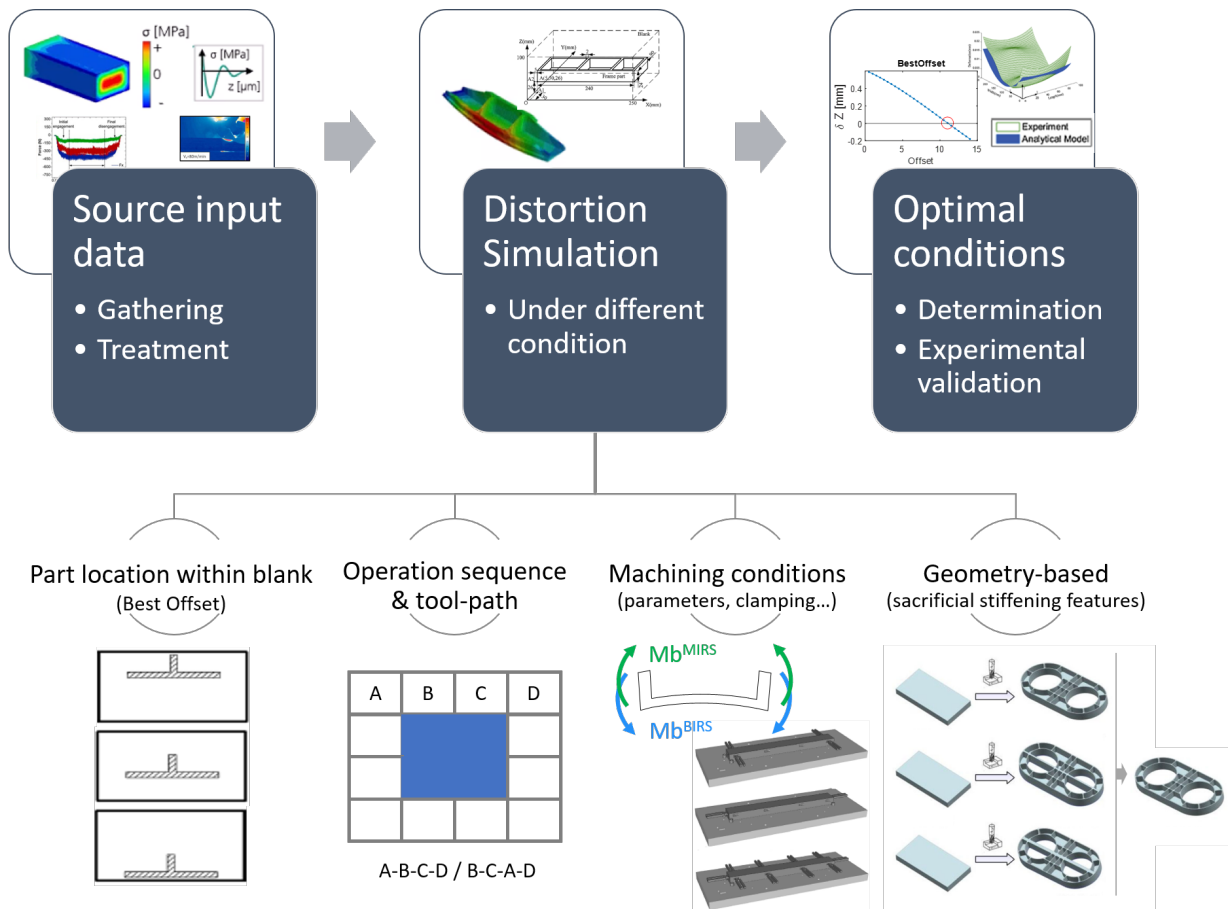


FIGURE 2.23: General workflow for offline distortion control.

The advantage of these methods is their lower cost and easier implementation in comparison to online methods thus, making them more affordable for small and medium-size industrial companies. On the contrary, they are not able to adapt to variabilities during the process. In any case, the use of offline methods does not need to be exclusive, opening the possibility of employing online methods in conjunction.

Part location within blank or Best Offset

The machining blank has to envelop the target part geometry so that the final component can be properly manufactured and often, the blanks are big enough so that they offer the possibility of locating the final part in different positions. In this regard, this first control technique prevents distortion by simulating it for different part locations within the blank (Fig. 2.24), thus, it is also called Best-Offset strategy. This approach is the most reported distortion control strategy for aerostructures [21, 25, 38, 70, 73, 118, 135, 206, 207].

The main shortcomings of the best offset approach are that, with the increased demands of cost reduction, blanks have minimal size, not leaving much room for locating the part in different positions in some occasions. Besides, using this strategy as the only distortion

control mean is assuming that the main cause for distortion is BIRS relaxation (ignoring MIRS effect), and if that is not true, changing the offset may not have the desired effect in the final distortion. Alternatively, the solution by D'alvise et al. [21] combined the best offset with the simulation of the BIRS gradual relaxation after a machining pass for cutting paths representation (material removal sequence). In fact, choosing the optimal sequence in which the material is removed is also used as a distortion control tactic, as it is reviewed below, and many authors used the two strategies together.

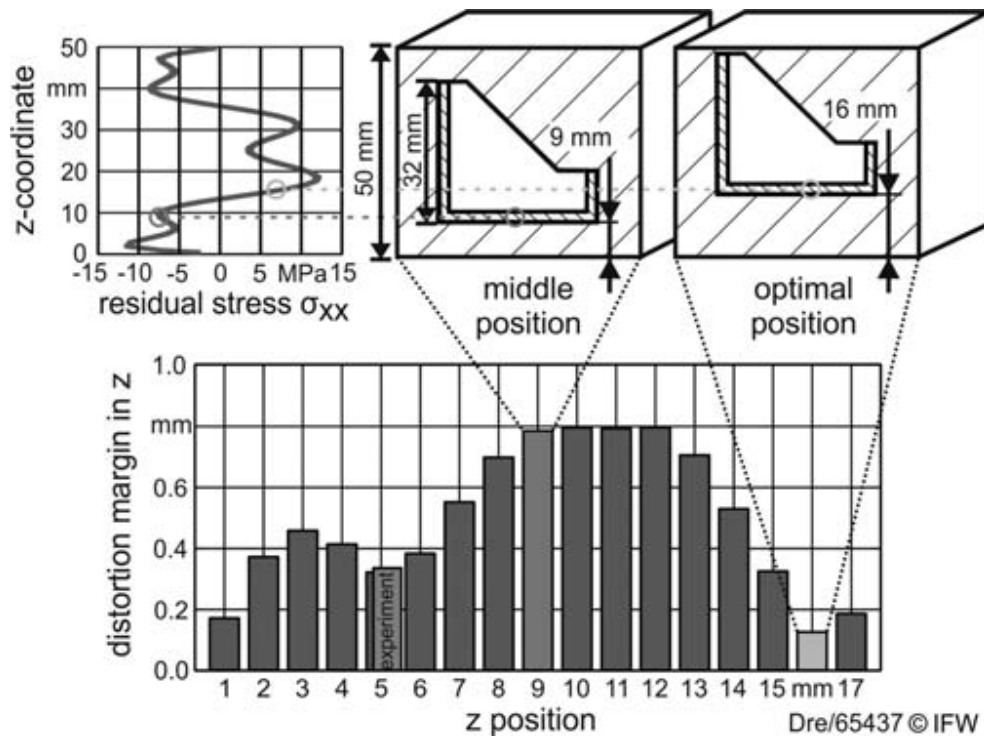


FIGURE 2.24: Best-offset strategy for machining distortion control [135].

Operation sequence and tool-path

The option of controlling distortion based on finding the optimal operation sequence and tool-path, is done defining preliminarily a discrete number of different sequences/tool-paths to test by simulation and then choosing the one resulting in minimal distortion.

In the case of material removal sequence, the level of discretization or division can be at feature level (e.g. pocket) [125, 208], height or machining pass level [70], or even finite volume level [209], which not only affects the accuracy, but also affects the complexity and duration of the study. Drafting properly the case may reduce significantly cost and effort. One way of determining directly the optimal operation sequence, is calculating the natural frequencies of the component at the machining interim stages of the different sequences evaluated, and selecting the sequence which could make the most use of the stiffness of the component [208]. Similarly to the previous case, some works studied the effect of

the different sequences on strain energy, concluding that strain energy provides beneficial information for the determination of the optimal operation sequence [125, 209].

In order to evaluate the results of the optimal sequence and tool-path strategy, not only the machining distortion is considered, but also the dimensional variations along machining stages. In fact, these enable to determine the over-cut or under-cut that may occur at interim machining states, and ensuring that there is enough material to finalize properly the component (Fig. 2.25). According to this, choosing a strategy in which the major distortion happens in the roughing operations and minimal in the finishing operations is feasible, guaranteeing the material allowance [38, 209–211].

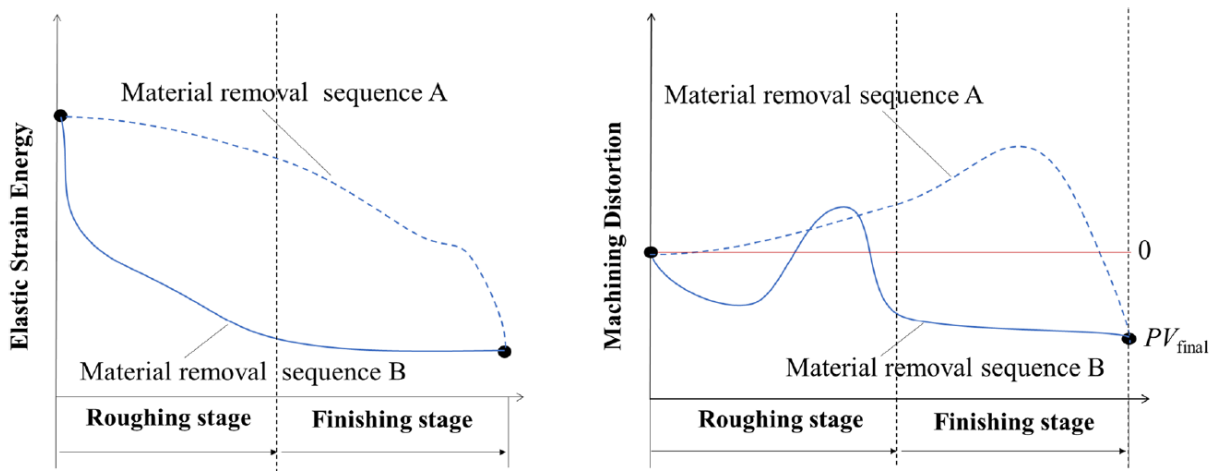


FIGURE 2.25: The material removal sequence vs. evolution of machining distortion [209].

Alternatively, some works adapt the tool-path to simulated distortion (offline) so that distortion problems are minimized. The simulated distortion can be due to different sources as, static deflections [212, 213], thermal effects [86], and MIRS [135]. In this regard, Dreier et al. [135] remarked that productivity could increase or decrease by choosing one tool-path or another.

Finally, the compromise between productivity and accuracy is sometimes difficult to achieve, and multi-objective algorithms may be helpful for these cases [214, 215]. This way, not only machining sequence and tool-path, but also machining conditions (which also influence greatly productivity), can be used intentionally to control distortion as it is explained hereafter.

Machining Conditions

The change in machining conditions (cutting speed, feed, clamping, coolant...), causes different MIRS profiles, as depicted in Figure 2.26.

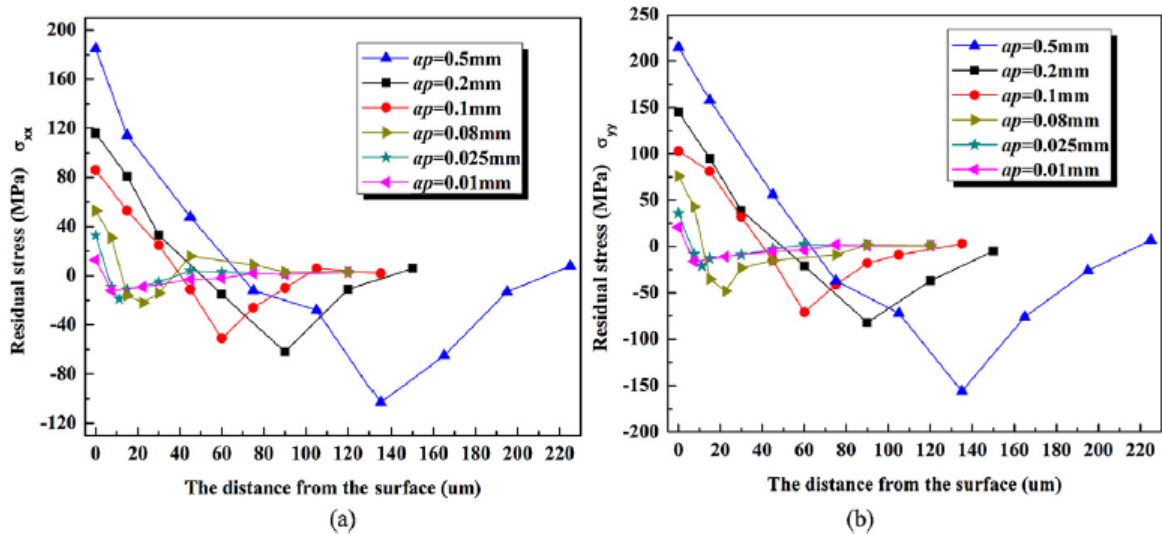


FIGURE 2.26: MIRS profiles for different depths keeping constant the other machining conditions [53].

In this way, Dreier et al. [135] considered that, when the previously mentioned strategies were not sufficient, a local adjustment of the parameters adapting the G-code could modify MIRS, hence counteracting distortion actively. In fact, they showed indirectly that final distortion could be influenced modifying the MIRS. In line with this, experimental results showed that even considering the BIRS, the MIRS could lead to a difference in machining distortion of 65% depending on the cutting conditions [123].

However, even though the strategy of changing the milling conditions to customize MIRS and control distortion seems promising, studies analyzing directly this topic were not found.

Geometry-based optimization

The part geometry plays an important roll in machining distortion. In fact, research proved that machining distortion is inversely proportional to the stiffness of the part for different geometries of the same wall thickness [32], and decreases with the increase of the bending stiffness in the length direction [121].

In this regard, scholars explored the possibility to act through the geometry of the part, using sacrificial structures or features which increase the stiffness of the component at interim machining stages, and are removed afterward [216]. This concept was also combined with setting the parts free and performing stress relieve treatments between machining steps [217], as depicted in Figure 2.27.

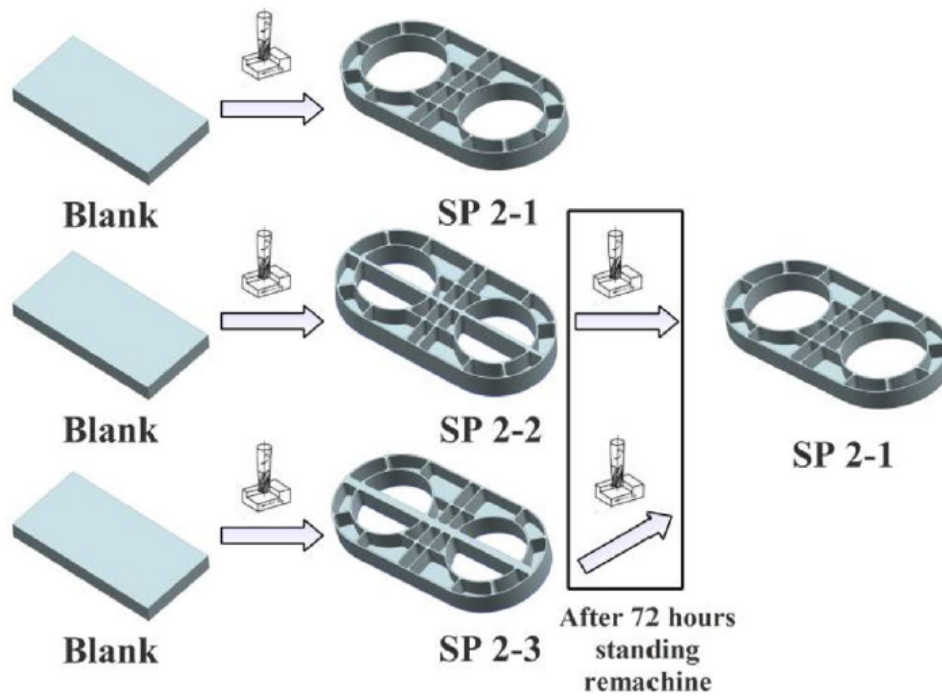


FIGURE 2.27: Control method based on the combination of enhancing equivalent stiffness and applying a interim step of stress relieve (setting parts freely for a time, aging or vibratory stress relieve [217]).

2.5.2 Online Methods

Online methods are those which actuate while the machining process is taking place, as depicted in Figure 2.22. Hereafter online methods are summarized in two categories, smart clamping devices and online adaptive machining, although they are frequently used in combination.

Smart clamping

A further possibility for influencing the machining distortion is provided by the clamping of the component in the machine-tool. These are the scenarios where a smart clamping is sought in relation to machining distortion:

1. Automatically detect distortion as it occurs, and release the part ensuring that the follow-up operations are performed under low stress and also ensuring the positioning accuracy related to design datum [218–224].
2. Compensate distortions by applying intentionally certain loads [135].
3. Integrate sensors and actuators, which enable to obtain in-process information and respond actively [225–227].

4. The combination of No. 2 and 3 [176, 228, 229].

Although these investigations seem promising, the smart clamping is still in an incipient state of development, so yet not ready for industrial use.

Online adaptive machining

By definition, online adaptive machining adapts manufacturing parameters and tool-paths to suit the changing conditions, taking into account the response of the system. It takes as input not only previously developed predictions, but also in-process monitoring data. This data can be directly measured distortions or other process variables, and often is acquired through smart clamping systems.

The superposition of the nominal and actual surfaces results in the compensation of the part distortion. It is mostly used for distortions due to cutting forces and/or in thin features (walls, blades...) [230–234], and not so much in complete parts as aerostructures.

Conversely, looking into the whole monolithic component, Hao et al. [235] proposed a method to dynamically adjust the machining sequence at each machining layer, based on deformation monitoring data obtained from a responsive fixture. Shortly after, a method for dynamic upside/downside allowance allocation (Best Offset determination) was presented, which also was based on deformation monitoring data obtained from a smart clamping [236].

2.5.3 Discussion upon distortion control

Along this section the offline and online methods for distortion control are reviewed, which are summarized in Table 2.5.

Regarding the readiness level for industrial implementation, offline methods surpass online methods. Besides, online methods imply higher investment cost.

The main advantage of offline methods is that they can be performed systematically in the process planing phase, reducing this way the associated costs. However, the big differences between simulation and experimental results reported by many authors, imply that there is an accuracy limitation on this regard. This is because these methods rely on the results obtained with distortion models and often inaccurate RS input data.

In aerostructures, the most extended practices are the best offset and the optimal machining sequence.

TABLE 2.5: Review of machining distortion control research.

Machining Distortion Control				Offline methods		Online methods			
#REF	Material	Test-case	AI algorithms	Best Offset	Optimal Sequ./Tool-path	Machining conditions	Geom.-based optimization	Smart Clamping	Adaptive machining
[73]	Aluminium alloy	T-shaped beam		X					
[206]	Al 7050-T7451	T-shaped beam		X					
[25]	Al 7050-T7451	Wing rib specimen		X					
[207]	Al 7075-T7451	U-shaped beam		X					
[135]	Al 7075-T651	Aerostructure specimen		X	X				
[70]	Al 2050-T84,	Aerostructure specimen		X	X	X			
[38]	Al 7075-T651	Specimen 3 pockets		X		X			
[118]	Al 7050-T7451	Wing rib specimen	ANN & SA	X					
[21]	Al 2024 T3	Airfoil		X	X				
[236]	Al 6062	Aerostructure specimen	ARIMA, (P)ACF	X				X	X
[208]	Al 7075-T7451	Specimen 3 pockets			X				
[125]	Ti-6Al-4V	Aero engine case			X				
[209]	Al 6061-T3	Specimen 1 pocket			X				
[212]	TC4 Ti-alloy	Thin-wall (blade)			X				
[213]	TC4 Ti-alloy	Thin-wall (semicircular)			X				
[86]	Al 2024	Axisymmetric specimen			X				
[211]	TC4 Ti-alloy	Thin-wall	GA		X				
[235]	Al 6061	Aerostructure specimen	HCA		X			X	X
[53]	Al2024-T3	Specimen 7 pockets				X			
[123]	Al 7175-T7351	T-shaped beam				X			
[237]	Steel 16MnCr5	Gears				X			
[238]	Ti-6Al-4V	—				X			
[215]	Al 5083	Thin plate	RSM & ABC			X			
[133]	Aluminum alloy	Prismatic part	NN			X			
[32]	Al 7075-T6	Plates pockets (7 geom.)					X		
[216]	Al 7050-T7	Thin-wall specimen(1 pocket)					X		
[217]	Al 7075-T6	Plates pockets (2 geom.)					X		
[219]	Aluminum alloy	Aerostructure specimen						X	
[220]	Al 7050-T7351	Aerostructure specimen						X	
[223]	GH4169 Ni-alloy	Thin-wall (blade)						X	
[221]	Aluminum alloy	Thin plate (2 geom.)	GA					X	
[222]	Polymer foam	Car dashboard	GA					X	
[224]	Aluminum alloy	Aerostructure specimen	GA					X	
[225]	—	Prismatic part						X	X
[229]	Ti-6Al-4V	Thin-wall (blade)						X	X
[228]	Inconel 718	Tail bearing house						X	
[176]	AISI 316L	Prismatic part						X	
[230]	—	Thin-wall (blade)							X
[231]	—	Thin-walled curved plate							X
[233]	Ti-6Al-4V	Thin-wall (blade)							X
[234]	Aluminum alloy	Thin-wall (blade)							X
[232]	Al 7075	Plates pockets/Thin-walls	ARIMA						X

ANN: Artificial Neural Networks

SA: Simulated Annealing

GA: Genetic Algorithm

RSM: response surface method

ABC: Artificial Bee Colony

ARIMA: autoregressive integrated moving average

HCA: hierarchical clustering algorithm

ACF: autocorrelation function

PACF: partial autocorrelation function

Although many scholars consider that through machining parameters and MIRS, distortion could be compensated, literature proving direct proof of the concept in aerostructures was not found.

Finally, a big part of the research emphasizes the need for methods which enable systematic industrial implementation.

2.6 Conclusions and research lines

From the bibliography study the following conclusions were withdrawn:

- The main distortion sources in aerostructures are the residual stresses (RS) inherent in the machining blanks coming from the upstream manufacturing processes (BIRS), and the residual stresses induced by the machining processes in the surfaces due to the high thermal and mechanical loads (MIRS).
- Distortion prediction models can be analytical, only applicable to very simple geometries, and numerical, requiring long computational times. Hybrid models can overcome the limitations of both approaches, combining their advantages, agility and accuracy respectively.
- The results obtained with distortion prediction models often show discrepancies when comparing to experimental results, and the main reason of these simulation errors is linked to the inability to determine accurately RS, BIRS and MIRS.
- Although RS estimation with calculation models has improved along these years, due to the RS variability the distortion models require an accuracy that only measurements can suffice. Moreover, the uncertainty of RS measurements in relation to machining distortion is barely assessed.
- Performing BIRS measurements requires long and complex measuring methods only implementable in laboratory environments by trained staff, which are limited in size to laboratory test samples. Moreover, the most extended BIRS measuring methods are destructive, which imply that BIRS cannot be measured in blanks from which final parts are obtained. This is especially important because even trying to control and replicate in detail the blanks manufacturing processes, BIRS vary from one blank to another.
- Although MIRS measurements are more extended, their variability upon machining conditions together with the contradictory published results regarding cause-effect relationships makes difficult to determine in advance their effects in machining distortion. Moreover, research upon the change of MIRS due to machining conditions

states that distortion can be controlled through the proper selection of cutting parameters, but evidence was not published yet.

- The machining distortion calculation is a mathematical problem with a reasonable approximation of the physical reality that it is supposed to represent. Considering that there are unavoidable errors associated with the input data used for the calculation, the numerical approximation in the best case should be within acceptable bounds. For this reason, an important part of machining distortion calculation relies on being able to determine accurately these bounds (prediction uncertainty).

Based on these outcomes and considering the objectives defined in Chapter 1, the research lines of the thesis were defined.

- Development of a method to measure BIRS in industrial environments and ribbed geometries (Chapter 3).
- Uncertainty assessment of BIRS measurements (Chapter 3).
- Inter-method comparison of MIRS measurements and uncertainty assessment (Chapter 4).
- Empirical model for the determination of the MIRS based on a set of cutting conditions (Chapter 4).
- Experimental and virtual implementation of the developments in BIRS and MIRS characterization in different study cases (Chapter 5).
- Distortion calculation in real-parts, using an agile distortion model fed with BIRS and MIRS data measured in the same part (Chapter 5).

Chapter 3

Bulk or blank-initial residual stresses

3.1 Introduction

As explained in Chapter 2, BIRS in the machining blanks are unavoidable because they are the result of the thermal-mechanical loads from the upstream manufacturing chain. Especially in aluminium, BIRS are often acknowledged to be the predominant source of distortion [21, 23, 25, 26, 32, 73, 92, 98, 103, 171, 239–242]. Moreover, even the low stresses remaining in blanks after stress relief treatments are applied can generate distortion.

Therefore, it is important to have accurate BIRS data for the implementation of distortion calculation tools. However, getting reliable BIRS data is a difficult task for several reasons. On the one hand, BIRS vary from one blank to another, which creates the need for measuring BIRS in each blank in order to identify the actual stress state. On the other hand, due to the lower cost and better availability of destructive methods, these are the preferred choice for the task. However, destructive methods do not allow to measure BIRS and manufacture the final part from the same blank. The alternative non-destructive methods, do not represent a real industrial solution for BIRS measurement. For instance, in the neutron diffraction method the component must be brought to a neutron source (reactor), each measurement requires long times (several hours) and, after measurement the parts must be set apart for being radioactive for a period that can last months [18].

In general, the cost of all BIRS measuring methods is high, due to the need of trained technicians and laboratory facilities to be performed. Furthermore, typically these methods are limited in size to laboratory samples.

For these reasons, the objective of this chapter is to develop a BIRS characterization method, which can be performed in real-size blanks at the shop-floor level, enabling to obtain the final parts from blanks with measured BIRS. In other words, the development of an industrial-friendly semi-non-destructive on-machine LR method.

In order to accomplish the main objective of the chapter, a series of secondary objectives are defined:

- Understanding of BIRS in machining blanks for aerospace structural parts, as well as the on-machine LR method.
- Expanding the on-machine LR to include all the effects affecting the measurements.
- Assessment of the measurement uncertainty for the on-machine LR method.

Aerospace parts are usually machined from rolled plates or forged parts. This work focuses on the first ones, as these are common in the manufacturing of structural parts [174].

The thermal-mechanical history of these blanks starts with melting the mix of alloying elements and casting them into an ingot. To obtain a plate, the ingot is hot-rolled and, after that, it is heat-treated and quenched, where large RS are generated (> 200 MPa).

In order to decrease them, different means can be used. Currently, the cold working techniques (compression and stretching) are extensively applied in industry for being considered as cost-effective RS relief methods [243]. For instance, the cold stretching stress relief is done in the rolling direction until a uniform plastic strain is reached [109]. In fact, about 2% cold stretching can reduce BIRS by a factor of approximately 10 in quenched aluminum plates, as depicted in Figure 3.1, demonstrating the effectiveness of the method.

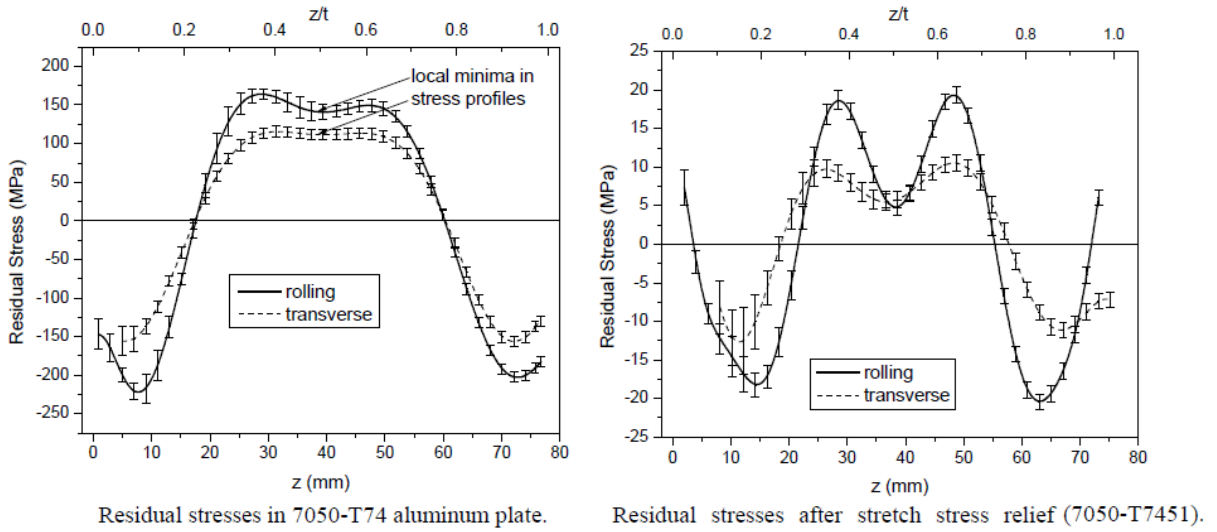


FIGURE 3.1: BIRS measured in aluminium 7050: a) before stress relief, T74; b) after stress relief, T7451 [24].

Alternative stress relief treatments are based on thermal means which, go from reheating the blanks [244] to freezing them [205]; mechanical means through vibration [245]; or on the combination of thermal and mechanical means [246].

The stress relief treatments aim at reducing BIRS-related problems, including machining distortion, by lowering BIRS to values within the uncertainty range of the measuring methods (± 20 MPa approx.) [247, 248]. However, in aerostructures even these low BIRS can cause significant distortion [21, 243]. For this reason, the accuracy of the BIRS measurements is key in distortion prediction [24].

The shape of the BIRS profiles in rolled plates are generally assumed symmetric and approximated by polynomial functions. Figure 3.2 shows an example of a BIRS profile for half of a part section, where the longitudinal or rolling direction is labelled as L and the transverse direction as LT [92]. The effects of these assumptions in relation to machining distortion remain unexplored.

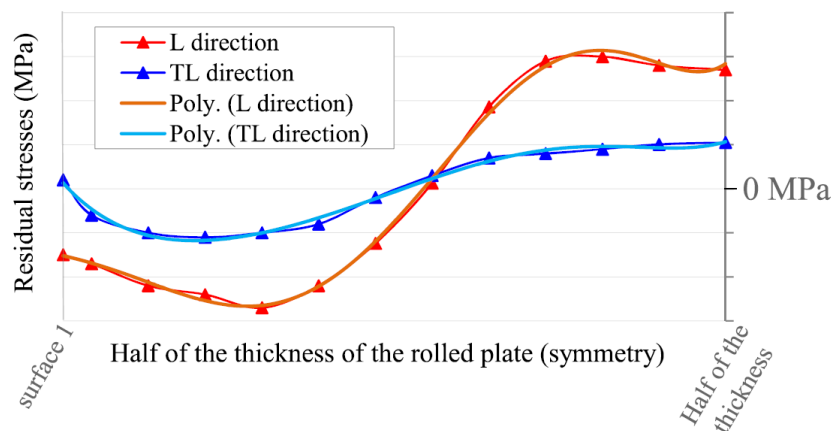


FIGURE 3.2: BIRS profile example using polynomial functions to approximate experimental BIRS measurements in rolled plates. Only one half of the profiles is shown because of the symmetrical distribution assumption. [92].

Finally, it must be highlighted that different cross-sections of the blanks may have different RS [112], as depicted in Figure 3.3.

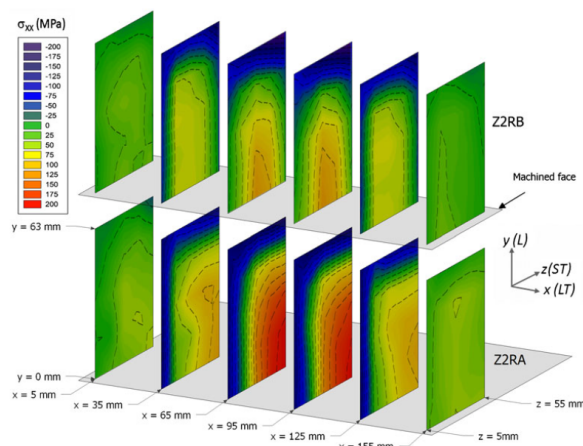


FIGURE 3.3: BIRS measured in different sections of Al7449 blanks by neutron diffraction [112].

Therefore, measuring methods only providing in-line through-thickness BIRS or stress-maps in single arbitrary sections, may not provide the accuracy required for distortion calculation.

3.2 BIRS measurement by on-machine LR

In the on-machine LR method, a milling machine or machining centre is used for the removal of full layers of material with a constant thickness. The deformations due to stress relaxation (Fig. 2.10) are measured with a touch-probe inside the machine. To obtain BIRS in depth, the method iterates the measurements for m machining steps. In each iteration, a layer of material is machined, the part is unclamped, measured and clamped back. This way, a curvature progression is obtained from all measurements.

Figure 3.4 depicts schematically the method, where H is the thickness of the plate (in mm), e is the layer thickness in the blank discretization (in mm), b_x and b_y are the widths of the blank in both spatial directions (mm), p is the probing or deformation measurements, and χ is the curvature obtained from the probing by regression to a second order surface (in mm^{-1}).

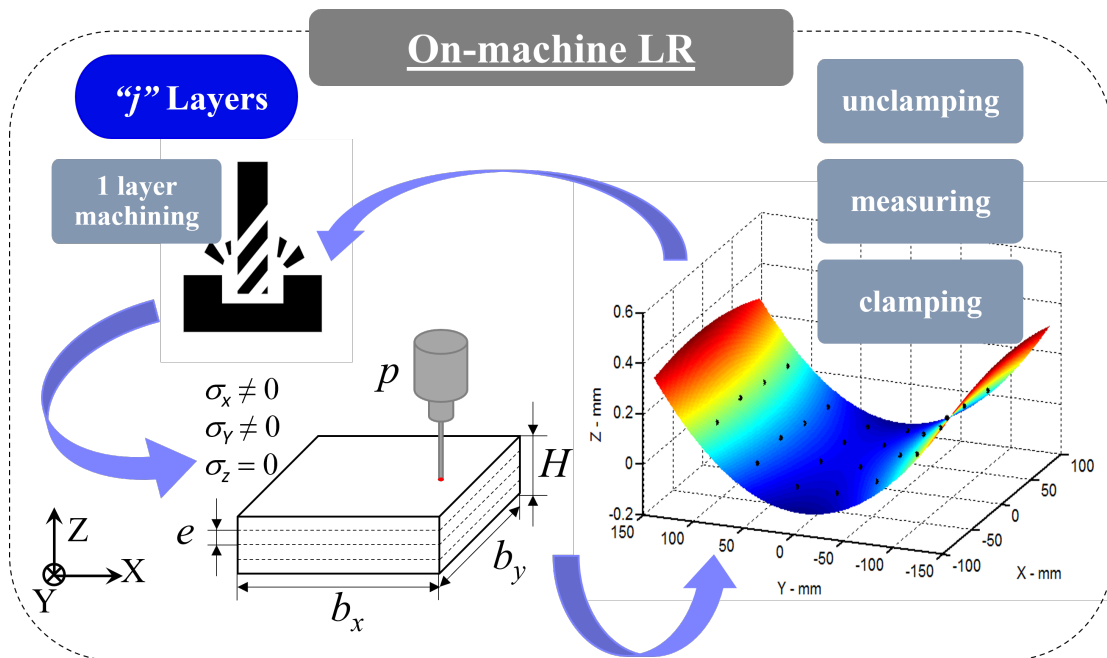


FIGURE 3.4: On-machine LR method procedure for BIRS measurement.

The on-machine LR shares the assumptions of the traditional LR method [100]. First, the bending moments acting in both spatial directions (X-Y) of the plane are associated with the measured curvatures in each direction. Second, the stresses in depth direction (Z) are not considered for being negligible in comparison to the ones of the plane directions and

assumed uniformly distributed along the length and width, changing only in Z direction. Finally, the blank material is considered isotropic and homogeneous. In contrast to the traditional LR formulation, the width of the part is herein considered.

In order to perform the machining of the layers, the part is clamped to the machine-tool table, which is assumed totally flat. This way, the flatness of the raw specimen during the process is ensured in order to fulfill the initial assumption of machining layers of uniform thickness. After a layer is machined, the measurements are performed in the clamped blank.

3.2.1 Formulation

When the parts have a plate shape and fulfil the condition of $(1/80-1/100) < H/b$ (height/width) $< (1/5-1/8)$ [99], the 2D formulation is used. Otherwise, when parts have a longitudinal shape, 1D formulation is used.

3.2.1.1 One dimensional (1D) formulation

Using the Euler-Bernoulli beam theory, the relation between bending moments and curvatures is obtained (Eq. 3.1), as shown by Equation 3.1:

$$Mb = \frac{-I \cdot E}{\chi} \quad (3.1)$$

where, χ is the curvature of the part (in mm^{-1}), I is the second moment of area of the part cross-section (mm^4), and Mb is the bending moment (in Nmm).

To perform bending moment calculation, first the cross-section is discretized in n layers in the Z direction (Fig. 3.5). This number influences the resolution of the BIRS profile, as well as the time needed to perform a BIRS measurement. The bending moment of a single layer is calculated (Eq. 3.2), as the mean bulk stress σ_i^B of each layer i (in MPa) multiplied by the area a_i , and the leverage to the neutral fiber k_{ij} (in mm). The area is the multiplication of the layer thickness e_i and the layer width b_i (Eq. 3.3).

$$Mb_i = \sigma_i \cdot k_{ij} \cdot a_i \quad (3.2)$$

$$a_i = e_i \cdot b_i \quad (3.3)$$

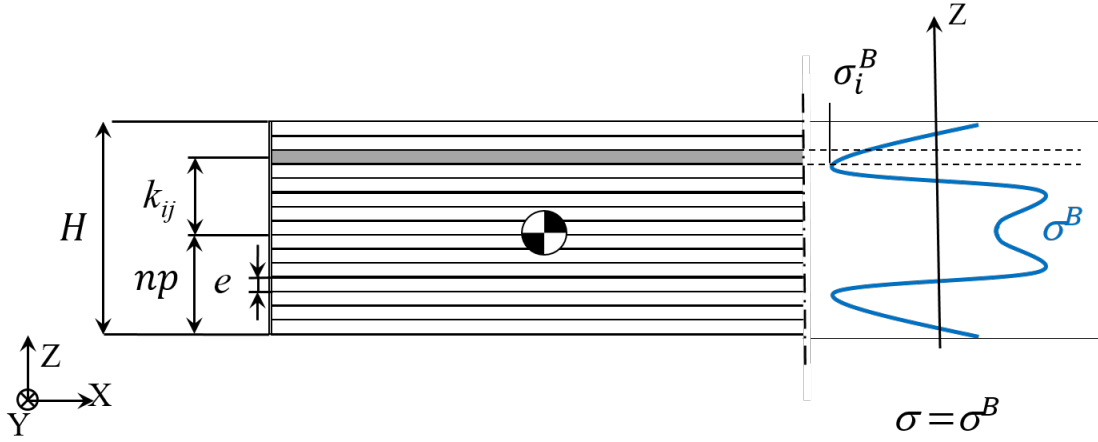


FIGURE 3.5: Discretization of the cross-section and mean stress σ_i^B of the layer i .

The effect of the previously removed layers on the new measurements is taken into account through the solution of the system of equations 3.4 for all successive removed layers, where G_{ij} is the kernel function accounting for the geometric and material properties of each layer (Eq. 3.5).

$$\begin{bmatrix} G_{11} & 0 & \dots & 0 \\ G_{21} & G_{22} & \dots & 0 \\ \vdots & \vdots & \ddots & \vdots \\ G_{n1} & G_{n2} & \dots & G_{nm} \end{bmatrix} \cdot \begin{Bmatrix} \sigma_1^B \\ \sigma_2^B \\ \vdots \\ \sigma_n^B \end{Bmatrix} = \begin{Bmatrix} \chi_1 \\ \chi_2 \\ \vdots \\ \chi_m \end{Bmatrix} \quad (3.4)$$

$$G_{ij} = \frac{e_i \cdot b_i \cdot k_{ij}}{E \cdot I_j} \quad (3.5)$$

In the on-machine LR, the curvatures are calculated from the probing measurements in Z direction (Fig. 3.4) by regression to a second order curve (Eq. 3.6) [120]. The curvature value (χ) is obtained from the second order coefficient with Equation 3.7.

$$z(x) = A \cdot x^2 + B \cdot x + C \quad (3.6)$$

$$\chi = 2 \cdot A \quad (3.7)$$

3.2.1.2 Two dimensional (2D) formulation

If the deformation in the second direction is not assumed negligible, a two dimensional (2D) formulation is used. In this case, the measurement of the curvature is carried out by measuring the height of the machined surface on different points of the plane (Fig. 3.4). The measured values are fitted by least-squares means to a quadratic surface function, and the plate curvature values (χ_x, χ_y) are obtained from the second order coefficients of Equation 3.8, i.e. with Equation 3.9 [249].

$$z(x, y) = A \cdot x^2 + B \cdot y^2 + C \cdot x \cdot y + D \cdot x + E \cdot y + F \quad (3.8)$$

$$\chi_x = 2 \cdot A; \quad \chi_y = 2 \cdot B \quad (3.9)$$

The formulation relating curvatures and stresses is based on the Plate Bending Theory [99], and shown in equations 3.10 to 3.13, where Equation 3.11 represents the bending moment corresponding to the contribution of the first layer.

$$Mb_x = \frac{E \cdot I_x}{(1 - \nu^2)} \cdot (\chi_x + \nu \cdot \chi_y) \quad (3.10)$$

$$Mb_x = \sigma_{1,x}^B \cdot e_i \cdot b_{i,y} \cdot k_{ij} \quad (3.11)$$

$$\begin{bmatrix} G_{11,x} & 0 & \dots & 0 \\ G_{21,x} & G_{22,x} & \dots & 0 \\ \vdots & \vdots & \ddots & \vdots \\ G_{n1,x} & G_{n2,x} & \dots & G_{nm,x} \end{bmatrix} \cdot \begin{Bmatrix} \sigma_{1,x}^B \\ \sigma_{2,x}^B \\ \vdots \\ \sigma_{n,x}^B \end{Bmatrix} = \begin{Bmatrix} (\chi_{1,x} + \nu \cdot \chi_{1,y}) \\ (\chi_{2,x} + \nu \cdot \chi_{2,y}) \\ \vdots \\ (\chi_{m,x} + \nu \cdot \chi_{m,y}) \end{Bmatrix} \quad (3.12)$$

$$G_{ij,x} = \frac{e_i \cdot b_{i,y} \cdot k_{ij} \cdot (1 - \nu^2)}{E \cdot I_{j,x}} \quad (3.13)$$

Analogous expressions applying to Y direction.

If these expressions (equations 3.12 and 3.13) are compared to the Equation 2.13 of the original LR formulation, the similarity can be seen. The only difference relies on that, in

this case, the width of the blanks is considered. On the contrary, the way the problem is solved is very different in the case of the on-machine LR. While in the original LR it was solved by graphical differentiation and integration at convenient intervals[152], the equation system here presented is solved rapidly (below a second) using the calculation software Matlab.

3.2.2 Expansion of the on-machine LR formulation

The following sections introduce the concepts and formulation used for the expansion of the on-machine LR method, both in terms of accuracy and industrial practicality. If these considerations are ignored, the results of the LR can be invalid.

3.2.2.1 Initial curvature consideration

Although the blanks often appear flat to the naked eye in its initial state before removing any material, reality shows that this is not necessarily true. When the blank is clamped to the machine-tool table, which is assumed flat, the clamping is responsible of flattening the curved shape of the blank so that the removal of constant thickness layers is ensured, introducing additional bending stresses on the blank. Thus, the consequence of assuming that blanks are flat in their initial condition implies ignoring the initial curvature of the blanks, as well as these additional clamping stresses (Fig.3.6).

Therefore, in order to reduce errors linked to the initial curvature of the blanks (χ_0), the bending moment due to the clamping force Mb^0 and stresses linked to it σ_x^0 need to be considered in the on-machine LR formulation.

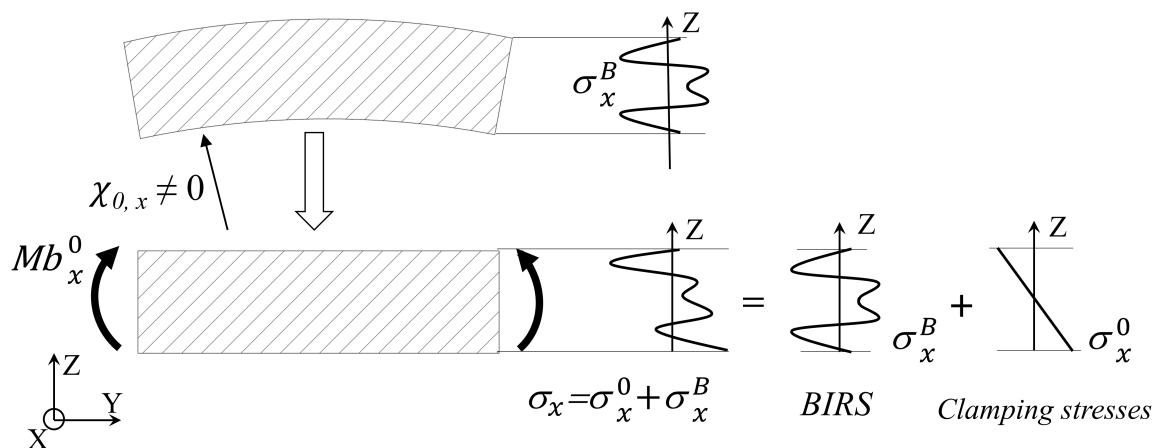


FIGURE 3.6: Initial deformation of the machining blank in the unclamped form and, bending moment and stress applied by the clamping to flatten the initial curvature.

To obtain the initial deformation of the machining blank, the plate is measured, unclamped and clamped, so that the effect of surface irregularities can be removed. The bending moment of the clamping is determined from the measured initial deformation (Eq. 3.14), and the associated stress $\sigma_{i,x}^0$ related to the bending moment of the clamping corresponding to each layer is calculated with Equation 3.15. This way, the typically symmetric stress profile of rolled machining blanks loses its symmetry as it is depicted in Figure 3.7.

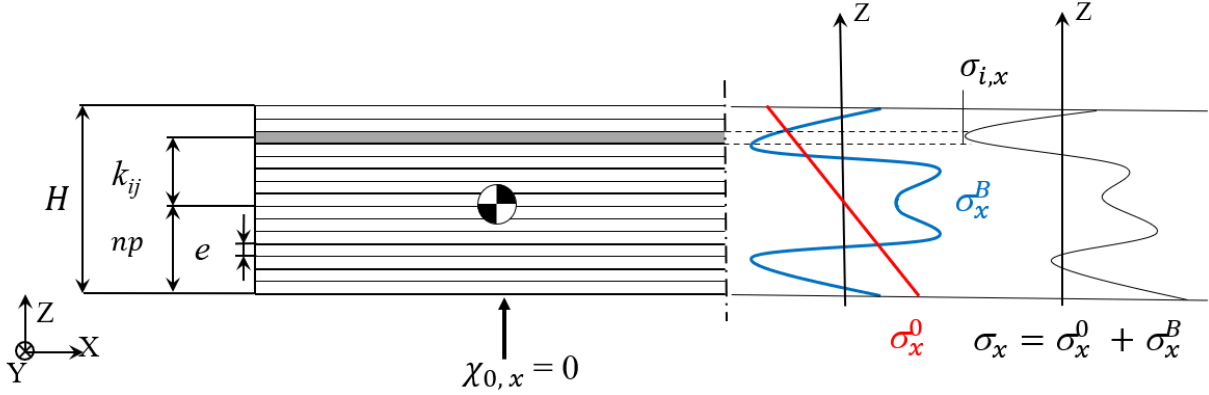


FIGURE 3.7: Discretization of the cross-section and stresses acting when the raw part with initial curvature is clamped.

$$Mb_x^0 = \frac{E \cdot I_x}{(1 - \nu^2)} \cdot (\chi_{0,x} + \nu \cdot \chi_{0,y}) \quad (3.14)$$

$$\sigma_{i,x}^0 = \frac{Mb_x^0 \cdot k_{ij}}{I_x} = \frac{E \cdot k_{ij}}{(1 - \nu^2)} \cdot (\chi_{0,x} + \nu \cdot \chi_{0,y}) \quad (3.15)$$

To obtain the system of equations for all successive removed layers for blanks with initial curvature, Equation 2.9 takes a slightly different form as illustrated in Equation 3.16. In this, the bending stiffness, as the multiplication of the Young modulus by the second moment of area including the Poisson term, is factorized and moved to the right side, becoming the vector XEI ; remaining left side the matrix of areas and leverages Ak . This way, the bending moments appear at both sides of the equation, which simplifies the resolution of the system.

$$[Ak] \cdot \{\sigma\} = \{XEI\} \quad (3.16)$$

Equation 3.17 shows its expanded form, where the bending moment related to the initial curvature Mb_x^0 also needs to be considered in all machining steps. Moreover, the stress

acting in the blank σ_x , are the sum of the bulk stress σ_x^B and the stress due to flattening the initial curvature σ_x^0 .

$$\begin{bmatrix} -b_{1,y}e_1k_{11} & 0 & \dots & 0 \\ -b_{1,y}e_1k_{12} & -b_{2,y}e_2k_{22} & \dots & 0 \\ \vdots & \vdots & \ddots & \vdots \\ -b_{1,y}e_1k_{1m} & -b_{2,y}e_2k_{2m} & \dots & -b_{n,y}e_nk_{nm} \end{bmatrix} \cdot \begin{Bmatrix} \sigma_{1,x} \\ \sigma_{2,x} \\ \vdots \\ \sigma_{n,x} \end{Bmatrix} = \begin{Bmatrix} \frac{(\chi_{1,x} + \nu\chi_{1,y})EI_{1,x}}{(1-\nu^2)} - Mb_x^0 \\ \frac{(\chi_{2,x} + \nu\chi_{2,y})EI_{2,x}}{(1-\nu^2)} - Mb_x^0 \\ \vdots \\ \frac{(\chi_{m,x} + \nu\chi_{m,y})EI_{m,x}}{(1-\nu^2)} - Mb_x^0 \end{Bmatrix} \quad (3.17)$$

Thus, to obtain the BIRS profile from the calculated stresses σ_x of the equation above, the stresses due to the clamping force to flattening the initial curvature σ_x^0 need to be subtracted (Eq. 3.18).

$$\sigma_x^B = \sigma_x - \sigma_x^0 \quad (3.18)$$

Analogous expressions apply to the Y direction. For the 1D formulation, the same formulation can be used, just by setting the Poisson coefficient to zero.

3.2.2.2 MIRS consideration

One of the assumptions upon which the LR method is built is that the material removal process should not disturb the stress in the remaining material. In the traditional LR the use of EDM to remove the material changes the stress state minimally on the machined surface. However, in the case of milling this is not true as explained in Section 2.2.1.2. Moreover, the stress magnitude is usually much higher for MIRS than for BIRS, and when the inertia of the section decreases below a critical point, their effect can even become the primary contributor of the final machining distortion [41, 206]. For this reason, in order to reduce errors linked to the MIRS, their effect needs to be considered in the on-machine LR formulation.

The MIRS values cannot be directly summed to BIRS due to the very different penetration depths. While for BIRS this is the whole plate thickness, for MIRS the penetration is typically up to 0.2 mm depth from the surface [34, 141]. Nevertheless, conceptually the effect of the MIRS is introduced similarly as with BIRS, discretizing in S sub-layers the depth affected by the mechanical and thermal loads during the machining process, as depicted in Figure 3.8.

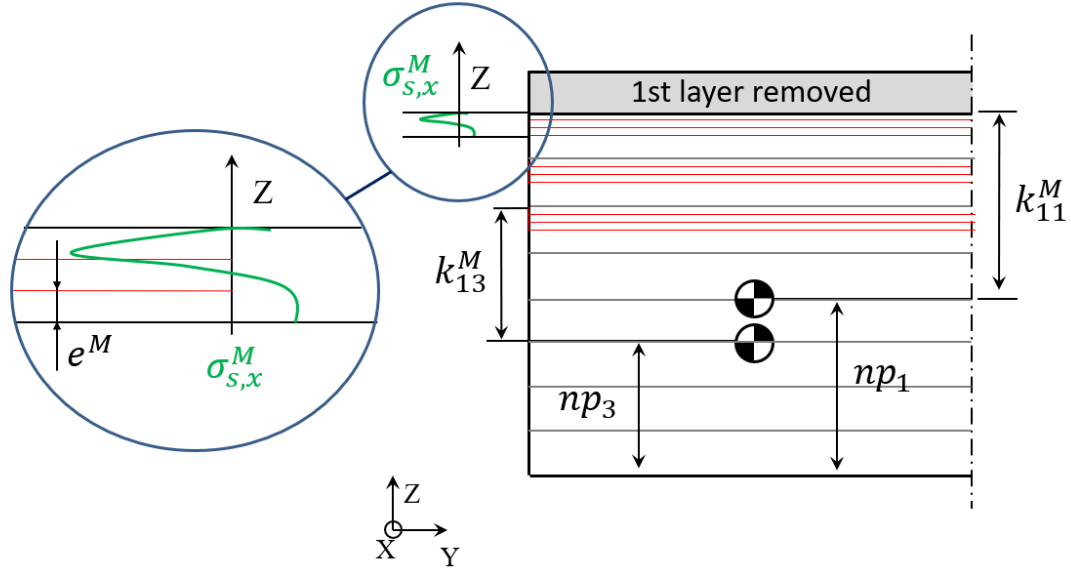


FIGURE 3.8: MIRS on the surface, sub-layers after machining the three first layers and distances to the neutral plane of each of the affected layers.

In this, $\sigma_{s,x}^M$ is the average MIRS in each sub-layer s of thickness e^M , and k_{ij}^M (in mm) is the distance of the center of mass of each of the sub-layers to the center of mass of the whole part at each machining step, np_j . The generated bending moment is calculated with Equation 3.19.

$$Mb_x^M = \sum_1^S (\sigma_{s,x}^M \cdot b_j \cdot e^M \cdot k_{ij}^M) \quad (3.19)$$

This way, the total bending moment acting in the cross-section (Eq. 3.20) can be calculated as the sum of the different bending moments.

$$Mb_x = Mb_x^B + Mb_x^0 + Mb_x^M = \frac{E \cdot I_x}{(1 - \nu^2)} \cdot (\chi_x + \nu \cdot \chi_y) \quad (3.20)$$

For obtaining the stresses in the complete cross-section in the system of equations (Eq. 3.16), the vector XEI takes the form of Equation 3.21 due to the bending moment generated by the MIRS Mb^M . It is important to note that for the first layer, the effect of machining stresses cannot be added ($Mb_{x,1}^M = 0$), as the upper surface of this layer is not machined and therefore stresses are not induced. Analogous expressions apply to the Y direction.

$$\{XEI\} = \left\{ \begin{array}{l} \frac{(\chi_{1,x} + \nu \cdot \chi_{1,y}) \cdot E \cdot I_{1,x}}{(1 - \nu^2)} - Mb_x^0 \\ \frac{(\chi_{2,x} + \nu \cdot \chi_{1,y}) EI_{2,x}}{(1 - \nu^2)} - Mb_x^0 + Mb_{2,x}^M \\ \vdots \\ \frac{(\chi_{1,x} + \nu \cdot \chi_{1,y}) EI_{m,x}}{(1 - \nu^2)} - Mb_x^0 + Mb_{m,x}^M \end{array} \right\} \quad (3.21)$$

3.2.2.3 Ribbed geometries: Semi-non-destructive method

One of the major drawbacks of the on-machine LR is being a destructive measuring method. In full LR, manufacturing a component of known BIRS is not possible, which is a need considering that BIRS change from one blank to another (Chapter 2.2.1.1).

For this reason, the aim of this section is describing a method that enables measuring BIRS in blanks while leaving certain amount of material unmachined. This material, left in the form of ribs, enables to obtain the final component from the ribbed part with measured BIRS. For this reason, under the ribbed LR formulation, the method becomes semi-non-destructive. It is important to note the difference respect to non-destructive methods which are not based on stress relaxation.

To include the ribbed geometry in the formulation, first an approximation is used, which is done calculating equivalent cross-sections with the same bending behaviour as the real one (Fig. 3.9).

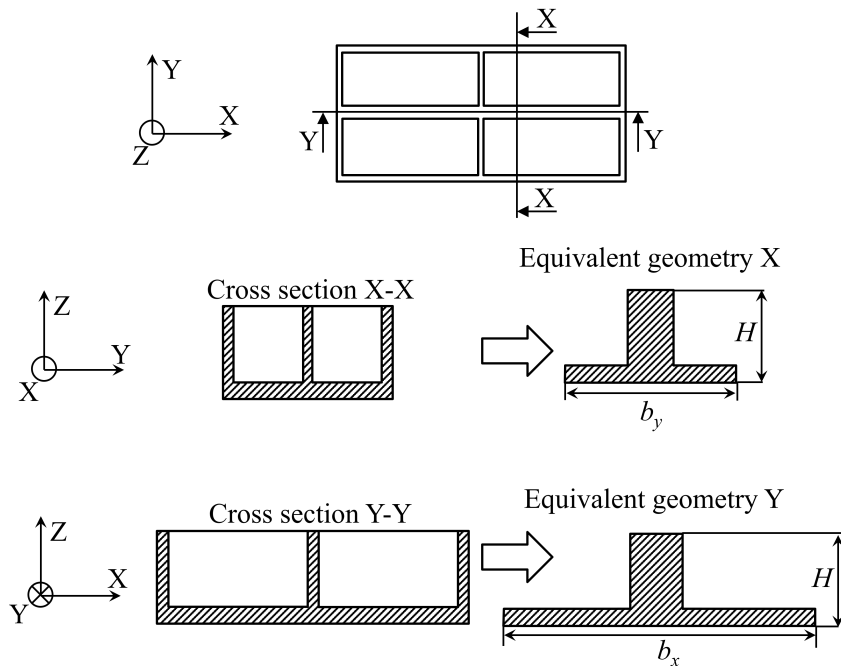


FIGURE 3.9: Representation of the equivalent cross-sections in X and Y directions.

Like in the full LR, in the ribbed LR the section is discretized in the thickness direction. The difference relies on the amount of material removed at each layer. While for full LR the whole layer width b_i is removed, here a fraction of the width, w_i , is left unmachined. Figure 3.10 depicts the discretization of the cross-section equivalent geometry of the same bending stiffness for X direction.

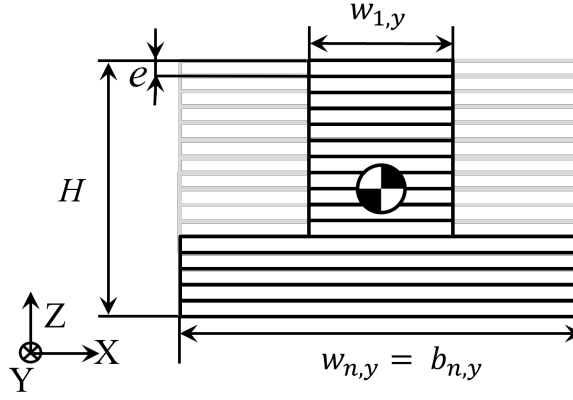


FIGURE 3.10: Discretization of the equivalent geometry cross-section for the ribbed LR.

This changes the formulation in the areas defining the bending moment, which consider also the unmachined width of the layers (Eq. 3.22). Also, the second moment of area of the equivalent geometry I_x^{geo} takes the form of Equation 3.23.

$$Mb_x = \sum (\sigma_{i,x} \cdot (b_{i,y} - w_{i,y}) \cdot e_i \cdot k_{ij}) \quad (3.22)$$

$$I_x^{geo} = \sum_{i=1}^n \frac{(e_i)^3 \cdot w_{i,y}}{12} + e_i \cdot w_{i,y} \cdot (k_{ij})^2 \quad (3.23)$$

The equivalent cross-section of one rib with the same flexural behavior as the original one, offers a simple formulation agile in the calculation. With this, a simulation of the LR is performed using the analytical inverse LR formulation. In contrast to the LR formulation, this one calculates the curvature considering the material of the part, instead of the removed material. Equations 3.24, 3.25 and, 3.26 show the mathematical relations from which the curvature is obtained. Analogous expressions apply to Y direction. In longitudinal parts for which the 1D formulation is required, Equation 3.24 can be used just by setting the Poisson coefficient to zero.

$$\chi_x = \left(\frac{Mb_x}{E \cdot I_x} - \nu \cdot \frac{Mb_y}{E \cdot I_y} \right) + \left(\frac{Mb_x^M}{E \cdot I_x} - \nu \cdot \frac{Mb_y^M}{E \cdot I_y} \right) \quad (3.24)$$

$$Mb_x = \sum_{i=1}^n ((\sigma_{i,x}^B + \sigma_{i,x}^0) \cdot e_i \cdot w_i \cdot k_{ij}) \quad (3.25)$$

$$Mb_x^M = \sum_{i=1}^n (\sigma_{i,x}^M \cdot e_s \cdot w_i \cdot k_{ij}^s) \quad (3.26)$$

However, the equivalent cross-section neglects effects such as the positioning of the ribs, the contribution of the transverse ribs to the bending behavior and the rib buckling. Figure 3.11 depicts the curvature progression of a LR simulation, using the analytical inverse LR formulation and a FEM model, in a Al7050-T7451 blank of dimensions 200x400x30 and BIRS from bibliography fitted to a cosine sum function [73]. As can be seen, the curvatures obtained with the analytical inverse LR formulation (χ^{an}) and numerical model (χ^{FEM}) do not match. It is because the equivalent geometry used as an approximation for the second moment of area (I^{geo}) causes errors in the analytical curvature progression, which in general are small when the inertia of the part is high (first layers) and increases as the layers of material are removed.

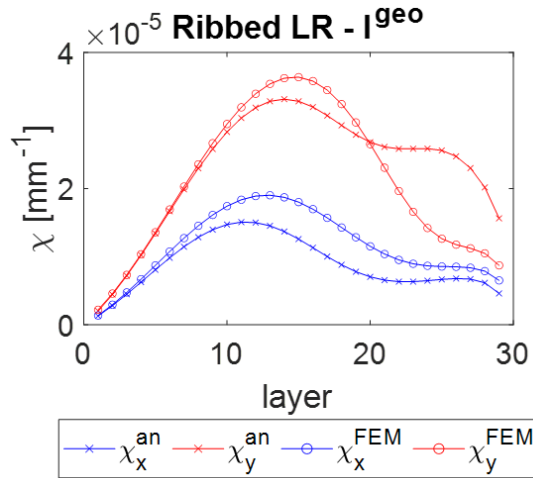


FIGURE 3.11: Curvature progression due to ribbed LR simulation with the analytical formulation for the equivalent cross-section and the numerical model.

Therefore, accurate implementation of the ribbed LR requires a second step in order to reduce the errors linked to the second moment of area of the equivalent geometry. For this, the equivalent bending stiffness concept based on a hybrid approach is used (Fig. 3.12). This makes use of FEM calculations to extract the accurate bending behaviour of a given

geometry. Then, this is extracted and applied to the analytical formulation through an equivalent bending stiffness I^{eq} .

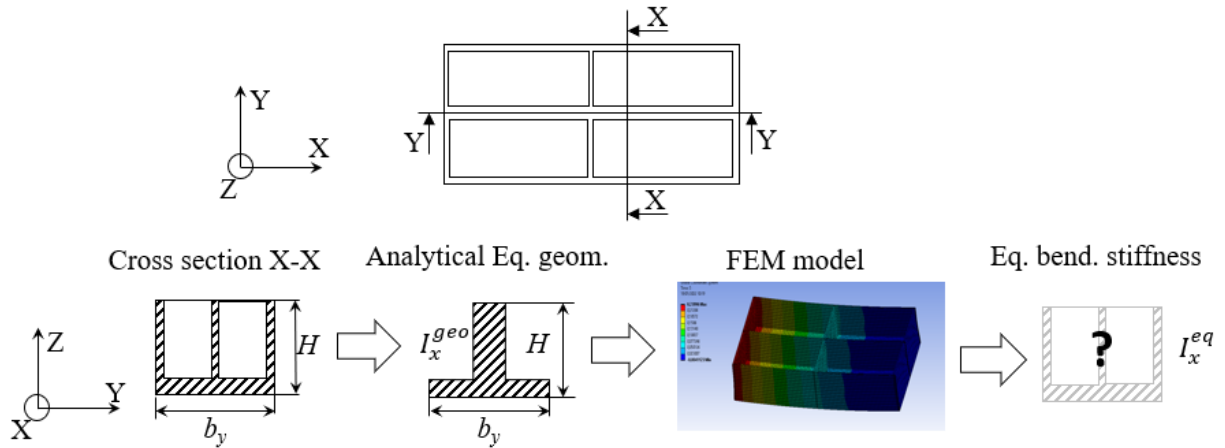


FIGURE 3.12: Workflow for equivalent bending stiffness calculation in ribbed part.

This way, the hybrid approach combines analytical and numerical LR simulations. In this, the numerical model increases the accuracy, while the analytical model keeps the agility of the calculation required for the use in industrial environments. Figure 3.13 illustrates the calculation process for obtaining the equivalent bending stiffness, where I^{eq} is the equivalent bending stiffness; I^{geo} is the second moment of area corresponding to the equivalent cross-section; χ^{an} is the analytical curvature progression; χ^{FEM} is the numerical curvature progression; and χ^{exp} is the experimental curvature progression measured in the on-machine LR test.

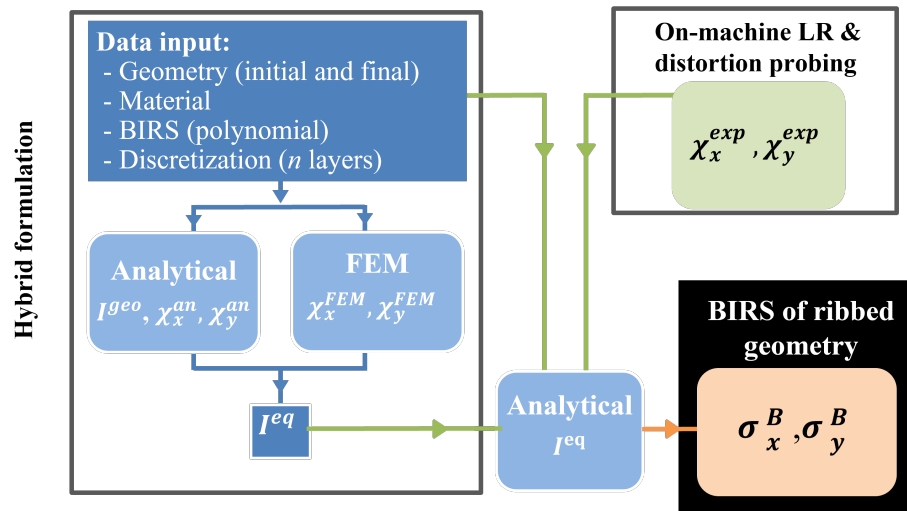


FIGURE 3.13: Diagrams for the BIRS characterization in ribbed geometries using the on-machine LR based on hybrid approach and I^{eq} .

To obtain the equivalent bending stiffness, first I^{geo} must be calculated with Equation 3.23. In parallel, a simulation of the LR is also performed using a FEM model. In this, the mesh

layout must be defined in specific heights in Z direction, so that RS (BIRS and MIRS) can be introduced layer by layer. Moreover, the mesh must fit the heights of the layer discretization of the analytical model, including the thin layers corresponding to MIRS (Fig. 3.14), to match the curvature progressions. If the part targeted is symmetric and shear stresses are not considered, in order to reduce computational requirements, just one quarter of the part can be modelled (Fig. 3.14). On the contrary, when the part is not symmetric or shear stresses must be considered, the whole part geometry is modelled.

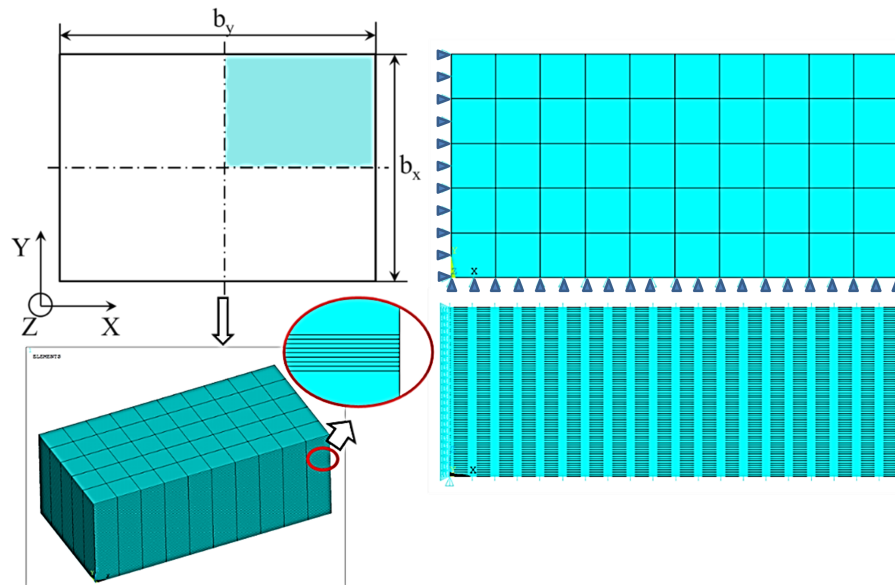


FIGURE 3.14: Representation of the FEM model of a quarter of a machining plate and detail of the sub-layers discretization (left); front and top views of the model including boundary conditions (right).

In the FEM model, the element type used (*Solid 186*), is a higher order 3-D solid element with 20-nodes, which exhibits quadratic displacement behavior having three degrees of freedom per node: translations in the nodal X, Y, and Z directions. The geometry of the element is the brick type, to facilitate the meshing in layers and match the predefined discretization. The input loads are stresses introduced with the command *Inistate* as actual load state values, by selecting the elements in layers according to their node position.

The boundary conditions must restrict the solid-rigid movement of the part, while allowing the deformation. In this way, the movement of the simulated solid is restricted, but the solid has the possibility of deforming until it reaches a new state of equilibrium as a consequence of the RS unbalance. If one quarter of the part is modelled, the boundary conditions are introduced restricting the displacement of the nodes at $X=0$, and $Y=0$ in X and Y directions respectively, and the vertex node at $X=0$, $Y=0$, $Z=0$ in Z direction (Fig. 3.14) to represent the support condition. If the complete part geometry is modelled, the boundary conditions are introduced as a remote displacement. It is performed selecting the nodes of one external face (excluding the upper and lower faces), and creating a remote

point, to which all the selected nodes of the face are linked with certain displacement allowance by setting them a deformable behavior. Then, the translation and rotation of the remote point is restricted, as depicted in the sketch of Figure 3.15. Independently of which of the lateral faces is selected for setting the remote displacement boundary conditions, results are the same, being the aim of the calculation to obtain the relative displacement of the nodes from which the distortion curvature is calculated.

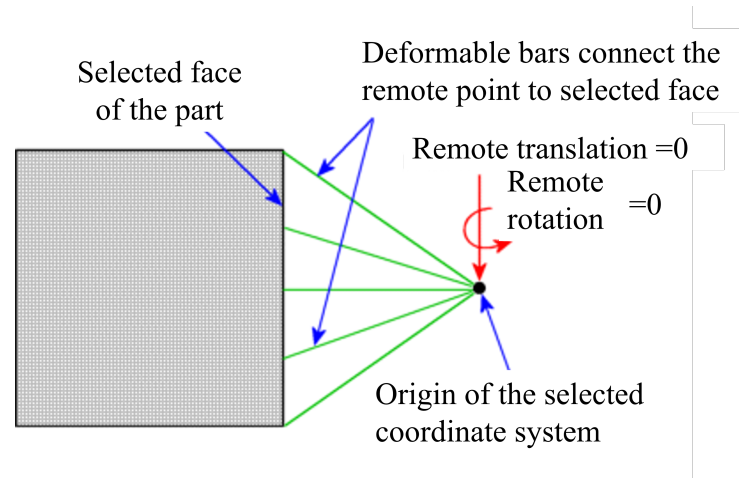


FIGURE 3.15: Remote displacement boundary conditions with deformable behaviour.

To perform the numerical LR simulation, the *Element Birth and Death* technique is used in the ANSYS software, which assigns a near-zero stiffness to the selected elements so that they are deactivated from the model (Fig. 3.16). For the ribbed LR, the only difference is that at each layer the elements corresponding to the ribs are not selected for deactivation.

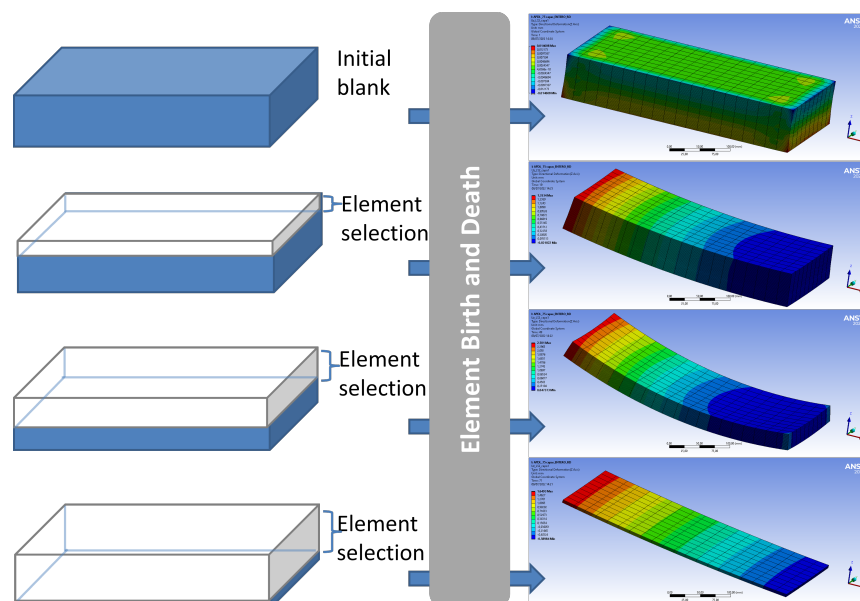


FIGURE 3.16: Element deactivation in FEM using the Birth and Death technique for the simulation of the full LR.

From the analytical and numerical LR simulation, two curvature progressions are obtained. While the analytical one refers to the second moment of area of the equivalent cross-section, the numerical one is linked to the real geometry of the part.

Assuming that the material properties are fixed parameters, the bending stiffness is a function of the second moment of area. Moreover, for a hypothetical case with no MIRS neither initial curvature, the bending moment by definition is the same for both, the analytical and FEM models. Hence, equating the bending moment of equations 3.27 and 3.28, the equivalent bending stiffness I^{eq} (Eq. 3.29) can be obtained.

$$Mb_x = \frac{E \cdot I_x^{geo}}{(1 - \nu^2)} \cdot (\chi_x^{an} + \nu \cdot \chi_y^{an}) \quad (3.27)$$

$$Mb_x = \frac{E \cdot I_x^{eq}}{(1 - \nu^2)} \cdot (\chi_x^{FEM} + \nu \cdot \chi_y^{FEM}) \quad (3.28)$$

$$I_x^{eq} = I_x^{geo} \cdot \frac{(\chi_x^{an} + \nu \cdot \chi_y^{an})}{(\chi_x^{FEM} + \nu \cdot \chi_y^{FEM})} \quad (3.29)$$

Analogous expressions apply to the Y direction.

This way, using the equivalent bending stiffness in the LR analytical formulation, ribbed geometries can be tackled agilely without accuracy penalties. Figure 3.17 shows that the curvatures of a LR simulation with the analytical inverse formulation (χ^{an}) and equivalent bending stiffness (I^{eq}) match with the curvatures obtained with a FEM model (χ^{FEM}).

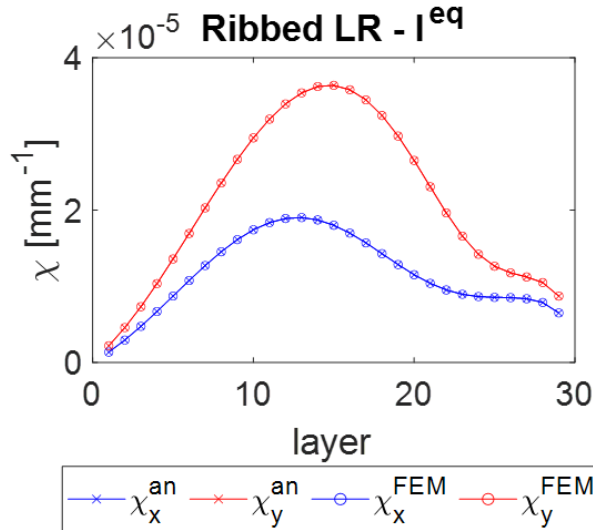


FIGURE 3.17: Curvature progression due to ribbed LR simulation with the the numerical model and analytical formulation using the equivalent bending stiffness I^{eq} .

3.2.2.4 Multicoupled formulation

In ribbed LR, also the initial curvature and MIRS must be considered. Figure 3.18 represents a discretized ribbed section, including the BIRS, clamping stress to flatten the initial curvature, and the MIRS on the machined surface. The effect of the MIRS on the walls is not considered under the assumption of being equal at both sides of the walls. The two main differences respect to the previous formulation are the appearance of the material left (w) in the matrix of areas and leverages, and the equivalent bending stiffness, I^{eq} .

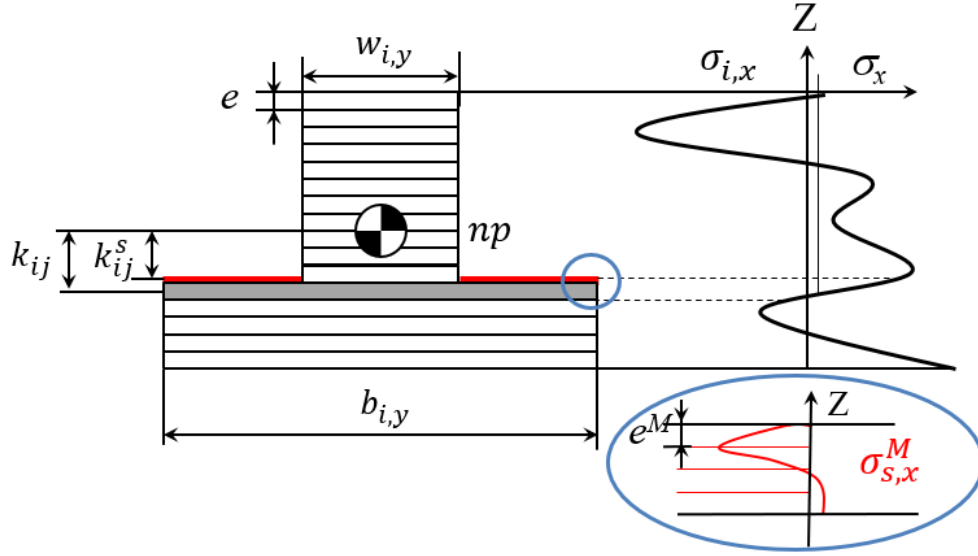


FIGURE 3.18: Discretization of the cross-section and stresses considered in the multicoupled formulation: a) Equivalent geometry discretization; b) Stresses throughout the cross-section BIRS, MIRS and stresses due to clamping forces to flatten the initial curvature.

This way, to obtain the system of equations for all successive removed layers for blanks with initial curvature and ribbed LR, the equations 3.22 and 3.29 are integrated in Equation 3.16, so that the matrix Ak and the vector XEI take the form of equations 3.30 and 3.31 respectively.

$$[Ak] = \begin{bmatrix} (b_{1,y} - w_{1,y}) \cdot e_1 \cdot k_{11} & 0 & \dots & 0 \\ (b_{1,y} - w_{1,y}) \cdot e_1 \cdot k_{12} & (b_{2,y} - w_{2,y}) \cdot e_2 \cdot k_{22} & \dots & 0 \\ \vdots & \vdots & \ddots & \vdots \\ (b_{1,y} - w_{1,y}) \cdot e_1 \cdot k_{1m} & (b_{2,y} - w_{2,y}) \cdot e_2 \cdot k_{2m} & \dots & (b_{n,y} - w_{n,y}) \cdot e_n \cdot k_{nm} \end{bmatrix} \quad (3.30)$$

$$\{X EI\} = \left\{ \begin{array}{l} \frac{(\chi_{1,x} + \nu\chi_{1,y})EI_{1,x}^{eq}}{(1-\nu^2)} - Mb_x^0 \\ \frac{(\chi_{2,x} + \nu\chi_{1,y})EI_{2,x}^{eq}}{(1-\nu^2)} - Mb_x^0 + Mb_{2,x}^M \\ \vdots \\ \frac{(\chi_{1,x} + \nu\chi_{1,y})EI_{m,x}}{(1-\nu^2)} - Mb_x^0 + Mb_{m,x}^M \end{array} \right\} \quad (3.31)$$

Analogous expressions apply to the Y direction.

As explained in Section 3.2.2.1, when considering the initial curvature of the blank, to obtain the BIRS profile from the calculated stresses σ_x of the equation above, the stresses due to the clamping force to flattening the initial curvature σ_x^0 need to be subtracted (Eq. 3.18).

Experimental evaluation of the on-machine LR in ribbed geometries is performed in Chapter 5.

3.3 Uncertainty assessment of the on-machine LR

The on-machine LR method averages the stresses in the whole part, providing a two-dimensional cross-sectional stress map. Its multi-coupled formulation enables the consideration of MIRS and the clamping stresses due to the initial curvature of the blanks, improving its accuracy. Moreover, the on-machine LR can be performed in real-size parts with ribbed geometries using the equivalent bending stiffness, from which final components can be obtained.

On the contrary, its accuracy is affected by the accuracy of the machine tool and touch probe, as well as by the quality of the clamping-cutting process, and the deformation data treatment. While for other stress characterization methods, the uncertainty and best practices are determined, these have never been addressed for the LR method. In fact, measurement noise, high stress values near the edges, and asymmetric stress profiles [38, 169, 174, 242] can be seen in bibliography, which show the need for guidelines regarding data treatment when performing on-machine LR measurements linked to machining distortion.

This section analyzes the different uncertainty sources that affect the results of the on-machine LR method, trying to assess the uncertainty linked to uncontrollable sources. The errors linked to the main uncertainty sources are quantified using Monte Carlo simulations. Finally, this section provides best practice guidelines regarding the analysis and treatment of deformation data for its use in the on-machine LR method.

3.3.1 Procedure for uncertainty assessment

The present analysis explores the uncertainty generated by different variables related to the part geometry and material, and probing accuracy (Table 3.1).

TABLE 3.1: Uncertainty sources of the on-machine LR method.

Group	Variable
Geometry	Width (b)
	Layer thickness (e)
Mechanical properties of the material	Young Modulus (E)
	Poisson ratio (ν)
Deformation measures	Probing (p)

The procedure for uncertainty assessment is based on applying known and decoupled errors for each of the uncertainty sources exposed above. The effect of these controlled errors is analyzed in three different phases (Figure 3.19):

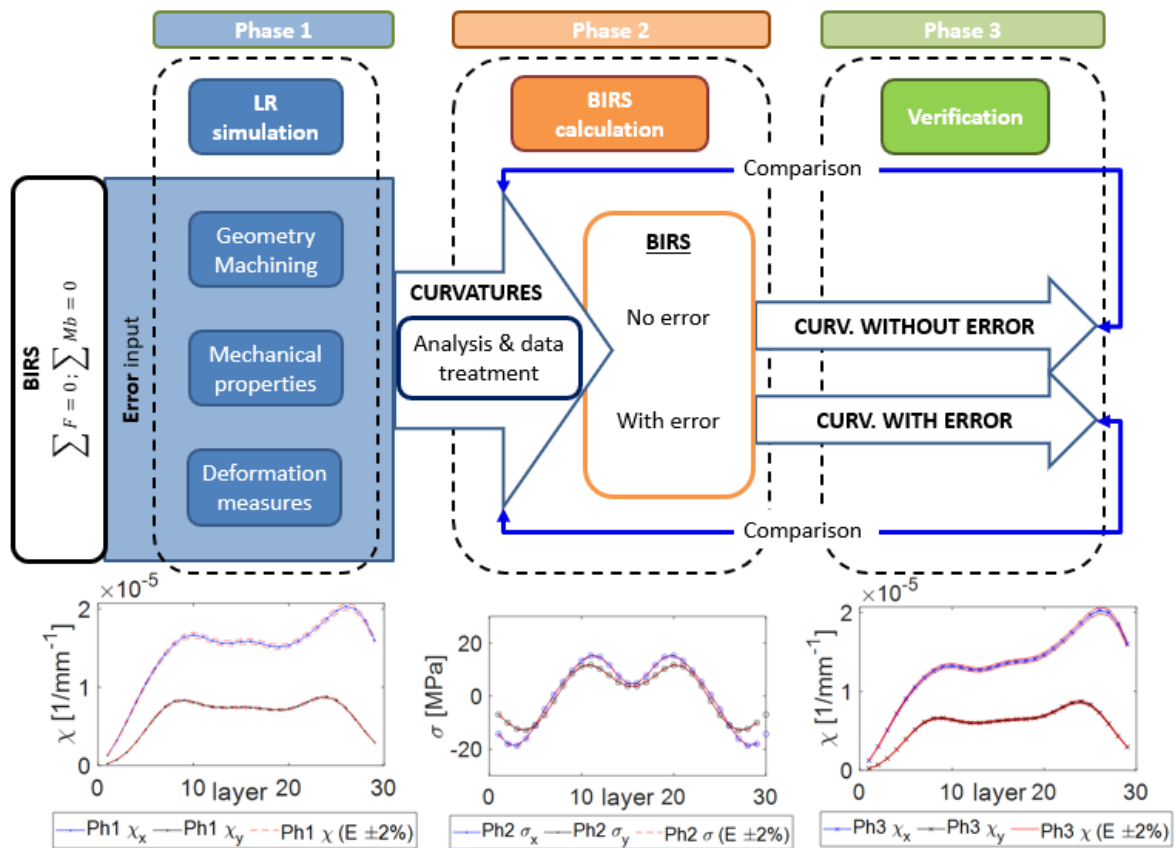


FIGURE 3.19: Methodology used for uncertainty assessment of the on-machine LR method.

- Phase 1 - Layer Removal simulation: Simulation of the appearance of uncontrollable uncertainty sources during the LR test. Based on a known BIRS field, the LR is simulated obtaining a curvature progression. Such simulation is performed both for a case without errors and the cases where the controlled errors are applied to the variables from Table 3.1.
- Phase 2 - BIRS calculation from the curvatures of the previous phase: As there are different curvature progressions from the Phase 1 (with and without errors), different BIRS profiles are obtained: one representative of the ideal case without errors, others bearing the consequences of the error introduced in one of the variables. In this way, the effect of the LR curvature errors on the stresses can be quantified for each variable.
- Phase 3 - Verification: The curvatures for a LR test are recalculated from the BIRS profiles obtained from Phase 2, using the same formulation as in Phase 1, but without the uncertainty sources. The deviation between the curvatures from phases 1 and 3 enables to quantify the effect of the uncertainties in the on-machine LR test.

The uncertainty assessment study is divided in three stages. First, a preliminary study is performed, where the order of magnitude of input errors' effect in all the variables (Table 3.1) is determined. Thus, the variables showing higher sensibility to input errors, both in stresses and curvatures, are considered for further analysis. Then, these critical variables are more deeply studied, not only for the base test-case, but also for different geometries and BIRS profiles. In this analysis, only BIRS are considered in order to ease the understanding. Finally, the analysis is completed with the introduction of the effects of MIRS, clamping stresses due to the initial curvature and equivalent bending stiffness.

3.3.1.1 Data treatment

The on-machine LR method cannot determine the stresses in the entire cross-section. Removing all the material of the section is not feasible because a minimum thickness must remain to hold the part and enable measuring deformations. For this reason, in the Phase 1 at least one layer must be left unmachined, meaning that the curvature progression has one element less than the original stress profile. This effect is higher when applying the LR method experimentally, since the minimum thickness below which no more material can be removed is usually much greater than one layer. Therefore, when calculating the stresses from the curvatures, it is impossible to calculate the stresses associated to the whole part height. Thus, it is necessary to apply a procedure to complete the stress profile in order to carry out the Phase 3 of the analysis. From different possibilities to assign stress values

to the layers without associated curvature, next four options are analyzed in the present study (Figure 3.20):

- Option 1: Uses the values of the layers at the same distance from the center of the blank for the layers without stress values.
- Option 2: Direct symmetry of the first half of the BIRS profile: discards the stress values calculated for the layers of the second part half, and replaces them with the symmetric of those from the first half.
- Option 3: Average of the measured layers: calculates the average of the layers at the same distance from the center of the blank, and replaces the values of the second half with the calculated average.
- Option 4: Average of the measured layers with preferential selection: A preferred selection of layers is made with a value (val), and determines the amount of data for the averaging, while the rest of stress values are obtained by symmetrization of the data from the first half.

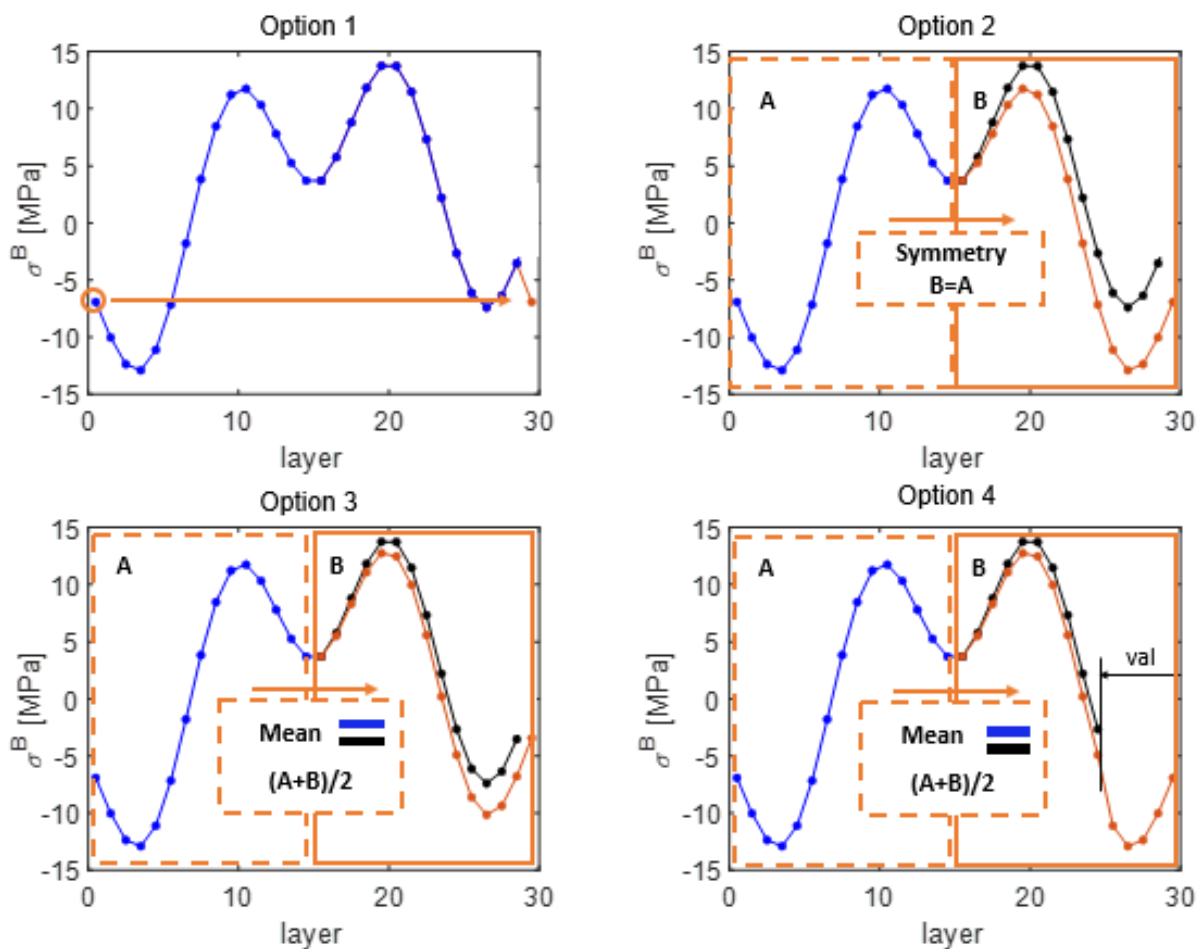


FIGURE 3.20: Options for assigning values of bulk stresses in the layers without curvature.

Besides the need to fill the stress profile, it must be considered that the curvatures from which the stresses are calculated are obtained through instrumentation, and they are prone to the appearance of experimental variability or noise [169]. Trying to avoid the possible uncertainty introduced by this, data filtering is analyzed in the present work for the removal of measurement noise. This filtering is performed as a weighting average of the curvature values by convoluting the curvatures with a function of two different shapes, triangular and Gaussian.

While the effectiveness of the filtering is usually carried out by comparing visually the original and filtered data, the three-phase procedure (Fig. 3.20) followed here offers an objective criterion for the evaluation of the effect of applying such filtering on the final stress results.

3.3.1.2 Test-case definition

Because of its extended use in the manufacturing of aerospace monolithic components, aluminum alloy Al 7050-T7451 is selected for the present study. The geometry of the test-piece is a rectangular part in full LR and ribbed LR with four pockets (Fig. 3.21), whose dimensions and mechanical properties are indicated in Table 3.2.

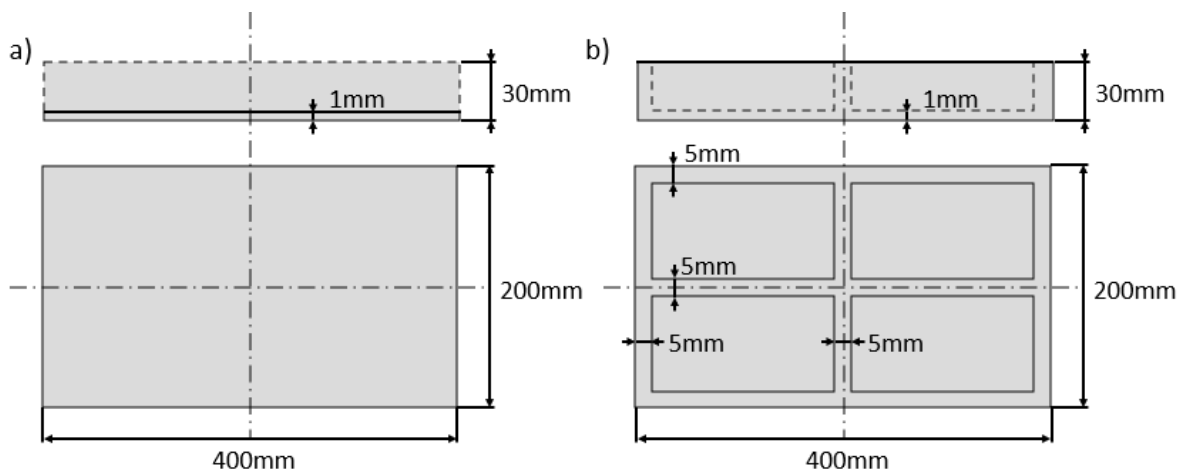


FIGURE 3.21: Geometry of the test-cases for the on-machine LR uncertainty assessment:
a) Full LR; b) Ribbed LR.

To ease the understanding, 1D analysis is performed in some of the cases and in some others, 2D analysis is performed.

The BIRS data used for the study are based on two different BIRS profiles, a simple one for the preliminary analysis [123] and a more complex one for the subsequent analysis [250]. In order to have a mathematical expression for those BIRS applicable to any height location and different total height values, the initial BIRS are fitted to a cosine sum function of

order six [73], and the data is treated so that the conditions of initial equilibrium are fulfilled (Fig. 3.22).

TABLE 3.2: Parameter definition for the analysis of the main uncertainty sources in the on-machine LR.

	1D	2D	
Young modulus – E (MPa)	71700	71700	
Poisson ratio – ν		0.33	
Layer thickness - e (mm)	1	1	
Blank height – H (mm)	30	30	
Blank width – b (mm)	400	200	400
Fins width – (mm)	5	5	5
Fins amount	3	3	3
Points for Probing - p	9	5	9

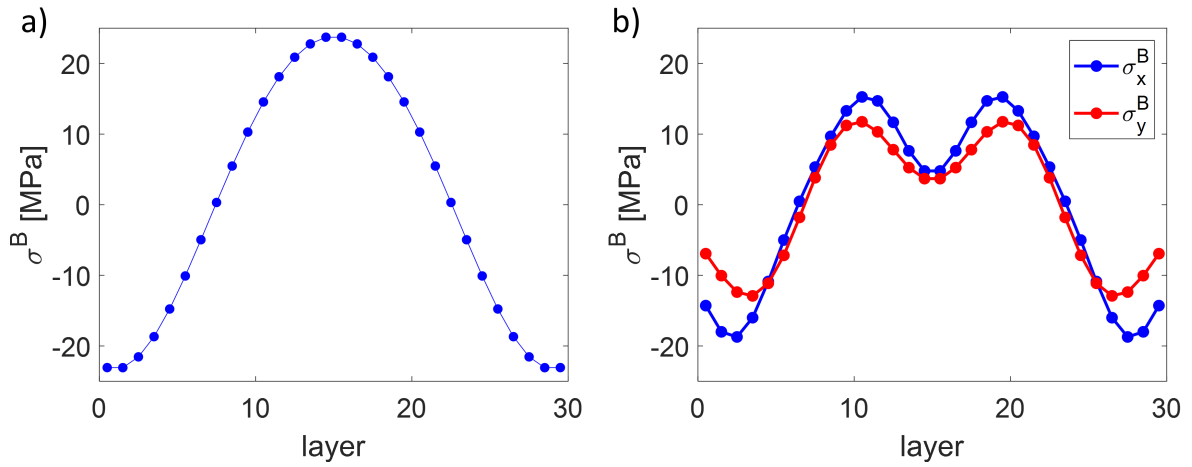


FIGURE 3.22: BIRS profiles used for the uncertainty assessment in Al 7050-T7451: a) Preliminary study; b) Study of critical parameters.

3.3.2 Preliminary analysis

In order to identify the main uncertainty sources, controlled input error values are introduced on each tested variable (Table 3.1) and the uncertainty generated by each of them is analyzed applying the procedure exposed above (Fig. 3.19). In order to simplify this preliminary analysis, only BIRS are considered and, as far as possible, 1D analysis is performed. However, the case of the mechanical properties requires from 2D analysis. Table 3.3 gathers the different cases explained in below.

3.3.2.1 Mechanical properties (E , ν):

The error applies to all layers equally, and can be in either absolute or a percentage value within reasonable limits for the material.

TABLE 3.3: Summary of the cases studied in the preliminary analysis.

	Variable	Analysis	LR	Error	Layer(s)	Figures
Mec. prop.	E	2D	Full	2% [69.6-72.4GPa]	All (uniform)	3.23
	ν	2D	Full	4% [0.317-0.343]	All (uniform)	3.24
Geometry	b	1D	Ribbed	2% [± 8 mm]	All (uniform)	3.25
	e	1D	Full	± 0.05 mm	All (uniform)	3.26
	e	1D	Full	± 0.05 mm	Layer 2	3.27
	e	1D	Full	± 0.05 mm	Layer "i"	3.28
	e	1D	Full	± 0.05 mm	Layer 2 compens. in layer 3	3.29
Probing	p	1D	Full	random [± 0.010]	All 9 points	3.31

Young modulus (E)

Figure 3.23a represents the original curvature in both directions of the plane (X, Y) and the curvature after introducing an error in Young's modulus of 2%, meaning as it may vary in a range between 69580 and 72420 MPa, causing errors of approximately 1.6%.

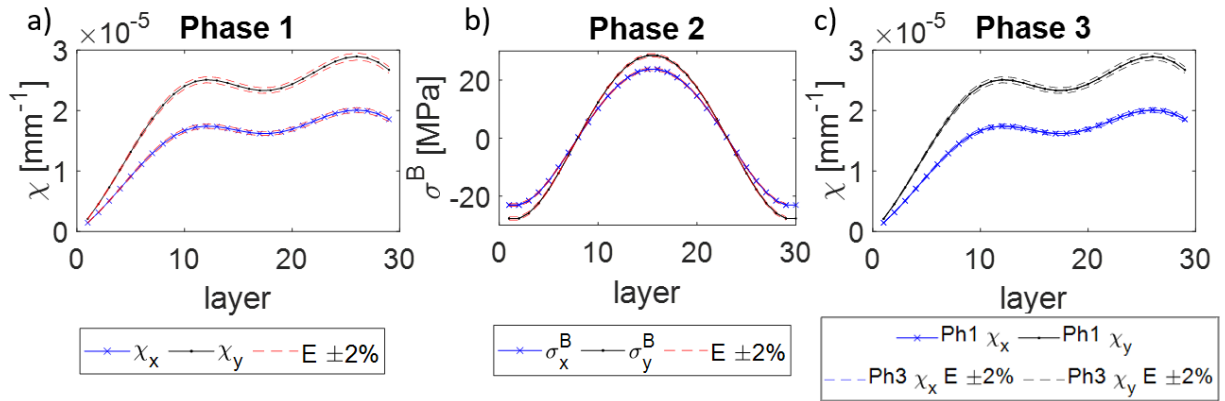


FIGURE 3.23: Uncertainty assessment with a Young modulus E error of $\pm 2\%$ for the full LR 2D: a) curvatures (Phase 1), b) stresses (Phase 2) and, c) curvatures (Phase 3).

In Phase 2, in which the stresses are calculated from the curvatures with error (Fig. 3.23b), the differences between the original BIRS profile and the calculated ones are very low, taking maximum values that do not reach 0.5 MPa in the center and the ends (Fig. 3.23b). In Phase 3, the curvatures (Fig. 3.23c) are calculated using the option 2, symmetry as default for being the most reported option (Fig. 3.20). Results, show that the curvatures in Phase 3 do not surpass the curvatures of Phase 1, meaning that the difference is approximately 1.6%.

Poisson coefficient (ν)

Similarly, when analyzing the uncertainty linked to the Poisson's ratio ν , a percentage error on the nominal value of $\pm 4\%$ is chosen, which analyzes a range between 0.317 and 0.343. Figure 3.24a shows how the effect on curvatures corresponding to Phase 1, where

similar results to the previous case can be observed in both spatial directions. Therefore, concerning the stresses of Phase 2 depicted in Figure 3.24b, results are also very similar to the Young modulus case. For this reason, in Phase 3 (Fig. 3.24c) the error remains the same as in Phase 1.

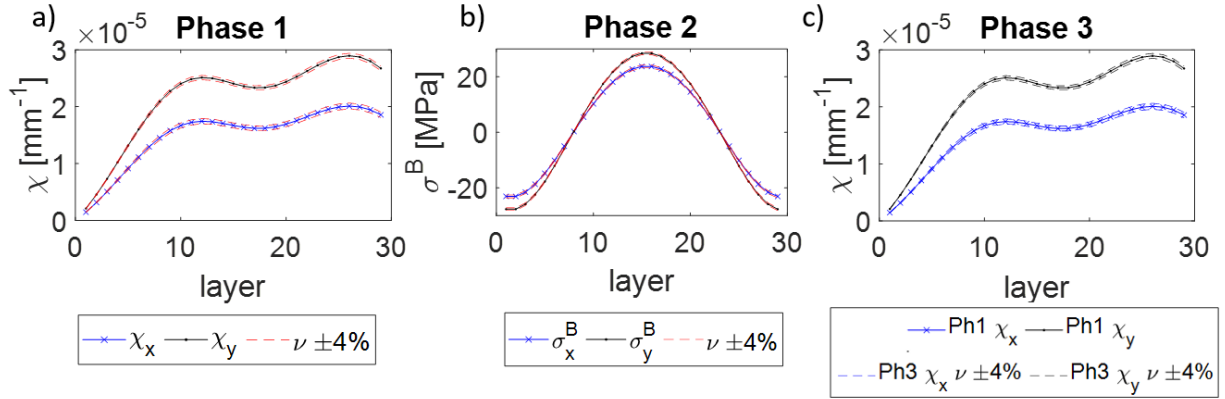


FIGURE 3.24: Uncertainty assessment with a Poisson coefficient ν error of $\pm 4\%$ for the full LR 2D: a) curvatures (Phase 1), b) stresses (Phase 2) and, c) curvatures (Phase 3).

Although the effect of errors in the determination of the mechanical properties is not completely negligible, it is moderate and practically constant at δ_z 0.05mm for the ranges analyzed.

3.3.2.2 Geometry (b , e):

The uncertainty linked to the errors in the geometric variables can also be entered as an absolute or percentage value and, unlike the previous case, it could also occur only in specific layers. In addition, significant differences can be observed between the Full LR and Ribbed LR cases.

Blank width (b):

The input error is introduced uniformly in all the layers. The analysis shows that, for the case of Full LR, an error in the width of any value has no effect. This is because this variable vanishes in the full LR formulation. On the contrary, for the Ribbed LR case, the errors in the width of the part produce non-zero uncertainty (Fig. 3.25).

Introducing an input error percentage of $\pm 2\%$, equivalent to 8mm, generates an uncertainty in the curvatures (Phase 1) and stresses (Phase 2) difficult to appreciate to the naked eye (Fig. 3.25a and b respectively). As a consequence, the effect on the curvatures and deformations of Phase 3 is also very low (Fig. 3.25c). Therefore, the effect of the errors in the width of the blanks are considered negligible.

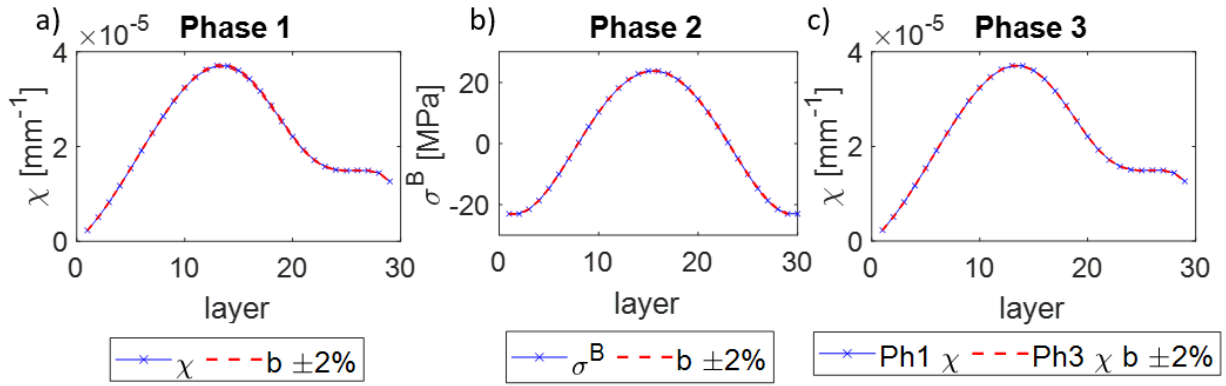


FIGURE 3.25: Uncertainty assessment with a blank width b error of $\pm 2\%$ for the ribbed LR 1D: a) curvatures (Phase 1), b) stresses (Phase 2) and, c) curvatures (Phase 3).

Layer thickness (e):

To begin with, a uniform input error in the layer thickness (e) is applied to all layers. This, either in absolute or percentage value, must be between reasonable values. A uniform absolute value of 0.05mm is chosen, obtaining the results shown in Figure 3.26.

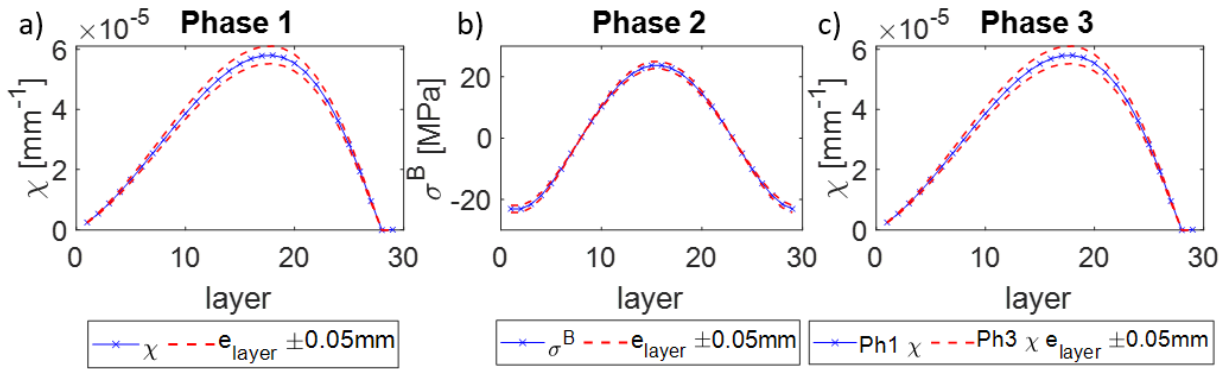


FIGURE 3.26: Uncertainty assessment with a layer thickness e error of $\pm 0.05\text{mm}$ for the full LR 1D: a) curvatures (Ph. 1), b) stresses (Ph. 2) and, c) curvatures (Ph. 3).

In fact, in contrast to the variables discussed above, a uniform and equal error in all layers is unlikely in this case. For this reason, it is decided to analyze the effect of a single error in the thickness of one of the layers. Thus, the effect of an error in the firstly machined layer is analyzed, reaching the conclusion that it has no effect in the stresses and deformations.

Repeating the analysis but this time introducing the input error in the second layer, non-negligible results are obtained, as shown in Figure 3.27. Although the effect of the variability in the thickness of a single layer is not noticeable in the curvatures, deformations and stresses (Phases 1 and 2), in the last layers of Phase 3 the deviations increase considerably (Fig. 3.27c), reaching values above 0.5mm, that is, 10 times more than the introduced variability.

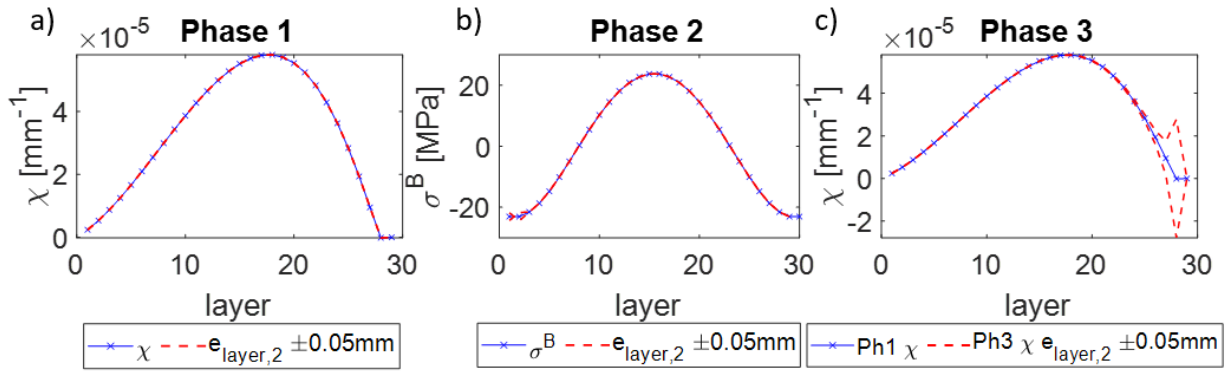


FIGURE 3.27: Uncertainty assessment with a layer thickness e error of $\pm 0.05\text{mm}$, only in the second layer e_2 for the full LR 1D: a) curvatures (Phase 1), b) stresses (Phase 2) and, c) curvatures (Phase 3).

This calculation is repeated changing the affected layer, to see in which specific layer the error in layer thickness has greater consequences. Figure 3.28a shows the maximum difference between the input BIRS and the BIRS calculated in Phase 2 when an input error in the layer thickness e_i of 0.2mm is applied in different layer i ; and Figure 3.28b shows the difference between the curvatures of Phase 1 and Phase 3.

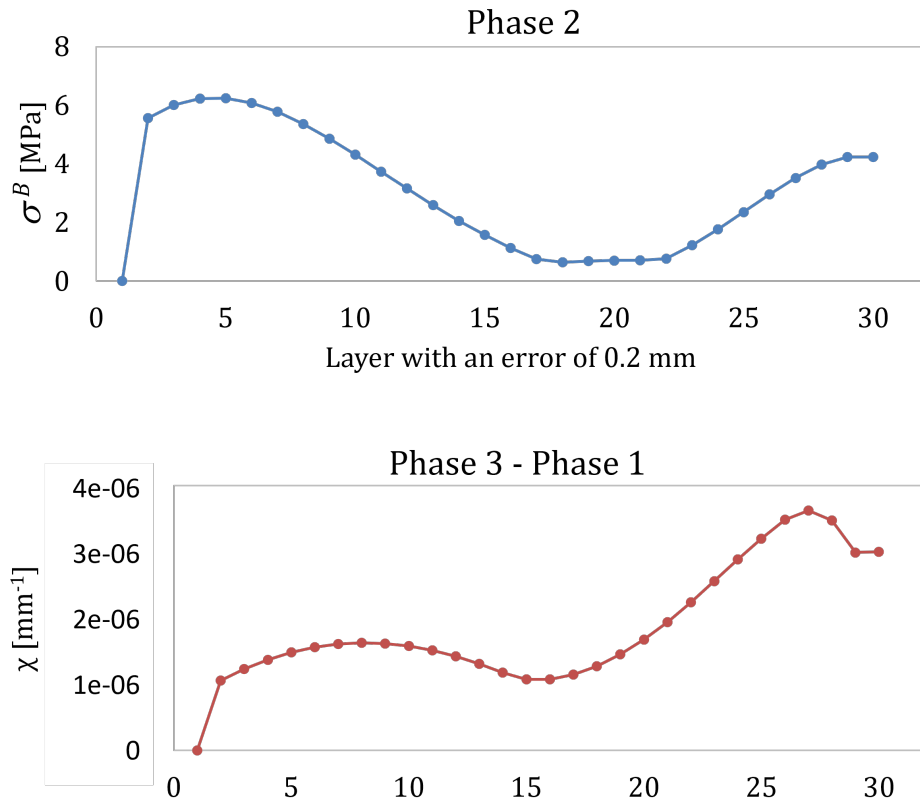


FIGURE 3.28: Uncertainty due to an input error of 0.2mm in the thickness of different layers “ i ”, e_i , in the stresses (Phase 2) and deformations (Phase 3, option 2) for the Full LR 1D.

Next, the effect of error compensation on the layer thickness e is analyzed. In this way, if the error is generated in the layer “ i ”, it is compensated in the next layer “ $i + 1$ ”. In other words, if the thickness of layer 2 with error becomes 0.95mm, that of layer 3 will be 1.05mm. In view of the results shown in Figures 3.29, it is concluded that although the effects on curvatures and stresses of Phases 1 and 2 are small, in Phase 3 the errors are significantly amplified in the last layers. This behavior is similar to the previous case of input error applied in a single layer without compensation (Fig. 3.27c), but changing the sign.

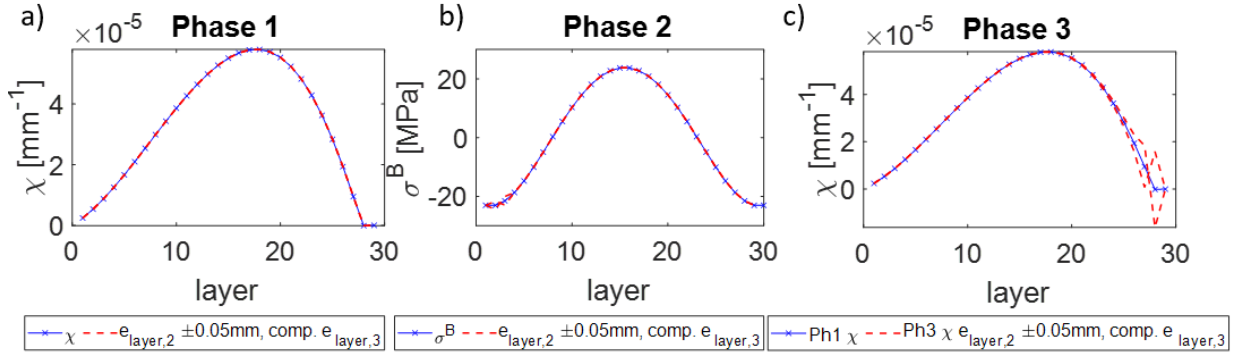


FIGURE 3.29: Uncertainty assessment with a layer thickness e error of ± 0.05 mm, only in the second layer e_2 and compensated in the third layer e_3 for the full LR 1D: a) curvatures (Phase 1), b) stresses (Phase 2) and, c) curvatures (Phase 3).

In view of the results of the uncertainty assessment related to the layer thickness e , the following conclusions are reached:

- When the error is introduced uniformly in all the layers, although in Phases 1 and 2 the effects are noticeable, in Phase 3 the curvatures and deformations do not increase with respect to those of Phase 1. In addition, the effect becomes maximum at as the curvature increases, which is, near half height of the blank; and it becomes minimal at the ends, thus, in the first and last layers.
- When the error is introduced in only one layer, the effects on curvatures (Phase 1) and stresses (Phase 2) are practically imperceptible. However, in Phase 3 the curvatures and deformations increase significantly in the last layers by an approximate factor of 10 in comparison with the input error magnitude.
- When the error is introduced in one layer and in the next layer is compensated, the effects on curvatures and stresses of phases 1 and 2 are also negligible. Analogously to the previous case, in Phase 3 the uncertainty in curvatures and deformations increase for the last layers, while, this happens to a lesser extent (and the sign of the curvature changes).

With all this, it is considered that the experimental errors in the layer thickness (e) must be further studied, especially considering the multiple possible ways of introducing the error and the magnitude of its effects in the last machined layers.

3.3.2.3 Probing (p):

In order to quantify the uncertainty linked to probing (p) errors, a probing process is simulated by the introduction of deviations from the theoretical probed surface. With a given curvature the theoretical surface is calculated, and the defined errors are introduced on the probing points, from which the curvature value obtained with those errors is calculated back.

Considering different ways of analyzing the uncertainty linked to probing, one option is applying a random error within a specific range which. Figure 3.30 represents this alternative of introducing the probing error p with nine points. The black solid line represents the theoretical surface, the black dots the probing points on the theoretical surface, the red hollow circles the probing points with the random errors introduced and the red dashed line the resulting surface based on the probing with errors.

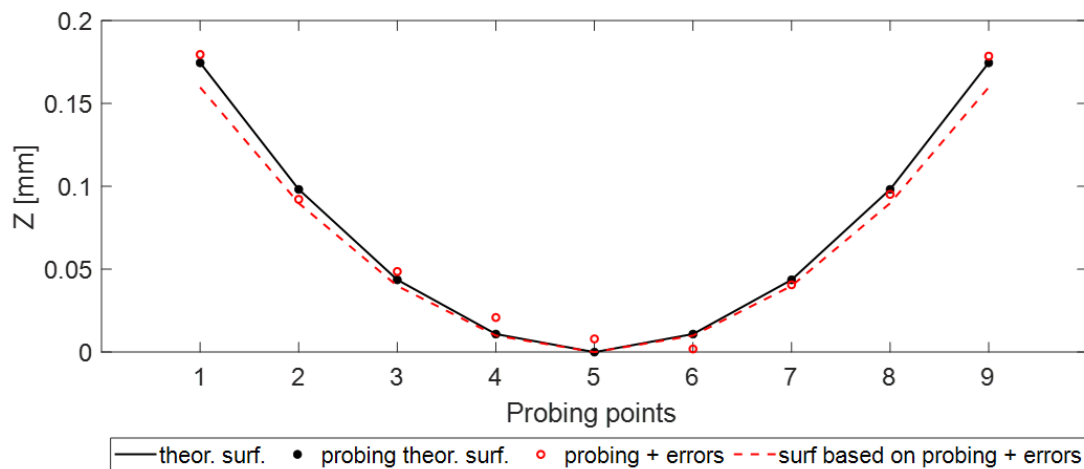


FIGURE 3.30: Random probing error introduction on curvature calculations.

This analysis provides results depicted in Figure 3.31, where a random error in the probing p limited in a range of $\pm 0.010\text{mm}$ continues producing high deviations in the curvatures of Phase 3. It must be noted that the results linked to introducing random probing errors in each layer “ j ”, vary if the LR is again simulated. Thus, in order to assess the magnitude of the effects of a random error in probing p , multiple iterations should be performed to determine the uncertainty range linked to this way of introducing the probing error. For this, a Monte Carlo simulation can be used, as described in the next section.

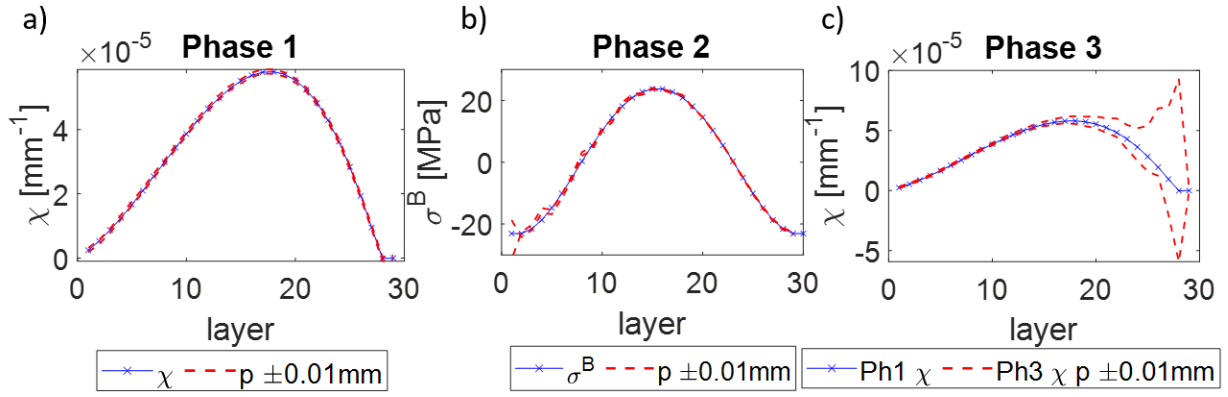


FIGURE 3.31: Uncertainty assessment with a random probing p error within a $\pm 0.010\text{mm}$ range for the full LR 1D: a) curvatures (Phase 1), b) stresses (Phase 2) and, c) curvatures (Phase 3).

Finally, despite theoretically probing errors could occur in a single layer, these are linked to the machine-tool touch-probe accuracy and repeatability. For this reason it does not make sense to perform the single layer analysis as probing errors occur in all layers.

3.3.2.4 Preliminary study summary

- The effect of the errors in the mechanical properties, Young's Modulus (E) and Poisson's ratio (ν), is proportional to the change in these. As it is estimated an error range of $\pm 5\%$ to be a limiting case, the uncertainty caused errors on the mechanical properties are limited and, from now on not considered a factor of study.
- The uncertainty linked to errors in the part width (b), distinguishes two cases. In the case of full LR nothing occurs because the variable width vanishes in the formulation. On the contrary, in the ribbed LR, the effect linked to errors in the width is not zero, but still very small compared to others. For example, a deformation δ_z of 0.05mm would occur if the width of the part changes by 10% , which is 40mm for the test-case. For this reason, the width of the part is not further considered a source of uncertainty.
- The uncertainty linked to errors in the probing p and layer thickness e_{layer} cannot be diminished, both regarding the stresses (Phase 2) and the curvatures (Phases 3). For this reason, these two variables are further analyzed in the next section.

3.3.3 Analysis of critical variables

3.3.3.1 Monte Carlo simulations

The effect of layer thickness and probing is further analyzed using Monte Carlo simulations. In both variables, random error values within a range are introduced. For probing, the

error is introduced as described above (Fig. 3.30), and for the layer thickness the random error is applied in one layer and compensated in the next to avoid negative layer thickness problems.

While this process is repeated for each layer on a LR simulation during Phase 1, a Monte Carlo simulation is used to evaluate the effect of the random errors in the two critical variables, performing 2000 iterations for the LR simulations. Figure 3.32 shows the histogram for the curvatures obtained on a given layer for those 2000 iterations. As can be seen, this histogram shows a normal distribution, indicating that the number of iterations is enough to properly capture the effect of the random errors during the probing. Analogously Monte Carlo simulations are used to analyze the effect of random errors in the layer thickness e_{layer} .

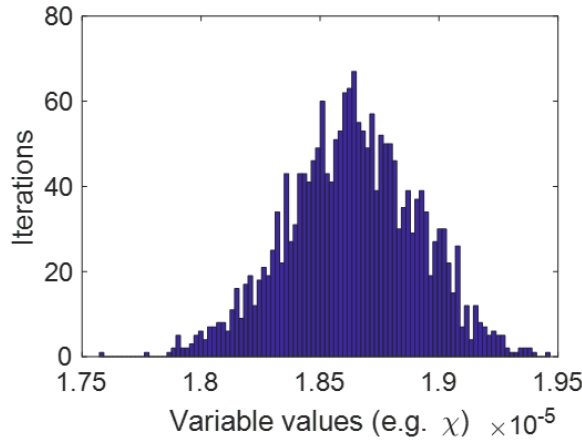


FIGURE 3.32: Histogram for the curvatures obtained in machining step ‘j’ when introducing random probing errors for 2000 iterations.

The analysis is performed in 1D and 2D for the full LR and ribbed LR. Analogously to the preliminary analysis, only the BIRS are considered to simplify the understanding. The BIRS profile depicted in Figure 3.22 is used in this analysis, to compare later the 1D and the 2D cases. The results obtained from the Monte Carlo simulation of Phase 1 (curvatures), 2 (BIRS) and 3 (curvatures) can be seen in the figures detailed in Table 3.4. In each graph, the black crosses represent the nominal results from the LR simulation without error; the red dots are the average values for the 2000 iterations with random errors; the red dashed line unifies the uncertainty confidence interval of 99.7% (3σ) for the 2000 iterations; and the grey band represents the results for all the iterations with random errors.

TABLE 3.4: Cases studied in the analysis of critical variables.

1D	Phases 1 & 2	Phase 3
Full LR	Fig. 3.33	Fig. 3.34
Ribbed LR	Fig. 3.35	Fig. 3.36

As it can be seen in figures 3.33 and 3.34, in both full and ribbed LR, the uncertainty linked to layer thickness is lower than that of probing.

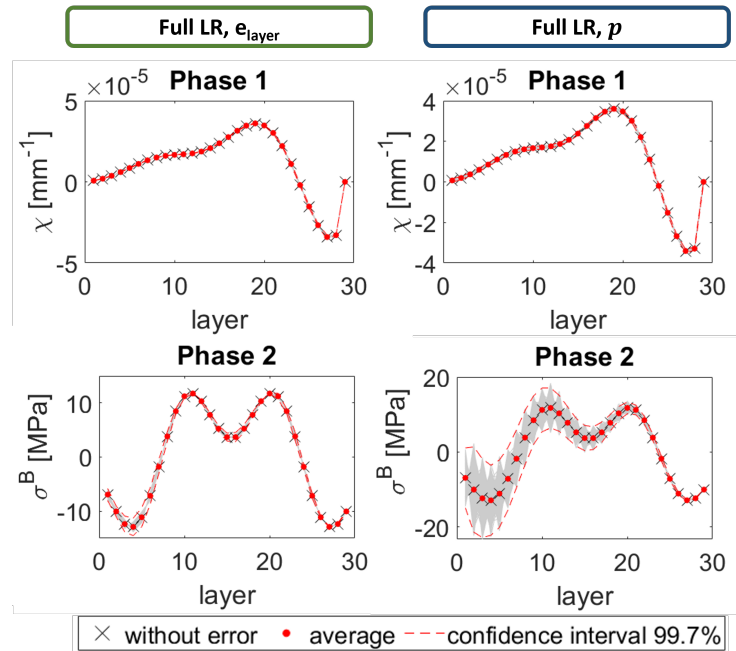


FIGURE 3.33: Results for Monte Carlo simulations of layer thickness and probing random errors for a full LR in 1D: Phase 1 curvatures and Phase 2 stresses.

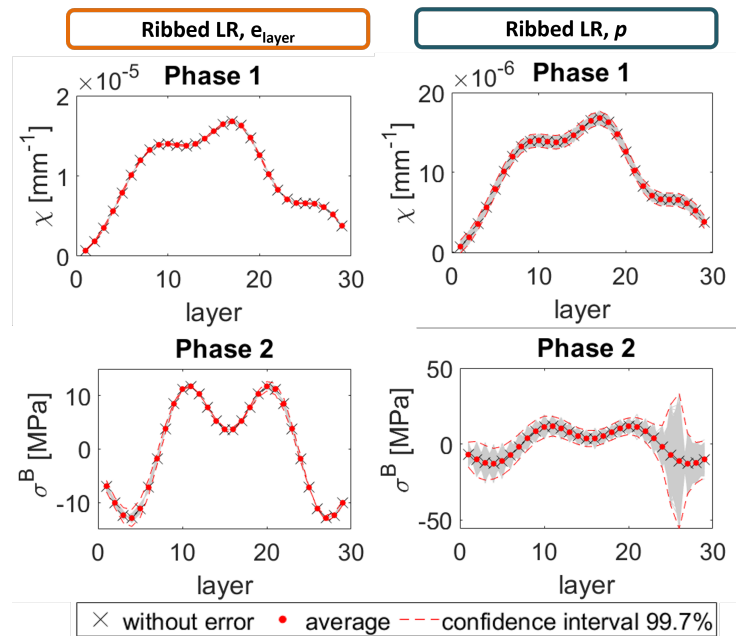


FIGURE 3.34: Results for Monte Carlo simulations of layer thickness and probing random errors for a ribbed LR in 1D: Phase 1 curvatures and Phase 2 stresses.

The curvature deviations generated by the random layer thickness and probing errors on Phase 1 are low in comparison to the curvature results without errors. Moreover, the average for the tests with random errors matches the results without errors. In the case of

the BIRS from Phase 2, different results can be seen between full and ribbed LR. In the case of full LR, the BIRS profile shows deviations in the first half of the profile. However, in the case of ribbed LR and probing errors it should be noted that, while the first half of the BIRS profile shows a deviation similar to the one on the full LR, the second half of the BIRS profiles show a peak of very high deviations.

Figures 3.35 and 3.36 show the curvature results of Phase 3 for the 2000 iterations from the Monte Carlo simulation, where the 4 BIRS data treatment options from Section 3.3.1.1 are applied (Fig. 3.20).

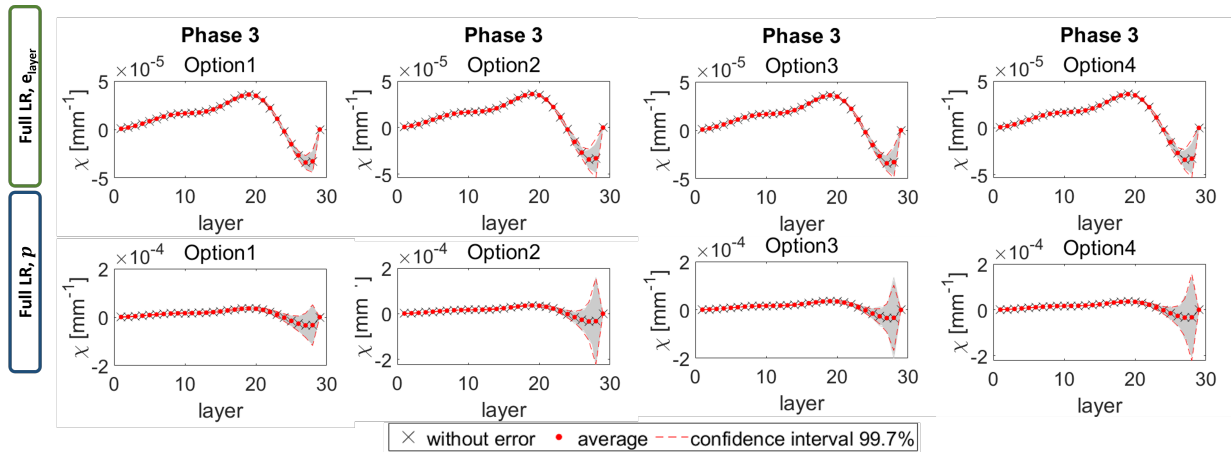


FIGURE 3.35: Results for Monte Carlo simulations of layer thickness and probing random errors for a full LR in 1D: Phase 3 curvatures, curvatures obtained using the different options from Figure 3.20.

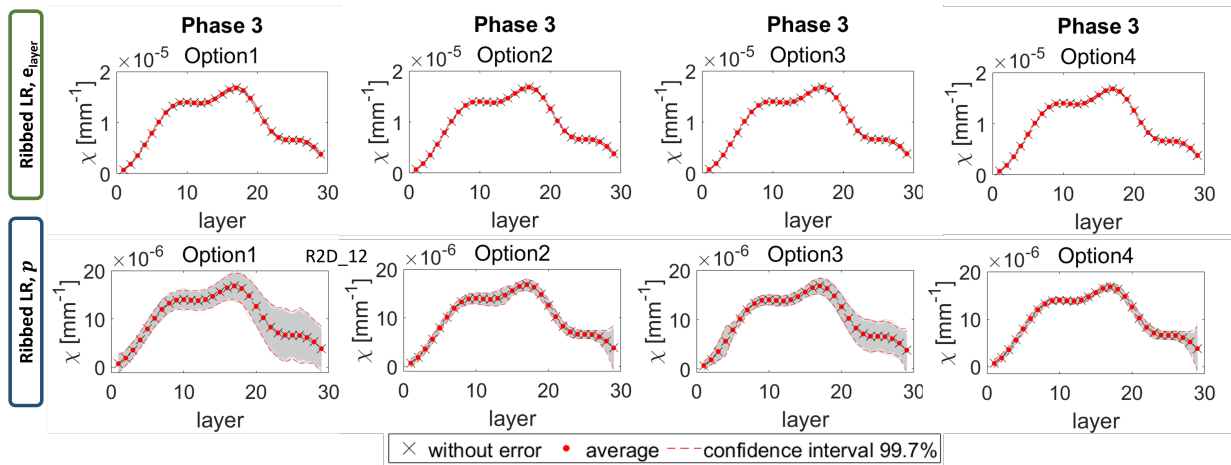


FIGURE 3.36: Results for Monte Carlo simulations of layer thickness and probing random errors for a ribbed LR in 1D: Phase 3 curvatures, curvatures obtained using the different options from Figure 3.20.

As it can be seen, although in full LR both variables show non-negligible deviations, in the ribbed LR the effect of the layer thickness can be dismissed. Focusing on the ribbed LR, the results from options 1 and 3 for the BIRS data treatment generate very high deviations

on the curvature results obtained on Phase 3, which are linked to the deviations on the BIRS profiles from figures 3.33 and 3.34. In the case of the results from options 2 and 4, a significantly lower deviation can be observed, indicating that those BIRS data treatment options are more suitable than options 1 and 3 to avoid the effect of the deviations on the BIRS.

Considering that probing errors have a bigger effect in the uncertainty, especially in ribbed LR, next figures (Fig. 3.37 and 3.38) show the uncertainty linked to probing in 2D for the ribbed LR.

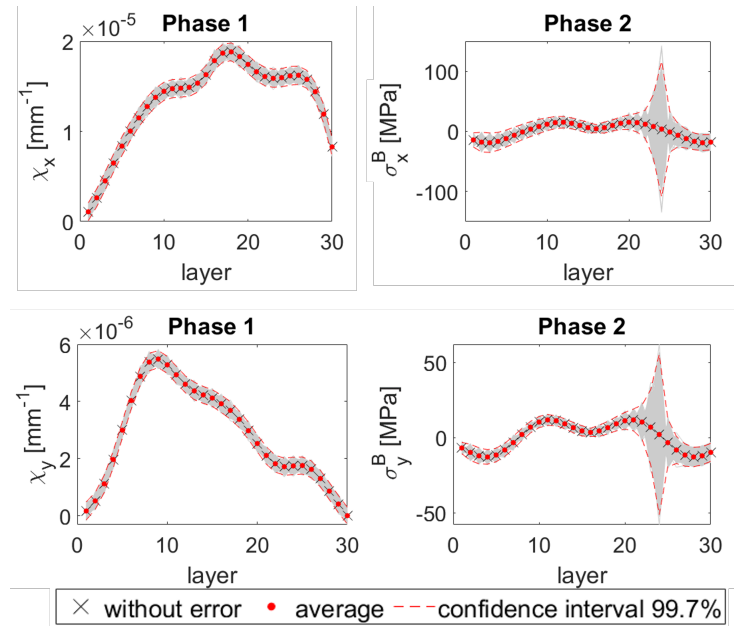


FIGURE 3.37: Results for Monte Carlo simulations of random probing errors for a Ribbed geometry in 2D: a) Phase 1, curvatures; b) Phase 2, stresses.

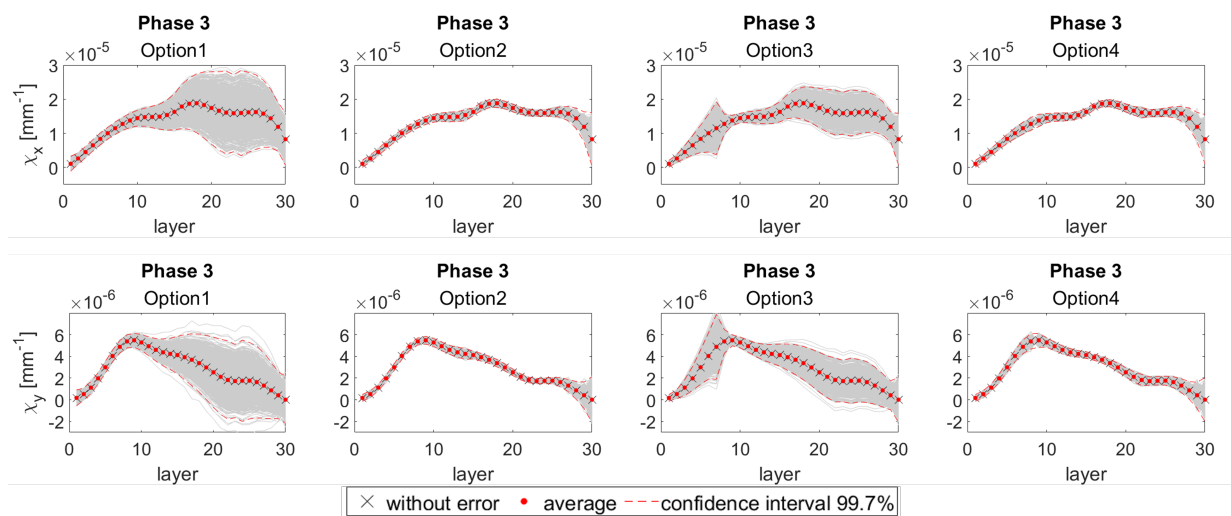


FIGURE 3.38: Results for Monte Carlo simulations of random probing errors for a Ribbed geometry in 2D: Phase 3, curvatures obtained using the different options from Figure 3.20.

While the effect in the curvatures of Phase 1 are similar to the 1D case, in the case of the BIRS from Phase 2 it should be noted that the peak in the second half of the profile increases significantly. Once again, the results obtained when applying the 4 BIRS data treatment options show very different deviations, and options 2 and 4 highly lower the effect of the deviations on the BIRS.

3.3.3.2 Data Filtering

Next, the effect of filtering the curvature results of Phase 1 with random probing errors is investigated. Starting with the 1D analysis, results from raw data and filtered data are compared. The filtering is performed by convoluting the raw probing data with a weighting function. Different filtering options are used to determine the optimal filtering parameters (Table 3.5), where dx is the distance between points, and *cutoff* is the window or amount of points considered. The analysis is performed using option 1 for assigning stress values to the layers without curvature, to magnify the deviations and better visualization.

TABLE 3.5: Parameters used in the filtering analysis.

Convolution filter		
Weighting function	dx	<i>Cutoff</i>
Gaussian	1	2
Gaussian	1	3
Gaussian	1	4
Triangular	1	2

Figure 3.40 shows that the filtering has a positive effect on the deviations for both the BIRS (Phase 2) and the curvatures (Phase 3), reducing such deviations in comparison to the ones obtained without filtering. The filtering parameters with best results are dx 1 and *cutoff* 2 with both weighting functions, triangular (Fig. 3.39a) and Gaussian (Fig. 3.39b). Besides the effect on the curvature and stress variability, a slight shift ($\sim 10\%$) between the iterations average and the nominal value of Phase 3 can be seen when filters are used.

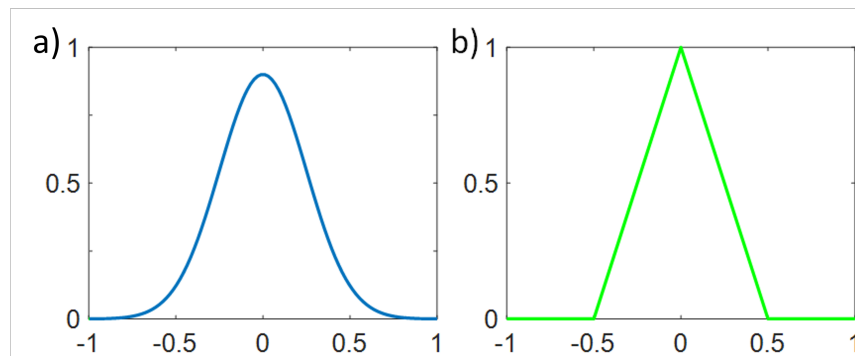


FIGURE 3.39: Weighting functions for data filtering by convolution: a) Gaussian; b) Triangular.

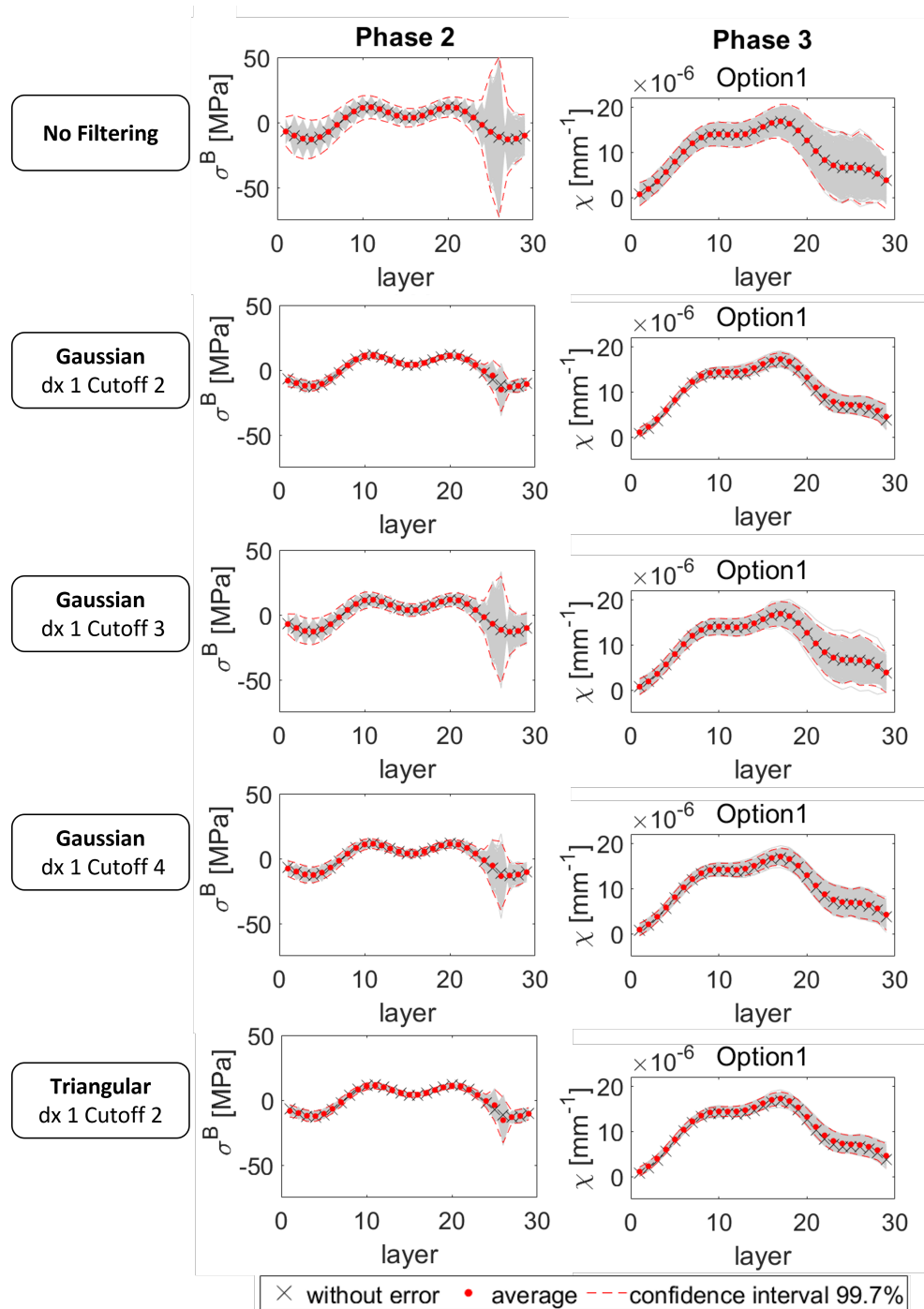


FIGURE 3.40: Different curvature filtering applied to Monte Carlo simulations of random probing errors for a Ribbed geometry in 1D: Phase 2, stresses, and Phase 3, curvatures, obtained using different filtering parameters and option 1 stress data treatment (Fig. 3.20).

Using the filtering parameters identified before, Figure 3.41 shows the results obtained from the Monte Carlo simulation for curvature (Phase 1) and BIRS (Phase 2) for the 2D ribbed LR with probing error. The filtering also reduces deviations in comparison to the ones obtained without filtering (Fig. 3.37). In the case of the stresses, while still a peak of

deviations can be seen in the second half of the BIRS profiles, they are much lower than the one observed for the results without filtering.

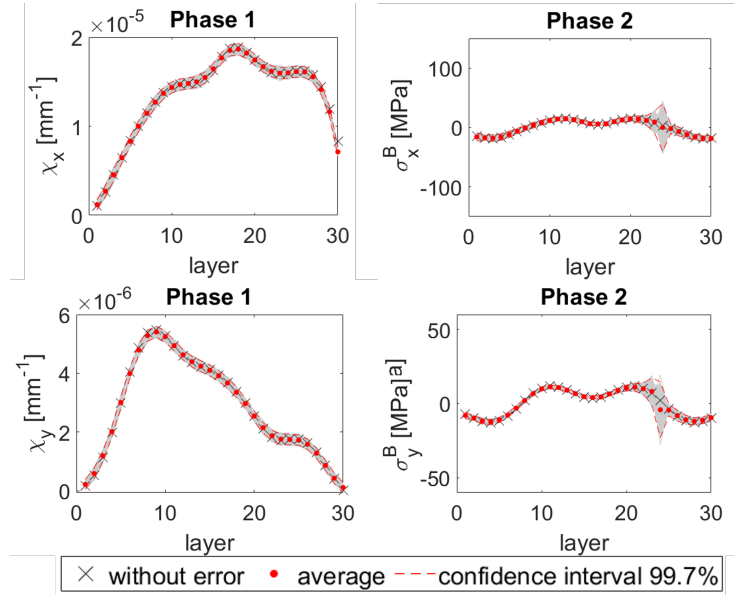


FIGURE 3.41: Results with curvature filtering for Monte Carlo simulations of random probing errors for a Ribbed geometry in 2D: a) Phase 1, curvatures; b) Phase 2, stresses.

The curvature with filtering results obtained from Phase 3 for the 2000 iterations are shown in Figure 3.42 for the 4 BIRS data treatment options. In comparison to the results obtained without filtering (Fig. 3.20), it is clear that the filtering reduces significantly the curvature deviations, especially for BIRS data treatment options 1 and 3.

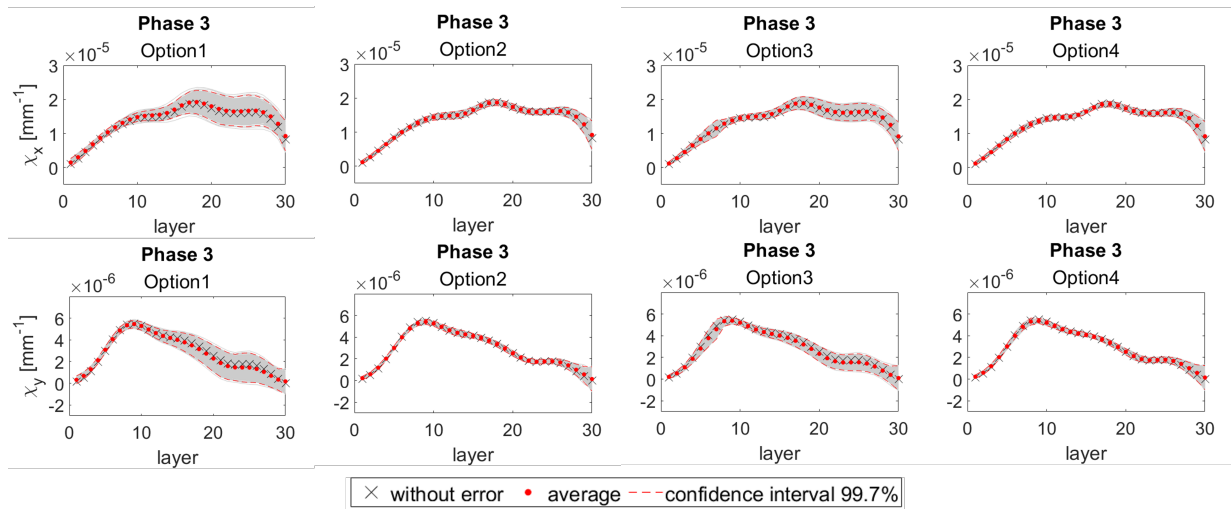


FIGURE 3.42: Results with curvature filtering for Monte Carlo simulations of random probing errors for a Ribbed geometry in 2D: Phase 3, curvatures obtained using the different options from Figure 3.20.

Table 3.6 shows the values obtained for the maximum uncertainty ranges (3σ) obtained from all the cases exposed in figures 3.37, 3.38, 3.41, and 3.42. As can be seen, filtering

significantly reduces the maximum uncertainty in all cases, by a factor of approximately 2 in the case of curvatures and 3 for stresses. Nevertheless, a slight shift from the results without random probing errors can be seen for the average of the values from the 2000 iterations, within a 10% of the nominal value, indicating a possible detrimental effect when using curvature filtering.

TABLE 3.6: Quantification of the confidence interval (3σ) for the raw and filtered data of the probing uncertainty assessment.

Max. Uncertainty (3σ)	Ph 1 (χ)	Ph 2 (σ^B)	Ph 3 (χ)				
			Option 1	Option 2	Option 3	Option 4	
X							
Raw data	1.04E-06	113.3	1.25E-05	7.82E-06	7.75E-06	7.23E-06	
Filtered	6.41E-07	40.1	4.68E-06	4.11E-06	4.17E-06	4.27E-06	
Y							
Raw data	3.14E-07	53.3	3.75E-06	2.12E-06	2.98E-06	2.03E-06	
Filtered	1.91E-07	18.8	1.36E-06	1.12E-06	1.13E-06	1.11E-06	
Ratio Raw/Filtered							
X	1.63	2.83	2.67	1.9	1.86	1.69	
Y	1.65	2.84	2.75	1.9	2.63	1.83	

3.3.3.3 Extension of the analysis to different geometries and BIRS profiles.

Continuing the uncertainty assessment in ribbed LR, three different part geometries and three BIRS profiles are studied. Regarding geometries, all of them are ribbed, analogous to the base test-case geometry, i.e. with three fins of 5 mm each. The dimensions of the parts are defined in Table 3.7. To simplify the understanding, the analysis is performed in 1D.

TABLE 3.7: Different geometries analyzed in the extension of the uncertainty assessment due to probing p errors.

Dimensions [mm]	A	B	C
H	30	60	30
b	400	400	800

The BIRS profiles used in the analysis are labelled as follows. First, labelled as 1, the one used for the analysis of critical variables [250] (Fig. 3.22b). Secondly, labelled as 2, the one used in the preliminary analysis [123] (Fig. 3.22a). Thirdly, labelled as 3, a theoretical BIRS profile with a triangle shape and small details on the sides. In this way, nine different cases are analyzed. Figure 3.43 shows the deviations of the nine cases on the stresses of Phase 2. It can be seen that, although the magnitude of the errors vary, the height of the layer at which the error peak is triggered matches in all cases, meaning that this effect does

not depend upon the BIRS profile shape. Besides, increasing the part height, H , increases the magnitude of the deviations peak, while increasing the part width, b , diminishes it.

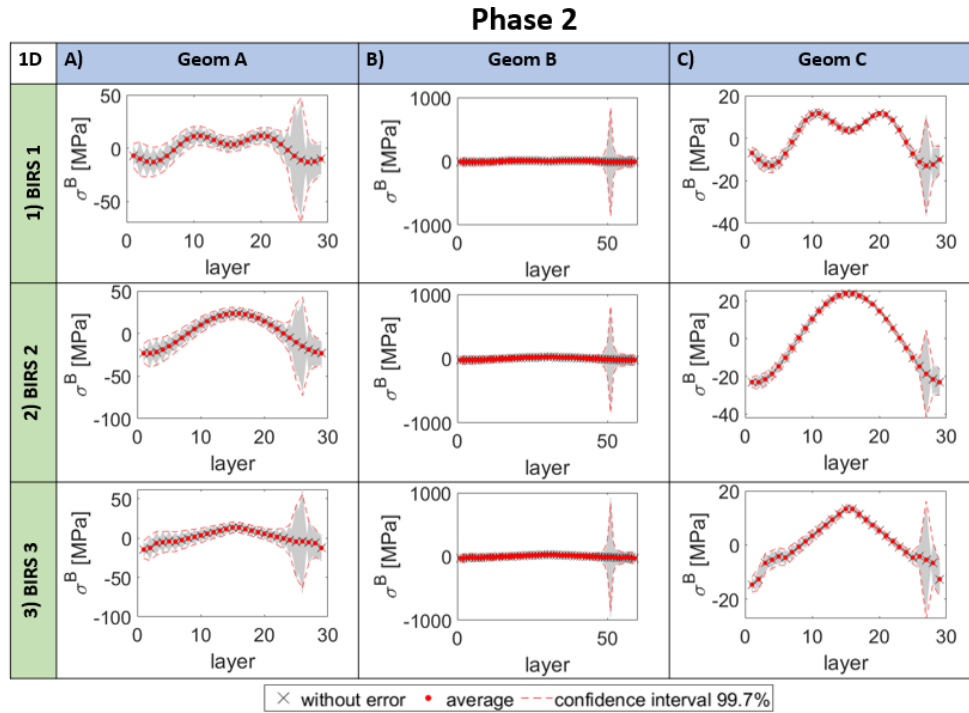


FIGURE 3.43: Results for Monte Carlo simulations of random probing errors for a Ribbed geometry in 1D with different geometries and BIRS profiles: Phase 2, stresses.

A final study is performed increasing the BIRS by an order of magnitude (x10), aiming at reflecting the cases where BIRS are not stress relieved [24] (Fig. 3.44).

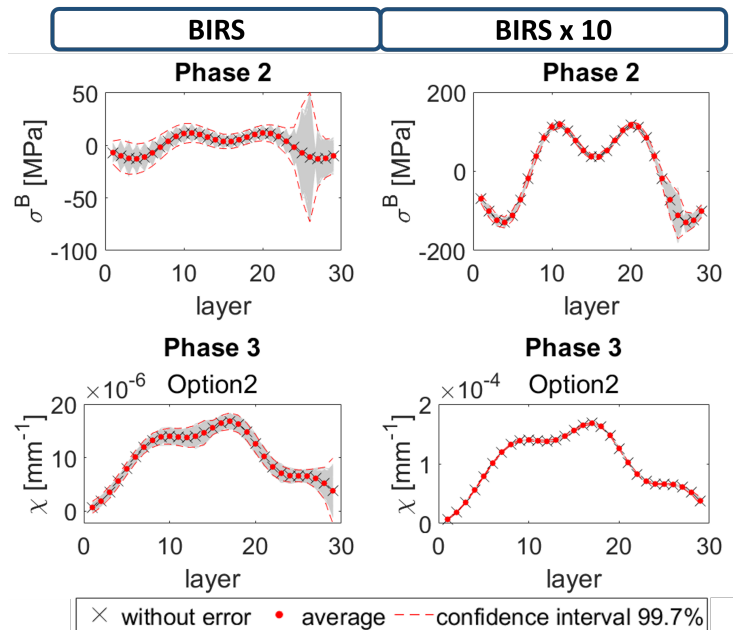


FIGURE 3.44: Results for Monte Carlo simulations of random probing errors for a Ribbed geometry in 1D with BIRS profiles of the same shape and different magnitude: Ph.2, stresses.

The results show that probing uncertainty does not depend on the magnitude of the input BIRS, meaning that the uncertainty range is kept when the BIRS magnitude increases if the probing error range is kept constant. Proportionally this reduces the uncertainty percentage for blanks with high BIRS.

3.3.4 Conclusions of the uncertainty assessment

This section analyzed the effect of the different uncertainty sources of the on-machine LR method for the characterization of BIRS on machining blanks. After a preliminary analysis, which showed that probing is the main uncertainty source, Monte Carlo simulations were used to quantify the uncertainty range generated by probing errors. Next conclusions are withdrawn for the obtained results:

1. On-machine probing measurements are the main uncertainty source for the on-machine LR method for BIRS characterization in ribbed geometries.
2. The proposed three phase procedure in conjunction with Monte Carlo simulations proves to be appropriate to determine the uncertainty for results obtained from the on-machine LR method.
3. The data treatment option 2 (direct symmetry) proposed for the BIRS data treatment should be used during LR tests, as it generates the most accurate results when using those BIRS for the calculation of curvature data through the simulation of a LR test (Phase 3).
4. The filtering of the curvature data obtained from the on-machine LR tests provides a higher increase on the accuracy of the results from those tests. However, filtering should be used with caution, as the theoretical study indicates a slight shift ($\sim 10\%$) between the iterations average and the nominal value of Phase 3 when filters are used.
5. Concerning changes in the blank size, the uncertainty due to probing increases with the part height, and decreases with the width. On the other hand, different input BIRS profiles of similar magnitude provide similar results. When the BIRS magnitude increases, the uncertainty due to probing errors becomes proportionally less significant.

3.4 Summary and discussion

In this chapter a deeper insight of bulk or blank-initial residual stresses (BIRS) is given, and basic concepts of the BIRS profiles in rolled blanks for aerospace structural parts are introduced.

Considering the unavoidable variabilities of BIRS between blanks, and aiming at the industrial applicability of the BIRS measuring method, the on-machine LR method is developed further. These developments are focused on three concepts:

- Considering the clamping stresses due to the initial curvatures of the machining blanks.
- Considering the MIRS introduced in the surface during the on-machine LR.
- Developing a formulation with which BIRS can be measured in ribbed geometries, enabling to obtain final parts from blanks with measured stresses.

The formulation related to these three concepts is merged into a multicoupled formulation, which corresponds to the upgraded on-machine LR method in ribbed geometries. This novel formulation improves the accuracy of the method and avoids destroying completely the blanks to measure BIRS. With this method, two-dimensional cross-sectional stress maps can be obtained, where in each layer the stresses of all sections are averaged, enabling direct correlation with machining distortion curvatures.

Finally, the uncertainty linked to different sources is assessed, for which a procedure consisting in three phases is defined and Monte Carlo simulations are used. Using this procedure the theoretical uncertainty is quantified and best practice guidelines are defined regarding data treatment and filtering. Experimental verification of on-machine LR measurements in ribbed geometries is performed in Chapter 5, for which MIRS data obtained along Chapter 4 is used.

Chapter 4

Machining-induced residual stresses

4.1 Introduction

As explained Chapter 2, residual stresses in the machined surfaces, MIRS, are inevitable due to the high temperatures, forces and strain fields inherent to the machining process. The effect of MIRS can be an important source of distortion depending on the material, work-piece geometry and machining conditions.

For these reasons, MIRS measurement is important to provide the necessary data for the implementation of distortion calculation tools. However, MIRS measurement application and uncertainty assessment by different measuring techniques is limited. Besides, there are few studies that directly compare available techniques for MIRS measurement and build prediction models for aerospace alloys. For these reasons, the objective of this chapter is to obtain MIRS values to be used as input for the distortion studies of the next chapter, as well as to build a model capable to predict the MIRS induced by the finishing milling process of aeronautic monolithic components.

In order to accomplish the main objective of the chapter, a series of secondary objectives are defined:

- Understanding of MIRS and its measuring methods.
- Measurement and analysis of the MIRS profiles induced by milling operations in aluminium and titanium alloys.
- Comparison between the Incremental Hole Drilling and the X-Ray Diffraction methods.
- Empirical model development and evaluation for MIRS prediction, including its evaluation.

The shape of MIRS induced by milling operations results from a combination of thermal, mechanical and physical-chemical causes (Chapter 2). Figure 4.1 shows the typical shape of a MIRS profile, in which four different parameters can be distinguished for its description: RS Peak at the surface (σ_{Sur}^M), maximum compressive RS ($\sigma_{C,max}^M$) and its location ($x_{C,max}$), and the response depth at which the induced RS stabilize (x_{sta}).

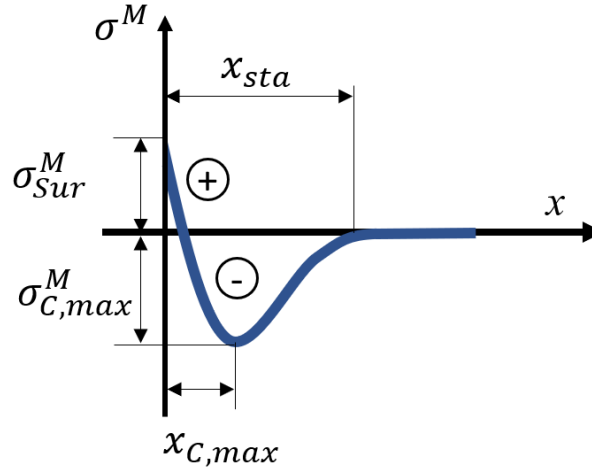


FIGURE 4.1: Schematic representation of MIRS profile in milling including parameters for a simplified description.

There are multiple factors that influence the shape and magnitude of MIRS, and contradictory results can be easily found in literature (Section 2.2.1.2). This is in a great extent linked to the measurement uncertainty, thus, next section presents the two main measuring methods in detail.

4.2 Measurement methods

Quantitative MIRS measurement is mainly performed using the X-ray diffraction (XRD) and hole drilling (HD) method, including their variants. Hereafter both methods are described.

4.2.1 Hole Drilling (HD) method

The Hole Drilling (HD) method is based on stress relaxation after material removal. Although it is a destructive measuring method, it is often considered as semi-destructive because the low damage performed in the parts. The method consists of drilling a small hole in the surface of the component, where a strain gauge glued to the surface measures the generated strains. From these strain measurements, the stresses are calculated.

The assumptions on which the HD is built are that the material is isotropic in linear-elastic regime, and that RS fields are uniform and do not vary significantly in depth.

The design of the strain gauges may vary, as depicted in Figure 4.2 where the three most typical designs can be observed, being D the hole diameter and β the principal stress direction. According to the ASTM E837-08 standard [188], the penetration depth of the hole must be approximately equal to its diameter, as at deeper penetration depths the strain gauges lose sensitivity.

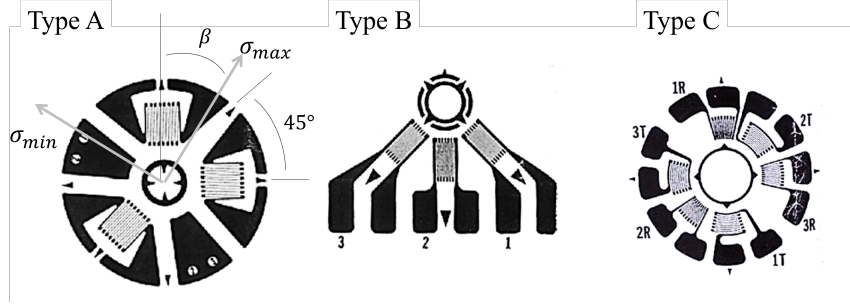


FIGURE 4.2: Typical design of strain gauges for HD, including principal stress directions of the type A strain gauge.

In this way, the surface strain, ϵ is related to principal stresses as indicated by Equation 4.1, where the coefficients \bar{A} and \bar{B} are two calibration constants that depend on the geometry of the gauge, the elastic properties of the material, and the diameter and penetration depth of the hole.

$$\epsilon = (\bar{A} + \bar{B} \cos 2\beta)\sigma_{max} + (\bar{A} - \bar{B} \cos 2\beta)\sigma_{min} \quad (4.1)$$

For a material with defined elastic properties, the constants \bar{A} and \bar{B} are calculated using the Equation 4.2, where \bar{a} and \bar{b} are dimensionless standardized constants tabulated in [188]. The \bar{a} and \bar{b} constants do not depend on the material, and vary with the depth of the hole. They represent the deformations measured for the cases in which $\sigma_{max} = \sigma_{min} \neq 0$ and $\sigma_{max} = -\sigma_{min}$, respectively.

$$\bar{A} = \frac{-\bar{a}(1 + \nu)}{2E}; \quad \bar{B} = \frac{-\bar{b}}{2E} \quad (4.2)$$

In thick samples, the combination of stresses should be considered (Eq. 4.3), where P represents the mean pressure of the RS, Q and T represent the components of the tangential stress, and 1 and 3 indicate the stress (perpendicular) directions.

$$P = \frac{\sigma_3 + \sigma_1}{2}; Q = \frac{\sigma_3 - \sigma_1}{2}; T = \frac{\tau_{13}}{2} \quad (4.3)$$

This way, using the Mohr's circle, the angle β can be calculated using Equation 4.4, and the principal stresses with Equation 4.5.

$$\beta = \frac{1}{2} \arctan(T/Q) \quad (4.4)$$

$$\sigma_{min}, \sigma_{max} = P \pm \sqrt{(Q^2 + T^2)} \quad (4.5)$$

If the stresses are non-uniform, meaning that the combined strains deviate from the given stress distribution by more than $\pm 3\%$, the stress distribution should be treated as non-uniform and the ASTM E837 calculations should not be applied [189]. To determine whether the stresses are unevenly distributed, the hole should be drilled incrementally, recording the stresses at a series of hole depths. This method is known as the *Incremental Hole Drilling (iHD) method*.

During the iHD, the material removal in the first drilling increment results in surface stresses that are directly related to the RS relieved at the boundary of the hole within that increment. In the second increment, the material removal produces two effects:

- First, the stiffness of the specimen is modified so that there is a new relaxation of the stresses within the layer of material corresponding to the first increment, producing a change in deformation in the strain gauge.
- Second, the stresses relieved at the boundary of the second increment hole produce an additional change in the strain of the gauge. For this reason, even without stresses in the new increments, strain relaxation can continue growing [251].

For this reason, different coefficients are needed to relate the changes in the surface strain with RS for each of the stress depth and hole depth combinations. In Figure 4.3 a calculation example is depicted for three increments with the corresponding \bar{a} coefficients. The \bar{b} coefficients are analogously obtained.

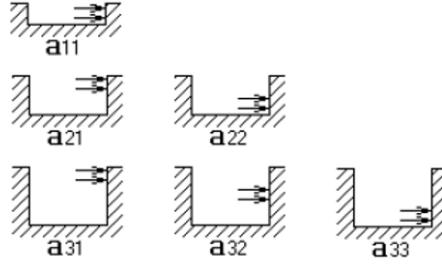


FIGURE 4.3: Hole and stress depths corresponding to coefficients \bar{a} [189].

The strain data obtained from drilling the hole in small increments can be filtered to reduce noise [189]. This way, the combined strains p , q , and t are calculated from the smoothed strain data.

In this way, the accumulative strain relaxation functions for the measured hole diameter (A and B) are calculated by interpolation, from the sets of triangular matrices given in [252, 253]. After that, the coefficients \bar{a} and \bar{b} are obtained and the stresses P , Q and T are calculated for the successive increments by means of the Equation 4.6.

$$\bar{a}P = \frac{pE}{1 + \nu}; \quad \bar{b}Q = qE; \quad \bar{b}T = tE \quad (4.6)$$

For instance, the combined pressure stress P is calculated by the first two increments (Eq. 4.7 and 4.8):

$$P1 = \frac{\frac{p1 \cdot E}{(1+\nu)}}{\bar{a}_{11}} \quad (4.7)$$

$$P2 = \frac{\frac{p2 \cdot E}{(1+\nu)} - (P1 \cdot \bar{a}_{21})}{\bar{a}_{22}} \quad (4.8)$$

To obtain the combined stresses Q and T , the same procedure must be followed considering zero the Poisson ratio. Finally, the stresses in each increment are calculated from the corresponding combined stresses with Equation 4.5.

4.2.2 X-Ray Diffraction (XRD) method

The X-Ray Diffraction (XRD) method is not based on measuring strains due to stress relaxation after material removal. In this method, the strain present in the material is calculated based on the deviation of the inter-planar distance of the crystal lattice. From

this value, the stress is calculated with the elastic constants of the material, assuming a linear elastic distortion of the corresponding lattice plane.

To perform it, the material must be crystalline with a relatively small or fine grain size, with no preferential grain texture in which the diffraction peak reaches a certain intensity and is not interfered by other nearby peaks [197].

The principle beneath the method is linked to the interactions between the X-ray beam and the crystal lattice, where a crystal can be defined as a solid composed of atoms arranged in a pattern recurring in three dimensions (Fig. 4.4). In this process, the X-rays are scattered by the electrons of the atoms of the crystal, without changes in the wavelength. The Bragg's Law (Eq. 4.9), relates the inter-planar distance d (in nm) and the wavelength of the incident radiation λ (in nm), given a reflection order N and knowing the diffraction angle (in degrees) θ .

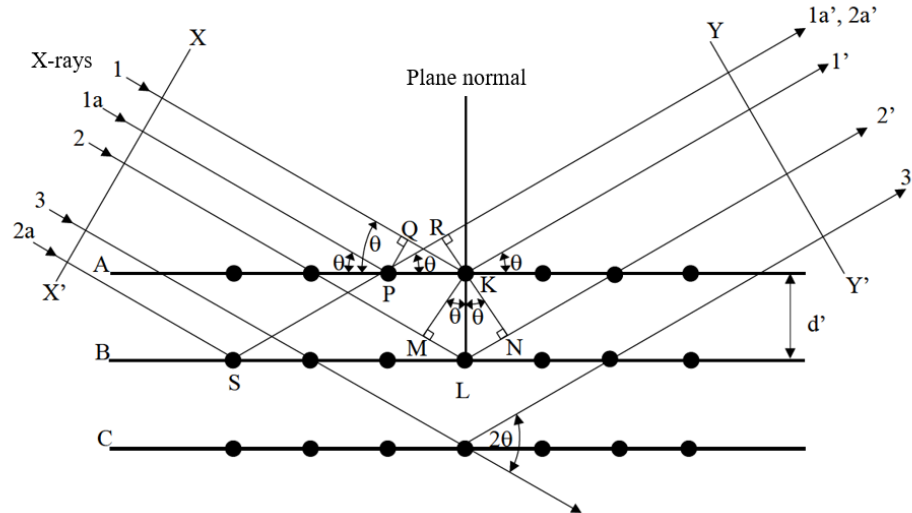


FIGURE 4.4: Diffraction of X-rays by a crystal lattice, in which planes hkl are parallel to the surface [197].

$$N \cdot \lambda = 2 \cdot d \cdot \sin(\theta) \quad (4.9)$$

Obtaining the RS measurements by XRD is based on the scattering of the diffraction peak due to inter-planar distance modifications generated by mechanical strain. In the directions in which Bragg's Law is satisfied, the scattered waves are in phase, giving lead to constructive interference and therefore producing a measurable diffracted intensity. Thus, using X-rays of known wavelength and measuring the diffraction angle, the inter-planar distance of a crystal can be determined, and stresses calculated. Figure 4.5 depicts three

different scenarios of crystal lattices and inter-planar distances, with their corresponding diffraction peaks [19].

- If the material is stress-free and there is no strain, the inter-planar distance d_0 is equal for all families of planes (Fig. 4.5a).
- In the case of uniform stresses, whether compressive or tensile, the inter-planar distance decreases or increases uniformly for all families of planes, leading to a shift of the diffraction peak (Fig. 4.5b).
- Non-uniform stresses cause a symmetric broadening of the diffraction peak (Fig. 4.5c). The width of the peak is measured by the Full Width at Half Maximum (*FWHM*), namely, the width of the peak at half height.

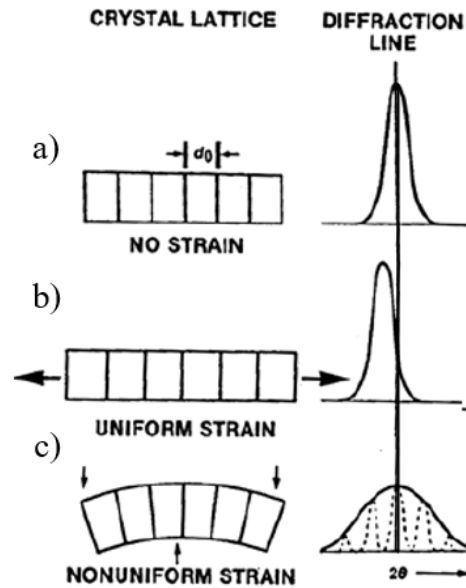


FIGURE 4.5: Strain effect on the diffraction peaks [19].

In this way, the strain can be defined by the variation of the inter-planar distance d and the stress-free inter-planar spacing d_0 . The variation of the inter-planar distance is obtained from the derivative of the equation of Bragg's Law (Eq. 4.10), being θ the position of the diffraction peak with stresses and θ_0 the position of the diffraction peak without stresses.

$$\epsilon = \frac{d - d_0}{d_0} = \frac{\Delta d}{d_0} = -(\theta - \theta_0) \cdot \cot \theta_0 = -\Delta\theta \cdot \cot \theta_0 \quad (4.10)$$

It is important to note that only the normal component of the deformation perpendicular to the crystallographic planes can be directly measured by XRD. Shear strains are calculated from the normal strains measured at angles 0° , 45° , and 90° .

The normal strain along the normal direction of the crystallographic plane can be measured by the displacement of the diffraction peak along the 2θ axis. By measuring the normal strains in various directions at the coordinates of the sample, the strain in the desired direction can be calculated. Figure 4.6 shows the relationship between the direction of the measured normal strain and the coordinates of the sample.

The fundamental equation (Eq. 4.11), which relates the measured normal strain and the strain tensor expressed in the coordinates of the sample, is expressed as follows:

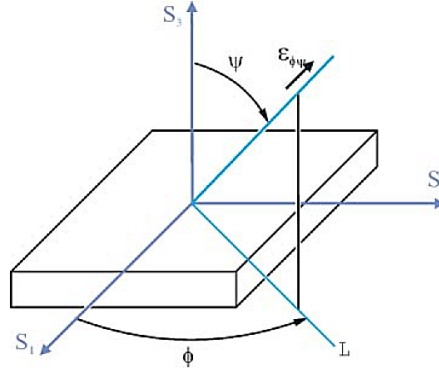


FIGURE 4.6: Deformation measured by XRD at the sample coordinates [254].

$$\begin{aligned} \epsilon_{\phi\psi} = & \epsilon_{11} \cdot \cos^2 \phi \cdot \sin^2 \psi + \epsilon_{12} \cdot \sin 2\phi \cdot \sin^2 \psi + \epsilon_{22} \cdot \sin^2 \phi \cdot \sin^2 \psi + \\ & + \epsilon_{13} \cdot \cos \phi \cdot \sin 2\psi + \epsilon_{23} \cdot \sin \phi \cdot \sin 2\psi + \epsilon_{33} \cdot \cos^2 \psi \end{aligned} \quad (4.11)$$

Where $\epsilon_{\phi\psi}$ is the deformation measured as a function of the angles ϕ and ψ , and ϵ_{11} , ϵ_{12} , ϵ_{22} , ϵ_{13} , and ϵ_{33} are the components of the strain tensor at the sample coordinates S_1 , S_2 , and S_3 . Being ϕ the rotation angle around the normal of the sample (S_3), and ψ the inclination angle respect to the normal of the sample within a plane defined by L and S_3 .

The Equation 4.11 can be easily obtained by the unit vector $h_{\phi\psi}$ in the direction of $\epsilon_{\phi\psi}$ expressed in the coordinates of the sample, the unit vector being expressed in Equation 4.12:

$$h_{\phi\psi} = \begin{bmatrix} h_1^{\phi\psi} \\ h_2^{\phi\psi} \\ h_3^{\phi\psi} \end{bmatrix} = \begin{bmatrix} \cos \phi \cdot \sin \psi \\ \sin \phi \cdot \cos \psi \\ \cos \psi \end{bmatrix} \quad (4.12)$$

In this way, the relationship between the measured strain $\epsilon_{\phi\psi}$ and the strain tensor can be expressed by Equation 4.13.

$$\epsilon_{\phi\psi} = \epsilon_{ij} \cdot h_i^{\phi\psi} \cdot h_j^{\phi\psi} \quad (4.13)$$

This equation is the simplified form of Equation 4.11, and can be obtained by expanding this equation for the strain values 1, 2 and 3 in i and j . Also, the strains can be also expressed by Equation 4.14:

$$\epsilon_{\phi\psi} = \frac{d_{\phi\psi} - d_0}{d_0} = \frac{\lambda}{2 \cdot d_0 \sin \theta - 1} \approx \Delta\theta \cdot \theta_0 \quad (4.14)$$

Equation 4.11 is a linear expression of the strain tensor components. The strain tensor can be obtained solving the linear equation if the six independent strains are measured, or by least squares linear regression if there are more than six independent measurements. In order to obtain a reliable solution, independent strains must be measured in different orientations.

The stresses can be determined from the measured strains using Hooke's Law for homogeneous and isotropic materials by Equation 4.15 or Equation 4.16 for anisotropic materials.

$$\begin{aligned} \epsilon_{\phi\psi} = & -\frac{\nu}{E}(\sigma_{11} + \sigma_{22} + \sigma_{33}) + \frac{1 + \nu}{E}(\sigma_{11} \cos^2 \phi + \sigma_{12} \sin 2\phi + \sigma_{22} \sin^2 \phi) \sin^2 \psi + \\ & \frac{1 + \nu}{E}(\sigma_{13} \cos \phi + \sigma_{23} \sin \phi) \sin 2\psi + \frac{1 + \nu}{E}\sigma_{33} \cos^2 \psi \end{aligned} \quad (4.15)$$

$$\begin{aligned} \epsilon_{\phi\psi}^{hkl} = & S_1^{hkl}(\sigma_{11} + \sigma_{22} + \sigma_{33}) + \frac{1}{2}S_2^{hkl}(\sigma_{11} \cos^2 \phi + \sigma_{12} \sin 2\phi + \sigma_{22} \sin^2 \phi) \sin^2 \psi + \\ & \frac{1}{2}S_2^{hkl}(\sigma_{13} \cos \phi + \sigma_{23} \sin \phi) \sin 2\psi + \frac{1}{2}S_2^{hkl}\sigma_{33} \cos^2 \psi \end{aligned} \quad (4.16)$$

Where $\epsilon_{\phi\psi}^{hkl}$ is the measured strain of the specific lattice plane hkl in the direction defined by ϕ and ψ , and S_1^{hkl} and $\frac{1}{2}S_2^{hkl}$ are the elastic constants of the X-rays for the lattice plane.

Being the depth of penetration of the X-rays limited, the normal deformation on the surface of the sample can be considered negligible, $\sigma_{33} = 0$, since the surface is in plane stress conditions. The components of the stress along the L direction (Fig. 4.6) are the normal stress σ_ϕ and the shear stress τ_ϕ , and are obtained by the components of the stress tensor at the coordinates of the sample by Equation 4.17 and 4.18:

$$\sigma_\phi = \sigma_{11} \cos^2 \phi + \sigma_{22} \sin^2 \phi + \tau_{12} \sin 2\phi \quad (4.17)$$

$$\tau_\phi = \sigma_{13} \cos \phi + \sigma_{23} \sin \phi \quad (4.18)$$

Then, the equation for the measured strain can be simplified into the Equation 4.19, and Equation 4.20 for biaxial stress state.

$$\epsilon_{\phi\psi}^{hkl} = S_1^{hkl}(\sigma_{11} + \sigma_{22}) + \frac{1}{2}S_2^{hkl}\sigma_\phi \sin^2 \psi + \frac{1}{2}S_2^{hkl}\tau_\phi \sin 2\psi \quad (4.19)$$

$$\epsilon_{\phi\psi}^{hkl} = S_1^{hkl}(\sigma_{11} + \sigma_{22}) + \frac{1}{2}S_2^{hkl}\sigma_\phi \sin^2 \psi \quad (4.20)$$

For a given sample, the measured strain is a linear function of $\sin^2 \phi$. Obtaining the first derivative respect to $\sin^2 \phi$, the Equation 4.21 can be reached, where M is the slope of the strain measured on the graph $\epsilon_{\phi\psi}^{hkl} - \sin^2 \psi$.

$$\frac{\partial \epsilon_{\phi\psi}^{hkl}}{\partial (\sin^2 \psi)} = \frac{\partial d_{\phi\psi}^{hkl}}{\partial (\sin^2 \psi)} = \frac{1}{2}S_2^{hkl}\sigma_\phi = M \quad (4.21)$$

Therefore, from Equation 4.22 the stress can be obtained with the macroscopic elasticity constants:

$$\sigma_\phi = \frac{M}{\frac{1}{2} \cdot S_2} = \frac{M \cdot E}{1 + \nu} \quad (4.22)$$

The graph of $d_{\phi\psi}$ versus $\sin^2 \psi$ for a value ϕ is a characteristic representation in the calculation of RS by XRD. Depending on the type of shape obtained by the graph, different cases can be distinguished (Fig. 4.7).

If the material is isotropic and has a bi-axial stress state, the graph takes the shape of a straight line, as depicted in Figure 4.7a. This is the ideal situation.

When the grains of the material are large ($> 100\mu\text{m}$), the irradiated area contains a small number of grains, thus, a small number of diffracting crystals. This makes the diffraction peak very irregular, obtaining a big dispersion in the measured values as shown in Figure 4.7b. In these cases, better results can be obtained enlarging the irradiated area (increasing the number of grains), using oscillation.

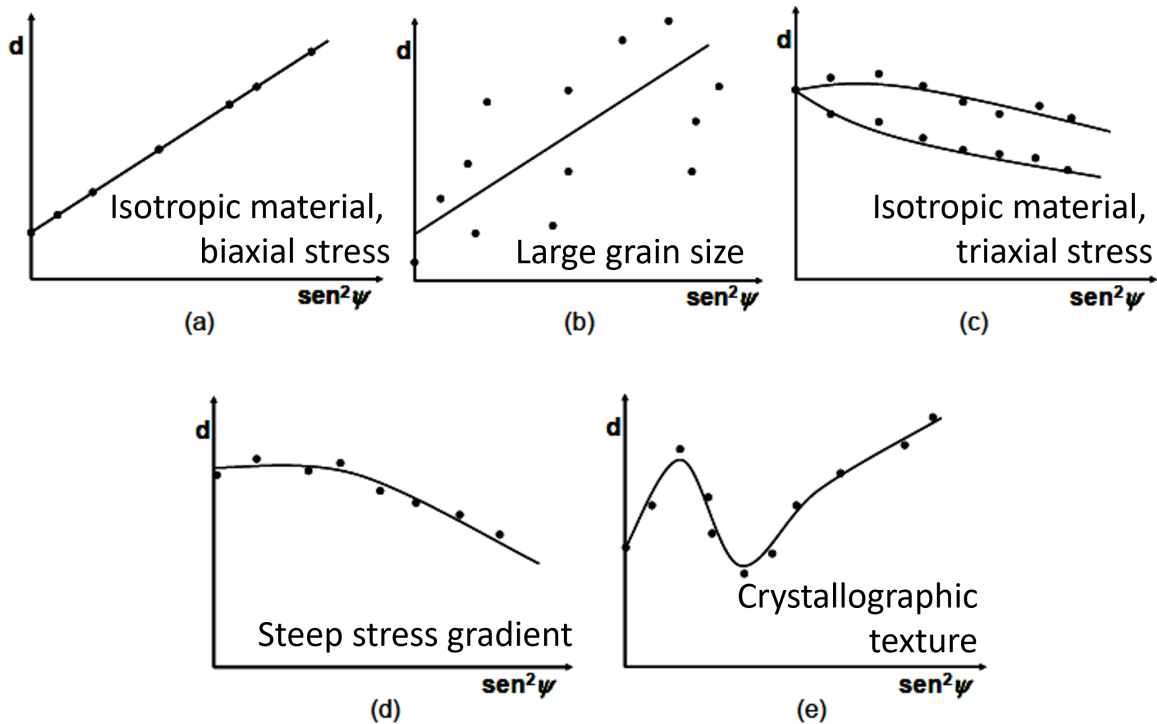


FIGURE 4.7: Different scenarios of $d_{\phi\psi}$ vs. $\sin^2\psi$ curves: a) isotropic material, with a biaxial state of stress; b) material with large grain size; c) isotropic material, with triaxial stress state; d) material with steep stress gradient; e) material with preferential crystallographic texture [19].

For isotropic materials with a triaxial stress state, considering Equation 4.15, the graph takes different values for positive ψ and negative ψ (Fig. 4.7c). This is often called, ψ - *splitting*.

Gradients in the composition and/or stresses give the graph a parabolic shape, as illustrated in Figure 4.7d, which is difficult to explain with the equations above described, requiring other methods.

Finally, if the material is not isotropic and the elastic constants vary for the different angles, waving shapes appear in the $d_{\phi\psi}$ versus $\sin^2\psi$ graph (Fig. 4.7e). This is very common for

materials with crystallographic texture, and require measurements of the elastic constants for the different orientations [255].

Based on the $\sin^2\psi$ technique, there are two variants of the XRD method depending on the sample rotation (Fig. 4.8). The Omega (Ω) method, is the most common method for most conventional diffractometers and the sample rotates around the Ω axis. On the contrary, the Chi (χ) method is mechanically more complex and the sample rotates around the χ axis. .

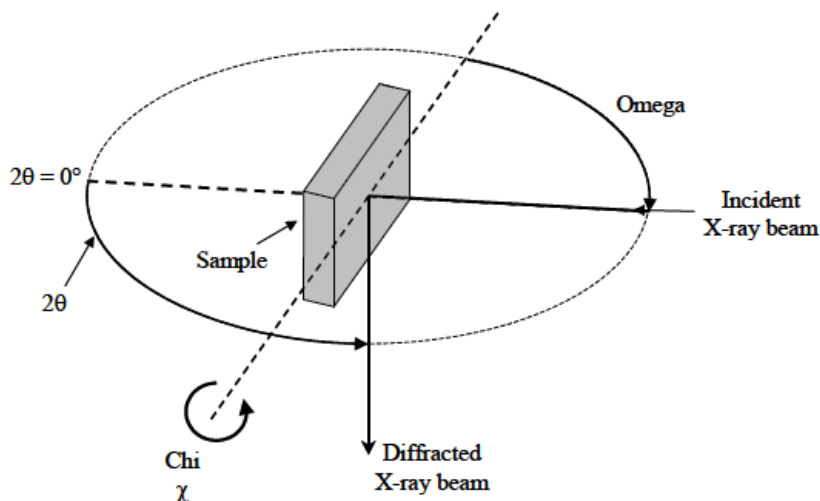


FIGURE 4.8: Sample rotations possibilities for measuring stresses by XRD.

The X-ray penetration distance from the surface is limited to few microns [16] so, in order to reach the stresses beneath the surface, thin layers of material must be removed and the method becomes destructive to a certain extent. The material removal is performed by electropolishing to alter minimally the stress state of the material. This is based on the first Faraday's Law, which establishes that the mass of material removed (Δm) is proportional to the intensity (ΔI^+) that exists over a period of time (Δt), being k the electro-chemical equivalent of the sample material, as defined in Equation 4.23.

$$\Delta m = k \Delta I^+ \Delta t \quad (4.23)$$

4.2.3 Discussion upon MIRS measurement methods

In the present work, MIRS on aluminium and titanium aerospace alloys are measured and analyzed, for their later use in Chapter 5 as input data.

Regarding which measuring method is best to perform the measurements, iHD or XRD, the main differences relate to being destructive or non-destructive, and their availability, cost and accuracy. For measuring in-depth MIRS profiles, the destructiveness is similar for both, thus, this does not represent a factor for selection. Regarding availability, although in general terms iHD rigs are more available than XRD equipments, there is an XRD measuring equipment at projects' disposal. This translates to the cost, which in this case is very similar (although in general XRD is more expensive than iHD). Finally, the accuracy comparison is not straightforward.

One way to assess the accuracy of different stress measuring methods consists on evaluating the uncertainty ranges for them. Again, this depends on different contributors, including factors arising from the component, measuring process, equipment and operator. While for the iHD there are guides to calculate uncertainty ranges (Table 4.1) [189], the XRD depends very much on the actual grain arrangement of the measured material.

TABLE 4.1: Uncertainty ranges for the iHD in Al-alloy and Ti-alloy, calculated according to [189].

Depth range [mm]	Al7050-T7451	Ti6Al4V
0-0.008	± 27	± 43
0.008-0.256	± 5	± 27
0.256-0.512	± 10	± 18

In fact, the XRD method only provides reliable results when no preferential crystallographic texture is present. When this is present, the integrated diffraction intensity varies for different ϕ, ψ angles. According to the BS EN 15305:2008 Standard [190], strongly textured materials should be excluded. In this way, preliminary XRD measurements were performed in both materials to analyze if these issues could occur. In the case of the aluminium samples, intensity ratios higher than the limit set in the standard were found (Fig. 4.9a). Due to this, Figure 4.9b shows that the $d_{\phi\psi}$ versus $\sin^2 \psi$ plot of these measurements took the shape of the theoretical textured material, depicted in Figure 4.7e.

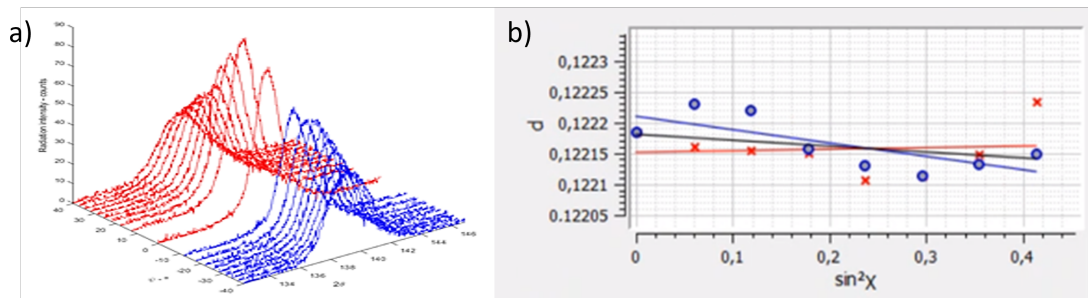


FIGURE 4.9: XRD measurement in Al7050-T7451 showing texture: a) Diffraction peaks of different intensities; b) $d_{\phi\psi}$ versus $\sin^2 \psi$ graph showing the typical curved shape.

For this reason, it is decided to use the iHD as preferred method for MIRS measurement in aluminium within this study.

In the case of titanium, and considering not only the availability of the measuring equipment, but also the possibility to perform repeated measurements, which improve the accuracy, the XRD method is chosen as the preferred method. Furthermore, in order to perform an accuracy assessment, also iHD measurements are performed in titanium for subsequent inter-method comparison.

4.3 Aluminium MIRS measurement by iHD

In this section MIRS measurements are performed for their use in two different analysis carried out in Chapter 5 . One corresponds to the experimental verification of the BIRS characterization in ribbed geometries by on-machine LR, and it is performed in Al 7050-T7451 samples. The other one is for the distortion calculation in a real-part of Al 7175-T7351.

4.3.1 Materials and procedure for machining test

The materials used for the study are the aluminium alloys Al 7050-T7451 and Al 7175-T7351, whose chemical composition and properties are shown in Tables 4.2 and 4.3.

TABLE 4.2: Chemical composition of Al-alloys 7050-T7451 and 7175-T7351.

% Weight	Al	Zn	Cu	Mg	Fe	Zr	Si	Ti	Cr	Mn	Other, each
Al7050-T7451	Base	5.7-6.7	2-2.6	1.9-2.6	<0.15	0.08-0.15	<0.012	<0.06	<0.04	<0.010	<0.05
Al7175-T7351	Base	5.1-6.1	1.2-2	2.1-2.9	<0.2	-	<0.15	<0.10	0.18-0.28	<0.010	<0.05

TABLE 4.3: Mechanical properties of Al-alloys 7050-T7451 and 7175-T7351.

Properties	Density (g/m ³)	Hardness (HRb)	Young Mod. (GPa)	Poisson coef. (-)
Al7050-T7451	2.83	140	71.7	0.33
Al7175-T7351	2.8	135	71.7	0.33

The dimensions of the Al 7050-T7451 part were $400 \times 200 \times 31.3\text{mm}$, and the dimensions of the Al 7175-T7351 part were $665 \times 100 \times 66\text{ mm}$.

The machine-tool used was a Soraluze FMT multitasking machine. The machining process was a face milling process, with a milling strategy following corners outwards (Fig. 4.10), where all passes were made in up milling.

The cutting tools are introduced in Table 4.4, which are specific for aluminium alloys. Tool A1 is a tool suitable for roughing with 3 inserts and a big diameter for achieving high material removal rate (MRR). Tool A2, instead, is an end mill of 3 edges, specific for performing finishing operations. The diameter of the tool is selected as a compromise between minimal pocket radius and maximal MRR. Table 4.5 shows the cutting conditions used with each tool. Coolant is not used.

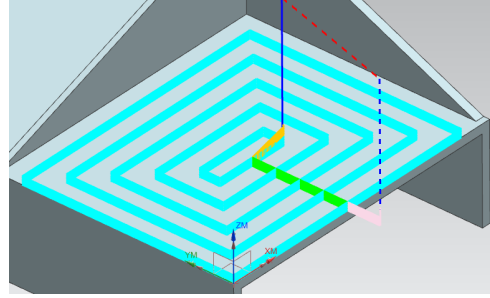


FIGURE 4.10: Face milling process, helical outwards strategy in up/down milling.

TABLE 4.4: Tools used for inducing the MIRS in the aluminium parts.



Cutting Tools		
	Tool A1	Tool A2
Brand	Ceratizit	Ceratizit
Reference	AHPC.40.R.03-19 / XDHX 190404 FR-27P	W.H-SA.16,0.45.Z3.R1,0.HA.K TI1005
Edge number	3	3
Diameter	40 mm	16 mm
Image		

TABLE 4.5: Cutting parameters used with Tool A1 and Tool A2.

Parameter	Al 7050-T7451 part	Al 7175-T7351 part
Cutting speed – v_c (m/min)	500	200
Feed per tooth – f_z (mm/z)	0.1	0.16
Axial depth of cut – a_p (mm)	1	0.5
Radial depth of cut – a_e (mm)	30	8

4.3.2 iHD measurement procedure

As mentioned, due to the high crystallographic texture of the aluminium specimens XRD measurements are not performed. Thus, iHD measurements are outsourced to the company Stresscraft.

For the measurement to a maximum depth of 0.512mm, the type of strain gauges used in the Al 7050-T7451 parts are EA-13-031RE-120 and in the Al 7175-T7351 are EA-06-031RE-120, both of the manufacturer Vishay Precision Group. The measuring procedure followed is here described:

1. Pre-drilling: Target surfaces were prepared for gauge installation. Two passes of fine (400 grade) SiC paper followed by degreasing (acetone) and then local etching (ortho-phosphoric acid) followed by neutralization (dilute ammonia). Then, gauges were bonded using Loctite 407 adhesive, after performing the part alignment. A loading and unloading of the plate prior to drilling was used to demonstrate the satisfactory nature of the gauge bonds.
2. Drilling: The part was fixed (cemented) to perform the orbital drilling in each gauge using an inverted cone tungsten carbide cutter with a pre-set orbital eccentricity (one cutter per hole). Datum depth detection at each hole is carried out using an iterative command in the drill control software to advance the rotating drill bit in 0.002 mm increments. Between successive advances, orbit and withdrawal movements were carried out so that the target site could be inspected for penetration through the gauge backing material and adhesive layer. Orbital drilling was carried out using depth increments set at $4 \times 16 \mu\text{m} + 4 \times 32 \mu\text{m} + 8 \times 64 \mu\text{m}$ to give a final hole depth of 0.704 mm, for stress data to 0.512 mm.
3. Post-drilling: Final hole diameters were measured using an optical head. Relaxed strain data was reduced to stresses using the Integral Method [189]. Within the data reduction program, the strain data was subjected to a smoothing process and, then, reduced to stress components at selected depth increments.

4.3.3 iHD Results

iHD measurements were performed in different locations within the machined surface corresponding to different uncut chip thickness. In the Al7050-T7451 part, these locations are depicted in Figure 4.11.

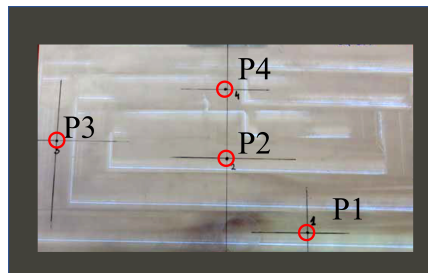


FIGURE 4.11: MIRS measuring points in the Al 7050-T7451 part.

Figure 4.12 shows the measured MIRS profiles for the four different locations, where the error bars correspond to the iHD measurement uncertainty calculation according to [189]. As it can be seen, compressive shallow (0.05mm penetration depth) MIRS are induced using these machining conditions in the two spatial directions, where the highest uncertainty is near the surface. This uncertainty for some of the points is above the stress value. Moreover, the highest variability is in the feed direction.

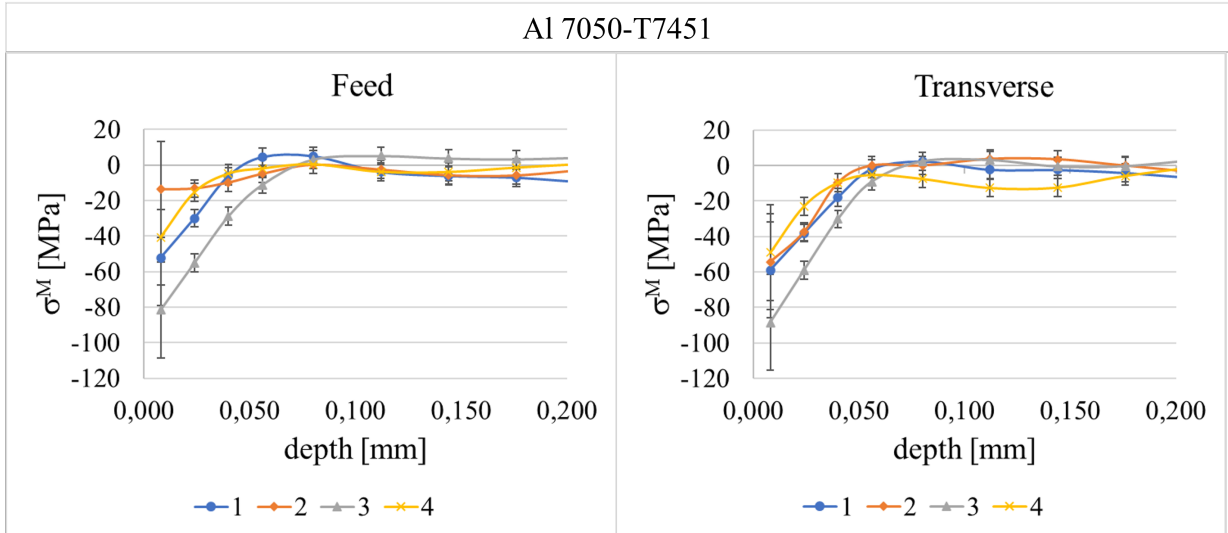


FIGURE 4.12: MIRS measured in the Al 7050-T7451 part by iHD in four different locations.

Figure 4.13 shows the average MIRS of the four locations, where the error bars represent the variability of stresses linked to measurement location (standard deviation) at each depth and direction. Although the high variability in relation to the stress magnitude, both perpendicular directions show similar stress curves.

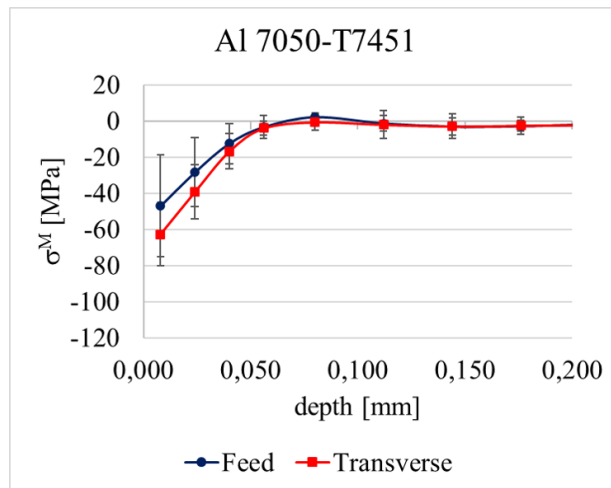


FIGURE 4.13: Average MIRS measured in the Al 7050-T7451 part by iHD.

Regarding the Al7175-T7351 part, the measuring locations are depicted in Figure 4.14, where measurements in the two parallel machined surfaces (pocket side and ribbed side) are taken (Fig. 4.15).

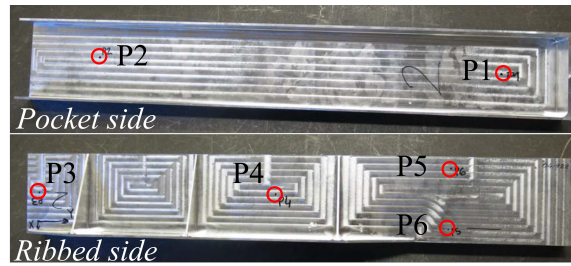


FIGURE 4.14: MIRS measuring points in the Al 7175-T7351 part.

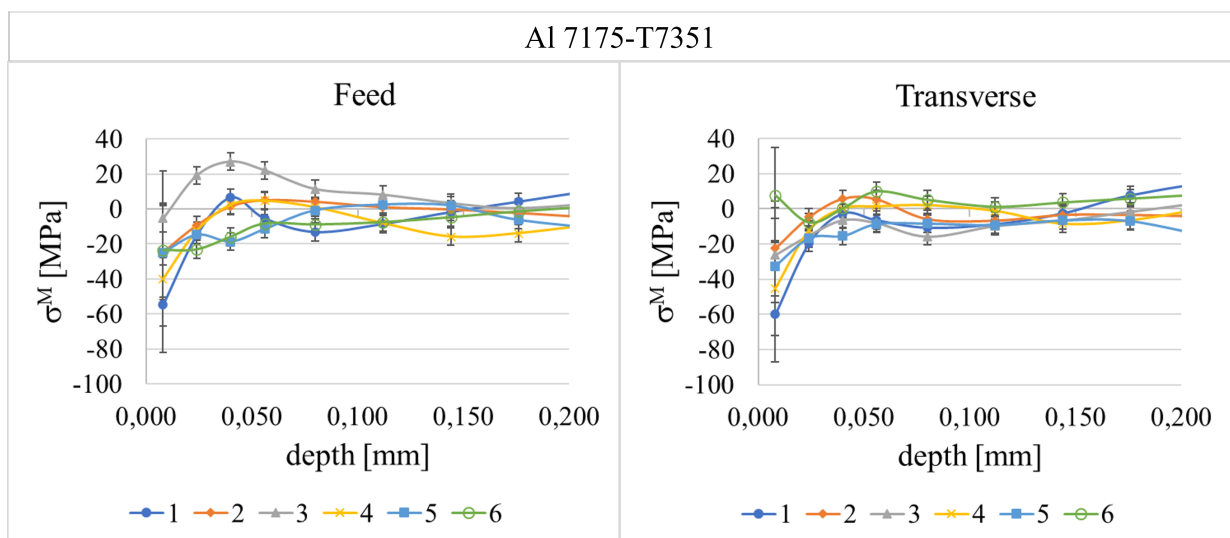


FIGURE 4.15: MIRS measured in Al 7175-T7351 parts by iHD in six different locations.

Averaging the MIRS of the six locations, Figure 4.16 shows the MIRS, where the error bars represent the variability of stresses linked to measurement location (standard deviation) at each depth and direction.

Also in this case, both perpendicular directions show similar stress curves.

In both parts, compressive shallow (0.05mm penetration depth) MIRS are induced. While the maximum amplitude of stresses for the Al 7050-T7451 part is -60 MPa, for the Al 7175-T7351 this is approximately -30 MPa. The reason for this values is probably because the cutting conditions for in the Al 7050-T7451 part are for roughing (linked to the LR experimental verification of Chapter 5) and the machining conditions of the Al 7175-T7351 part are for finish machining a real part (linked to the distortion prediction of Chapter 5). Besides, in both cases the amplitude and penetration of the averaged MIRS in two spatial directions (feed and transversal) is similar.

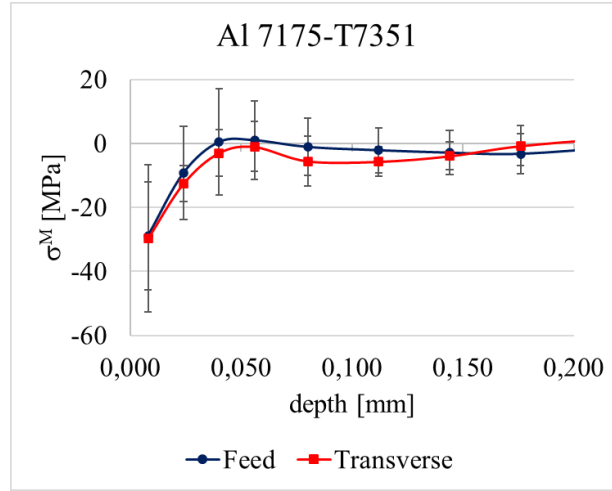


FIGURE 4.16: Average MIRS measured in the Al 7175-T7351 parts by iHD.

4.4 Titanium MIRS measurement: uncertainty assessment

In this section, MIRS in titanium parts are measured by two methods, iHD and XRD. The accuracy of XRD is evaluated in two different ways, internally with a repeatability and reproducibility analysis, and externally, against the measuring method iHD.

4.4.1 Materials and procedure for machining test

The material used for the study is the bi-phase Ti6Al4V alloy. The Tables 4.6 and 4.7 show the chemical composition and properties of this alloy:

TABLE 4.6: Chemical composition of Ti6Al4V alloy.

% Weight	Ti	Al	V	Fe	O	N	Y
Ti6Al4V	Base	5.5-6.75	3.5-4.5	<0.3	<0.2	<0.08	<0.005

TABLE 4.7: Mechanical properties of Ti6Al4V alloy.

Properties	Density (g/m ³)	Hardness (HB)	Young Mod. (Gpa)	Poisson coef. (-)
Ti6Al4V	4.43	334	120.2	0.36

The part dimensions were $270 \times 180 \times 30$ mm. The machine-tool used for the milling test is the multitasking machine Soraluca FMT. The machining process is a face milling process, with a Zig machining strategy (Figure 4.17).

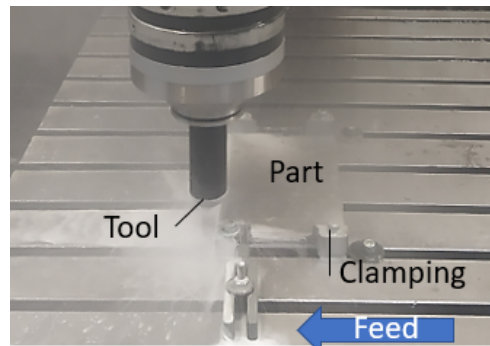
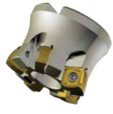


FIGURE 4.17: Face milling process, Zig strategy.

The cutting tool used is defined in Table 4.8.

TABLE 4.8: Tools used for inducing the MIRS at different cutting conditions.

Tool T1	
Brand	Kennametal
Reference	7793VXO12 (Inserts X500)
Edge number	5
Diameter	63 mm
Image	

Tool T1 is a high feed tool suitable for roughing with 5 inserts and a 63mm diameter for achieving high material removal rate (MRR). Table 4.9 shows the cutting conditions used with this tool.

TABLE 4.9: Cutting parameters used with tool T1.

Tool T1	
v_c	54
f_z	0.8
a_p	1
a_e	37.625

Due to the low machinability of titanium, tool wear can rapidly occur. Therefore, coolant is used to minimize the tool wear generation during machining and, during the test, the average flank wear (VB) was monitored avoiding values over 0.07mm.

4.4.2 XRD Measuring Procedure

This section describes the equipment and procedure used to get the MIRS profiles by XRD. Also, two evaluations of the XRD technique are included. One by inter-method

comparison against iHD method, and the other with a Repeatability and Reproducibility (RR) analysis.

The XRD measurements are performed with a Xstress 3000 G2R X-ray diffractometer (Fig. 4.18a). The equipment consists of a goniometer, a X-ray main unit and a XY movement table. Table 4.10 summarizes its main features. Also, an electropolishing machine was used to perform the in-depth measurements (Fig. 4.18b). The electrolytic liquid required to remove the Ti6AL4V material is the A3 type (Struers), which has a chemical composition of Methanol (55-75 %) and 2-Butoxyethanol (25-45 %).

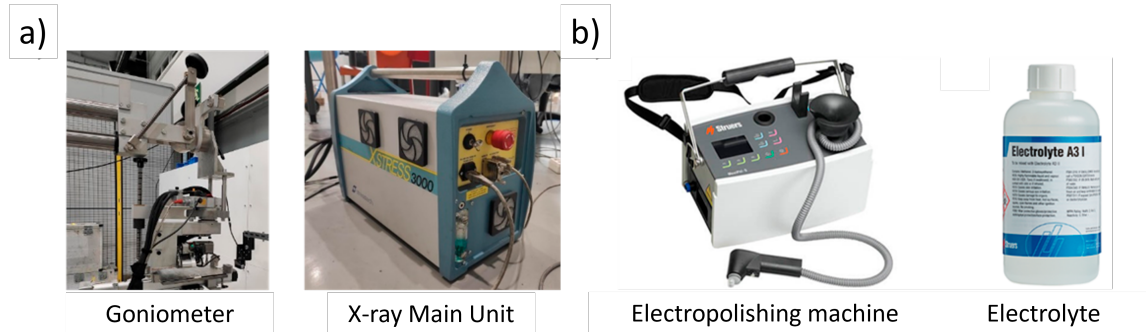


FIGURE 4.18: XRD equipment: a) Diffractometer including goniometer and main unit; b) Electropolishing machine and electrolyte.

TABLE 4.10: XRD equipment features: diffractometer and electropolishing machine.

X-ray diffractometer	
Brand	- Stresstech
Model	- Xtress 3000 G2R
Software	- Xtronic
Control Unity	- X-ray Voltage: 5-30kV / Intensity: 0-6.7 mA
Goniometer	- ψ Tilt: -45° to 45° programmable - ψ Oscillation: 0° to $\mp 6^{\circ}$ programmable - ϕ Rotation: $\mp 180^{\circ}$ optional
Other features	- Portable equipment - Rotation enables bi-axial and tri-axial stress state determination - Measurement methods: $d - \sin^2\chi$ and Ω
Electropolishing machine	
Brand	- Struers
Model	- MoviPol-5
Other features	- Electropolishing area of 9 mm^2

Considering that the material removal by electropolishing depends upon the voltage, flow-rate and time, keeping fixed the first two variables, the amount of material removed becomes proportional to the electropolishing time (Eq. 4.23).

Figure 4.19a shows a curve for the electropolishing depth versus time, where the dots represent the measured depth values and the dashed line the linear regression. As it can

be seen, the good linearity of the evolution enables a good control of the depth. Figure 4.19b illustrates the electropolishing process, in which the circular area inside a nozzle of the electropolishing machine is to be removed. If successive electropolishing sequences are performed for in-depth measurements, this location must be kept constant.

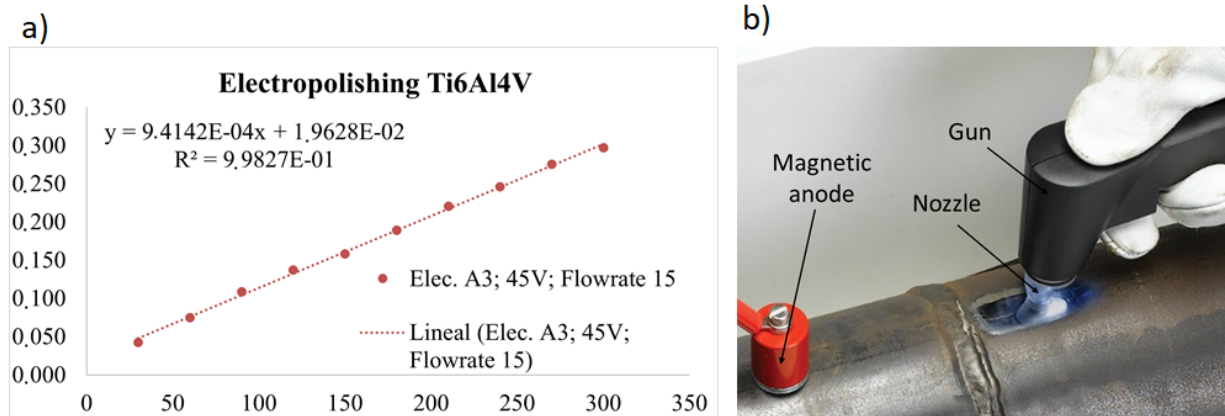


FIGURE 4.19: a) Electropolishing depth vs. time for a fixed set of variables; b) Electropolishing process.

Figure 4.20 shows the area of the footprint formed by the removal of the material to a depth of 0.12 mm after four electropolishing iterations.



FIGURE 4.20: Footprint after electropolishing at 0.12 mm depth after four iterations.

The XRD measurement consist of three phases: preparation of the measurement system, acquisition of diffraction patterns and data treatment for stress evaluation.

First, the preparation of XRD equipment consist of selecting the appropriate X-ray tube for the material to be measured. Despite the extended use of the copper (Cu) tube in Ti6Al4V [256], a titanium (Ti) tube was selected due to the recommendation of the equipment manufacturer. Linked to this, the 2θ angle, which depends on the combination of material, tube and crystallographic plane, is set for each of the detectors (Fig. 4.21). In the case of Ti-tube and Ti-alloy material, the angle between the detectors is 137.5° , being the measurement plane (110) [257].

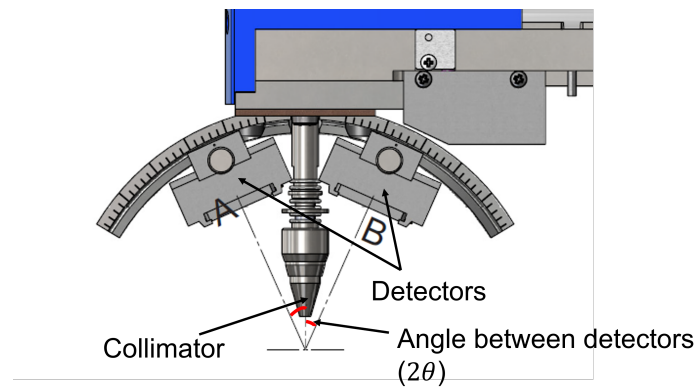


FIGURE 4.21: Detectors and collimator of the diffractometer.

Secondly, the calibration of the equipment is performed with a stress-free sample, in which the distance between the collimator tip and the sample surface is determined. The calibration is considered acceptable when the measured stress in the stress-free sample is below the established threshold value, typically 8MPa.

Thirdly, measurements in a high-stress reference sample on the same material are taken. This is not mandatory to perform a measurement, but enables one last verification. Table 4.11 shows both the nominal values of the high-stress titanium reference sample given by the XRD equipment manufacturer and the results measured using the diffractometer.

TABLE 4.11: Comparison between the experimental results and nominal values of the titanium high-stress titanium reference.

Rotation	σ [MPa]	τ [MPa]	FWHM [°]
Experimental			
0	-396.1 ± 9.0	-17.4 ± 1.5	3.00 ± 0.09
90	-393.5 ± 13.8	14.9 ± 2.5	3.00 ± 0.15
Theoretical			
0	-425.0 ± 26.0	1.0 ± 7.0	3.9 ± 0.17
90	-435.0 ± 15.0	4.0 ± 2.0	3.90 ± 0.15

Results show that the values measured with the diffractometer are close to the tolerances defined by the standard pattern, where the differences could be related to the threshold value used for the calibration and alignment. Despite this, the differences in the principal stresses are below 10% of the nominal value, thus the measurements are considered acceptable [257].

Once the XRD equipment is ready, measurements data is gathered and treated. The data treatment can be divided in three categories: adjustment of the intensity peak, analysis and correction, and others actions.

Adjustment of the intensity peak: the accuracy of the peak location (2θ) from which the stress is calculated greatly depends on the fitting of the diffraction data gathered by the receptors. This can be performed using local methods, which only use a part of the intensity distribution; and global methods, which use the entire intensity distribution. Focusing on global methods, cross correlation and peak fit to a mathematical function are the most used solutions. The most used mathematical functions to adjust the diffraction intensity peak are Gauss, Lorentz, Pearson VII and Pseudo-Voigt. In this study, the Pearson VII function (Fig. 4.22) is considered as it fitted best the intensity peaks.

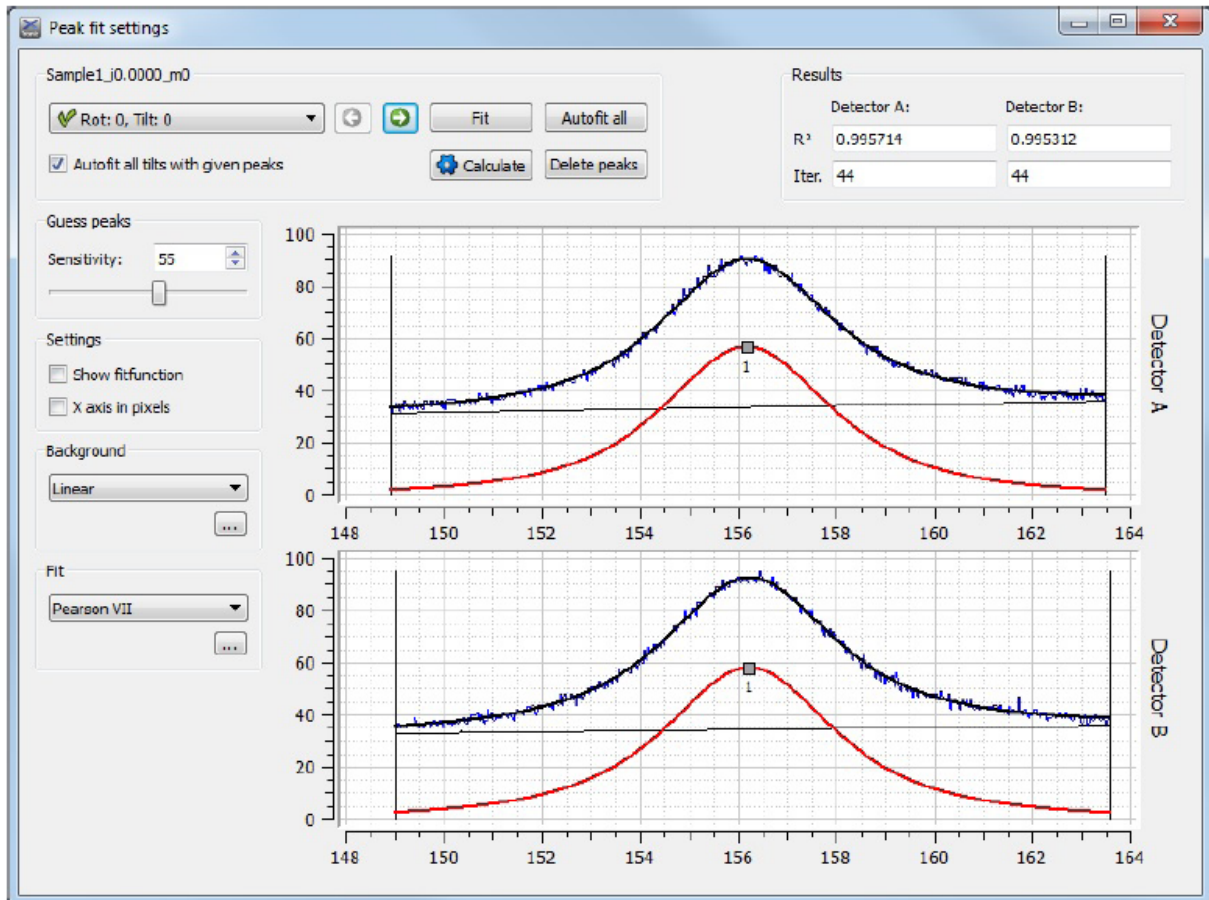


FIGURE 4.22: Peak fit method settings using a Pearson VII function.

Analysis and correction: according to the BS EN15305:2008 Standard [190], a critical assessment of the results must be performed, in which peak overlap is not observed by visual inspection. Besides, if large changes in intensity are observed, which are indicative of a highly textured material, deactivation of specific tilts and rotations is performed. Nevertheless, this must be done carefully not to reduce the measurement accuracy, and only in materials in which for the complete data set the ratio of the integrated intensity is smaller than 3.

Other actions: in a sample with a steep macro-stress gradient at the surface, the 2θ peak values for $\psi = 0$ and $\psi \neq 0$, represent the weighted averages for the in-depth layers [257].

In such case, the obtained stress does not only reflect the average stress due to the stress gradient, but the effect of the difference in the layer thickness at the ψ angles. This way, the measured stress gradients are corrected by the software (Fig. 4.23) [258]. The correction effect is only significant when the stress gradient is greater than $50 \text{ MPa}/\mu\text{m}$ [257].

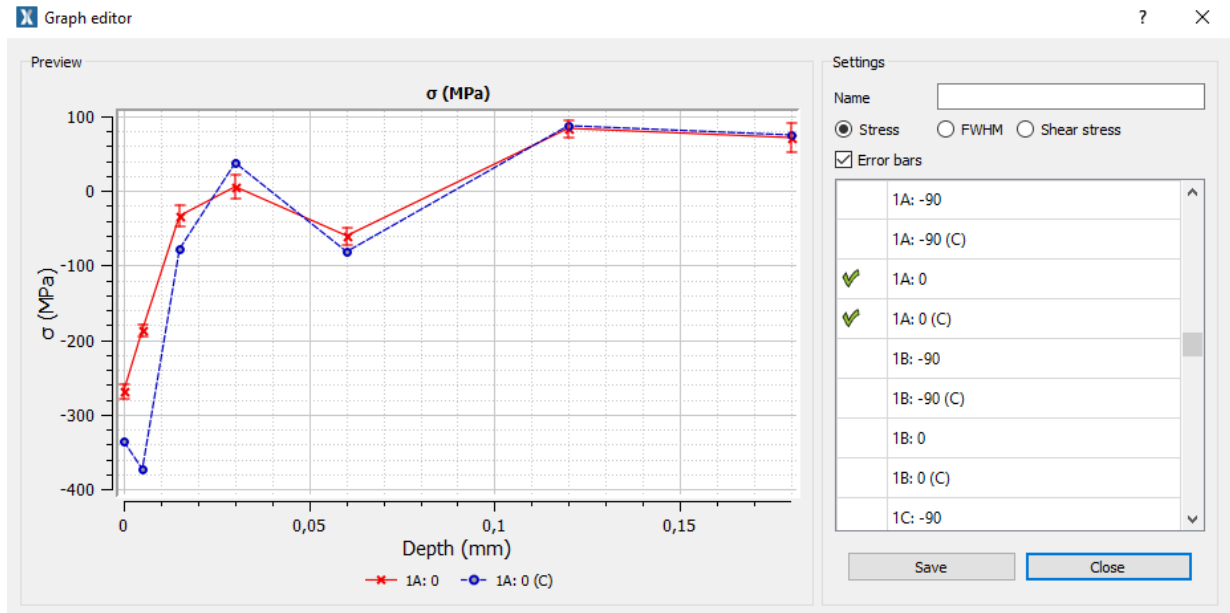


FIGURE 4.23: Example of a corrected, 1A:0(C), and non-corrected, 1A:0, stress profile.

4.4.3 Repeatability and Reproducibility (RR) study of surface MIRS measured by XRD

The RR study aims at determining the XRD measurement error budget corresponding to the equipment, different locations measurement and operators. This way, three measurement points on a surface machined with the cutting conditions v_c 70m/min, f_z 0.03mm, a_e 11.67mm, and a_p 0.5mm are analyzed. The variability of the equipment and measuring point location within the same line (approximately the point of maximum chip thickness) is analyzed (Fig. 4.24).

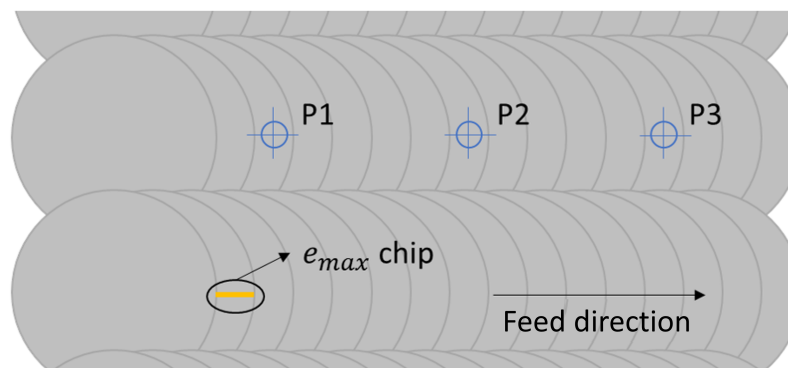


FIGURE 4.24: Measured points sketch for the RR study.

The XRD measuring parameters employed can be seen in Table 4.12, and Table 4.13 gathers the measurements of the three points in the feed direction measured by two operations (A and B).

TABLE 4.12: XRD measuring parameters used for the RR study.

XRD method measurement parameters	
Material / X-ray tube	Ti (110) 137.5° / Ti-tube
Young Modulus E [GPa]	115
Poisson ratio ν	$\nu=0.32$
Exposition time [s]	20
Collimator diameter [mm]	4
Rotation ψ angle [°]	0
Tilt ϕ angles [°]	5/5
Tilt ϕ angle range [°]	-39/39
Tilt ϕ angle oscillation [°]	± 6
Measurement mode	χ modified
X-ray voltage [kV]	30
X-ray intensity [mA]	8
Maximum penetration depth [mm]	0

TABLE 4.13: MIRS measured at 3 different locations (P1, P2, P3) by 2 operators.

σ [MPa]		Points		
		P1	P2	P3
Operators	A	-325.7	-427.4	-417.4
		-311.4	-430	-419.1
		-304.4	-423.4	-420.4
		-300.5	-423.5	-417.4
	B	-367	-497.1	-465.4
		-358.8	-498.3	-469
		-363.1	-492	-472.8
		-361.9	-498.7	-468.7

The results obtained following the procedure of [259] are graphically illustrated in Figure 4.25, where the values of the surface MIRS measurements are displayed with their variability range.

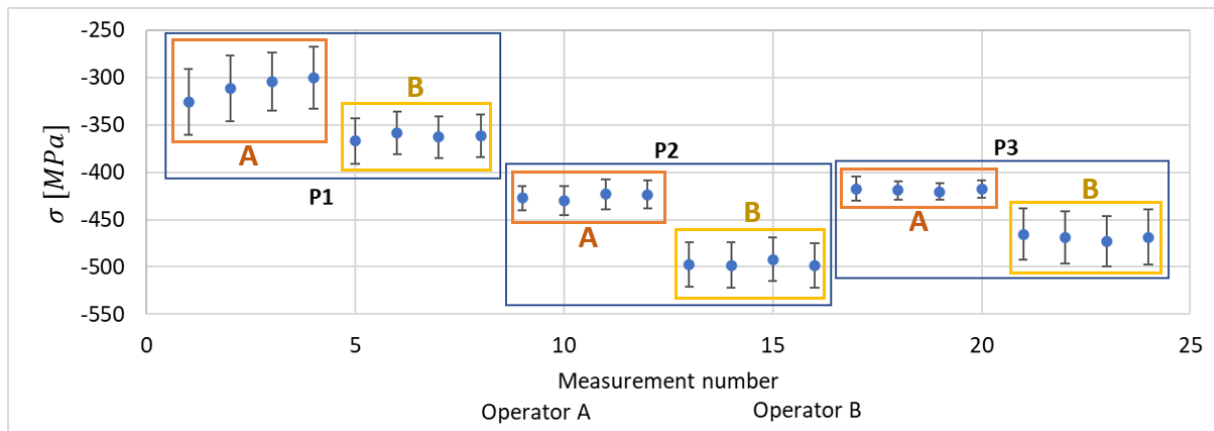


FIGURE 4.25: Variability of the measurements made at different points and by different operators.

Looking at the graph, the good repeatability of the measurement system can be seen. Theoretically, the uncertainty of the XRD method is approximately ± 20 MPa [19], which is very close to the value achieved in this study for the same point by the same operator, i.e. 46 MPa, and also to the mean uncertainty of all measurements of the RR study ± 18.5 MPa. However, for different operators this raised to 100 MPa. In fact, there is a poor reproducibility for the three points, which might be due to the work-piece material and the variabilities in the MIRS values at different locations [53, 260, 261]. In summary, while the repeatability of the system is good, the high variability of the stresses at different specimen locations (of similar chip thickness) appears to be affected by their positions on the plate, as well as, the influence of the milling cutter and the cutting direction at each point. This is an important factor to consider when using MIRS data in distortion simulation.

4.4.4 Inter-method comparison for in-depth MIRS measurements: iHD vs. XRD

Once the error budget of the XRD equipment was quantified for surface MIRS, in-depth MIRS profiles were evaluated. To do that, the accuracy of the XRD method against iHD is analysed.

Three measuring locations within the surface of the test-part are selected (Fig. 4.26a), where the red circles refer to the measurements made by XRD and the black squares to those of iHD. Again, each pair of measurements under comparison were aligned to refer to the same chip thickness. This way, the stresses at 0° angle rotation correspond to the feed direction, and 90° to the perpendicular direction (Fig. 4.26b).

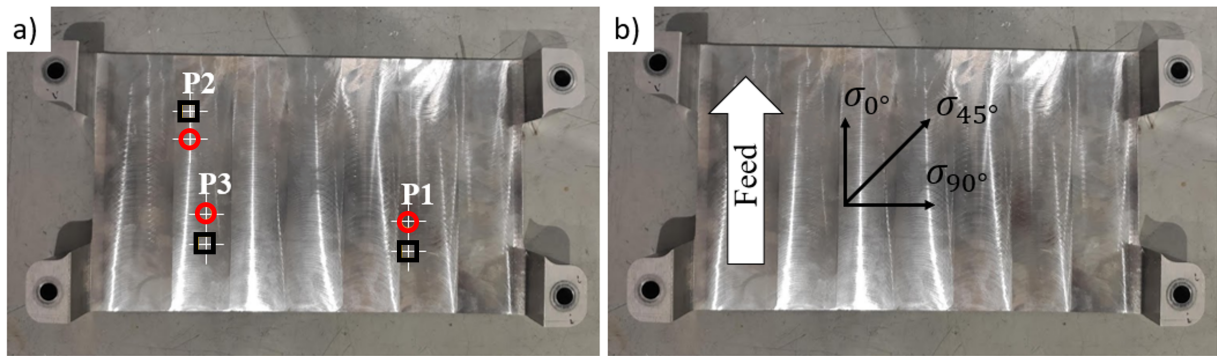


FIGURE 4.26: Locations and directions for in-depth MIRS measurements by XRD and iHD methods: a) point locations; b) directions.

4.4.4.1 XRD measurements

For the XRD measurements, the parameters displayed in Table 4.12 were used, with the exception of the tilt angles (ϕ) number, which in this case was 6. The in-depth MIRS profile is obtained by iterative XRD stress measurement and electropolishing actions. The maximum penetration depth was 0.39mm, and the penetration depth increments 0.03mm. Figure 4.27 illustrates the measurement setup, as well as, two electropolished areas.

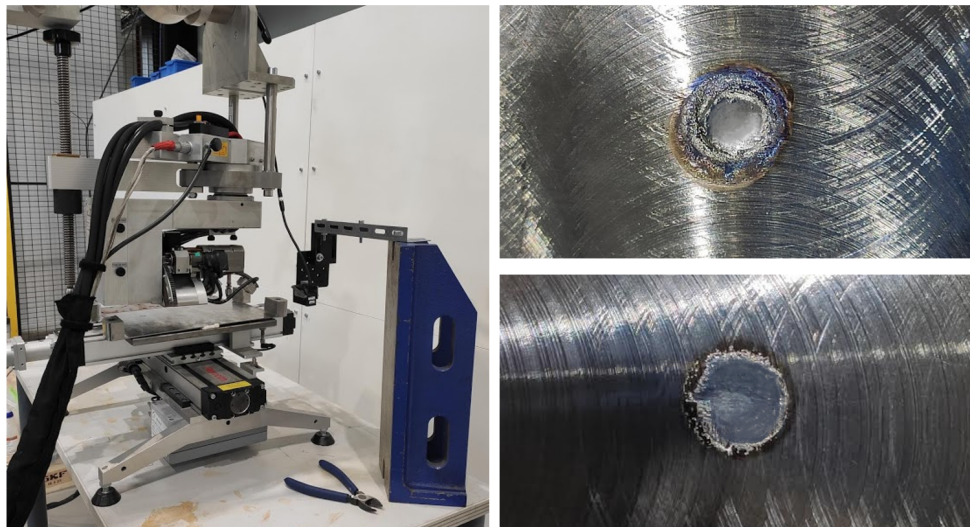


FIGURE 4.27: XRD measurement setup and electropolishing traced.

Table 4.14 displays the XRD MIRS measurements for the feed and transverse directions. Three rotations are necessary to calculate the principal and shear stresses. These values are the ones obtained directly from the software, using the Cross-correlation method, without performing any additional data treatment. It should be noted that the missing measurements reflect a compromise between available time and information provided by the measurements at high penetration depths.

TABLE 4.14: XRD MIRS measurements for the comparison between methods.

Depth[mm]	XRD measurements - σ^M [MPa]					
	P1		P2		P3	
	Feed	Transverse	Feed	Transverse	Feed	Transverse
0	-76.51	433.87	-30.53	363.79	94.06	263.28
0.03	-191.46	-72.89	-324.43	-47.79	-376.48	-127.78
0.06	-303.3	-213.8	-292.09	-72.18	-355.99	-141.36
0.09	-419.42	-316.2	-254.66	-116.97	-321.86	-271.9
0.12	-434.72	-314.32	-237.96	-253.56	-279.26	-219.81
0.15	-315.92	-285.22	-307.36	-249.68	-340.15	-156.04
0.18	-216.89	-363.2	-397.04	-301.41	-418.7	-88.78
0.21	-142.18	-286.1	-321.59	-311.35	-402.61	-45.48
0.24	-38.14	-149.92	-	-	-337.98	-98.62
0.27	-41.33	-97.04	-	-	-287.69	-76.68
0.3	39.86	-77.58	-78.7	-38.58	-	-
0.33	8.81	-40.48	24.18	-98.39	-106.85	-31.21
0.36	-9.09	62.13	-	-	-	-
0.39	24.08	19.81	-	-	43.88	-49.79

4.4.4.2 iHD measurements

For the iHD measurements, the parameters displayed in Table 4.15 are used. Figure 4.28 illustrates the measurement setup, the strain gauges wired to fixed terminals for monitoring, and the incremental drilling. Table 4.16 displays the iHD MIRS measurements for the feed and transverse directions.

TABLE 4.15: iHD measuring parameters.

iHD method measurement parameters	
Material	Ti6Al4V
Young modulus [GPa]	115
Poisson coefficient	0.32
Strain gauges	Vishay Precision Group EA-06-031RE-120
Gauge type (ASTM E837)	Type A
Drilling diameter[mm]	1
Max. penetration depth [mm]	0.512

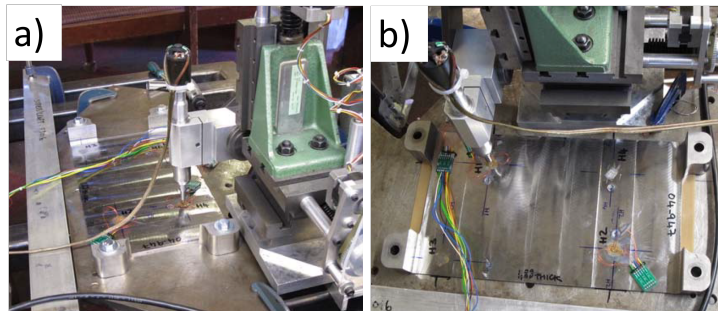


FIGURE 4.28: iHD in-depth MIRS measurement.

TABLE 4.16: iHD MIRS measurements for the comparison between measuring methods.

Depth[mm]	iHD measurements - σ^M [MPa]					
	P1		P2		P3	
	Feed	Transverse	Feed	Transverse	Feed	Transverse
0.008	-56.11	26.72	65.02	258.31	-69.49	75.74
0.024	-107.25	28.93	-52.72	140.13	-60.09	82.59
0.04	-147.98	50.26	-108.84	49.58	-57.28	59.30
0.056	-175.89	69.67	-141.00	16.72	-89.50	5.98
0.08	-228.12	61.71	-209.26	-3.85	-143.44	-49.15
0.112	-281.85	-8.16	-256.45	-72.32	-177.62	-86.70
0.144	-340.39	-82.91	-302.03	-151.03	-217.93	-118.26
0.176	-345.03	-118.46	-279.28	-201.26	-228.10	-135.42
0.224	-296.58	-102.82	-178.94	-173.29	-190.47	-113.45
0.256	-221.26	-71.94	-102.90	-128.41	-134.11	-80.68
0.32	-145.94	-41.07	-26.86	-83.52	-77.76	-47.91
0.384	-39.51	-2.57	-1.22	-55.00	1.23	7.21
0.448	13.71	16.68	11.60	-40.74	40.72	34.77
0.512	66.92	35.93	24.42	-26.48	80.21	62.32

4.4.4.3 Comparison results analysis

The MIRS profiles for the two measuring methods are displayed in Figure 4.29, where the XRD displays with a solid line with dots, and the iHD with a solid line with squares. The blue color represents the feed direction and the orange color the transverse direction (perpendicular to feed). The measured MIRS of P1, P2 and P3 are averaged and their standard deviation calculated and displayed as error bar for each method and depth.

The similarity between the evolution of the curves can be observed. Both methods provide a fairly wide compressive curve in depth, which stabilizes approximately at a similar depth value, 0.4 mm. However, the stresses obtained close to the machined surface differ considerably for both methods. The XRD method results in more compressive results than the iHD method, reaching a difference of almost 200 MPa in the feed direction for some depths.

The iHD data shows a relatively linear reduction in stress. In feed direction this reduction goes from -20 MPa at depth 0.008 mm to a minimum (approx. -285 MPa) at 0.176 mm, and in transverse direction from 120 to -150 MPa. Thereafter, the averaged iHD stress profiles in the two directions increase with depth to a compression/tension transition around 0.4 mm.

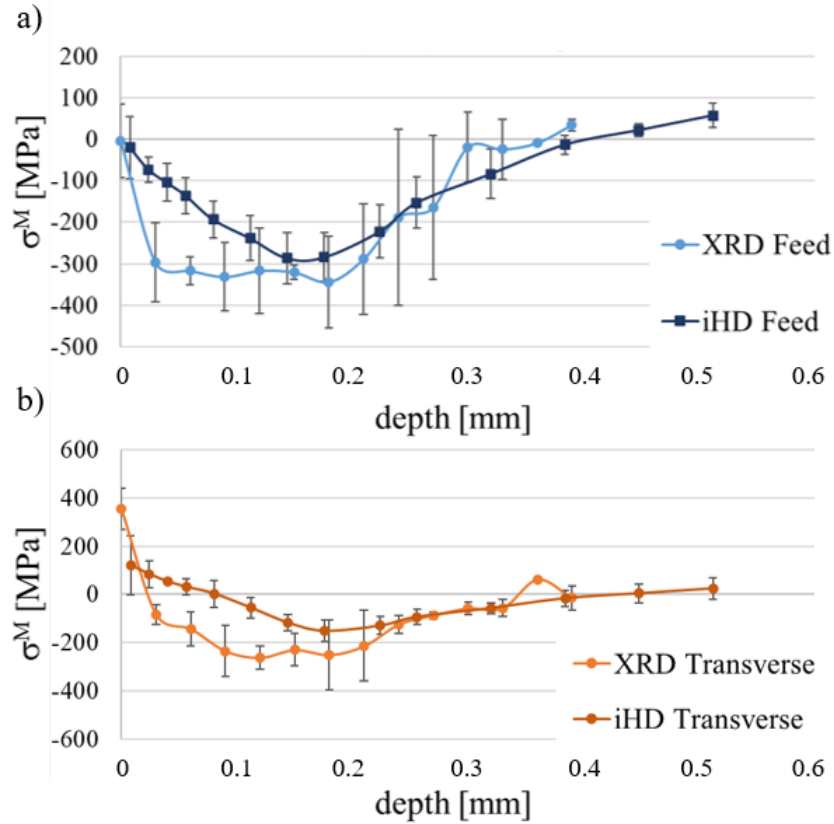


FIGURE 4.29: MIRS measured by XRD and iHD averaged for points P1, P2 and P3: a) Feed direction; b) Transverse direction.

The averaged distribution of the XRD method is more complex than that of iHD. First, surface stresses are more tensile, especially in the transverse direction. Then, there is a steep compression stress gradient, with minor change from 0.024 mm to 0.176 mm in feed direction. This tendency is less clear in transverse direction, even though quite uniform stresses appear at depths going from 0.09 mm to 0.21 mm. Besides, in both directions the maximum stress is more compressive than the maximum iHD stress, with an approximate difference of 60 MPa in feed direction and 100 MPa in transverse direction.

Concerning the variability between measuring points, which is shown by the error bars in Figure 4.29, XRD shows higher deviations between points than iHD. This might be linked to that the iHD data are previously filtered, according to [262].

Although theoretically both measurement methods should give the same results, in practice this is not the case. It could be related to the lack of uniformity of the specimens, different sensibilities to the specimens characteristics (e.g. grain size), and the effects of the electropolishing and hole drilling. In general terms, the iHD method is less reliable for measurements near the surface and for measurements at great depths compared to the size of the hole. The results should be comparable in the middle of the section, where the results match in a certain extent. Therefore, the XRD and iHD methods should not be

directly compared from a quantitative point of view due to the intrinsic factors involved in the measurement, though they do present qualitatively similar responses.

In summary, as the expected MIRS in the Ti6Al4V machined surfaces were expected to be shallow due to the finishing cutting conditions, for the development of the empirical model the XRD measuring technique was chosen due to its higher reliability at shallow depths.

4.5 MIRS modeling

As discussed in Chapter 2, the capability of controlling MIRS through the proper selection of cutting condition has the potential to reduce machining distortion [53, 123]. Therefore, building a simple and agile MIRS model as a function of the machining parameters can enable predicting the MIRS that a specific set of cutting parameters would induce in the component's surface.

MIRS are influenced by a large number of factors, namely the cutting parameters, tool geometry, use of coolant, the tool wear and chemical compatibility of tool and work-piece material, etc. However, cutting speed and feed per tooth have a significant impact on the distribution of process induced residual stresses in milling [49], and many studies focus just on the study of the correlation between these two cutting parameters and MIRS [48, 50, 58]. Thus, this section aims at providing a single mathematical expression based on the variables cutting speed (v_c) and feed per tooth (f_z).

Referring to Table 2.4, numerical models require long computation times and analytical models are difficult to formulate, and both approaches often do not agree with experimental results. Empirical models though, are practical, fast, and more accurate than other models. Furthermore, as a practical solution, empirical models can be created for specific cutting conditions combinations, which open up the possibility to influence the part distortion systematically through the process parameters [135].

For these reasons, and considering the gap existing on MIRS prediction of milling process with solid end-mills in aerospace alloys, in this section a MIRS empirical model is developed for finishing milling of Ti6Al4V with a solid end mill. This model is used in Chapter 5 as input to evaluate a potential distortion control through the proper selection of cutting conditions, i.e. MIRS customization.

4.5.1 Empirical models

Empirical models are based on statistically significant relationships between variables, whose equations are only valid for the context in which they are calibrated. They are

characterized by a high predictive power, but a low explanatory capacity, and for this reason are often considered as black box models, as depicted in Figure 4.30.

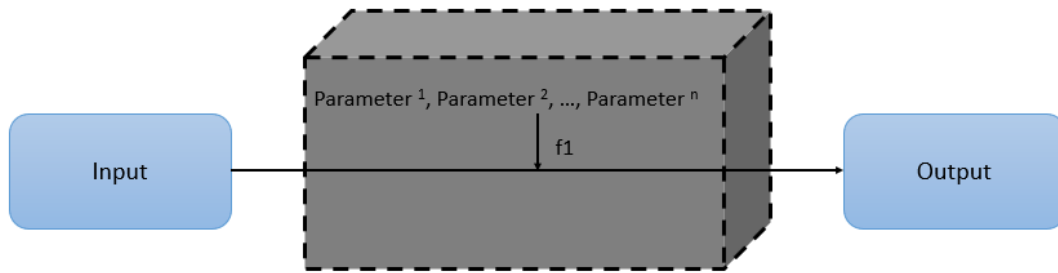


FIGURE 4.30: Flow-diagram of the structure of empirical models.

In this type of models, the lack of knowledge on the system is compensated with quality and quantity of the data experimentally obtained for the input and output variables. Even in the case of having accurate data, there are different circumstances that make difficult to build a successful empirical model, such as the data uncertainty or the uneven influence of the input variables in the output. Besides, some input variables can be difficult to control in production (e.g. tool wear).

Mathematical fitting functions

The first step for building a MIRS prediction empirical model is selecting a mathematical expression that represents properly the in-depth MIRS profiles shape (Fig. 4.1). In this way, polynomial fits have the advantage of the freedom in the number of terms determination. When polynomial fits are used with few terms the curve may not fit properly the data. On the contrary, by increasing the number of terms, despite the better fit the model becomes complex and is not easily applicable to other processes, materials or machining conditions [263]. Furthermore, overfitting can occur, implying that some of the data noise is extracted as if that variation represented the model.

Besides polynomial functions researchers also worked with other functions, with which MIRS profiles can be represented avoiding the complexity increase of the polynomial model. Amongst the most adequate functions, the exponential decay function (Eq. 4.24) [264] was used, where $\sigma(x)$ is stress, x is the depth below the surface, C_0 is the amplitude of the exponential and ζ is the damping coefficient. These coefficients are obtained by adjusting the MIRS data collected from the milling surfaces.

$$\sigma(x) = C_0 \cdot e^{-\zeta \cdot x} \quad (4.24)$$

Other authors, added a sine or cosine to Equation 4.24, generating an exponential decay sine/cosine function [48, 128, 183, 187], where ω_d is the damping frequency and φ is the phase angle.


$$\sigma(x) = C_0 \cdot e^{-\zeta\omega_d \cdot x} \sqrt{1-\zeta^2} \cdot \cos(\omega_d \cdot x + \varphi) \quad (4.25)$$

Due to its extended use and better fit to experimental MIRS profiles induced in milling operations, this equation was used for building the empirical model.

4.5.2 Materials and procedure for MIRS data acquisition

Machining tests were performed to generate MIRS in different conditions to later feed the empirical model. Two Ti6Al4V plates were used, of dimensions $260 \times 140 \times 25$ mm. The tool used for the machining test is defined in Table 4.17.

TABLE 4.17: Tool used for inducing the MIRS at different cutting conditions.

Tool T2	
Brand	Mitsubishi
Reference	VFMHVRBCHD1600R100
Edge number	4
Diameter	16 mm
Helix angle	42-45
Image	

Tool T2 is an end mill of 4 edges with internal cooling, specific to perform finishing operations. The diameter of the tool is selected as a compromise between minimal pocket radius and maximal MRR. Table 4.18 shows the recommended cutting conditions for the tool.

TABLE 4.18: Recommended cutting parameters for the tool T2.

Tool T2	
v_c	70
v_f	170
a_p	0.5-1.5D

Regarding the clamping configuration, a vise is used as depicted in Figure 4.31.

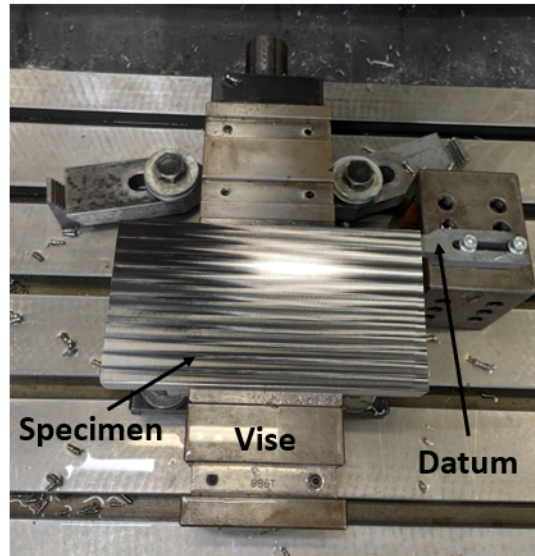


FIGURE 4.31: Clamping of the part with vise for the machining test.

Due to the low machinability of titanium, tool wear can rapidly occur. Therefore, coolant is used to minimize the tool wear generation during machining. To verify the low flank wear (VB) values, the edges of the tool were examined with a portable microscope (ProScope). Figure 4.32a shows the Tool T2 where the long edge labelled as Edge 1 and the short edge labelled as Edge 2.

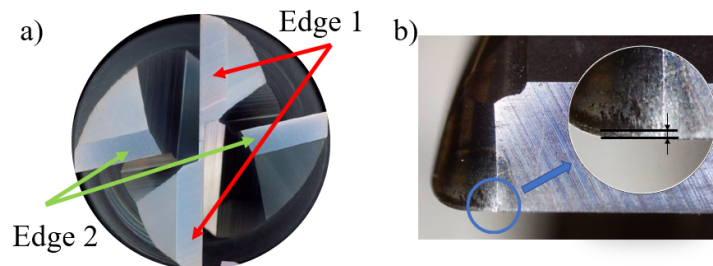


FIGURE 4.32: a) Edge naming in Tool T2; b) Tool wear on cutting edge 1 after cleaning machining.

The tool wear evolution over time, according to the ISO 8688-1:1989 Standard [265], is measured using the average flank wear VB (in mm). In the test performed all measured flank wear values remain below 0.07mm, being the average value 0.05mm. According to [265] and the study by Caldeiraini et al. [266], the effect of the tool wear measured is not considered relevant regarding the induced MIRS.

Before performing the milling test for inducing the MIRS profiles, cleaning passes on both specimens were carried out, using a face milling strategy at the recommended parameters to ensure the homogeneity of the surfaces, and thus guarantee a constant axial depth of cut (a_p) during the test.

The specimens are divided in zones of 35x65mm where different feeds and cutting speeds, v_c and f_z , are used to induce the different MIRS profiles. Table 4.19 gathers the cutting conditions used, from which the numbers 1 to 4 and the letters A to D correspond to the data for building the model. The cutting conditions corresponding to the numbers 5 to 7 and letters E to H were used for evaluating the predictive capability of the model. The v_c and f_z marked in bold correspond to the tool manufacturer recommendation. Finally, the depth of cut (a_p) and width of cut (a_e) were 0.5mm and 11.67mm respectively in all the machining test.

TABLE 4.19: Cutting conditions used in machining test for the MIRS empirical model.

Cutting speed [m/min]							
Building model				Evaluating model			
1	2	3	4	5	6	7	
60	70	80	90	65	75	85	
Feed per tooth [mm/z]							
Building model				Evaluating model			
A	B	C	D	E	F	G	H
0.02	0.03	0.04	0.05	0.015	0.025	0.035	0.045

Following the procedure exposed in Section 4.4.2, MIRS were measured by XRD. This method was selected because the expected MIRS penetration depth was low due to the finishing cutting parameters [267] and near-surface XRD results were more accurate than iHD (Section 4.4.4).

XRD measurements of all points of the specimen at one specific depth were obtained using the parameters of Table 4.12, only in two rotations (0 and 90), with 5/5 tilt angles and to a maximum penetration depth of 0.18mm (Fig. 4.33a).

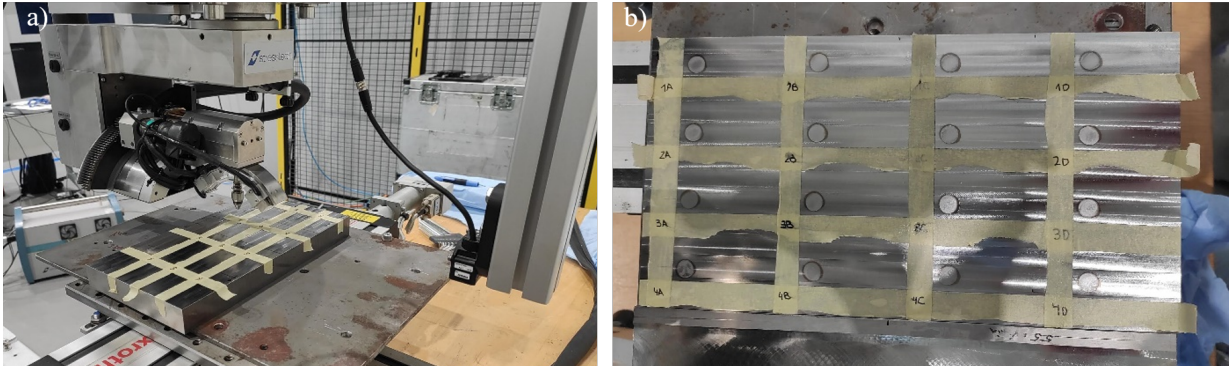


FIGURE 4.33: Stress data acquisition process: a) XRD measurement; b) electroplishing.

For the translation movement between measuring points, a XY table was used, as depicted in Figure 4.33b, which reduced the uncertainty linked to operator. After that, the electropolishing of all the points was performed before for a subsequent measurement. This process was repeated sequentially down to a depth of 0.18 mm. The measuring depths were not evenly distributed, because the high stress gradients close to the machined surface require higher resolution.

4.5.3 Development of the MIRS empirical model

After gathering all the experimental in-depth MIRS results for all the conditions, the development of the empirical model was undertaken.

The model was built in three regression steps, as depicted in Figure 4.34.

$$\begin{aligned} \text{1st Regression (R1)} &\longrightarrow \sigma = f(x) \\ \text{2nd Regression (R2)} &\longrightarrow \sigma = f(x, f_z) \\ \text{3rd Regression (R3)} &\longrightarrow \sigma = f(x, f_z, v_c) \end{aligned}$$

FIGURE 4.34: MIRS empirical model as a function of v_c and f_z based on three regressions.

The first regression was performed using the exponential decay cosine function, EDCF (Eq. 4.25) for fitting the experimental MIRS profiles in depth. The second and third regressions were polynomial, trying to fit the parameters from EDCF to the variations of v_c and f_z from the test. Aiming at developing a simple and clear model, first (1) and second (2) order polynomials were used for the R2 and R3 regressions. This way, four different models were built depending on the order of the polynomial combinations of the R2 and R3 regressions, which are gathered in Table 4.20.

TABLE 4.20: Regression combinations used for the construction of the MIRS empirical model, where the numbers 1 and 2 are the order of the polynomials of R2 and R3 respectively.

Label	R1	R2	R3
11	EDCF	1	1
21	EDCF	2	1
12	EDCF	1	2
22	EDCF	2	2

Next, the three regression steps are explained in detail.

1st Regression (R1):

First, the fitting of all in-depth MIRS profiles to Equation 4.25 was performed by least squares with a non-linear multi-objective optimization algorithm. As the mathematical optimization process could reach local minima that do not correspond to the global optimization values, in these cases, the result depended on the initial values from which the optimization process began. These initial values were unique for each of the curves obtained, since these values were defined in relation to different features of each data set of MIRS, which are depicted in Figure 4.1. In addition, these initial values were limited by an upper and lower limit for each of the parameters of the function. This way, the amplitude (C_o) was related to the absolute value of the stress obtained at the surface, the damping coefficient (ζ) was considered the last penetration value at which stress stabilized, the damping frequency (ω_d) was the value of the stress obtained at the surface (same as the value used for the amplitude but with its sign) and, finally, the phase angle (φ) was set at a value of $\pi/4$, since it was the value that best results provided.

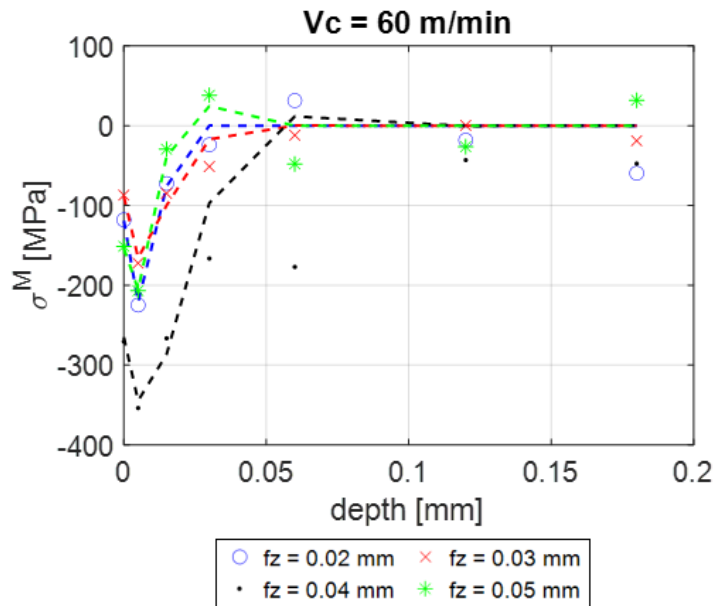


FIGURE 4.35: MIRS experimental values and obtained regression marked with dashed lines as a function of penetration depth ($v_c=60$ m/min and $f_z=0.02$ mm).

This way, the 32 MIRS profiles obtained including all the combinations of cutting speeds (4), feed per tooth (4) and stress directions (2) were fitted to the EDCF. Figure 4.35 shows the experimental values (marked with single icons, e.g. dots) and the exponential decay cosine functions' fitting curve (marked with dashed lines) for the cutting speed $v_c=60$ m/min. Analogous plots for the MIRS data corresponding to the other cuttings speeds can be obtained. Considering that the depth at which MIRS profiles stabilize in Ti6Al4V (with similar cutting conditions) is approximately 0.08 mm [46, 48, 55], more relevance is given to measurements below this depth. For this reason, the MIRS curves in this first regression

show a better fit at penetrations depths below this value and appear more scattered at higher penetrations. Moreover, considering the measurement uncertainty quantified in Section 4.4.3, the scatter at high penetrations is considered negligible.

2nd Regression (R2):

After obtaining the parameters for the exponential decay cosine function to fit each in-depth MIRS profiles (R1), the fitting of these parameters from this equation to the f_z values used in each test is performed in R2.

In order to simplify the nomenclature, the exponential decay cosine function coefficients are labelled in the next paragraphs as follows (Eq. 4.26), where a_1 is the amplitude (C_0), a_2 is the damping coefficient (φ), a_3 is the damping frequency (ω_d) and a_4 is the phase angle (ζ).

$$\sigma(x) = a_1 \cdot e^{-a_2 a_3 x \sqrt{1-(a_2)^2}} \cdot \cos(a_3 x + a_4) \quad (4.26)$$

Equation 4.27 and 4.28 polynomial functions were used to analyze the evolution of each parameter as a function of the feed per tooth (f_z) for first and second order polynomials respectively. Figure 4.36 displays the values obtained after R2 with polynomial regression of order 2 for the a_4 parameter from R1 (phase angle, ζ) and cutting speed 60 m/min, where the dots correspond to the a_4 parameter from R1, and the dashed line from R2.

$$a_i = a_{i1} \cdot f_z + a_{i0} \quad (4.27)$$

$$a_i = a_{i2} \cdot f_z^2 + a_{i1} \cdot f_z + a_{i0} \quad (4.28)$$

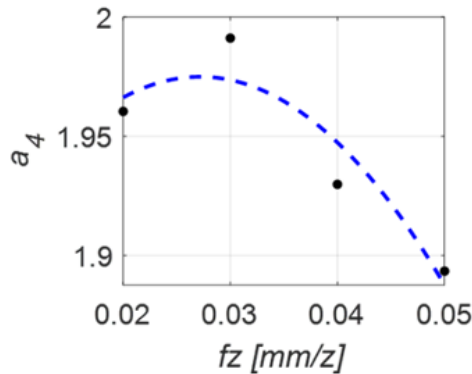


FIGURE 4.36: EDCF coefficient a_4 of R1 (dots) and regression R2 (dashed lines) as a function of the feed per tooth ($v_c=60$ m/min and $f_z=0.02$ mm, order 2 polynomial).

3rd Regression (R3):

Finally, in the third fitting step, the coefficients of the R2 polynomials were fitted as a function of the v_c (Fig. 4.34) using first and second order polynomials (Eq. 4.29 and 4.29).

This way, in the term a_{ij} , i refers to the coefficients obtained from R1 and j to the coefficients obtained in R2. At the same time, j varies depending on the polynomial order of R2. From R3, a_{ijk} coefficients were obtained, which represented all the coefficients of the empirical model. Figure 4.37 displays the third regression R3 with a polynomial of order 2 for a coefficient of the second regression R2 (a_{40}) from Figure 4.36.

$$a_{ij} = a_{ij1} \cdot v_c + a_{ij0} \quad (4.29)$$

$$a_{ij} = a_{ij2} \cdot v_c^2 + a_{ij1} \cdot v_c + a_{ij0} \quad (4.30)$$

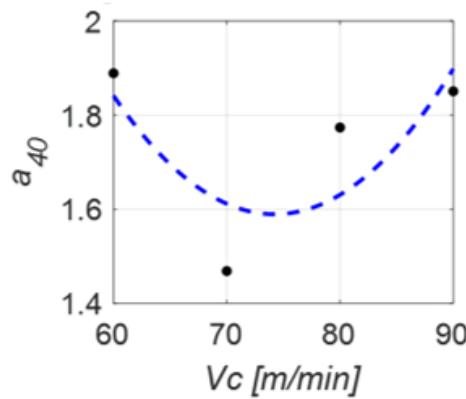


FIGURE 4.37: Coefficient of regression R2, a_{40} , (dots) and regression R3 (dashed lines) as a function of the cutting speed ($v_c=60$ m/min and $f_z=0.02$ mm, order 2 polynomial).

After performing the three regression steps, the equation for MIRS prediction as a function of the depth, cutting speed and feed per tooth ($\sigma = f(x, f_z, v_c)$), basis of the MIRS empirical model, was obtained. In this way, each of the coefficients of Equation 4.26 takes the form of the equations in Table 4.21, where the four regression combinations appear.

TABLE 4.21: Regression combinations and coefficients for Eq. 4.26.

Comb.	Coefficients of Eq. 4.26
11	$a_i = (a_{i11} \cdot v_c + a_{i10}) \cdot f_z + (a_{i01} \cdot v_c + a_{i00})$ (4.31)
21	$a_i = (a_{i21} \cdot v_c + a_{i20}) \cdot f_z^2 + (a_{i11} \cdot v_c + a_{i10}) \cdot f_z + (a_{i01} \cdot v_c + a_{i00})$ (4.32)
12	$a_i = (a_{i12} \cdot v_c^2 + a_{i11} \cdot v_c + a_{i10}) \cdot f_z + (a_{i02} \cdot v_c^2 + a_{i01} \cdot v_c + a_{i00})$ (4.33)
22	$a_i = (a_{i22} \cdot v_c^2 + a_{i21} \cdot v_c + a_{i20}) \cdot f_z^2 + (a_{i12} \cdot v_c^2 + a_{i11} \cdot v_c + a_{i10}) \cdot f_z + (a_{i02} \cdot v_c^2 + a_{i01} \cdot v_c + a_{i00})$ (4.34)

$i=1,2,3,4$

4.5.4 Model evaluation

In this section, the model results are evaluated against the experimental results with which the model is built. This evaluation is based on the Pearson correlation coefficient r (Eq. 4.35) [268] and the mean error $\bar{e}r$ (Eq.4.36) between experimental and predicted stress values, where σ is the measured stress (MPa), $\bar{\sigma}$ is the average measured stresses, $\hat{\sigma}$ (MPa) is the predicted stress, $\bar{\hat{\sigma}}$ is the average predicted stresses and n is the number of measurements.

$$r = \sqrt{\left(\frac{\sum((\sigma - \bar{\sigma}) \cdot (\hat{\sigma} - \bar{\hat{\sigma}}))}{\sqrt{\sum(\sigma - \bar{\sigma})^2} \cdot \sqrt{\sum(\hat{\sigma} - \bar{\hat{\sigma}})^2}}\right)^2} \quad (4.35)$$

$$\bar{e}r = \frac{\sum|\hat{\sigma} - \sigma|}{n} \quad (4.36)$$

In this way, the Table 4.22 gathers the evaluation results for the different models obtained using the EDCF and the different polynomial degrees combinations using data with which the model was built.

TABLE 4.22: Pearson coefficient and mean error of the MIRS empirical model against the experimental data.

Regr. Comb.	Transverse		Feed	
	r	$\bar{e}r$ [MPa]	r	$\bar{e}r$ [MPa]
11	0.8191	50.987	0.9203	37.015
21	0.8379	47.787	0.9306	37.730
12	0.8270	48.740	0.9359	35.147
22	0.8515	45.760	0.9375	32.290

Figures 4.38 and 4.39 display graphically values for r and $\bar{e}r$ between experimental and model data for the different regression combinations analyzed (Table 4.20), where the solid bars represent the feed direction and the bars with stripes the transverse direction. For all the regression combinations, the error is in the range of the XRD measurement uncertainty (Section 4.4.3). Besides, the correlation between experimental data and model data is in all cases above 0.8, being slightly higher in the feed direction. The model results are graphically represented using 3D surfaces against the measured values displayed with black dots. Figure 4.40 depicts an example for one only cutting speed (60m/min), and the surface represents the MIRS as function of depth and feed per tooth, using the regression combination 22.

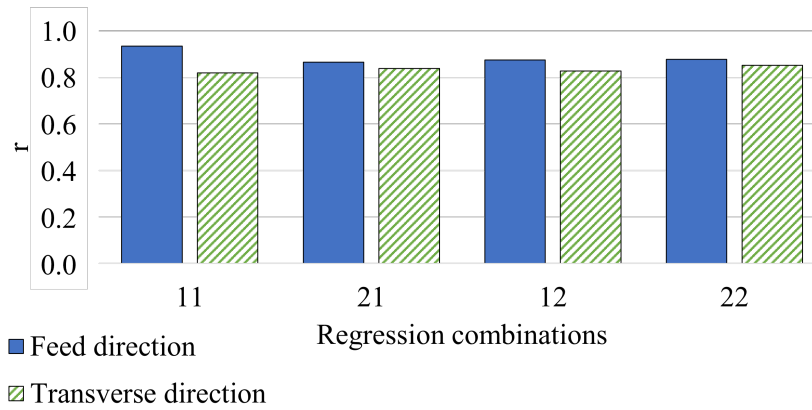


FIGURE 4.38: Pearson coefficient, r , values for the comparison of the different polynomial combinations against the experimental data used for building the model.

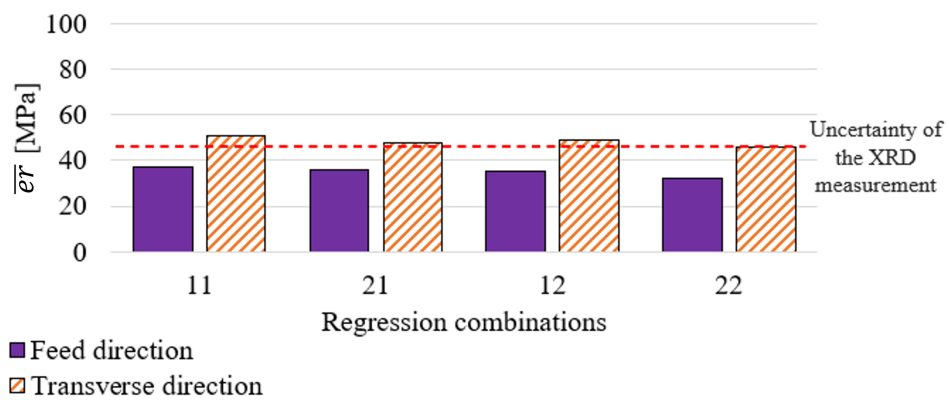


FIGURE 4.39: Mean error, \bar{e}_r , obtained for the comparison of the empirical model against the experimental data used for building the model.

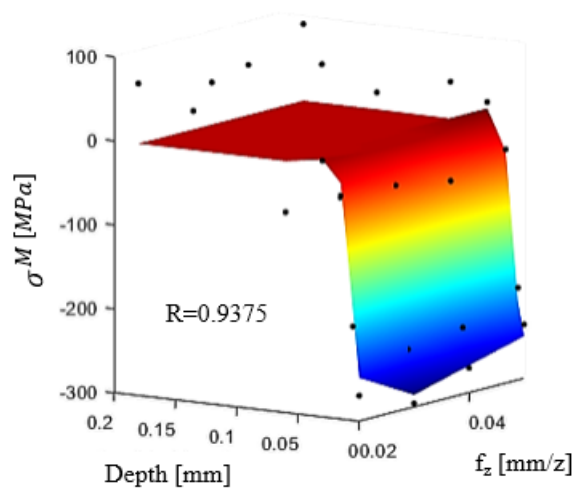


FIGURE 4.40: 3D representation of MIRS results obtained with the empirical model (surface) in comparison to experimental results (dots).

As it can be seen, the empirical model fits well the compressive stresses of high magnitude (reaching -300 MPa) at shallow depths (below 0.1mm), and as exposed before, ignores the data at deeper penetrations.

Besides the evaluation of the model with the data used for building it, the model results were also compared with MIRS corresponding to other cuttings conditions. More specifically, MIRS obtained with the combinations of cutting speed 5 to 7 and feed per tooth E to H of Table 4.19. The aim of this analysis was quantifying the predictive capacity of the model for input data different to the one used to build it.

This analysis is done in two steps. First, the entire data set obtained from the model is evaluated, meaning that, the model is evaluated globally for all conditions simultaneously (Table 4.23). After this, an analysis is performed locally considering each of the MIRS profiles independently.

In this case results of Table 4.23 show also correlation values above 0.8, with higher values in the transverse direction than those of Table 4.22. Consequently, the error also diminishes, resulting values below the uncertainty range.

TABLE 4.23: Pearson coefficient, r , and mean error, $\bar{e}\bar{r}$, values for the comparison of the model against experimental data not used for building the model.

Regr. Comb.	Transverse		Feed	
	r	$\bar{e}\bar{r}$ [MPa]	r	$\bar{e}\bar{r}$ [MPa]
11	0.8815	31.427	0.9214	34.108
21	0.8792	32.003	0.9094	37.452
12	0.8798	32.552	0.9209	34.521
22	0.8803	32.896	0.9132	37.190

Figures 4.41 and 4.42 show graphically the results for r and $\bar{e}\bar{r}$.

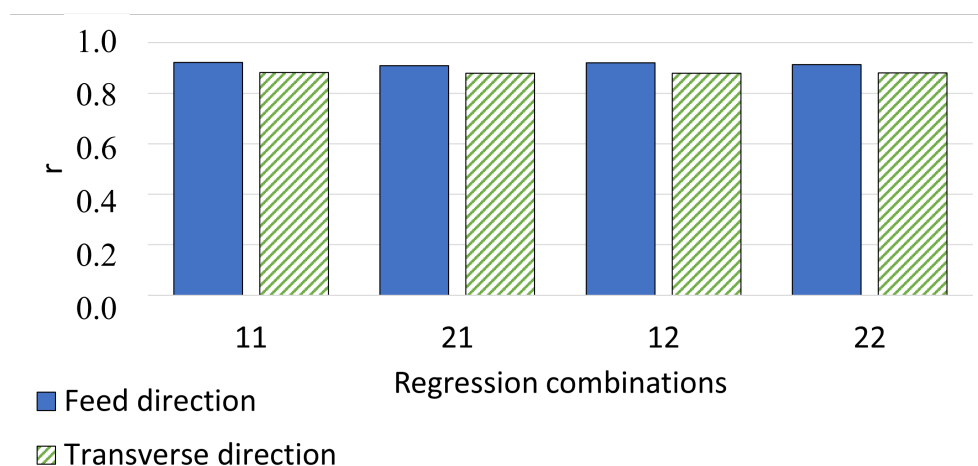


FIGURE 4.41: Pearson coefficient, r , values for the comparison of the model with different polynomial combinations against the experimental data used for validating the model.

As it can be seen, the different regression combinations provide similar results, being in this case the regression combination 11 the one providing the highest correlation (Fig. 4.41) and lowest error (Fig. 4.42).

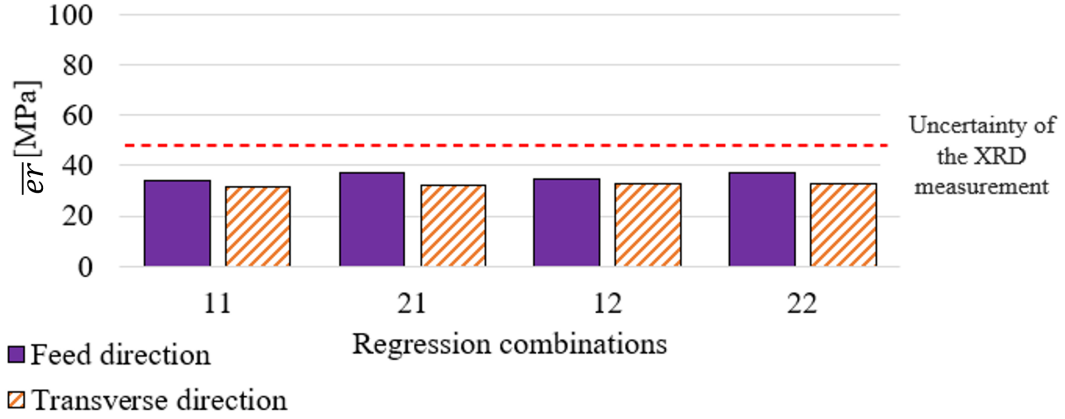


FIGURE 4.42: Mean error, $\bar{e}r$, values for the comparison of the model with different polynomial combinations against the experimental data used for validating the model.

Next, the model results are evaluated for single cutting conditions of v_c and f_z considering each of the MIRS profiles independently, i.e. locally. Table 4.24 shows the Pearson coefficient r evaluated locally for MIRS in the transverse direction. In this case, correlation values below 0.8 can be seen for v_c 65 m/min and f_z 0.045 mm/z in transverse direction.

TABLE 4.24: Pearson coefficient, r , values of the MIRS profiles predicted with the model with different polynomial combinations against experimental data in the transverse direction.

Regr. Comb.	v_c [m/min]											
	65				75				85			
	f_z [mm/z]											
	0.015	0.025	0.035	0.045	0.015	0.025	0.035	0.045	0.015	0.025	0.035	0.045
11	0.968	0.954	0.894	0.756	0.878	0.958	0.981	0.919	0.960	0.991	0.984	0.981
21	0.956	0.956	0.829	0.752	0.869	0.958	0.982	0.924	0.937	0.991	0.979	0.980
12	0.966	0.951	0.899	0.757	0.876	0.944	0.977	0.915	0.962	0.991	0.983	0.980
22	0.952	0.953	0.850	0.754	0.903	0.943	0.974	0.913	0.939	0.990	0.977	0.980

Figure 4.43 shows graphically the values of the Table 4.24, corresponding to the results in the transverse direction. The highest Pearson coefficient values are obtained at higher cutting speeds. Besides, the regression combinations (Table 4.20) 11 and 12 provide the best results, although in many cases the difference between them is negligible.

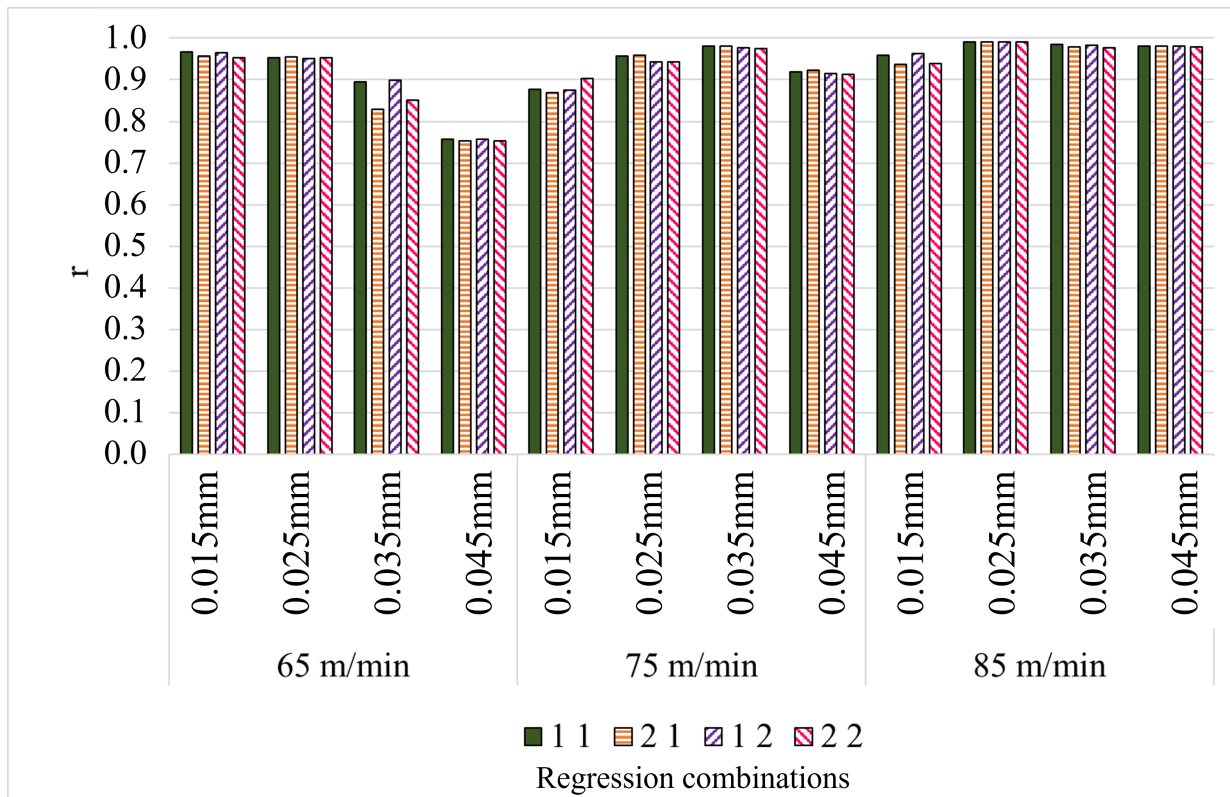


FIGURE 4.43: Pearson coefficient, r , values of the MIRS profiles predicted with the model with different polynomial combinations against experimental data in the transverse direction.

Concerning the feed direction, the results are displayed in Table 4.25.

TABLE 4.25: Pearson coefficient, r , values of the MIRS profiles predicted with the model with different polynomial combinations against experimental data in the feed direction

Regr. Comb.	v_c [m/min]											
	65				75				85			
	f_z [mm/z]											
	0.015	0.025	0.035	0.045	0.015	0.025	0.035	0.045	0.015	0.025	0.035	0.045
11	0.982	0.925	0.914	0.983	0.921	0.976	0.924	0.986	0.964	0.985	0.877	0.987
21	0.978	0.925	0.910	0.983	0.929	0.976	0.921	0.985	0.967	0.986	0.859	0.988
12	0.981	0.926	0.914	0.983	0.919	0.979	0.926	0.984	0.964	0.986	0.875	0.987
22	0.978	0.925	0.909	0.982	0.929	0.980	0.915	0.982	0.966	0.987	0.851	0.988

Analogously, the results of Table 4.25 are plotted in Figure 4.44. For this feed direction higher correlation values and lower variability than in transverse direction can be observed. Besides, the best results are for the v_c 70 m/min and f_z 0.03 mm, being these close to the tool manufacturer recommendation. Regarding regression combinations, in most cases

all combinations show similar correlation, being 11 the one providing the highest Pearson coefficient.

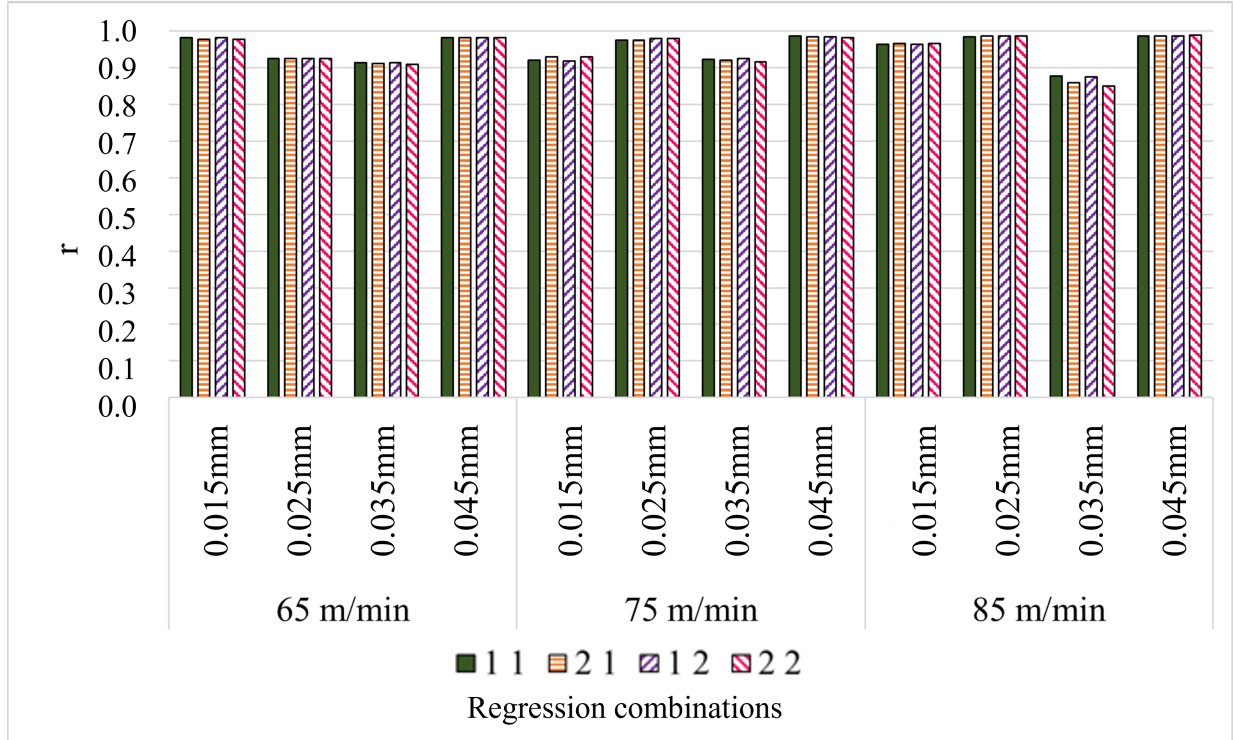


FIGURE 4.44: Pearson coefficient, r , values of the MIRS profiles predicted with the model with different polynomial combinations against experimental data in the feed direction

As the regression combination 11 provided the highest r values in comparison to experimental results, it was the one selected to build the final empirical model. To show the effect of the MIRS profiles according to v_c and f_z , Figure 4.45 shows the effect of the input parameters on the most characteristic parameters of the stress profiles (Fig. 4.1).

Taking a look at the effect of the cutting parameters in the stress peak at the surface, σ_{Sur}^M , both higher cutting speed and feed per tooth values generate more compressive stresses. The effect on the maximum compressive stress, $\sigma_{C,max}^M$, is the same for both cutting parameters. Concerning the response depth at which the MIRS stabilize, x_{sta} , and location of the maximum compressive stress, $x_{C,max}$, it can be seen that when increasing the feed per tooth value the penetration of the residual stress profile on the machines surface increases. The effect of the cutting speed is mixed with the feed employed as, when using low feed per tooth values, increasing the cutting speed increases slightly the penetration of the stresses. When using high feed per tooth values, on the contrary, the decrease of the cutting speed increases the penetration depth of the stress profiles. These results agree partially with bibliography considering the higher $\sigma_{C,max}^M$ and $x_{C,max}$ at higher v_c and f_z , but not with the more tensile σ_{Sur}^M when increasing v_c .

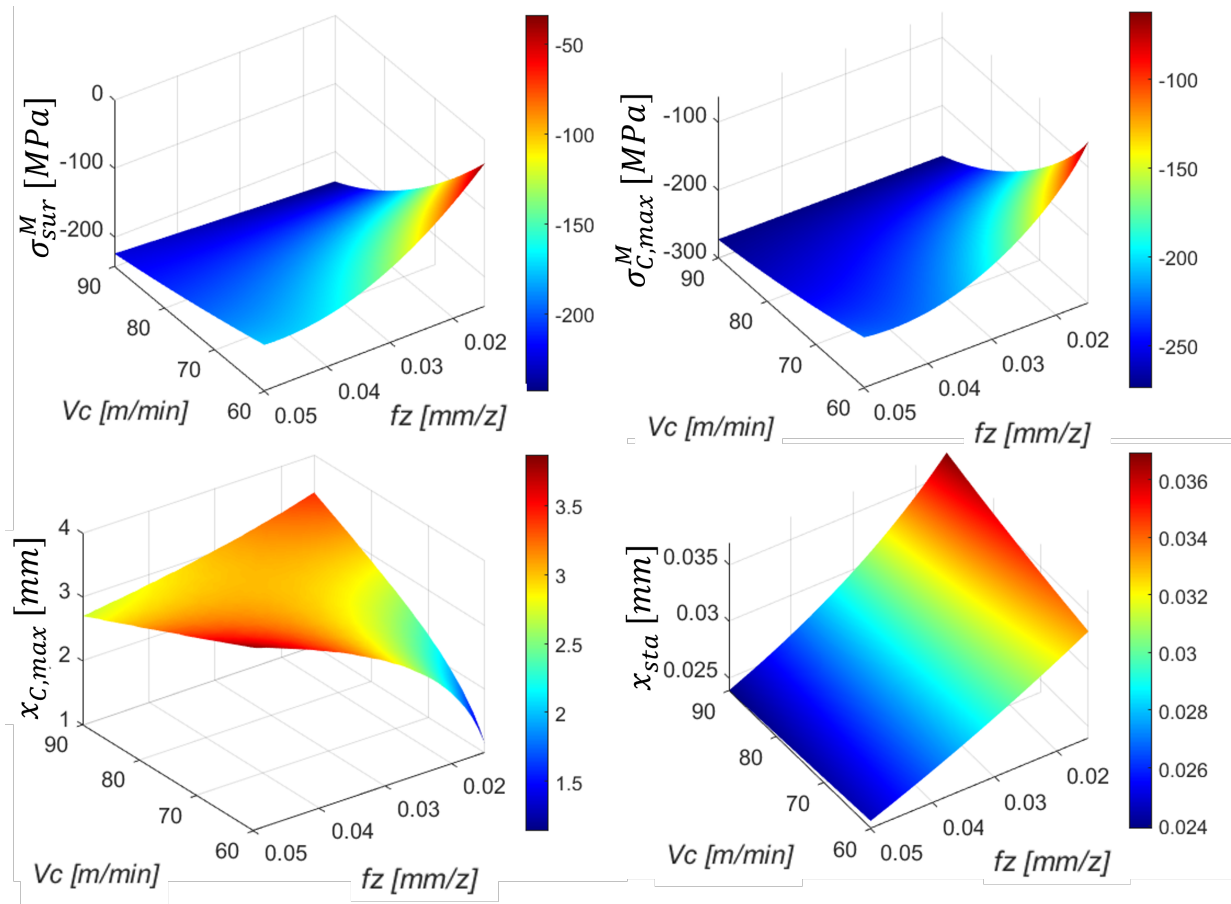


FIGURE 4.45: Effects of the cutting speed and feed per tooth on MIRS profile characteristic parameters in transverse direction.

Finally, the coefficients of the equation for the regression combination 11 (one degree polynomials) are gathered in Table 4.26.

4.5.5 Conclusions

This section shows the development of a MIRS empirical model, as well as its evaluation in comparison to experimental results. Results demonstrate the ability of the empirical modeling for performing MIRS predictions in face milling of Ti6Al4V using end-mills and finishing conditions.

Next conclusions can be withdrawn from the results obtained along this section:

- The experimental results agree with the theoretical premise which stays that, at greater feeds, the penetration depth and amplitude of compressive stresses increase. On the contrary, the premise of more tensile stresses on the surface at higher cutting speeds is not observed in these experimental results.

TABLE 4.26: Coefficients of the model constructed with 1st grade polynomials

Coefficients	Feed direction	Feed normal direction
a_{111}	-4.30E+02	4.56E+05
a_{110}	3.24E+04	-4.02E+04
a_{101}	1.53E+01	-1.56E+01
a_{100}	-5.57E+02	2.03E+03
a_{211}	-1.84E-01	3.64E-01
a_{210}	1.28E+01	-3.30E+01
a_{201}	5.76E-03	-1.43E-02
a_{200}	3.87E-01	2.01E+00
a_{311}	2.41E+01	2.29E+01
a_{310}	-2.45E+03	-8.36E+02
a_{301}	-1.19E+00	-9.62E-01
a_{300}	2.22E+02	1.43E+02
a_{411}	5.05E-01	-3.87E-01
a_{410}	-3.80E+01	3.34E+01
a_{401}	-1.73E-02	1.75E-02
a_{400}	3.44E+00	4.04E-01

- Using an exponential decay cosine function and polynomial functions, it is possible to define a simple mathematical expression for the accurate modeling the milling induced residual stresses.
- The empirical model built generates error values below the uncertainty of the XRD measurements, while the values for the correlation coefficient r obtained are higher to 0.9 when analyzing a single cutting condition.
- The model structure is directly applicable to process conditions (cutting speed and feed per tooth) in the working range indicated by the tool manufacturer different to the ones employed for building the model.

In conclusion, it can be said that the empirical model built is a practical solution for MIRS prediction providing data below experimental uncertainty and correlation values close to 0.9. Therefore, the MIRS profiles obtained with the empirical model can be used as input data for the distortion analysis performed in Chapter 5.

4.6 Summary

MIRS are one of the main sources of machining distortion in aerostructures. Before one can develop control and compensation techniques to minimize distortion, MIRS assessment must be fully understood. This means that not only an investigation of the effect of different

process parameters on the MIRS is important. Also, understanding the MIRS measuring process and the uncertainty involved is a necessity for the use of these data in distortion prediction models.

In this chapter, two different measuring techniques are studied, and measurements in different aerospace alloys (Al-based and Ti-based) are performed.

In view of the results, it is concluded that:

- MIRS measurement: Different measuring methods can be used to perform in-depth MIRS measurements, such as iHD and XRD. Although these methods are successfully employed for stress measurement, and enable comparison of stresses taken with each measuring method, inter-method comparisons are seldom. To use MIRS as input data in distortion prediction models, it is important to have reliable and accurate data, independent of the measurement method used. Within this section, the accuracy of the XRD is assessed, on its own and against the iHD method. This way, in the titanium alloy case the general trend in regards to maximum compressive stress and depth at which the stress stabilizes approximately match in both methods. However, results showed a significant measurement uncertainty, being ± 23 MPa for the XRD method, ± 85 MPa between measured points in the machined surface and an average difference between methods of 70 MPa, reaching at specific depths differences above 200 MPa. Considering the MIRS measurements in aluminium alloy, the iHD the measuring uncertainty range calculated following the guide [189] was lower, ± 27 MPa at the surface and ± 5 MPa at deeper penetrations. However, the average variability between points reached 28 MPa, which reached 50% of the measured stress value. The uncertainty linked to MIRS measurements may be linked to the errors in machining distortion prediction.
- Empirical model: MIRS empirical modeling can provide accurate results, as well as practical and fast prediction tool. Making use of the EDCF and polynomial regressions, MIRS profiles can be predicted as a function of the penetration depth, the cutting speed and the feed per tooth. Using the combination of the EDCF and first-degree polynomial regressions, correlations reaching values higher than 0.9 can be obtained and mean errors below the measurement uncertainty.

The data here gathered will be further used as input data in Chapter 5 for the evaluation of different developments linked to machining distortion.

Besides, future lines for improvement in relation to MIRS measuring and modeling were identified:

1. Stress measurement process and electropolishing: As mentioned, the data reliability is key for this kind of modeling. Along the study it was noticed that electropolishing process can be an important uncertainty source. Also, measuring the actual penetration depth more accurately would help reducing uncertainty.
2. EDCF regression: As mentioned, the algorithm used for fitting the experimental data to the EDCF requires from setting the initial values. These initial values are set according to features of each of the MIRS profiles. However, this practice is not very efficient and presents improvement potential.
3. Expansion of the model concerning affecting cutting parameters: Although the presented model considers the two cutting conditions most often reported as the highest effect on MIRS, other conditions such as the depth of cut, tool wear or the used of coolant can have a significant influence on MIRS development and, for this reason, should be gradually included in the MIRS model to broaden its application range.

Chapter 5

Distortion prediction for aerospace structural components

5.1 Introduction

This chapter performs three different studies to evaluate the applicability of the developments from the previous chapters. This way, the objectives of the chapter are summarized in the following points:

- O1: Experimental verification of the BIRS characterization method in ribbed geometries implementable in industrial environments.
- O2: Analysis of the potential of MIRS for controlling distortion through their customization, by selecting specifically the machining conditions.
- O3: Development of the reduced LR measurement and BIRS estimation procedure, implementable in-process, for subsequent distortion prediction.
- O4: Experimental validation of the reduced BIRS measurement and estimation procedure for distortion prediction in real aerostructure parts.

The chapter is divided in three sections following these objectives. First, an experimental verification of the BIRS characterization procedure introduced in Chapter 3 is performed (O1), where aluminium test-parts are machined to measure complete BIRS profiles by on-machine LR. Secondly, a theoretical analysis of the potential of controlling distortion using the MIRS empirical model developed in Chapter 4 is exposed (O2). In the third section the feasibility of the distortion prediction on a real-part is evaluated. Using experimental BIRS and MIRS data, this section performs the experimental verification of the hybrid

distortion model, where reduced BIRS measurements are performed in the blanks from which the final parts are obtained (O3 and O4).

The results show that the developments here presented can provide accurate machining distortion estimation, as well as an uncertainty range of this prediction, in a simple and fast form.

5.2 Experimental verification of BIRS characterization by on-machine LR

In this section, an experimental verification of the BIRS characterization method presented in Chapter 3 using the on-machine ribbed LR is performed. The different BIRS data treatment options and the filtering described in Section 3.3 are also analyzed experimentally, to validate previous simulation results. With this, experimental values are compared with distortion calculations, and their difference evaluated against the calculated uncertainty range through Monte Carlo simulations.

It is important to note that the clamping stresses due to the initial curvature measured in the blanks, the MIRS and the equivalent bending stiffness are considered for obtaining the results exposed below.

The process route followed for the calculation and experimental verification is displayed in Figure 5.1. In this two different sides can be distinguished:

- In the right side the 3σ uncertainty bands were obtained from a theoretical analysis that simulated the actual LR test. From the four options, the minimal 3σ was chosen in order to show the most restrictive case.
- The left side represents the experimental procedure to obtain BIRS (including the LR test, curvature filtering and data treatment options), and a Phase 3 where the curvatures were calculated from the BIRS obtained experimentally.

These uncertainty bands of the simulation study (right side) were used to evaluate if the deviations of curvatures from phases 1 and 3 (left side) were within the theoretical uncertainty generated by probing errors. If not, the stress results from the LR test were assumed to be erroneous.

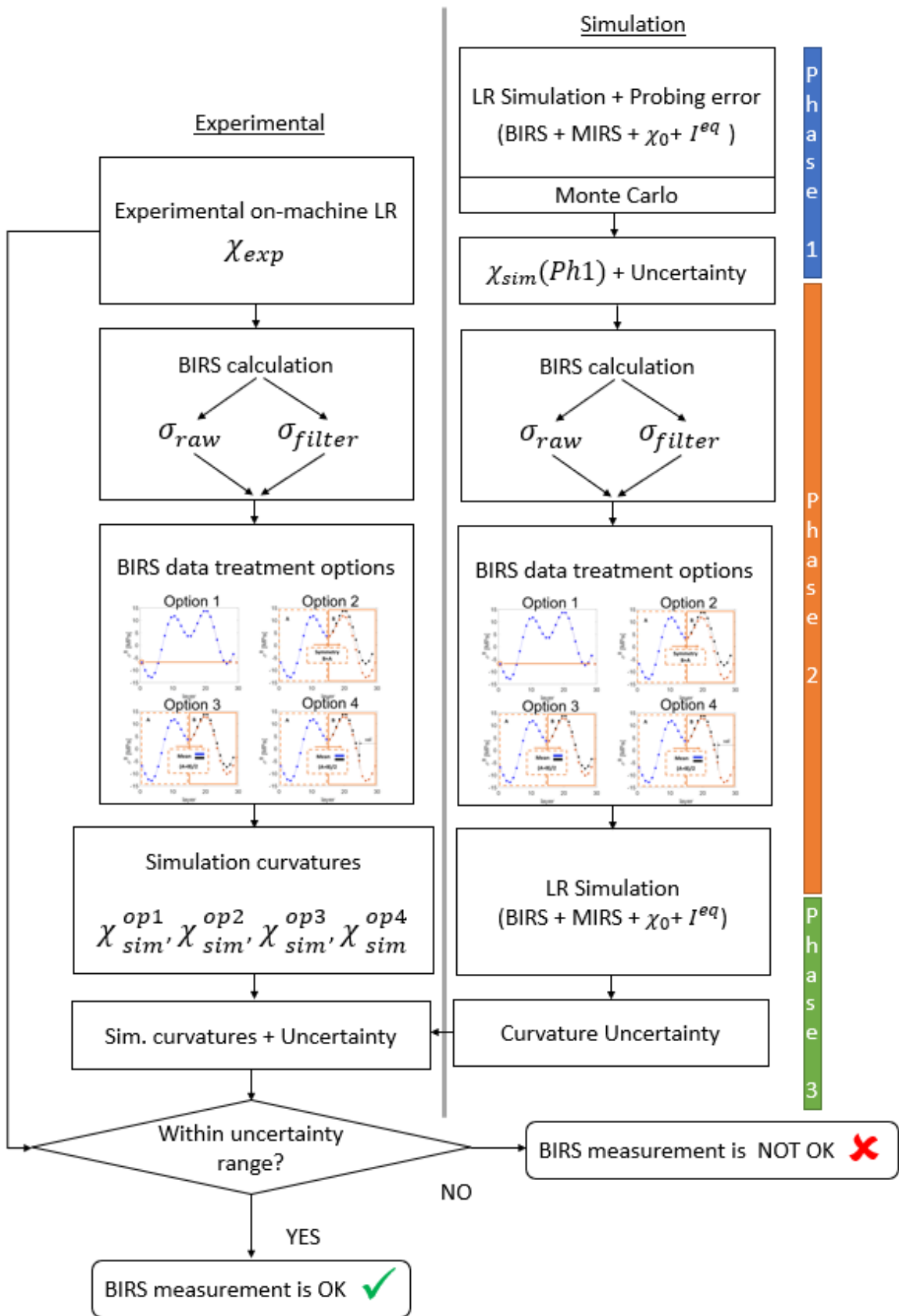


FIGURE 5.1: Process route for the experimental verification of the on-machine LR for BIRS characterization.

5.2.1 Test-case definition and experimental procedure

The analysis is performed on Al7050-T7451 parts, whose chemical composition and mechanical properties are displayed in tables 4.2 and 4.3 respectively. The part dimensions are 200x400x31.3mm, and the geometry is symmetric with 4 pockets, meaning 3 ribs in both directions of 5mm width each, and a floor thickness of 3mm (Fig. 5.2). The part includes some features to enable its clamping during the test by bolts and T-nuts. As the test-case geometry fulfills the criteria of plates, the 2D formulation is applied.

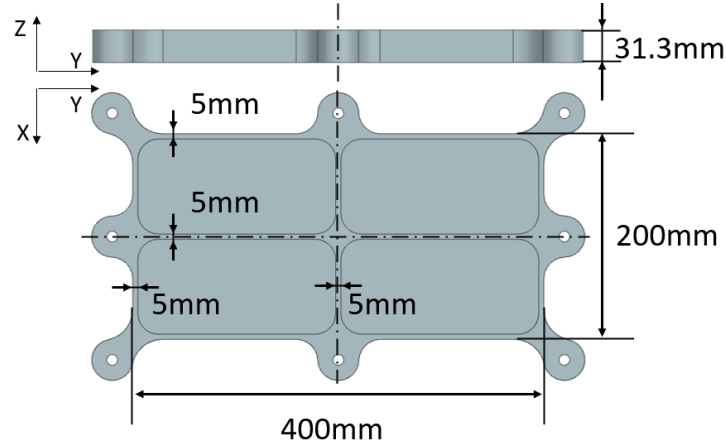


FIGURE 5.2: Geometry of the Al7050-T7451 aluminium part.

Two blanks of the same batch are used for the experimental evaluation. The tests are carried out on a Soraluec FMT 4000 multitasking machine. A milling tool D40 mm with 3 Ceratizit XDHX 190404 FR-27P inserts is used (Table 4.4). The machining conditions are exposed in Table 5.1.

TABLE 5.1: Machining conditions used for the experimental test

Parameter	Value
Cutting speed – v_c (m/min)	500
Feed per tooth – f_z (mm)	0.1
Axial depth of cut – a_p (mm)	1
Radial depth of cut – a_e (mm)	30

A sequence of layer machining, unclamping and measuring is repeated m times so the information related to different depths of the blank is obtained. Figure 5.3a shows the machining of a ‘j’ layer in the ribbed geometry, while Figure 5.3b shows the probing in the machining centre after the clamping is released.

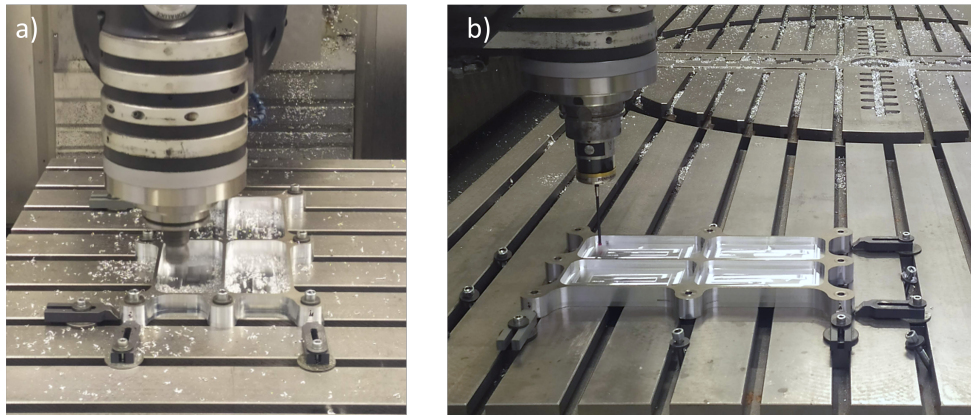


FIGURE 5.3: On-machine LR in a ribbed part for a 'j' layer: (a) Machining step; (b) Measuring step done by probing in the machining centre after the clamping is released.

The part deformation measurements are performed with a Renishaw RMP600 high-accuracy touch probe, probing the machined surface on a grid of 6x4 points, as depicted in Figure 5.4. The amount of measuring points is chosen as a compromise between accuracy and time. The MIRS generated on the machined surface are measured by iHD (Section 4.3, Fig. 4.13).

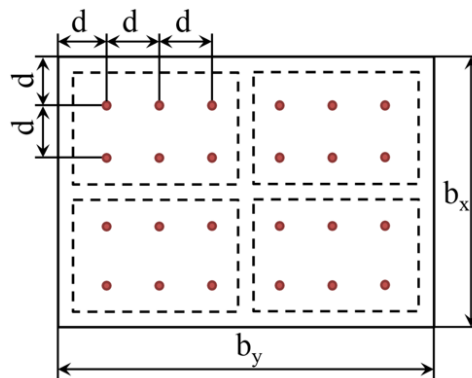


FIGURE 5.4: Probing grid of the BIRS measurement by on-machine LR.

The probing error is introduced following the procedure of Section 3.3.2.3. The initial curvatures and MIRS for the uncertainty assessment simulation, were measured in the test parts.

5.2.2 Results

First, the curvature progressions obtained from the probing data were used directly to calculate stresses. These curvature progressions could be used in their raw form (Fig. 5.5a), or after filtering (Fig. 5.5b), as explained in Chapter 3.

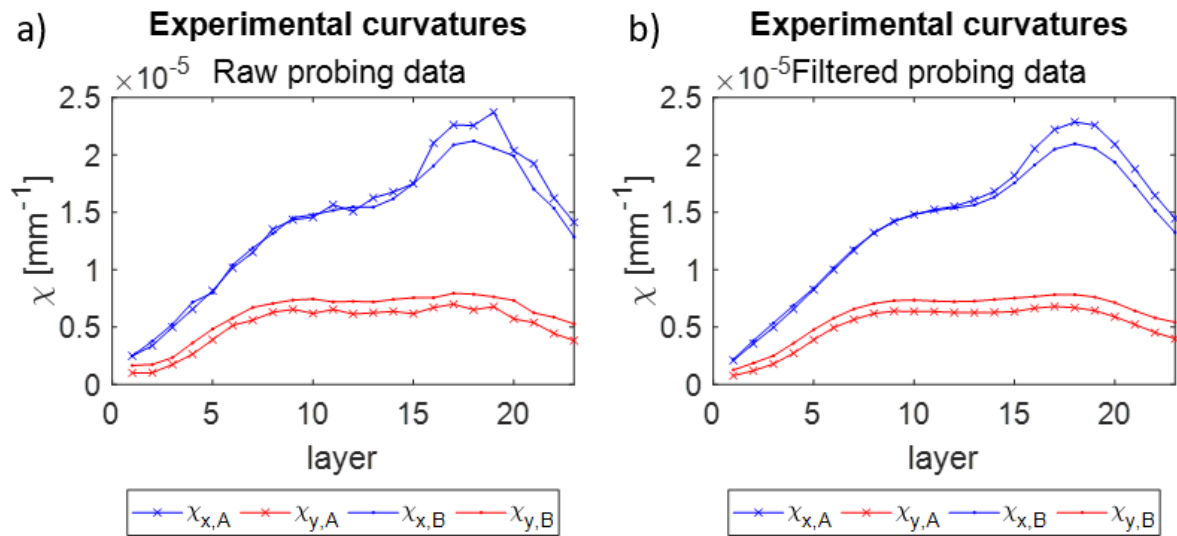


FIGURE 5.5: Curvature progressions obtained experimentally by on-machine LR in two parts (A and B), using: a) Raw probing data; b) Filtered probing data.

From these curvatures, using the multicoupled formulation (Section 3.2.2.4), BIRS profiles were obtained (Fig. 5.6). Notice that the BIRS profiles are shown only for the 23 layers machined during the LR tests.

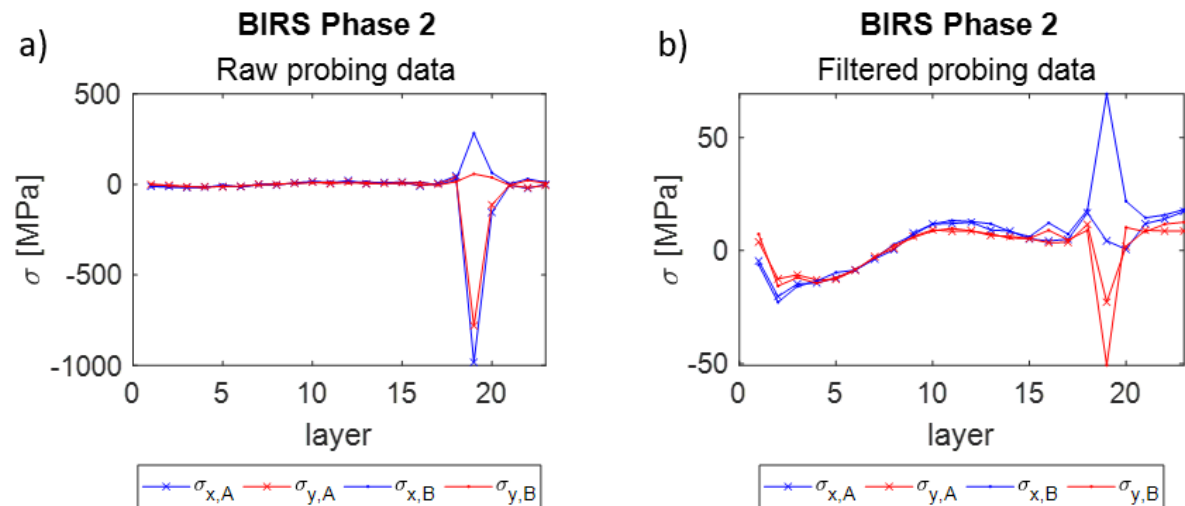


FIGURE 5.6: BIRS obtained experimentally by on-machine LR with the multi-coupled formulation in two parts (A and B), using: a) Raw probing data; b) Filtered probing data.

In both stress profiles high stress peak appear, similar to the shape of the theoretical analysis performed in Section 3.3.3 (Fig. 3.37 and 3.41). However, neither the sign nor the magnitude of the peak are the same for the two blanks. Moreover, if experimental results are compared with simulation data, the peak appears closer to the blank's middle height

and, also, it is much higher, reaching 1000 MPa for one of the blanks. Compared to the results of the theoretical analysis, when raw data is used for the stress calculation the peak is higher than the one obtained for the filtered data.

Next, both stress profiles, raw and filtered, are completed using the four BIRS data treatment options (Fig. 3.20). Figure 5.7 shows for the part A the stress profiles based on filtered curvature results using the four options to complete BIRS.

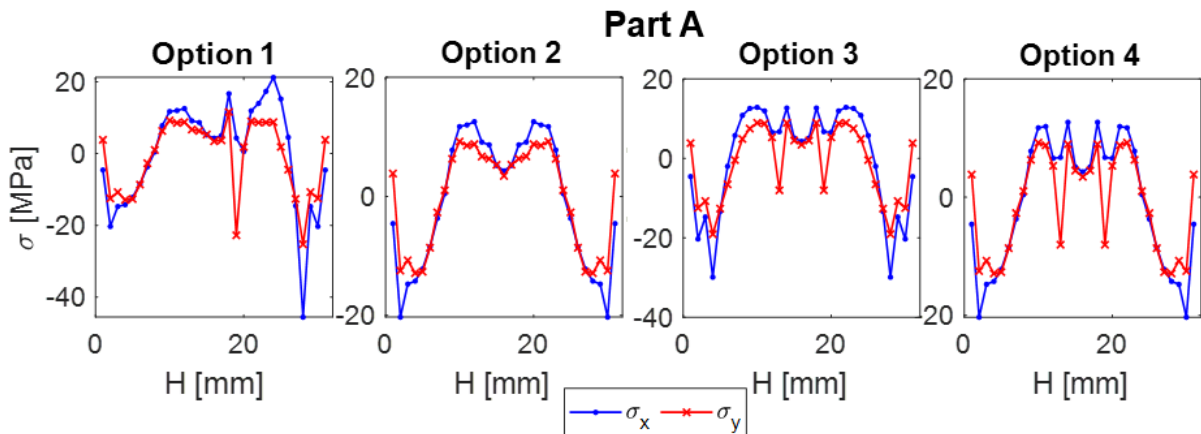


FIGURE 5.7: BIRS profiles completed using the four BIRS data treatment options in part A using filtered probing data.

Analogous plots could be obtained with for BIRS obtained with raw data and for part B.

From these BIRS profiles, the curvatures obtained from simulating a LR using the inverse LR formulation would be analogous to Phase 3 of the uncertainty assessment described in Section 3.3.1. These curvatures are then compared with the ones obtained from the experimental probing data, as depicted in figures 5.8 and 5.9.

In both figures the experimental curvature progressions obtained from probing data are displayed with black crosses, and the ones after data filtering with a black line. The uncertainty range for a probing error of 0.010mm with a confidence level of 99.7% is marked with red dashed lines, for which the minimum standard deviation, corresponding to option 2, is chosen. Finally, the simulation curvatures of Phase 3 are displayed in grey, where the round shallow marker displays the case of raw data without filter, and the filled round marker the case of filtered data. This is plotted for each of the stress data treatment options (Section 3.3.1.1, Fig. 3.20). Results show that, when using stress treatment option 2 and filtered curvature data, Phase 3 curvature results fall within the uncertainty range calculated as explained in Chapter 3.

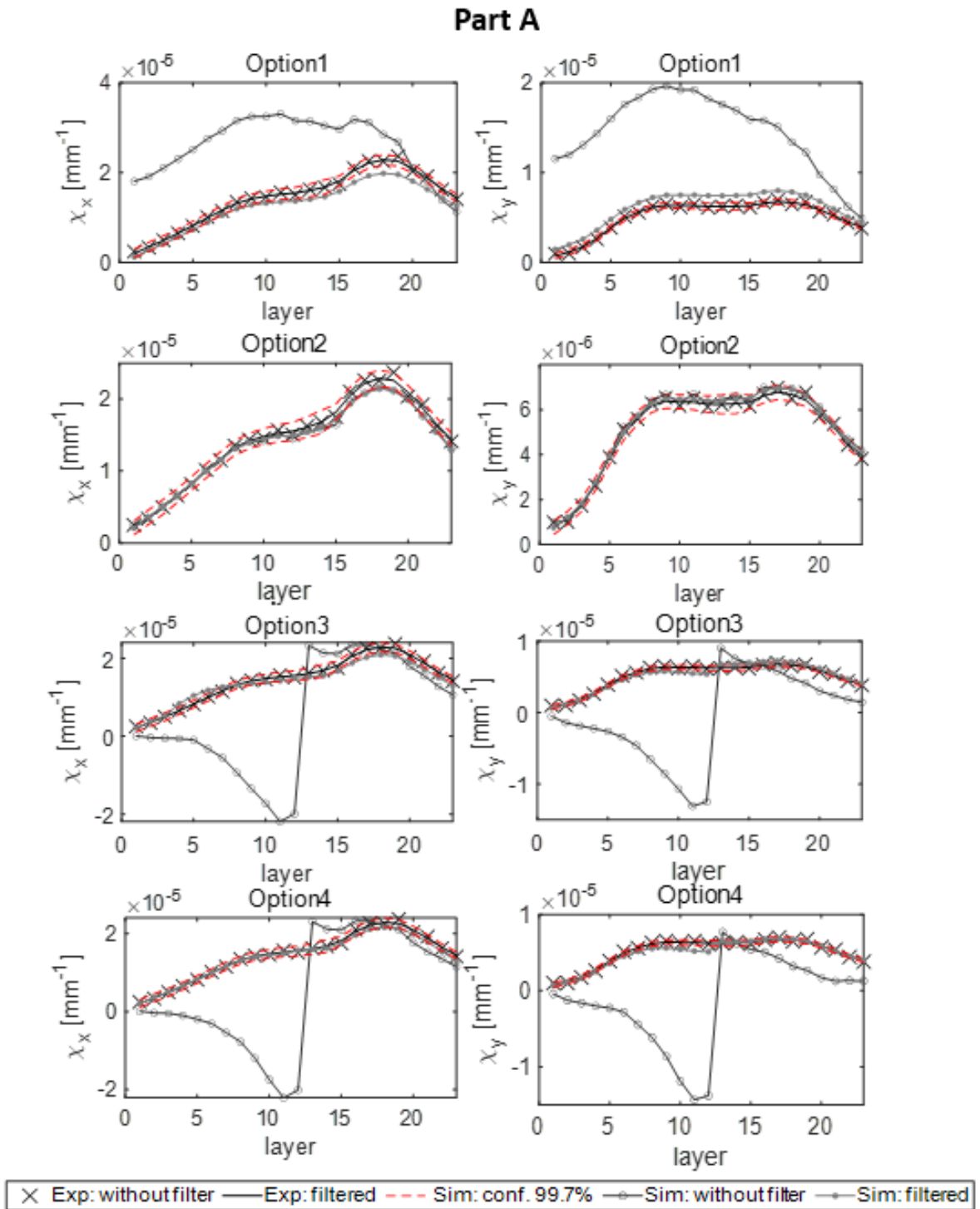


FIGURE 5.8: Part A: Experimental curvatures measured by probing compared with the ones obtained from stresses in Phase 3, for different data treatment options, displaying the uncertainty range for a probing error of 0.010mm.

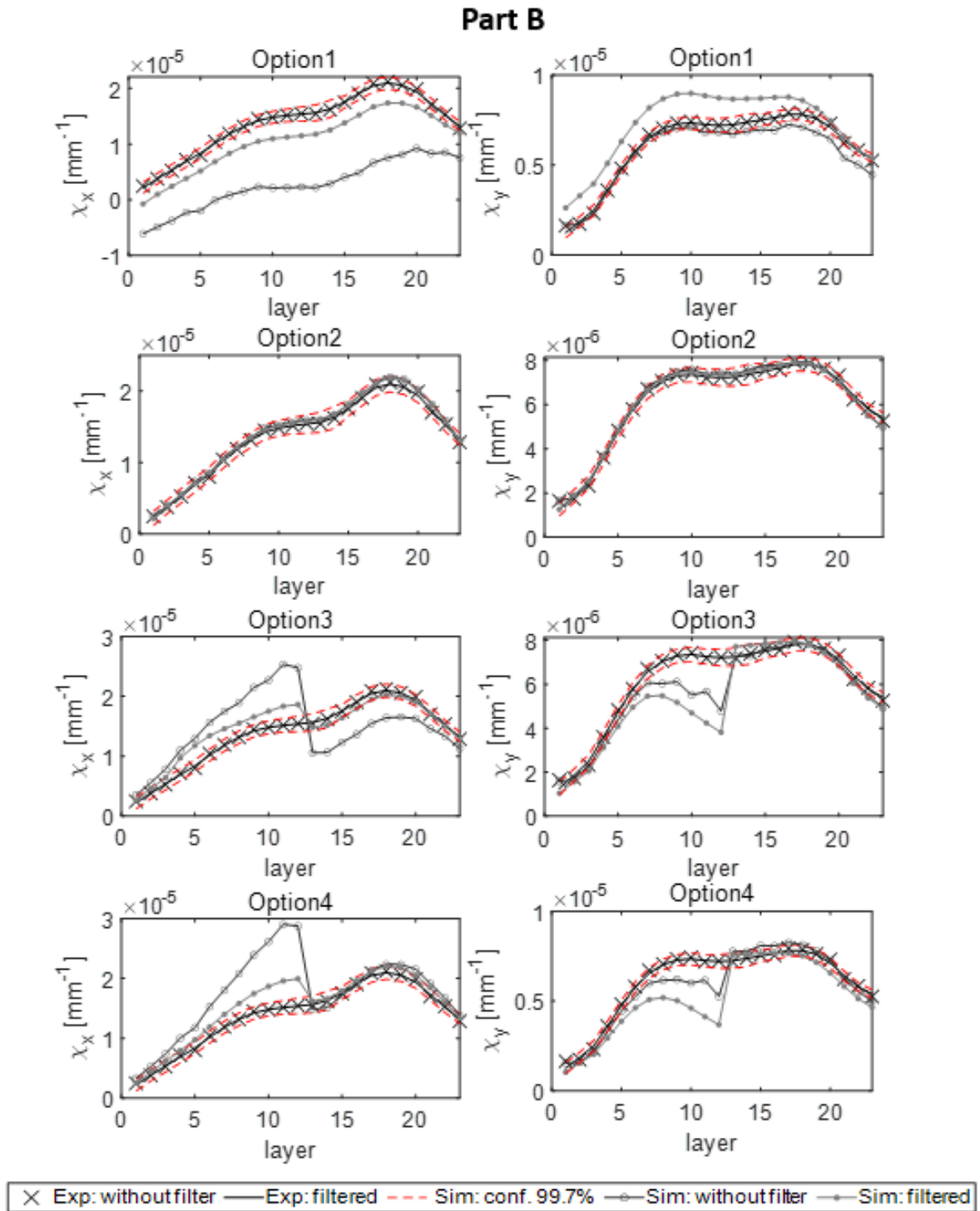


FIGURE 5.9: Part B: Experimental curvatures measured by probing compared with the ones obtained from stresses in Phase 3, for different data treatment options, displaying the uncertainty range for a probing error of 0.010mm.

The measured BIRS profiles of parts A and B are depicted in Figure 5.10, where the error bars represent the uncertainty of the on-machine LR method due to random probing errors of 0.010 mm.

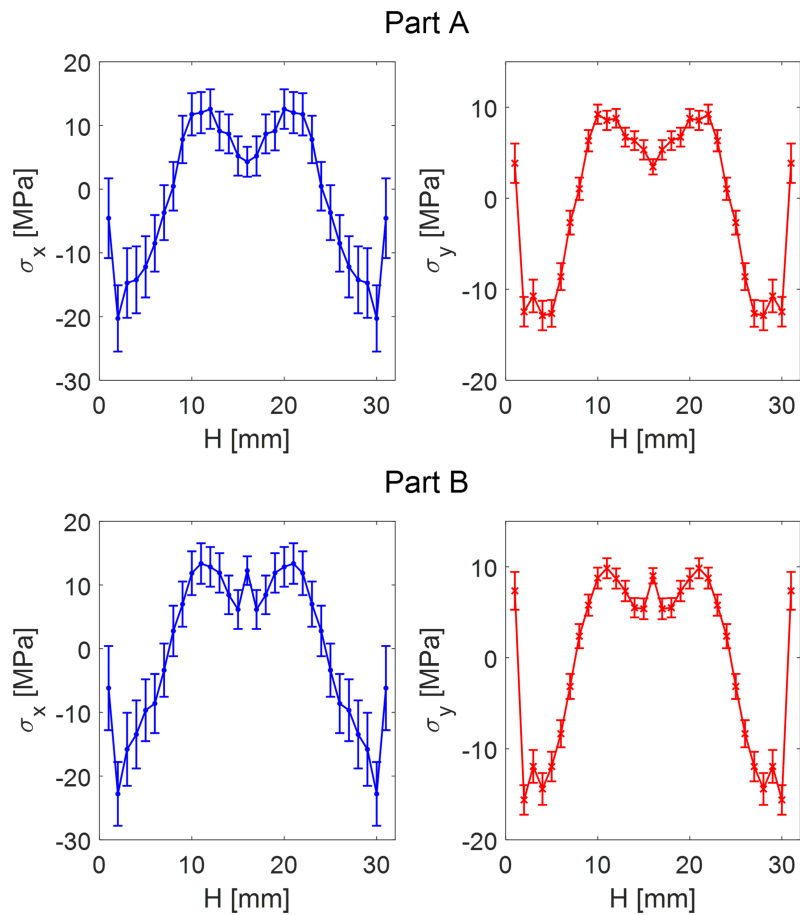


FIGURE 5.10: BIRS measured experimentally by on-machine LR for parts A and B including the uncertainty ranges.

Once the BIRS are characterized, and with their uncertainty range assessed, the final distortion of these parts leaving a floor thickness of 3mm can be predicted. This way, Figure 5.11 depicts the experimental curvatures measured in the final part with black crosses, and the simulation results including the uncertainty range (3σ) in blue for the X direction and in red for the Y direction.

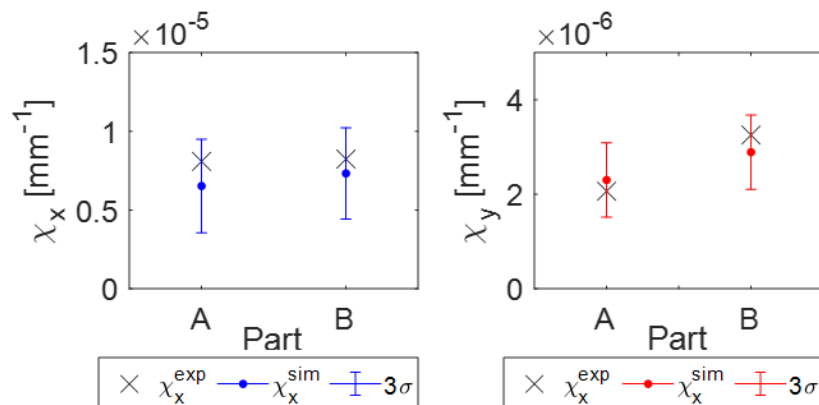


FIGURE 5.11: Distortion simulation including uncertainty range and experimental values for the two test parts A and B, using the BIRS measured by ribbed on-machine LR.

Results show that, in both test-parts, the final experimental curvatures are very close to the simulated values, falling within the calculated uncertainty range for them.

From these curvatures, the deformations in Z direction (δ_z) can be calculated for different part sizes. Table 5.2 displays the experimental deformations (δ_z^{exp}), simulation deformations (δ_z^{sim}), the difference amongst them (error) and the simulation uncertainty range for the test-part dimensions and for a theoretical 1000x1000mm part. Results show that for the dimensions of the test-parts, the errors between experimental and simulation results are below a 10%. In the case of a hypothetical part dimensions of 1000x1000mm, this error would be below 15%.

TABLE 5.2: Distortion results as deformations in Z direction (δ_z).

Part dimensions	δ_z^{exp} [mm]	δ_z^{sim} [mm]	Error [mm]	Uncertainty 3σ [mm]
200x400 mm				
A	0.082	0.079	0.003	0.031
B	0.106	0.095	0.011	0.030
1000x1000 mm				
A	1.271	1.100	0.171	0.469
B	1.437	1.278	0.159	0.461

5.2.3 Discussion

In this section the on-machine LR method for BIRS characterization is experimentally evaluated in ribbed geometries of Al 7050-T7451. In order to determine the accuracy of the measured BIRS, curvatures are calculated back (Phase 3) using the inverse formulation and the measured BIRS, and these are compared with experimental curvature measurements.

Analyzing the curvature results of figures 5.8 and 5.9, it can be seen that the BIRS data treatment options 1, 3 and 4 generate high deviations on the results for raw curvature data. When filtered curvature data is used, the deviations are greatly reduced, but the curvatures from Phase 3 lay still out of the uncertainty bands calculated for the experimental data when using those options, especially in the case of part B. When using the BIRS data treatment option 2, the curvature results from Phase 3 are considerably improved for both raw and filtered data, with slightly better results for the filtered data. These experimental results corroborate the conclusions withdrawn from the theoretical analysis (Section 3.3.4). It is important to remark that the effects of MIRS and clamping stress due to initial curvature are not negligible, and therefore its consideration in the formulation is required to avoid errors in BIRS measurement, as well as, in distortion prediction.

Moreover, almost all experimental curvature measurements fall within the uncertainty range obtained from the Monte Carlo simulation with a probing error of 0.010mm. As option 2 means direct symmetry of the obtained stress profile values, machining just until the middle height of the blanks would be enough to perform the BIRS characterization, which shortens the time needed for performing a BIRS measurement by on-machine LR method. Nevertheless, for the test part A, in X direction, just filtering seems to give good results for other options of completing the stress profile, such as option 4. Actually, this option has its benefits in cases where the deformations are expected to be very small in the first half of the profile, below the range of uncertainty of the measurement device, and practically only noise is measured. Also in cases where in the first half of the blank a change in the curvature sign appears, and therefore singularities could create high uncertainty peaks.

Finally, although the good results obtained regarding final part distortion calculation, it must be noted that in this analysis the aim was verifying that the on-machine LR method in ribbed geometries is a good method for BIRS measurement. Its capability of application in industrial environments by untrained staff and using common equipment and tools, enables industrial implementation, which is a novel and distinctive feature in comparison with available BIRS measurement methods. Besides, this method enables the characterization of BIRS in real-sized blanks with ribbed geometry, still usable for manufacturing final components, which offers the possibility of employing distortion control techniques based on accurate stress data in manufacturing lines. With the on-machine LR method, the uncertainty of the measurement and its relation to the final distortion can be quickly quantified, which provides useful information in regards of the achievable part precision both at the process planing stage and also at the shop-floor.

Nevertheless, its main limitation is that performing a complete BIRS measurement by on-machine LR implies the machining of half of the blanks' height layer by layer. This is very time consuming for industrial application and, in some part geometries it is not even feasible. For these reasons, Section 5.4 explores a different alternative to overcome these limitations.

5.3 Analysis of distortion control through MIRS customization

In this section, the results of the MIRS empirical model developed in Chapter 4 are used for analyzing their effect on the final distortion of different part geometries of titanium. In this way, this section evaluates the possibility of modifying the part distortion through the proper selection of machining conditions, namely MIRS customization.

In order to isolate the effect of MIRS and be able to determine to which extent distortion can be controlled through MIRS customization, BIRS are not included as input loads in the models of the study displayed next.

5.3.1 Test definition

Taking into account the typical size of titanium aircraft parts (fittings and hinges), a test-case dimension 260x140x10mm is chosen. With these dimensions, six different ribbed geometries are defined, three symmetric and three asymmetric, as depicted in Figure 5.12, with ribs and floor thickness of 2mm. The longitudinal direction corresponds to the X direction while the transverse one would be Y. The material of the parts is Ti6Al4V, and its chemical composition and mechanical properties are displayed in tables 4.6 and 4.7.

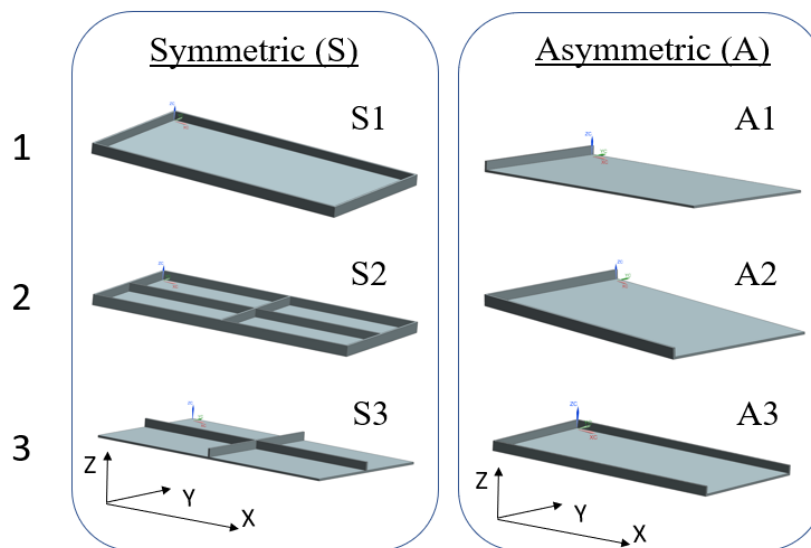


FIGURE 5.12: Geometries of the dist. analysis in Ti6Al4V upon MIRS customization.

Considering the results of the MIRS empirical model developed in Chapter 4, the two extreme cases of minimum and maximum MIRS corresponding to the cutting parameters combinations $v_c 60$, $f_z 0.02$ and $v_c 90$, $f_z 0.05$ respectively, as well as, the two perpendicular directions (feed and transverse), are considered (Fig. 5.13).

It is important to note that, due to the machining finishing conditions within which the MIRS model is built, the penetration depth of MIRS is very shallow and no tensile stress values appear. For these reasons, the variability amongst them is not very high. Nevertheless, the difference between the MIRS profiles MAX feed and MIN feed is approximately 200 MPa, which is significant.

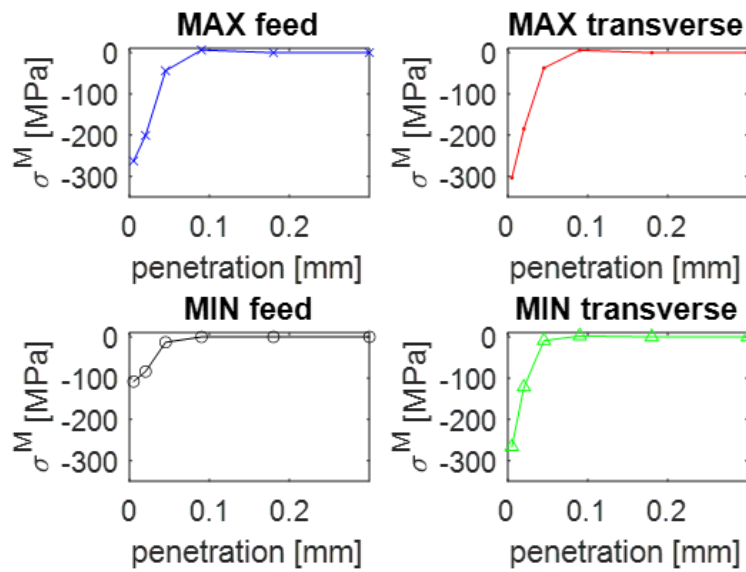


FIGURE 5.13: MIRS profiles used for building different case combinations for the distortion analysis on Ti6Al4V upon MIRS customization.

For each of the geometries, MIRS are introduced in the upper and lower sides of the machined floors, marked in grey in Figure 5.14 as example for the geometry with one pocket (S1). This way, the four different MIRS profiles depicted in Figure 5.13 and the two surfaces in which these are introduced are combined, generating 16 case combinations.

The 16 different cases analyzed are labelled according to Table 5.3, which combine the magnitude and direction of the four MIRS profiles (Fig. 5.13) in the two machined surfaces (Fig. 5.14). Taking as example the case 1, the MIRS profile in the upper surface (Fig. 5.14) in the longitudinal (X) direction is MAX feed, and in the transverse (Y) direction is MAX transverse. In the lower surface of the case 1, the MIRS profile in the longitudinal (X) direction is MAX feed and in the transverse (Y) direction is MAX transverse, for being these equal in magnitude and direction. On the contrary, in case 15 MAX transverse would be applied in the upper surface in longitudinal (X) direction and MAX feed in (Y). In the lower surface, MIN feed would be applied in longitudinal (X) direction and MIN transverse in transverse (Y) direction.

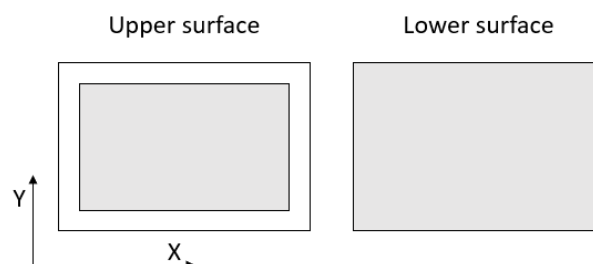


FIGURE 5.14: Sketch of the upper and lower surfaces in which MIRS loads are applied for the geometry S1.

TABLE 5.3: Case combinations analyzed regarding MIRS magnitude and direction variations.

Cases	Magnitude		Direction		MIRS Upper surface, longitudinal direction (X)
	Equal	Reverse	Equal	Reverse	
1	X		X		MAX feed
2	X		X		MIN feed
3	X		X		MAX transverse
4	X		X		MIN transverse
5	X			X	MAX feed
6	X			X	MIN feed
7	X			X	MAX transverse
8	X			X	MIN transverse
9		X	X		MAX feed
10		X	X		MIN feed
11		X	X		MAX transverse
12		X	X		MIN transverse
13		X		X	MAX feed
14		X		X	MIN feed
15		X		X	MAX transverse
16		X		X	MIN transverse

5.3.2 Results

Starting with the geometry S1, a single-pocket part, Figure 5.15 shows the curvatures in the two spatial directions (χ_x , χ_y) for each of the cases analyzed.

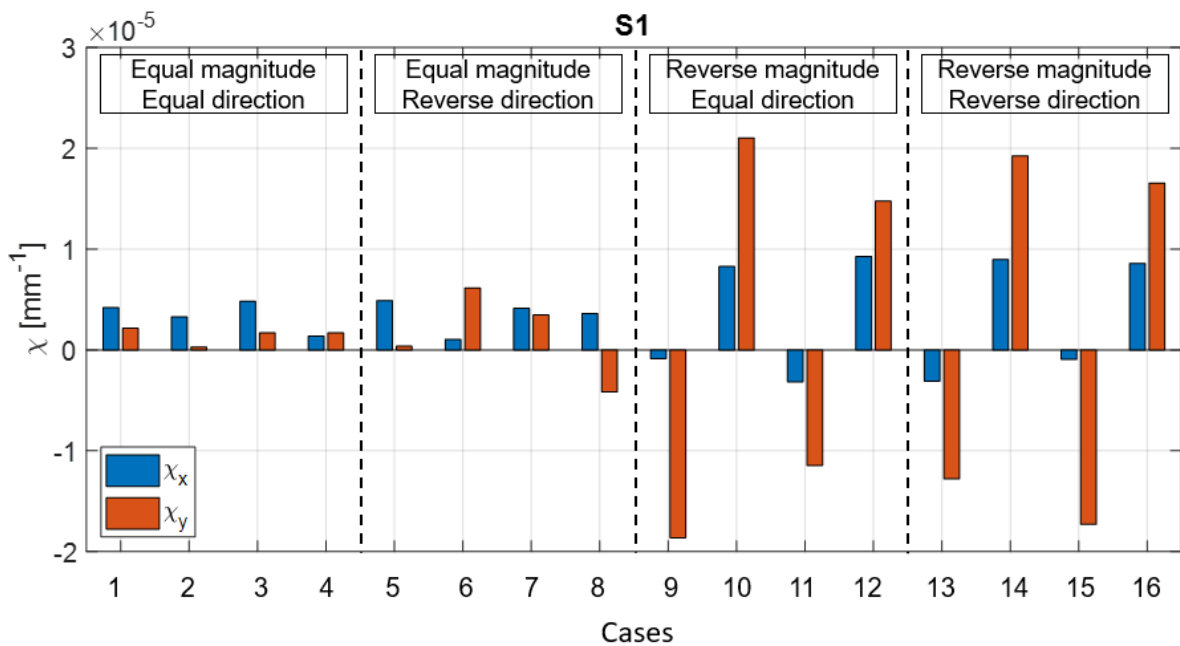


FIGURE 5.15: Curvatures obtained under different MIRS variations in the part geometry S1 of Ti6Al4V.

Results demonstrate that both the curvature magnitude and sign can be modified by selecting properly the MIRS induced in each of the machined surfaces (upper and lower) of the floor. The combination of these curvature signs and magnitude causes different final part distortion shapes, as depicted Figure 5.16, where six different final part distortion shapes can be seen for the geometry S1.

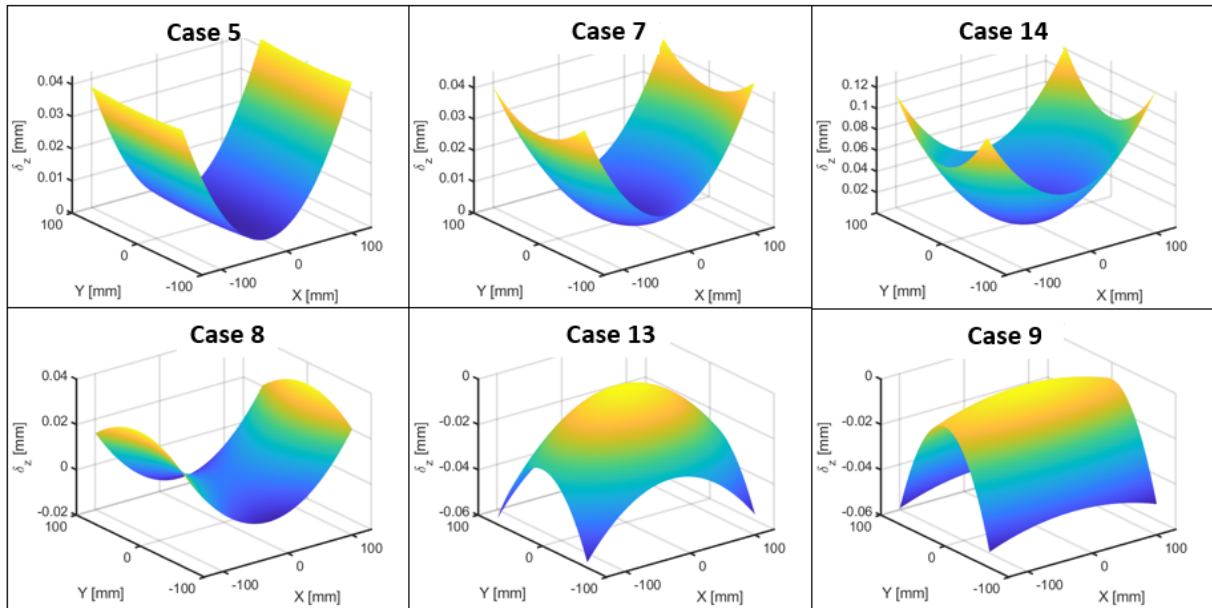


FIGURE 5.16: Different distortion shapes as a result of the curvatures combinations for the cases 5, 7, 8, 9, 13 and 14 in the part geometry S1.

When the input MIRS in the upper and lower surfaces of the floor have the same magnitude, cases 1 to 8 (Table 5.3), minor changes in the resulting curvatures can be seen. On the contrary, when the magnitude of MIRS is different in both faces, cases 9 to 16, the choice of specific MIRS in each of the surfaces can change the curvature sign, as well as, increase or decrease it. In terms of deformations in Z direction, δ_z , the case 4 results in a minimum absolute deformation of 0.016mm and the case 14 in a maximum absolute value of 0.122mm.

The following figures (Fig. 5.17 to 5.19), correspond to the curvatures of the part geometries S3, A1 and A2 for better representing the potential distortion control through MIRS customization. Results are similar but higher than the ones of part S1. In regards of part symmetry, there are no big differences, with the exception of the cases 5 to 8 (equal magnitude and reverse direction) which, in part A2 manage to modify the curvature amplitude and sign. In terms of deformations in Z direction, δ_z , for the curvatures displayed in figures 5.15 to 5.19, are gathered in Table 5.4.

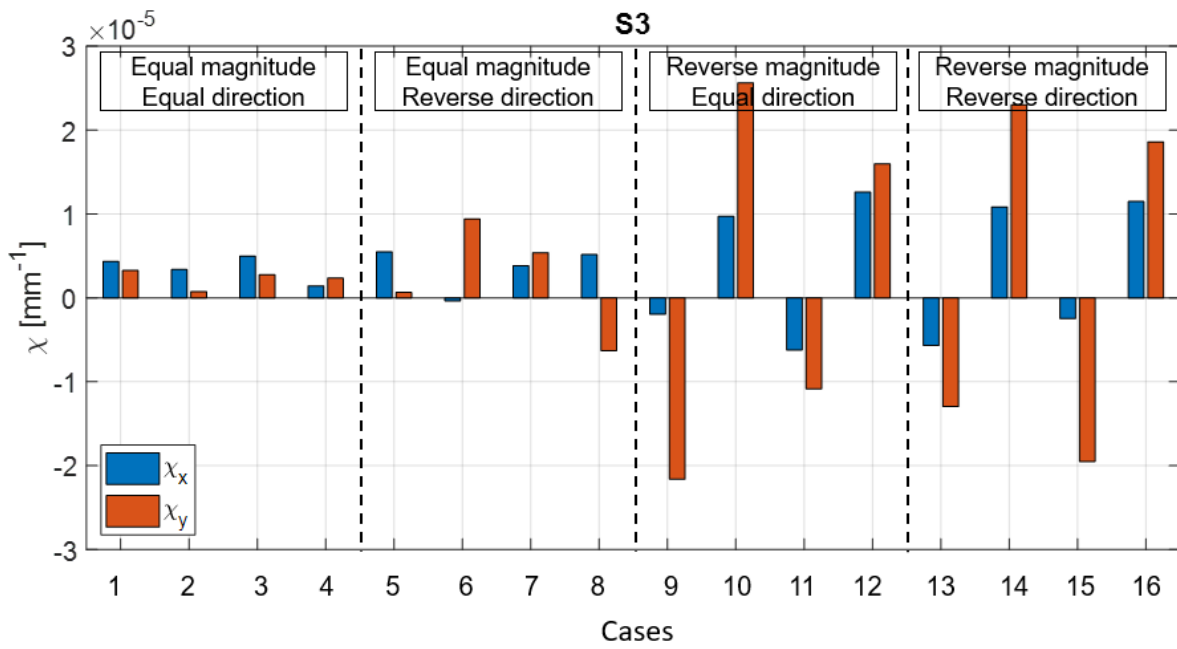


FIGURE 5.17: Curvatures obtained under different MIRS variations in the part geometry S3 of Ti6Al4V.

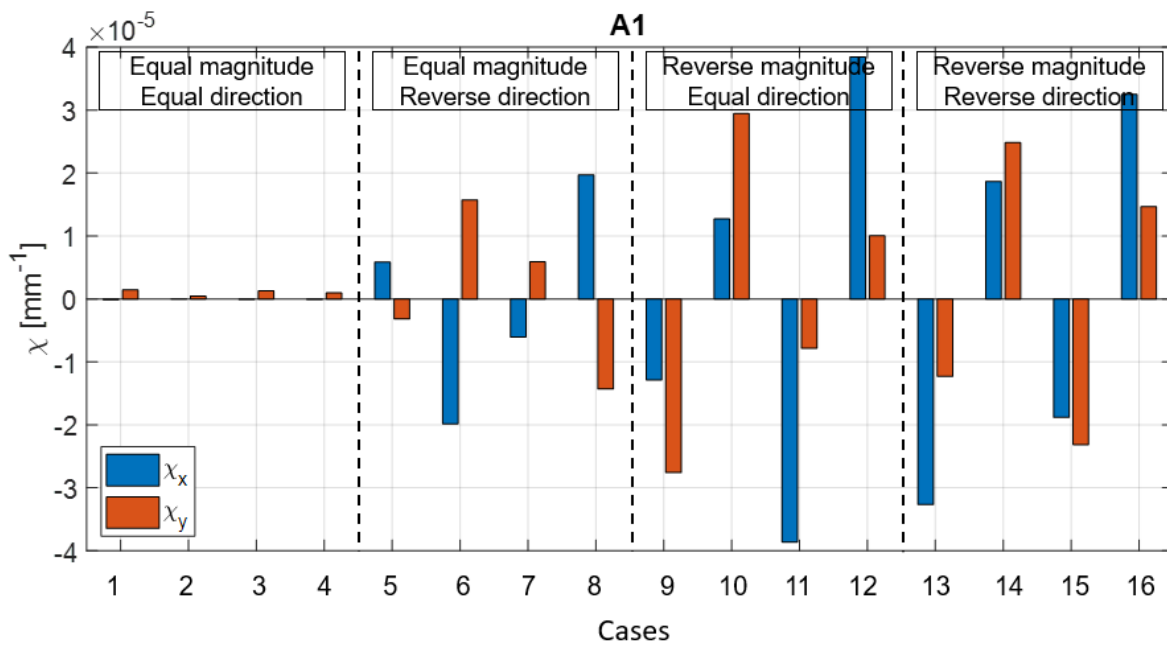


FIGURE 5.18: Curvatures obtained under different MIRS variations in the part geometry A1 of Ti6Al4V.

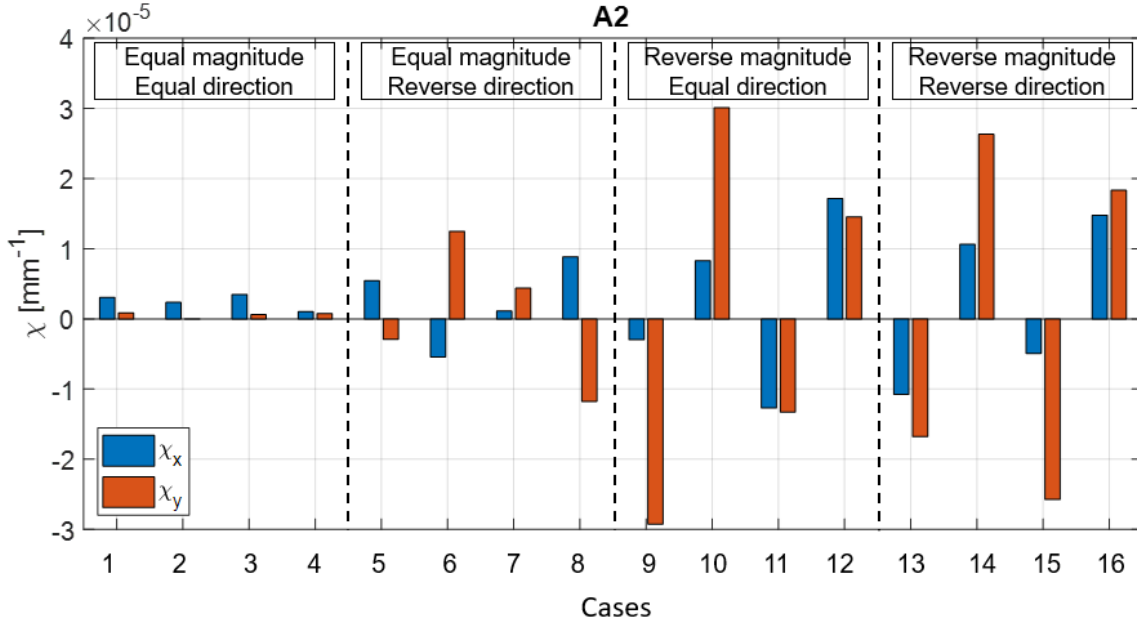


FIGURE 5.19: Curvatures obtained under different MIRS variations in the part geometry A2 of Ti6Al4V.

TABLE 5.4: Maximum and minimum deformations in Z direction, δ_z , for the curvatures of parts S1, S3, A1, and A2 under different combinations of MIRS.

Part	δ_z^{max} [mm]	Case	δ_z^{min} [mm]	Case
S1	0.122	14	0.016	4
S3	0.148	14	0.018	4
A1	0.35	12	0.001	2
A2	0.181	12	0.011	4

In some of the cases depicted in figures 5.15, 5.17, 5.18, and 5.19, MIRS generate high curvatures of different sign. This results in very different final part distortion for each of the cases depending on the MIRS values and directions. In this way, for a given part geometry, BIRS and distortion issues, the selection of some appropriate MIRS values/directions could work as a countermeasure to minimise this final part distortion. If the BIRS of the part cause significant distortion, MIRS could be customized as a countermeasure to minimize the final part distortion.

The combination of the MIRS profiles MAX-feed and MIN-feed is the main driver of the curvature sign change. When, from these two MIRS profiles, the maximum is input in the upper surface and the minimum in the lower surface, the curvature takes negative values, and vice versa. From the combinations of magnitude and direction simulated, results can be grouped in pairs for showing a similar behaviour, as displayed in Table 5.5. In this table, the cases marked in bold are the two chosen for further study in which the height of the part walls is increased from the original 10mm, to 20 and 50mm. This choice is based

on their higher longitudinal curvature (χ_x). The third case included in this analysis is the case 8, for combining a positive and a negative curvature. Figure 5.20 shows the results of the part geometries S3 and A2.

TABLE 5.5: Cases grouped according to the results similarity in magnitude and trend.

	Trend	
	Neg. χ trend	Pos. χ trend
Similar behaviour	9 ~ 15 11 ~ 13	10 ~ 14 12 ~ 16

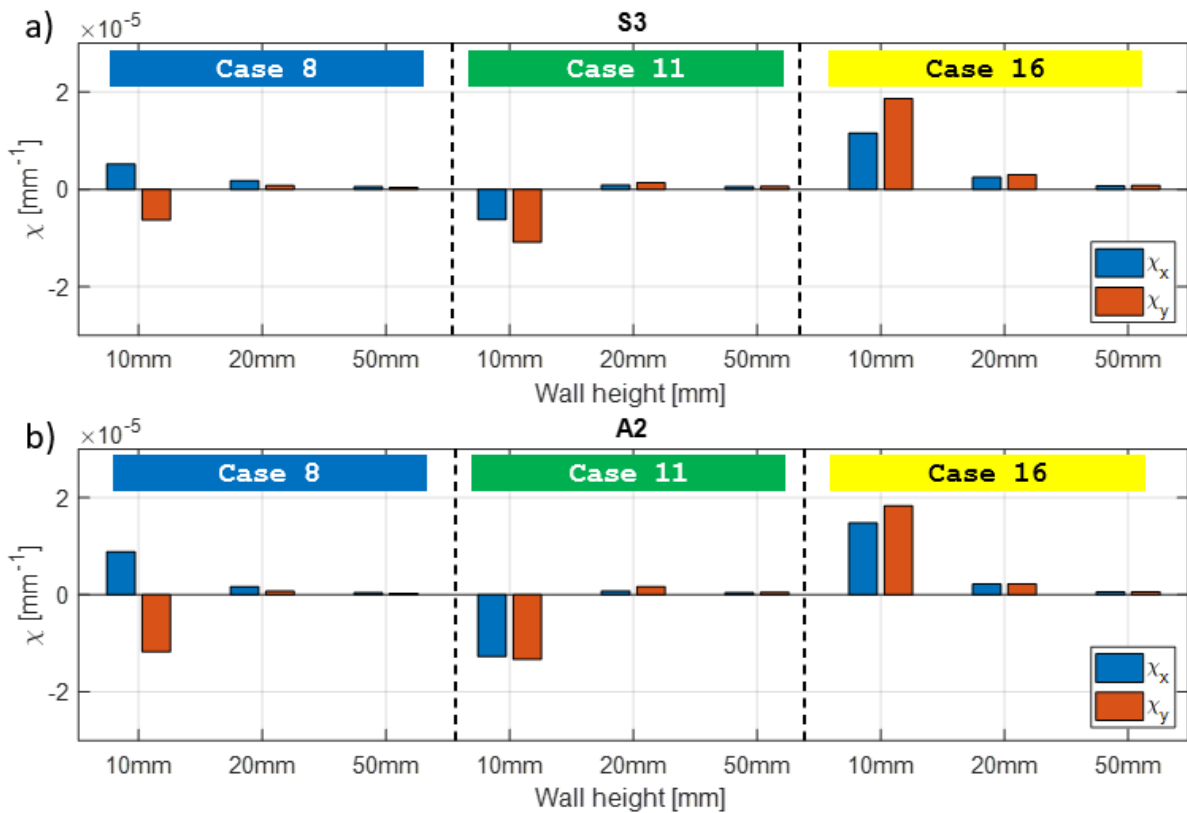


FIGURE 5.20: Analysis of the influence of wall height on the study of distortion control through MIRS customization.

It can be observed that with an increase of the wall height, thus an increase of the stiffness of the component, the effect of MIRS in distortion decreases and in, this way, also the possibility of controlling distortion through it. Performing a simple I^{geo} calculation with Equation 3.23 can draw the criterion for which this concept is applicable. Nevertheless, it is important to note that the limit value depends on the MIRS magnitude and penetration, and increases as they do.

5.3.3 Discussion

In this section the concept of modifying the distortion through MIRS customization is analyzed. Different ribbed part geometries, symmetric and asymmetric, of Ti6Al4V are studied, where different combinations of MIRS amplitude and direction in the two parallel sides of the parts' floor are introduced as input loads.

Results show that, through the proper selection of cutting parameters and machining strategy (MIRS direction linked to tool path), the curvature as effect of MIRS can be changed, in magnitude and sign. The changes mainly relate to the introduction of different MIRS in each of the parallel surfaces, which are obtained using a single tool. This knowledge can be used at the process planning stage to control distortion in two different ways. In one way, to reduce the distortion caused by MIRS choosing the parameter combination providing lower distortion. On the contrary, as previously explained, for a given part geometry unavoidable distortion issues could be caused by BIRS relaxation due to material removal. Considering the wide range of curvatures magnitudes and directions obtained in this analysis, the selection of the appropriate MIRS values/directions could work to compensate the curvature caused by BIRS relaxation and be a countermeasure to minimize the final part distortion.

It must be noted that the input MIRS used for the analysis have shallow penetration in comparison to other profiles in milled Ti6Al4V parts (Chapter 4). This way, MIRS induced by other tools and machining parameters could imply bigger MIRS profile changes and a wider range of actuation in relation with machining distortion.

Nevertheless, the concept of controlling distortion through MIRS customization is limited by the effect that MIRS have in the final distortion. Therefore, in cases where the MIRS effect on distortion is negligible in comparison to the effect of BIRS relaxation due to material removal, other distortion control methods should be used.

In summary, the control of machining distortion through MIRS customization is a potential strategy when other common strategies, such as best offset, are not sufficient. By a local adjustment of the parameters adapting the G-code, which modify MIRS (customize MIRS) distortion can be counteracted actively.

5.4 Prediction of final part distortion

Predicting machining distortion in aerostructures is the key to eliminate the costly and long sequential machining processes based on machining layer by layer, turning the part, and compensating distortion as it occurs. In order to use distortion prediction models,

BIRS data is necessary, which vary from one blank to another. The on-machine ribbed LR method enables measuring BIRS in the blanks from which final parts can be obtained. Besides being semi-non-destructive, it is implementable at the work-shop with common equipment and tools. However, the LR remains requiring long times to be performed, which hinders its applicability in production lines. Therefore, an alternative procedure is presented here, based on performing a reduced LR from which BIRS of the actual blanks are estimated and, in this way, the parts can be machined in one go.

In this section a distortion analysis is performed to obtain the final distortion of an aluminium part, analogous to a real aerostructure provided by an aerospace part manufacturer. The BIRS data is obtained through the combination of a reduced LR measurement and a BIRS estimation, representing a procedure implementable in production lines. For MIRS, iHD measurements are used. Experimental tests are carried out to validate the distortion simulation results.

5.4.1 Reduced LR measurement and BIRS estimation

In order to avoid a complete LR test, the proposed reduced LR is based on performing only 5 LR steps on the blank and, then, estimate the BIRS profile by the comparison of results with a full LR in a whole blank (all LR steps). This way, the reduced LR, consisting of 5 layers, does not require long times to be performed and, thus, has higher potential to be implemented in production lines.

With the stresses from the full LR test performed on an analogous blank and the curvatures of the ribbed and reduced LR, the concept of BIRS estimation assumes that, although BIRS vary from one blank to another, blanks of analogous characteristics have analogous stress profile shape [103], as Figure 5.21 illustrates.

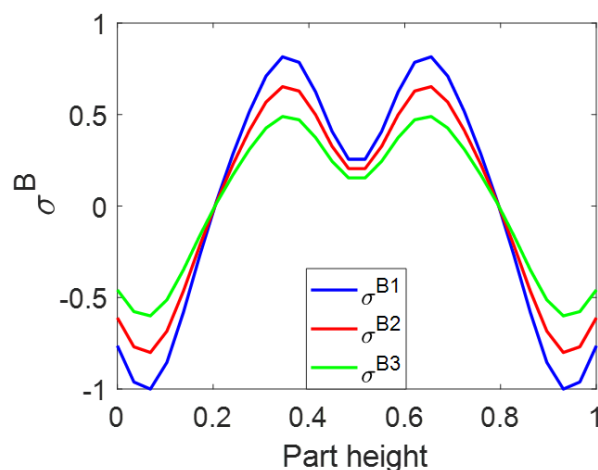


FIGURE 5.21: Normalized BIRS profiles in different blanks fulfilling the hypothesis analogous stress profile shape.

This way, the procedure of reduced LR and BIRS estimation consist of the following steps, which are depicted in Figure 5.22.

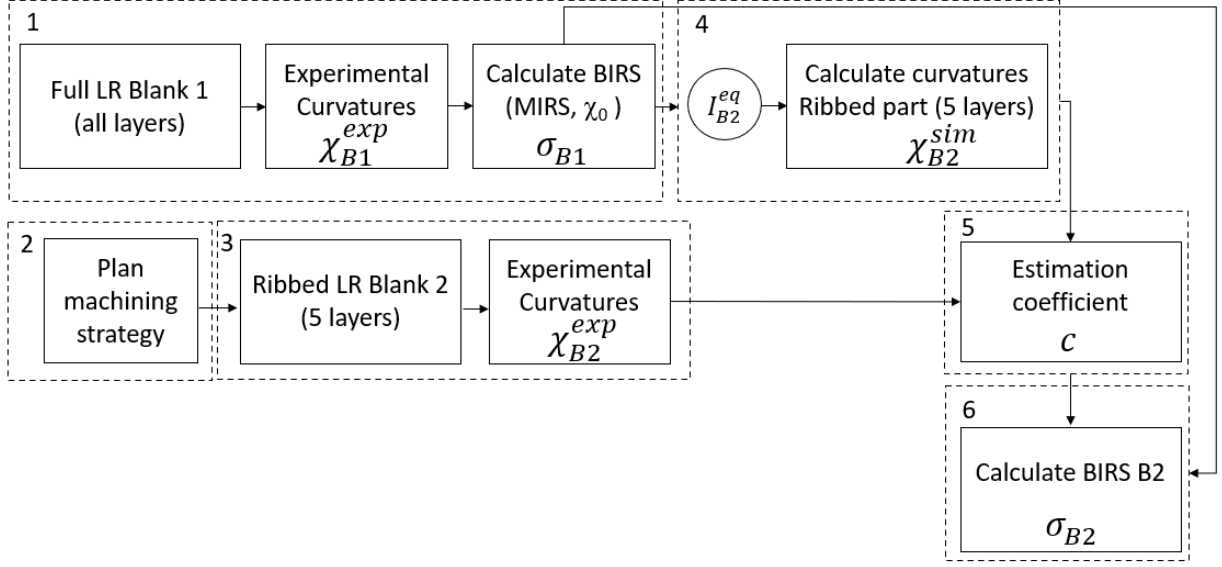


FIGURE 5.22: Procedure of reduced LR and BIRS estimation.

1. Perform a BIRS measurement in one blank ($B1$) by on-machine full LR. By this, the through-thickness stress profile (σ_{B1}) of a blank of the same characteristics (material, geometry, supplier and batch) as the one that will be used for manufacturing the final part ($B2$) are obtained.
2. Plan the machining strategy of the final part, including 5 layers machining, full roughing and finishing phases. These layers can be machined with ribs if the final part geometry requires it. As a minimum, an approximate depth of 15% of the height is considered to provide good results accuracy.
3. Perform the ribbed reduced LR of 5 layers in the blank from which the final part will be manufactured ($B2$), and measure the associated curvatures (χ_{B2}^{exp}).
4. Calculate the curvatures χ_{B2}^{sim} with the inverse LR formulation, using as input data the BIRS measured in the blank $B1$, the layer discretization and geometry (ribs layout) of $B2$, and the equivalent bending stiffness I_{B2}^{eq} .
5. Determine the BIRS estimation coefficient c_x using the equations 5.1 and 5.2 (with analogous expressions applying to Y direction), being m the number of LR steps performed, i.e. 5 LR steps.

$$c_{x,i} = \frac{(\chi_{B2,x}^{exp})_i + \nu \cdot (\chi_{B2,y}^{exp})_i}{(\chi_{B2,x}^{sim})_i + \nu \cdot (\chi_{B2,y}^{sim})_i} \quad (5.1)$$

$$c_x = \frac{\sum c_{x,i}}{m} \quad (5.2)$$

6. Obtain the estimated BIRS corresponding to blank $B2$ with Equation 5.3.

$$\sigma_{B2,x} = c_x \cdot \sigma_{B1,x} \quad (5.3)$$

For the longitudinal cases in which 1D formulation should be used, same equations apply, just by setting the Poisson coefficient to zero value.

5.4.2 Distortion prediction and uncertainty assessment

Once the BIRS of the blank $B2$ (σ_{B2}) are obtained, and the MIRS in the machined surfaces are measured, the final part distortion can be calculated. An important part of the distortion prediction consist of determining the uncertainty of the predicted values (linked to the BIRS measurement uncertainty). The workflow used to calculate this confidence range is depicted in Figure 5.23 where, following the analysis and procedure shown in Chapter 3, only probing errors are introduced as uncertainty source of the BIRS measurement, because of their major effect in comparison to other variables (Section 3.3.4).

This way, starting with the BIRS profiles measured by on-machine full LR in blank $B1$ (σ_{B1}^{exp}), and using the procedure described in Section 3.3.3.1, a cloud of BIRS profiles with probing error (σ_{B1}^{MC}) is obtained, which correspond to 2000 iterations.

After this, the cloud of BIRS profiles with probing error is used for calculating the curvatures, but this time with the layer discretization and width and ribbed geometry of the blank $B2$. As $B2$ is the blank from which the final part is obtained, if the LR is ribbed, the equivalent stiffness (I_{B2}^{eq}) is required for obtaining the cloud of curvatures (χ_{B2}^{MC}) in this step.

Relating this cloud of simulation curvatures with the experimental curvatures measured in the reduced LR of $B2$ (χ_{B2}^{exp}) using the Equation 5.1, a cloud of estimation coefficients (c^{MC}) can be obtained. With these coefficients and Equation 5.3, the cloud of BIRS of $B2$ (σ_{B2}^{MC}) are calculated. From this cloud of stresses, the BIRS estimation uncertainty linked to probing errors is obtained.

Finally, the distortion of the final component ($\chi_{B2,F}^{MC}$) is calculated using the estimated BIRS, the equivalent bending stiffness of the final part ($I_{B2,F}^{eq}$), and the MIRS and clamping stresses linked to the measured initial curvature of the blank. As the estimated BIRS are not a single profile, but a cloud of them representing the measuring uncertainty from the

LR test, the hybrid distortion model (based on the analytical inverse LR formulation and equivalent bending stiffness, Section 3.2.2.3, Eq. 3.24 to 3.26), is used for the distortion calculation. Thus, the distortion output is a cloud of final distortion values, from which the uncertainty of the distortion simulation can be calculated for a confidence level of 99.7% (3σ).

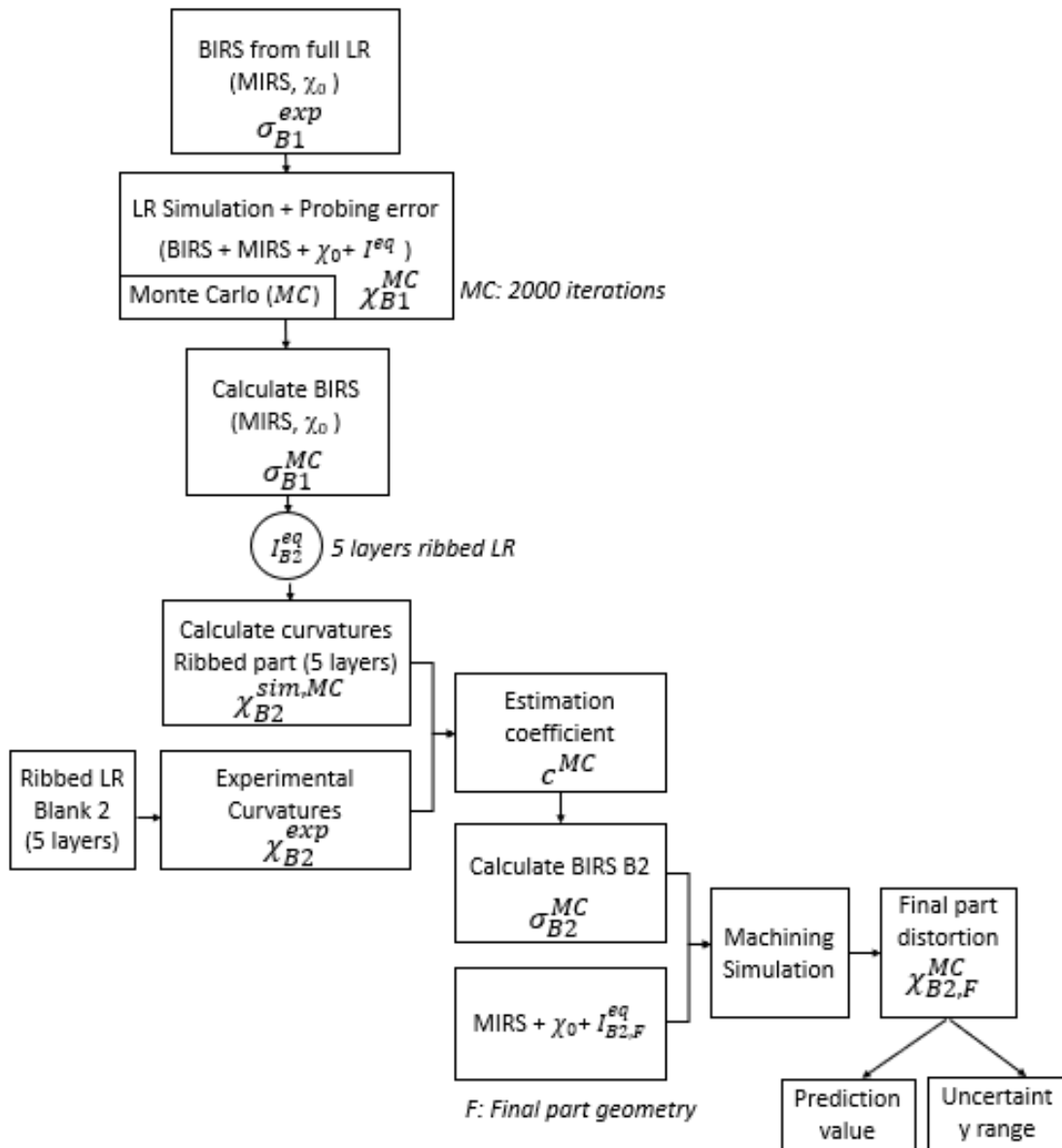


FIGURE 5.23: Workflow for final part distortion prediction, including uncertainty.

5.4.3 Test-case definition and experimental procedure

The proposed methodology was applied to Al7175-T3451 parts for experimental verification. The chemical composition and mechanical properties of this alloy are displayed in tables 4.2 and 4.3 respectively.

The part geometry represents a simplification of real part geometry, provided by an aerostructure manufacturer. Therefore, first a simplified part geometry, containing the key features (dimensions, ribs layout, walls and floors thickness) of the real part was carried out as depicted in Figure 5.24. The dimensions of this simplified geometry are defined in Figure 5.25.

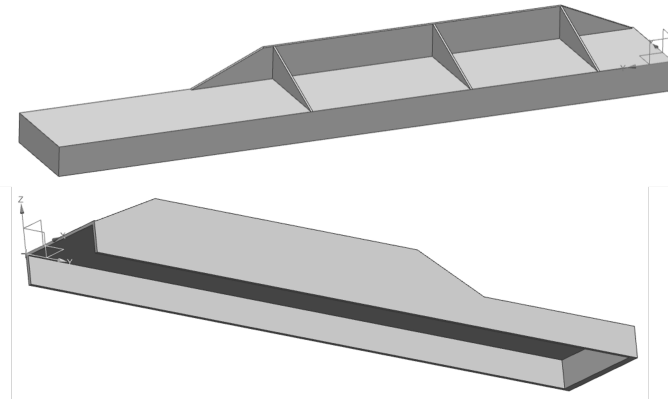


FIGURE 5.24: Simplified part geometry of Al7175-T7351 for the machining distortion analysis.

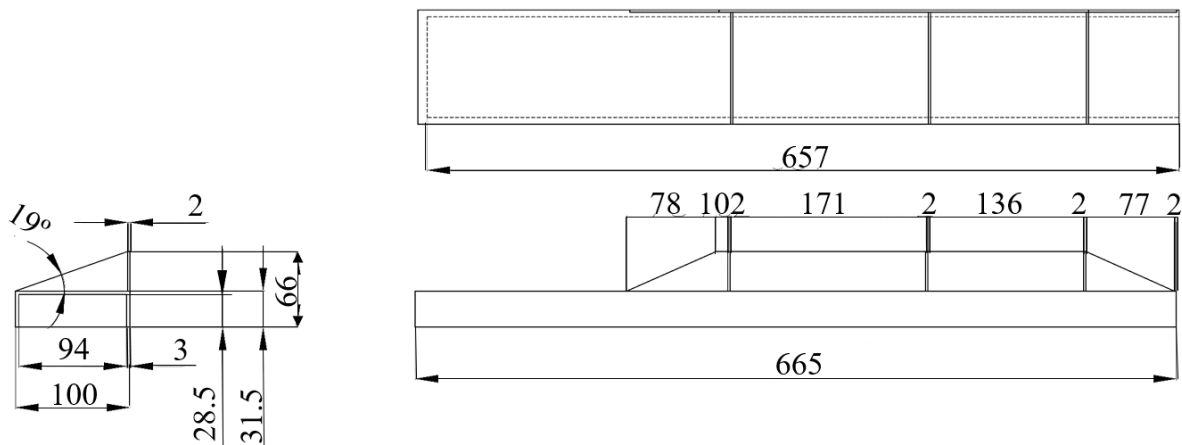


FIGURE 5.25: Dimensions of the simplified Al7175-T7351 part in millimeters.

According to the aerostructures manufacturer, in this part recurring non-conformities due to machining distortion were reported. More specifically, approximately a 50% of the parts showed significant distortions, being the flatness maximum tolerance 0.3mm (Figure 5.26).

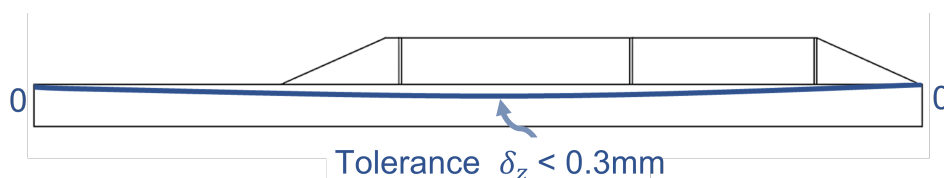


FIGURE 5.26: Recurring distortion shape in the machining of the Al7175-T7351 aerostructure.

In comparison with the previous test-case of Section 5.2 (a common geometry used for distortion investigations), the part here targeted had ribs in both sides of the floor with different heights and shapes. The ribs of the lower side of the part formed a U-shape or a pocket with one of the short sides open, and had a 3mm thickness. The upper side of the part though, had three triangular ribs in the transverse direction, and one in the longitudinal direction, being none of them centered on the part and having a thickness of 2mm.

The dimensions of the machining blanks used for machining these parts were 130x700x80 mm, leaving an offset for locating the part in different positions of 14mm. This way, each part was located in one specific offset as depicted in Figure 5.27. While Part *a* was located at the lowest position, just machining 1 mm from the pocket side for cleaning purposes, Part *b* was centered in the blank, leaving 7 mm at each side.

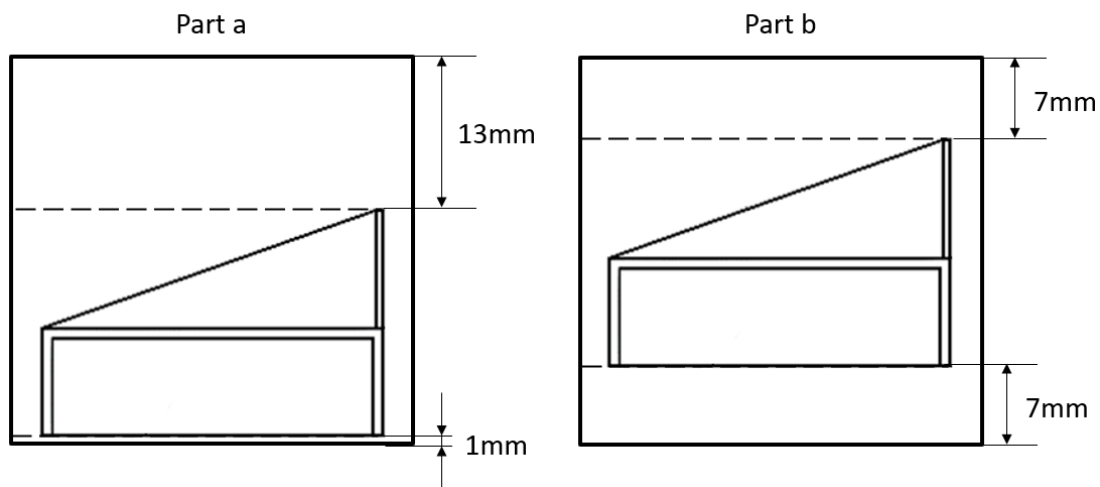


FIGURE 5.27: Part location within the blank and offset in each of the sides.

Considering the part dimensions and the high height to width ratio (> 0.6), the 1D formulation was used.

Concerning the RS input data for the distortion model, as mentioned, MIRS were measured by iHD (Fig. 4.16) and, BIRS were obtained using the concept of reduced LR and BIRS estimation introduced in Section 5.4.1. Therefore, the first step was performing a BIRS measurement by full on-machine LR in one blank, labelled for now on as σ_{full}^B .

Figure 5.28 shows the BIRS profile, σ_{full}^B , obtained from the blank after applying the LR method and uncertainty assessment procedure exposed in Chapter 3. Results show that the obtained BIRS have low magnitude and an M-shape profile, different from bibliography data on the same material, which showed a bell-shape profile measured by the contour method [123].

After obtaining the BIRS profile (Fig. 5.28), two blanks of the same batch, material and dimensions are used for the experimental verification of the distortion prediction introduced in sections 5.4.1 and 5.4.2.

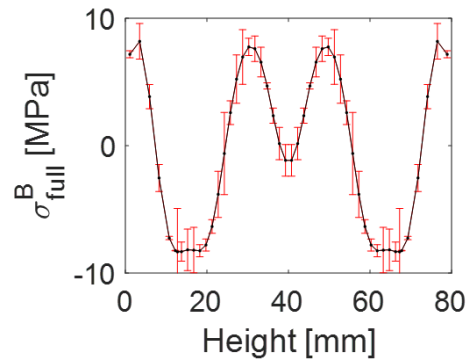


FIGURE 5.28: BIRS measured in a machining Al7175-T7351 blank of 130x700x80mm by on-machine Full LR.

The machining operations were carried out on a Soraluze FMT 4000 multitasking machine. For the test, two milling tools were used, a face mill of 80mm diameter from Kennametal 80A05RP90BG15C1WPM with 5 inserts BGHX15L5PCFRGG-K110M for the LR and the roughing operations, and the tool A2 (Table 4.4) for finishing operations. For the part deformation measurement a Renishaw RMP600 high-accuracy touch probe was used.

In order to perform the reduced LR, first, the part side in which these measurements are taken was chosen. Due to the test-case geometry, it was decided to perform the LR in the side where the fins have an open pocket shape. Considering this, a 4 setup machining strategy was chosen to reach all the faces of the part. Figure 5.29 depicts all the setups of the CAM simulations taken from the Nx software.

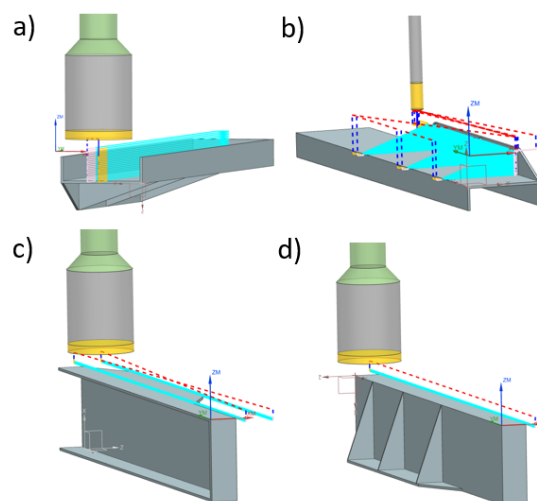


FIGURE 5.29: a) Setup 1: open pocket side machining; b) Setup 2: Triangle-ribbed side machining; c) Setup 3: small lateral side machining; d) Setup 4: large lateral side machining.

The first setup, depicted in Figure 5.29a, corresponds to the reduced LR, including layer machining and probing measurements (Fig. 5.30a and 5.30b respectively). In this setup the pocket-side machining was also carried out, including roughing and finishing operations.

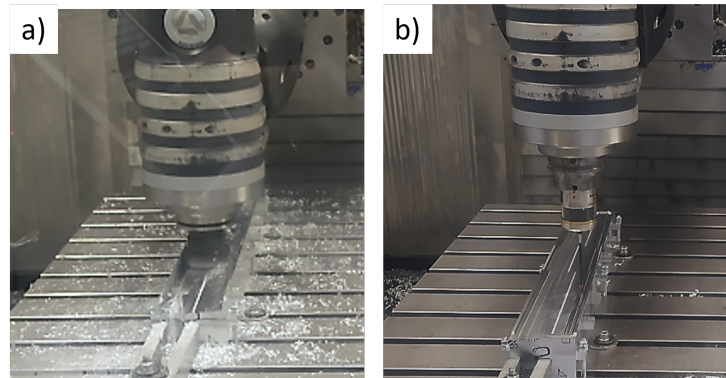


FIGURE 5.30: Reduced on-machine LR in Setup 1, open pocket side: a) machining of a layer 'j'; b) probing.

Then, the part was turned over and the side of the triangular ribs was machined (roughing and finishing), as shown in Figure 5.29b. Finally, the lateral sides of the part (figures 5.29c and 5.29d), which had an offset of 1mm each, were machined in the setups 3 and 4.

The machining conditions for the two tools are defined in Table 5.6. The axial and radial depth of cut varied for each operation. Figure 5.31 depicts the actual machining operations of parts *a* and *b* in setups 1 and 2 respectively.

TABLE 5.6: Machining conditions used for the experimental test.

Parameter	D80mm	D16mm
Cutting speed – v_c (m/min)	452	200
Feed rate – v_f (mm/min)	1620	2000

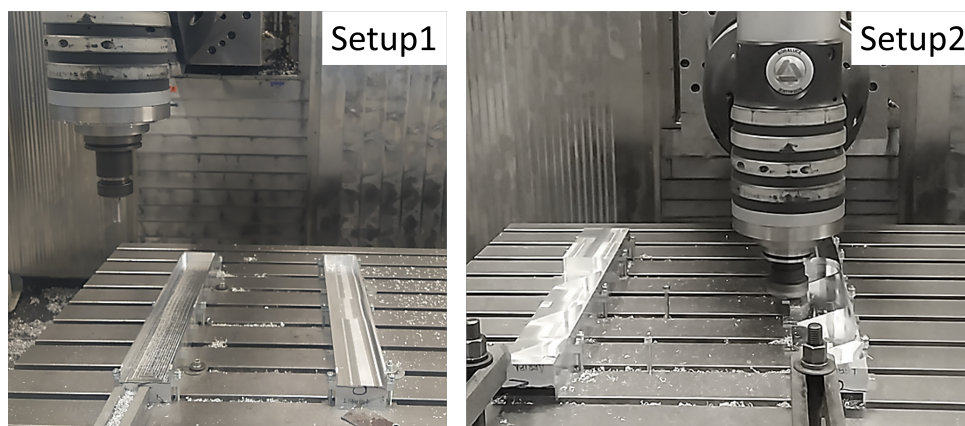


FIGURE 5.31: Machining of the two parts (*a* and *b*) in Setup 1, open pocket side, and Setup 2, triangle-ribbed side.

Regarding measurements, while the probing for the LR was performed in the machine with a touch-probe in a grid of 3x9 points, due to the low stiffness of the final part (Fig. 5.32a) and the corresponding swinging and elastic deflections caused by machine-integrated touch-probe, the final part measurements are made in a CMM Zeiss PRISMO 9/15/7 (Fig. 5.32b).

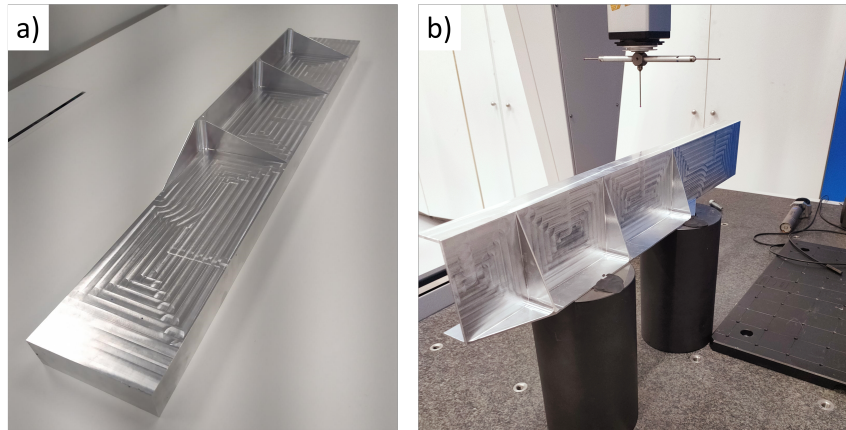


FIGURE 5.32: a) Final part machined; b) Measurements in a CMM.

Figure 5.33 shows the Part *a* deformation measurement results in comparison to a second order surface regression (Eq. 3.8 and 3.9). Two different measurements were taken in the final parts, one in a grid equal to the on-machine probing for the LR (Fig. 5.33a), and another one sweeping the surface, in the pocket side (Fig. 5.33b).

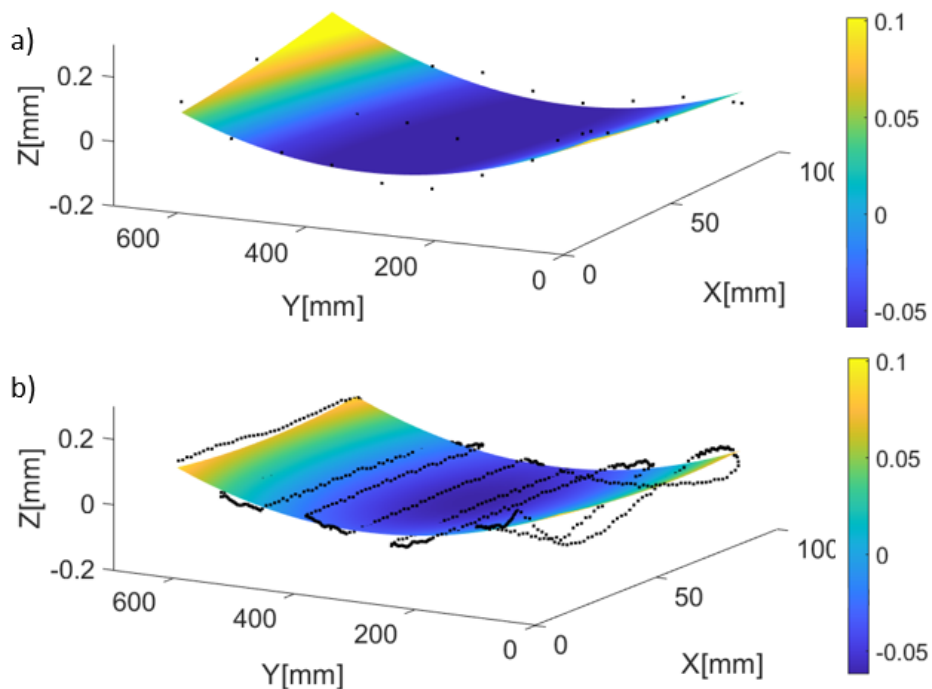


FIGURE 5.33: Final part probing in Part *a*: a) Grid 3x9; b) Sweeping the open pocket side.

5.4.4 Results

Simulations of ribbed LR with the inverse LR formulation were performed using as input the BIRS measured in the blank by full LR (σ_{full}^B), the MIRS measured in the machined surfaces, the initial curvatures, the geometry discretization and rib layout, and the equivalent bending stiffness (I^{eq}) of parts *a* and *b*. These simulation results and the experimental results from the reduced LR performed in parts *a* and *b* are depicted in Figure 5.34, where experimental curvatures are marked in lines with dots, and the simulation values in lines with crosses. As can be seen, while in the blank of part *a* the two curvature progressions cross each other, in the blank of part *b* they are parallel. Moreover, while on Part *b* all curvatures are near zero, in Part *a* they have higher absolute values, linked mainly to the initial curvature of the part.

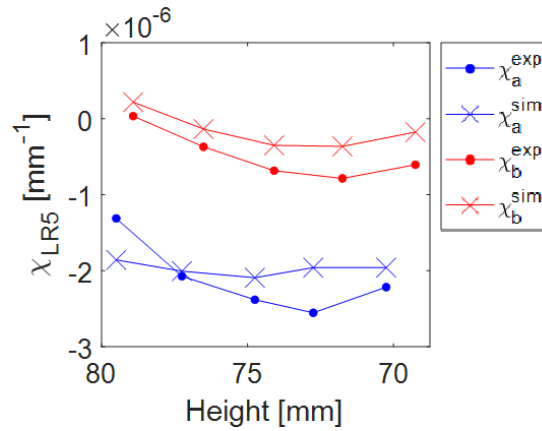


FIGURE 5.34: Data obtained in the reduced LR method: experimental and simulation curvatures of the reduced LR method.

With these values, the BIRS estimation coefficients were obtained with equations 5.1 and 5.2. The estimated BIRS profiles for the two blanks were calculated using Equation 5.3 and displayed in Figure 5.35.

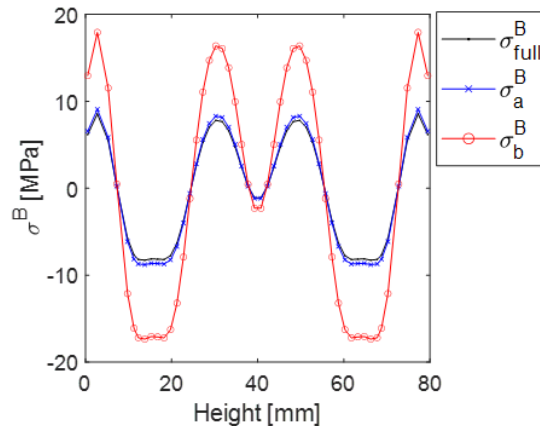


FIGURE 5.35: BIRS obtained by full LR in one sacrificial blank (σ_{full}^B) and estimated BIRS for the blanks *a* (σ_a^B) and *b* (σ_b^B), from which final parts were obtained.

Results show that, while the stress magnitude in blank *a* is slightly bigger than the base BIRS of the full LR (σ_{full}^B), in blank *b* the BIRS magnitude approximately doubles those values.

Following the workflow of Figure 5.23, the BIRS with probing uncertainty for each of the parts were obtained (Fig. 5.36). Looking at the results, it can be seen that the uncertainty of the BIRS of Part *b* is much higher than the uncertainty of Part *a*. This is because the curvature values obtained are near zero (Fig. 5.34), so the part deflections (δ_z) are close to the measurement uncertainty (0.01mm).

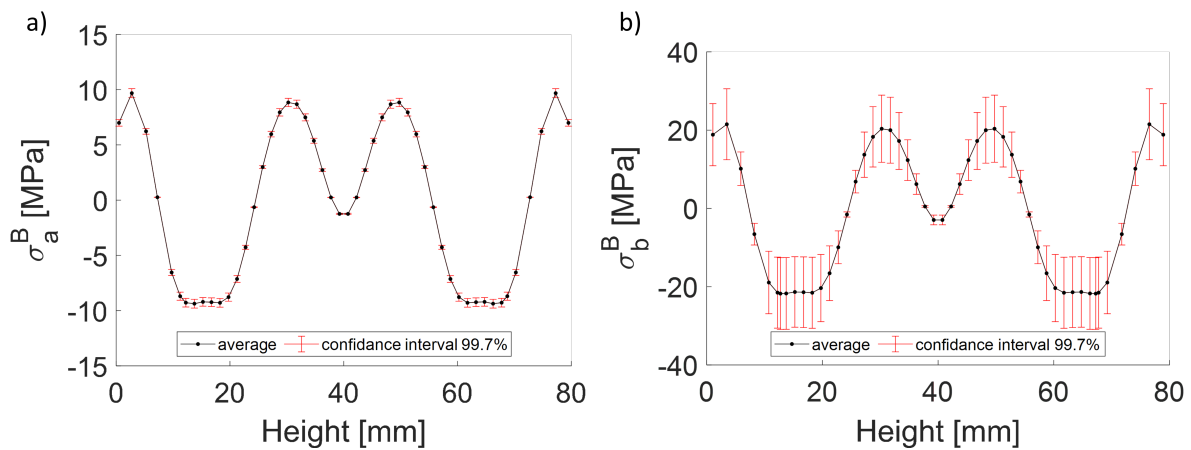


FIGURE 5.36: BIRS estimated with uncertainty ranges including measuring uncertainty due to probing errors: a) Part a; b) Part b.

To obtain the final part distortion, the estimated BIRS (Fig. 5.35), MIRS and initial curvature were introduced in the FEM model as depicted in Figure 5.37, from which the equivalent bending stiffness of the final part was calculated (Section 3.2.2.3).

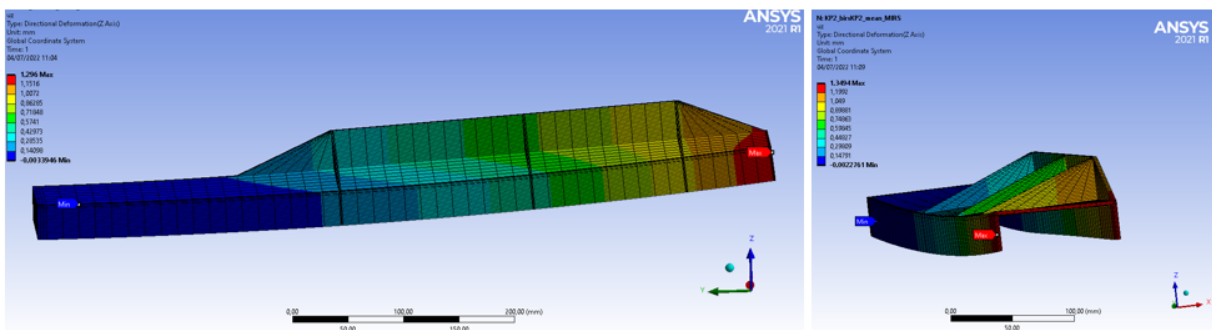


FIGURE 5.37: Distortion FEM simulation for obtaining the final part equivalent bending stiffness of parts *a* and *b*, displayed in two different orientations.

In order to obtain the uncertainty of the distortion prediction, first a hybrid distortion model was built combining the analytical inverse LR formulation with the numerical distortion model, which was used to obtain the equivalent bending stiffness. The numerical

part enabled to keep the accuracy of the model and it was just run once. This way, the hybrid model kept the agility of the analytical formulation. Using as input data the cloud of BIRS, the hybrid model was run iteratively for all BIRS profiles of the cloud, obtaining a cloud of final part distortions from which, the uncertainty of the distortion prediction was obtained.

Finally, distortion simulation results were contrasted with experimental results for both parts. Figure 5.38 shows the maximum part deformations in Z direction, where the black hollow circles are the experimental results, the red dots are the simulation results and the red bars represent their uncertainty range. These results are also gathered in Table 5.2, where experimental deformations (δ_z^{exp}), simulation deformations (δ_z^{sim}), the difference amongst them (error) and the simulation uncertainty range are gathered for both test-parts.

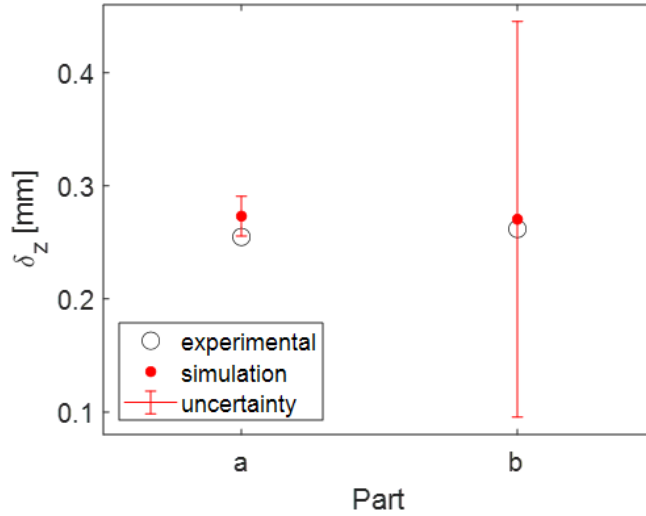


FIGURE 5.38: Distortion simulation using estimated BIRS, including uncertainty range and experimental values for the two test cases: a) Lowest offset; b) Same offset in both sides, upper and lower sides.

TABLE 5.7: Distortion results as deformations in Z direction (δ_z) of the parts *a* and *b*.

Part	δ_z^{exp} [mm]	δ_z^{sim} [mm]	Error [mm]	Sim. uncertainty [mm]
a	0.255	0.273	0.018	0.018
b	0.262	0.270	0.008	0.175

5.4.5 Discussion

In this section, a distortion prediction of real aerostructure parts is performed. For that, a reduced LR and BIRS estimation procedure is presented.

As it can be seen in Figure 5.38, the difference between experimental and simulation results are 7% and 3% for part *a* and *b* respectively. This demonstrates that accurate distortion predictions can be performed using estimated BIRS data obtained from a reduced LR test, as well as measured MIRS, initial curvatures and equivalent bending stiffness.

Regardless of the different magnitude of BIRS obtained through estimation, which are approximately double for part *b* respect to part *a* (Fig. 5.35), the difference in the experimental distortions is minimal in the two parts, 0.010mm, which is in the range of the probing uncertainty. This is because the offset locations have an impact in the distortion as explained in Chapter 2. In this way, for the hypothetical case of blanks with same BIRS, locating the part centered in the blank reduces the distortion for this particular geometry with ribs at both sides of the floor. However, as results show, the hypothesis of considering equal BIRS in blanks of the same batch, material and size is inaccurate and can lead to large distortion prediction errors.

Moreover, experimental results fall within the calculated uncertainty ranges in both cases. This simulation uncertainty is low compared with the experimental distortion value for part *a*, a 7%, while for part *b* is very large, a 67%. It must be noted that a large distortion prediction uncertainty limits in a certain extent the prediction capability of the simulation results. This large uncertainty is linked to the BIRS estimation (Fig. 5.35), which is very sensitive to curvatures values near zero because of the the relationship between part deformation and probing uncertainty. Thus, when the LR curvature progressions are near zero, these are more likely to have higher uncertainty ranges.

Summarizing, in this section, a real-part distortion prediction using the developments presented along this work is performed, which enable providing machining distortion estimations and uncertainty ranges in a simple and fast form. Experimental results demonstrate the prediction capability of the proposed method based on estimating the actual BIRS of the blanks. Moreover, the reduced LR and BIRS estimation procedure speeds up the BIRS data acquisition, as it enables fast BIRS characterization on bulks where the final parts can still be obtained, providing a powerful tool for distortion control in production lines.

5.5 Summary and conclusions

This chapter evaluates the practicality of the developments of chapters 3 and 4, BIRS characterization method and MIRS empirical model respectively, through experimental and simulation studies. For that, the relation between RS, BIRS and MIRS, and machining distortion is analyzed through different cases. Then, a real-part distortion calculation is performed, for which apart from measured MIRS, a concept of reduced LR test and BIRS estimation is presented. This novel concept enables easier implementation of machining

distortion control strategies in production lines for requiring shorter times to perform BIRS characterizations. In addition, considering the magnitude of the RS measurements obtained within this work, in aluminium greater attention must be put into BIRS, while in titanium parts to MIRS, as these are the main distortion drivers. In any case, considering their variability, both BIRS and MIRS should be used as input in distortion prediction models to reduce inaccuracies.

From the results of this chapter, the following general conclusions can be withdrawn:

- Experimental results verify the simulation results of Chapter 3. This way, the on-machine LR method proves to provide accurate BIRS data from which reliable distortion calculations can be performed.
- Simulation results show that controlling distortion in titanium thin parts by inducing customized MIRS in the machining surfaces is feasible. A distortion calculation model fed with data from a MIRS empirical model represents a powerful tool to initially investigate the effect of different machining conditions and MIRS profiles. In this way, determine worst and best case machining conditions regarding distortion without expensive machining trials. Furthermore, this control strategy offers new possibilities for parts in which the best offset strategy cannot be implemented because machining blanks are getting more adjusted to final geometries to reduce costs and waste.
- The hybrid distortion model is an agile and accurate tool for machining distortion calculation, which can be used in different ribbed geometries typical of aerostructures, and enables performing distortion analysis at the process planing stage. The model is validated experimentally in aluminium test parts showing a prediction accuracy within the uncertainty range calculated. This uncertainty range is linked to the BIRS measurement uncertainty (probing uncertainty of on-machine LR tests).
- Considering that performing a complete BIRS measurement is not industrially feasible, the reduced LR and BIRS estimation offers the possibility of obtaining estimated BIRS for the blanks in a cost-effective way. Having estimations of BIRS data in the machining blanks paves the way towards zero defect manufacturing enabling the use distortion prediction models and control strategies in production lines, and leading to cost, scrap, and manual labour reductions.
- Due to the uncertainty of RS measurements, which are the input of the hybrid distortion model, providing a distortion prediction uncertainty range is as important as the prediction on its own. In fact, the part geometry and its bending stiffness are factors from which it can be foresee if the distortion prediction procedure here introduced is valid or not.

In spite of the positive results of the chapter for the three studied cases, some aspects of the presented developments and analysis present limitations and enable improvement:

- The hybrid distortion model only considers RS (BIRS and MIRS), so it is only valid for cases where the effects of cutting loads (forces and heat) and clamping forces are negligible sources of distortion. Furthermore, the hybrid model only considers the distortions of the floors, ignoring the wall distortions, which are a significant cause of part rejections [93].
- The range of application of the reduced LR and BIRS estimation procedure is limited by two factors, the stiffness of the blank, directly related to the blank height and materials' Young modulus, and the initial curvature of the blanks. This way, in parts whose machining blanks have high Young modulus and near-zero initial curvature, this procedure should be used with caution.
- Performing a proper distortion analysis of titanium parts requires the consideration of not only MIRS but also BIRS. In this regard, the use of on-machine LR presents higher limitations than the aluminium due to its higher Young modulus. This is directly linked to the the experimental validation of the distortion control through MIRS customization, for which it would be interesting to include BIRS measurements in the distortion calculations of titanium parts.

Chapter 6

Conclusions and future work

This thesis worked towards the development of final part distortion prediction tools in aerostructures through the understanding of different distortion sources and the characterization of residual stresses, both previous and generated during machining process. This work pursued procedures implementable in production lines for the prediction of final part distortion.

In this chapter, the main accomplishments and conclusions are summarized. Then, future working lines are defined, which are considered of interest for the development of machining distortion control strategies for aerostructures in production lines. Finally, the scientific contributions resulting this work are listed.

6.1 Accomplishments

Agile method to characterize BIRS in industrial environments and ribbed geometries

Neither BIRS simulation nor measurements in other blanks can suffice the accuracy required for accurate distortion calculations, considering the unavoidable variabilities of BIRS between blanks. Current BIRS characterization methods are limited because the most extended methods are destructive and do not enable to measure BIRS and obtain parts from the same blanks; while the non-destructive alternatives are costly, slow and, due to radioactivity hazards, cannot be part of production lines. Moreover, BIRS characterization methods need to be performed at laboratory environments by specialists, are limited in size to laboratory samples and do not relate directly stresses and machining distortion.

The aforementioned limitations are overcome due to the following accomplishments:

- Industrially applicable, accurate and fast BIRS characterization method in blanks where final parts can still be obtained.

- Good practice guide definition for BIRS characterization through LR method.
- Uncertainty assessment procedure enabling to identify the range of application of the LR method.

MIRS empirical model and distortion avoidance through MIRS optimization

Contradictions in the effect of machining conditions on MIRS are recurring in the literature because inter-methods comparisons of MIRS measurements are barely performed and neither is the measurement uncertainty quantified. Besides, MIRS analytical modeling is complex and cannot be transferred to other tools and processes, while numerical modeling takes long time for its use as part of production lines and often requires calibration with experimental test. In parallel, distortion control is mainly centered in the best offset strategy, which is sometimes not possible due to blanks limited in size, and the feasibility of controlling distortion through the machining conditions is not analyzed.

The present work addressed these gaps achieving accomplishments in the following lines:

- Assessment of the measuring uncertainty of the XRD method, representing the basic knowledge and understanding of MIRS measurement.
- A MIRS empirical model which enables to fast and accurately predict MIRS over a range of machining conditions.
- A final part distortion model fed with the MIRS predictive tool which aids to predict and define countermeasures for the control of machining distortion both in the component and process design phases.

Accurate distortion prediction in aerostructures

The industrial use of distortion prediction in aerostructures manufacturing is hindered because analytical distortion models cannot cope with complex aerostructure geometries, and numerical distortion models take too long computational times to be implemented in production lines. Besides, distortion models are fed with BIRS data corresponding to other blanks, where destructive measurements are performed. On the other hand, distortion predictions are always given as single values and the uncertainty of this predictions is never quantified.

In this regard, this work achieved the following accomplishments:

- Hybrid distortion model for performing preliminary distortion studies during process planning stage and the development of optimized manufacturing strategies while minimizing the final part distortion and facilitating engineering decision-making.

- Method enabling avoiding typical layer-by-layer strategies, reducing the costs associated with long machining processes based on experimental trials.
- Reduced on-machine LR and BIRS estimation procedure speeding up the BIRS characterization, and enabling its implementation in production lines.

6.2 Conclusions

The outcomes from this doctoral dissertation entails advances in the field of machining distortion prediction for aerospace structural components. The conclusions of the work are stated as follows:

- BIRS from the blank where the final part is obtained are necessary for distortion prediction.
- Different BIRS measuring methods give different results.
- Accurate characterization of BIRS is possible on a blank through the ribbed on-machine LR, and it requires considering the initial curvature, MIRS and equivalent bending stiffness.
- Averaging of the BIRS in a layer is sufficiently precise for distortion prediction.
- The uncertainty of BIRS characterization can be theoretically identified by introducing known errors in simulations using the three-phase procedure presented here.
- It is possible to estimate the BIRS of a blank based on a reduced LR test (5 layers) and the BIRS data from another blank.
- Different MIRS measuring methods will yield different results. Even measuring with one only method will require the quantification of the measurement uncertainty.
- Empirical modeling of experimental MIRS data enables accurate and fast prediction.
- It is possible to control the final distortion of titanium thin parts by inducing customized MIRS in machining surfaces.
- The XRD method is not appropriate for measuring MIRS in the aluminum alloys considered within this work due to highly oriented crystallographic texture.
- The effect of cutting parameters on MIRS will greatly depend on the experimental test specifics (material, strategy, tool geometry, wear,...), resulting in possible discrepancies with literature data.

- The final part distortion can be calculated as the superposition of the effect of different distortion sources.
- It is possible to accurately predict the bending behavior of complex part geometries through the coupling of analytical and numerical approaches in a hybrid distortion model.
- The use of previously characterized BIRS and MIRS data in distortion prediction models enables improving precision for distortion results.
- Accurate distortion prediction bound to experimental uncertainties can be performed by the estimation of BIRS through reduced LR on aerospace structural components with complex geometries.

6.3 Future work

This study has deepened the understanding of machining distortion in aerostructures, the RS characterization, and the distortion calculations. Throughout this study, some assumptions and simplifications were taken, leaving room for improvement and further development in complementary investigations. Also, more experimental evidence, involving the prediction of the distortion of other real parts, would further validate the outcomes of the study.

Moreover, the following further work was identified that would complement the investigation and assist in creating an accurate and robust procedure for controlling machining distortion in aluminium and titanium aerospace structural parts:

- Aiming at an industrial application, the on-machine LR requires automation to reduce handwork and reduce associated costs. This could be done through a smart clamping that could release the blank and clamp it again keeping datum but enabling deformation measurements. To reduce measuring deformation probing times, deformation measurements could be performed by sweep-probing or with machine-integrated optical systems. An alternative idea of performing automated on-machine LR with reduced personnel costs would be using a smart clamping capable of measuring force variations due to stress relaxation.
- The distortion model only inputs MIRS loads in floor surfaces, but not in wall surfaces, which could also be a cause of distortion and part rejection. Analogously, the model assumes that the effects of machining sequence are negligible. Future analysis should investigate the effects on part distortions of MIRS induced in walls, as well as, the effects of machining sequence.

- Regarding MIRS measurements, due to the difference between methods, it would be necessary to analyze systematically these differences and determine which MIRS measuring method is most consistent regarding their effect on distortion.
- To verify the results upon distortion control through MIRS customization, experimental test should be carried out.

6.4 Scientific contributions

Within the framework of this doctoral thesis, the following scientific contributions were made:

6.4.1 Indexed articles

- Aurrekoetxea M, Llanos I, Zelaieta O, López de Lacalle LN (2022) Towards advanced prediction and control of machining distortion: a comprehensive review. *Int J Adv Manuf Technol* 122:2823–2848. <https://doi.org/10.1007/s00170-022-10087-5>.
- Aurrekoetxea M, Llanos I, Zelaieta O, López de Lacalle LN (2022) Uncertainty assessment for bulk residual stress characterization using Layer Removal method. *Exp Mech* (Accepted for publication)
- Aurrekoetxea M, Llanos I, Zelaieta O, López de Lacalle LN (2022) Machining distortion prediction based on bulk residual stresses estimation from reduced Layer-Removal. *Materials and Manufacturing Processes* (Under Review)
- Aurrekoetxea M, López de Lacalle LN, Llanos I (2020) Machining Stresses and Initial Geometry on Bulk Residual Stresses Characterization by On-Machine Layer Removal. *Materials* 13:1445. <https://doi.org/10.3390/ma13061445>.
- Aurrekoetxea M, López de Lacalle LN, Llanos I (2020) Modelo analítico para la predicción de la distorsión en componentes mecanizados. *DYNA Ingeniería e Industria* 95(1):205–210. <https://doi.org/10.6036/9387>.

6.4.2 Scientific conferences

- Robles A, Aurrekoetxea M, Plaza S, Llanos I, Zelaieta O (2022) Empirical modeling of residual stress profiles in Ti6Al4V after face-milling. *Procedia CIRP* 108:362–6. <https://doi.org/10.1016/j.procir.2022.03.059>.
- Aurrekoetxea M, Bilkhu R, Llanos I, Ayvar-Soberanis S, Lopez de Lacalle LN (2021) Residual stress characterization for ribbed geometries using On-machine Layer Removal method. *Procedia CIRP* 101:42–5. <https://doi.org/10.1016/j.procir.2020.10>.

-
- Aurrekoetxea M, Llanos I, Zelaieta O, Lopez de Lacalle LN (2021) Improving accuracy of bulk residual stress characterization in ribbed geometries through equivalent bending stiffness. *Procedia CIRP* 102:325–30. <https://doi.org/10.1016/j.procir.2021.04.012>
 - Llanos I, Aurrekoetxea M, Agirre A, de Lacalle LNL, Zelaieta O (2019) On-machine Characterization of Bulk Residual Stresses on Machining Blanks. *Procedia CIRP* 82:406–10. <https://doi.org/10.1016/j.procir.2019.04.012>.

Bibliography

- [1] Mounir I (2021) Boeing commercial market outlook 2021-2040. Tech. rep.
- [2] Bowden D.M. HJ (2001) Aluminium reliability improvement program final report 60606, 2001. Chicago, IL, USA: The Boeing Company.
- [3] Thoben KD, Lübben T, Clausen B, et al (2004) Distortion Engineering: A System-Oriented View on the Distortion of Component-Parts. *Jinshu Rechuli/Heat Treatment of Metals* 2004:43–50
- [4] Zoch HW (2006) From Single Production Step to Entire Process Chain - the Global Approach of Distortion Engineering. *Materialwissenschaft und Werkstofftechnik* 37(1):6–10. <https://doi.org/10.1002/mawe.200500958>
- [5] Zhang L, Wang H, Li S (2014) Simulating Assembly Geometric and Stress Variation Considering Machining-Induced Residual Stress. In: *Proceedings of the ASME 2014 International Design Engineering Technical Conferences and Computers and Information in Engineering Conference*, vol 4, V004T06A011. ASME, Buffalo, New York, USA, <https://doi.org/10.1115/DETC2014-34223>
- [6] Andersch C, Ehlers M, Hoffmann F, et al (2006) Systematic analysis of the correlation between part geometry and distortion due to heat treatment. *Materialwissenschaft und Werkstofftechnik* 37(1):23–28. <https://doi.org/10.1002/mawe.200500951>
- [7] Park S, Nam E, Gang M, et al (2019) Post-machining Deformation Analysis for Virtual Machining of Thin Aluminium Alloy Parts. *International Journal of Precision Engineering and Manufacturing* 20(4):687–691. <https://doi.org/10.1007/s12541-019-00028-w>
- [8] Beekhuis BLT, Brinksmeier E, Garbrecht M, et al (2009) Improving the shape quality of bearing rings in soft turning by using a Fast Tool Servo. *Production Engineering* 3(4-5):469–474. <https://doi.org/10.1007/s11740-009-0175-z>
- [9] Segurajauregui U, Arrazola PJ (2015) Heat-flow determination through inverse identification in drilling of aluminium workpieces with MQL. *Production Engineering* 9(4):517–526. <https://doi.org/10.1007/s11740-015-0631-x>

- [10] Boyer R, Cotton J, Mohaghegh M, et al (2015) Materials considerations for aerospace applications. *MRS Bulletin* 40(12):1055–1066. <https://doi.org/10.1557/mrs.2015.278>
- [11] Campbell F (2006) *Manufacturing Technology for Aerospace Structural Materials*. Elsevier Science, Oxford, <https://doi.org/https://doi.org/10.1016/B978-185617495-4/50000-7>
- [12] Gialanella S, Malandrucolo A (2020) *Aerospace Alloys*. Topics in Mining, Metallurgy and Materials Engineering, Springer International Publishing, Cham, <https://doi.org/10.1007/978-3-030-24440-8>
- [13] Lucintel (2020) *Titanium in the Global Aerospace Industry Report: Trends, Forecast and Competitive Analysis*. URL <https://www.reportlinker.com/p05483281>
- [14] Altintas Y (2012) *Manufacturing automation: metal cutting mechanics, machine tool vibrations, and CNC design*, 2nd edn. Cambridge university press, Cambridge
- [15] Li Jg, Wang Sq (2017) Distortion caused by residual stresses in machining aeronautical aluminum alloy parts: recent advances. *The International Journal of Advanced Manufacturing Technology* 89(1-4):997–1012. <https://doi.org/10.1007/s00170-016-9066-6>
- [16] Noyan IC, Cohen JB, Cohen JB, et al (1987) *Residual stress: measurement by diffraction and interpretation*, Springer Science, vol MRE Materials Reserach Engineering. Springer-Verlag, New York etc
- [17] Totten GE, Howes MAH, Inoue T (eds) (2002) *Handbook of residual stress and deformation of steel*. ASM International, Materials Park, Ohio
- [18] Schajer GS (ed) (2013) *Practical residual stress measurement methods*, 1st edn. Wiley, Chichester, Wessex
- [19] García Navas V (2006) *Optimización de procesos de mecanizado mediante control de tensiones residuales*. Doctoral dissertation, Tecnum
- [20] ENSPED (2022) *European Networking of Surface and Presstress Engineering and Design*. URL <http://www-ensped.utt.fr/aboutprestress/aboutprestressf.htm>
- [21] D’Alvise L, Chantzis D, Schoinochoritis B, et al (2015) Modelling of Part Distortion Due to Residual Stresses Relaxation: An aerOnautical Case Study. *Procedia CIRP* 31:447–452. <https://doi.org/10.1016/j.procir.2015.03.069>
- [22] Nervi S (2005) *A mathematical model for the estimation of the effects of residual stresses in aluminum plates*. Doctoral dissertation, Washington University, Saint Louis, Missouri, US, iSSN: 9780542219979

- [23] Yang Y, Li X, Li L, et al (2019) Investigation on deformation of single-sided stringer parts based on fluctuant initial residual stress. *Journal of Materials Processing Technology* 271:623–633. <https://doi.org/10.1016/j.jmatprotec.2019.04.031>
- [24] Prime MB, Hill MR (2002) Residual stress, stress relief, and inhomogeneity in aluminum plate. *Scripta Materialia* 46(1):77–82. [https://doi.org/10.1016/S1359-6462\(01\)01201-5](https://doi.org/10.1016/S1359-6462(01)01201-5)
- [25] Barcenas L, Ledesma-Orozco E, Van-der Veen S, et al (2020) An optimization of part distortion for a structural aircraft wing rib: an industrial workflow approach. *CIRP Journal of Manufacturing Science and Technology* 28:15–23. <https://doi.org/10.1016/j.cirpj.2020.01.007>
- [26] Wu Q, Li DP, Zhang YD (2016) Detecting Milling Deformation in 7075 Aluminum Alloy Aeronautical Monolithic Components Using the Quasi-Symmetric Machining Method. *Metals* 6(4):80. <https://doi.org/10.3390/met6040080>
- [27] Möhring HC, Wiederkehr P, Gonzalo O, et al (2018) Intelligent Fixtures for the Manufacturing of Low Rigidity Components. *Lecture Notes in Production Engineering*, Springer International Publishing, <https://doi.org/10.1007/978-3-319-45291-3>
- [28] Younger MS, Eckelmeyer KH (2007) Overcoming residual stresses and machining distortion in the production of aluminum alloy satellite boxes. Technical Report SAND2007-6811, Sandia National Laboratories, US, <https://doi.org/https://doi.org/10.2172/922073>
- [29] Chatelain JF, Lalonde JF, Tahan A (2012) Effect of Residual Stresses Embedded within Workpieces on the Distortion of Parts after Machining. *International Journal of Mechanics* 6(1):43–51. Number: 1
- [30] Chatelain JF, Lalonde JF, Tahan A (2011) A comparison of the distortion of machined parts resulting from residual stresses within workpieces. In: 4th International Conference on Manufacturing Engineering, Quality and Production Systems (MEQAPS). World Scientific and Engineering Academy and Society, Barcelona, Spain, pp 79–84
- [31] Dong Hy, Ke YI (2006) Study on Machining Deformation of Aircraft Monolithic Component by FEM and Experiment. *Chinese Journal of Aeronautics* 19(3):247–254. [https://doi.org/10.1016/S1000-9361\(11\)60352-X](https://doi.org/10.1016/S1000-9361(11)60352-X)
- [32] Gao H, Zhang Y, Wu Q, et al (2018) Investigation on influences of initial residual stress on thin-walled part machining deformation based on a semi-analytical model. *Journal of Materials Processing Technology* 262:437–448. <https://doi.org/10.1016/j.jmatprotec.2018.04.009>

- [33] Guo H, Zuo D, Wu H, et al (2009) Prediction on milling distortion for aero-multi-frame parts. *Materials Science and Engineering: A* 499(1-2):230–233. <https://doi.org/10.1016/j.msea.2007.11.137>
- [34] Huang X, Sun J, Li J (2015) Finite element simulation and experimental investigation on the residual stress-related monolithic component deformation. *The International Journal of Advanced Manufacturing Technology* 77(5-8):1035–1041. <https://doi.org/10.1007/s00170-014-6533-9>
- [35] Ma Y, Zhang J, Yu D, et al (2019) Modeling of machining distortion for thin-walled components based on the internal stress field evolution. *The International Journal of Advanced Manufacturing Technology* 103(9-12):3597–3612. <https://doi.org/10.1007/s00170-019-03736-9>
- [36] Marusich TD, Stephenson DA, Usui S, et al (2009) Modeling Capabilities for Part Distortion Management for Machined Components. Third Wave Systems, Inc
- [37] Richter-Trummer V, Koch D, Witte A, et al (2013) Methodology for prediction of distortion of workpieces manufactured by high speed machining based on an accurate through-the-thickness residual stress determination. *The International Journal of Advanced Manufacturing Technology* 68(9-12):2271–2281. <https://doi.org/10.1007/s00170-013-4828-x>
- [38] Wang Z, Sun J, Liu L, et al (2019) An analytical model to predict the machining deformation of frame parts caused by residual stress. *Journal of Materials Processing Technology* 274:116,282. <https://doi.org/10.1016/j.jmatprotec.2019.116282>
- [39] Ma K, Goetz R, Srivatsa SK (2010) Modeling of Residual Stress and Machining Distortion in Aerospace Components (PREPRINT):. <https://doi.org/10.21236/ADA523921>
- [40] Brinksmeier E, Cammett J, König W, et al (1982) Residual Stresses — Measurement and Causes in Machining Processes. *CIRP Annals* 31(2):491–510. [https://doi.org/10.1016/S0007-8506\(07\)60172-3](https://doi.org/10.1016/S0007-8506(07)60172-3)
- [41] Huang X, Sun J, Li J (2015) Effect of Initial Residual Stress and Machining-Induced Residual Stress on the Deformation of Aluminium Alloy Plate. *Strojniški vestnik – Journal of Mechanical Engineering* 61(2):131–137. <https://doi.org/10.5545/sv-jme.2014.1897>
- [42] Withers P, Bhadeshia H (2001) Residual stress. Part 2 – Nature and origins. *Materials Science and Technology* 17(4):366–375. <https://doi.org/10.1179/026708301101510087>

- [43] Liu Y, Xu D, Agmell M, et al (2021) Numerical and experimental investigation of tool geometry effect on residual stresses in orthogonal machining of Inconel 718. *Simulation Modelling Practice and Theory* 106:102,187. <https://doi.org/10.1016/j.simpat.2020.102187>
- [44] Weber D, Kirsch B, D'Elia CR, et al (2019) Concept to analyze residual stresses in milled thin walled monolithic aluminum components and their effect on part distortion. In: Wulfsberg JP, Hintze W, Behrens BA (eds) *Production at the leading edge of technology*. Springer Berlin Heidelberg, Berlin, Heidelberg, pp 287–296
- [45] Rao B, Shin YC (2001) Analysis on high-speed face-milling of 7075-T6 aluminum using carbide and diamond cutters. *International Journal of Machine Tools and Manufacture* 41(12):1763–1781. [https://doi.org/10.1016/S0890-6955\(01\)00033-5](https://doi.org/10.1016/S0890-6955(01)00033-5)
- [46] Daymi A, Boujelbene M, Ben Amara A, et al (2011) Surface integrity in high speed end milling of titanium alloy Ti-6Al-4V. *Materials Science and Technology* 27(1):387–394. <https://doi.org/10.1179/026708310X12738371692932>
- [47] Mantle A, Aspinwall D (2001) Surface integrity of a high speed milled gamma titanium aluminide. *Journal of Materials Processing Technology* 118(1-3):143–150. [https://doi.org/10.1016/S0924-0136\(01\)00914-1](https://doi.org/10.1016/S0924-0136(01)00914-1)
- [48] Yang D, Liu Z, Ren X, et al (2016) Hybrid modeling with finite element and statistical methods for residual stress prediction in peripheral milling of titanium alloy Ti-6Al-4V. *International Journal of Mechanical Sciences* 108-109:29–38. <https://doi.org/10.1016/j.ijmecsci.2016.01.027>
- [49] Chighizola CR, D'Elia CR, Weber D, et al (2021) Intermethod Comparison and Evaluation of Measured Near Surface Residual Stress in Milled Aluminum. *Experimental Mechanics* 61(8):1309–1322. <https://doi.org/10.1007/s11340-021-00734-5>
- [50] Tang ZT, Yu T, Xu LQ (2014) Study on the Deformations Caused by the Original Residual Stresses of Aluminum Alloy. *Advanced Materials Research* 875-877:1016–1020. <https://doi.org/10.4028/www.scientific.net/AMR.875-877.1016>
- [51] Denkena B, Boehnke D, de León L (2008) Machining induced residual stress in structural aluminum parts. *Production Engineering* 2(3):247–253. <https://doi.org/10.1007/s11740-008-0097-1>
- [52] Wimmer S, Hunyadi P, Zaeh MF (2019) A numerical approach for the prediction of static surface errors in the peripheral milling of thin-walled structures. *Production Engineering* 13(3-4):479–488. <https://doi.org/10.1007/s11740-019-00901-7>

- [53] Li B, Jiang X, Yang J, et al (2015) Effects of depth of cut on the redistribution of residual stress and distortion during the milling of thin-walled part. *Journal of Materials Processing Technology* 216:223–233. <https://doi.org/10.1016/j.jmatprotec.2014.09.016>
- [54] Tang Z, Liu Z, Pan Y, et al (2009) The influence of tool flank wear on residual stresses induced by milling aluminum alloy. *Journal of Materials Processing Technology* 209(9):4502–4508. <https://doi.org/10.1016/j.jmatprotec.2008.10.034>
- [55] Chen L, El-Wardany T, Harris W (2004) Modelling the Effects of Flank Wear Land and Chip Formation on Residual Stresses. *CIRP Annals* 53(1):95–98. [https://doi.org/10.1016/S0007-8506\(07\)60653-2](https://doi.org/10.1016/S0007-8506(07)60653-2)
- [56] Schoop J (2021) In-Situ Calibrated Modeling of Residual Stresses Induced in Machining under Various Cooling and Lubricating Environments. *Lubricants* 9(3):28. <https://doi.org/10.3390/lubricants9030028>, number: 3 Publisher: Multidisciplinary Digital Publishing Institute
- [57] (2022) Tackling Titanium. URL <https://www.ctemag.com/news/articles/tackling-titanium-0>
- [58] Weber D, Kirsch B, Chighizola CR, et al (2021) Analysis of machining-induced residual stresses of milled aluminum workpieces, their repeatability, and their resulting distortion. *The International Journal of Advanced Manufacturing Technology* 115(4):1089–1110. <https://doi.org/10.1007/s00170-021-07171-7>
- [59] Putz M, Richter C, Regel J, et al (2018) Industrial relevance and causes of thermal issues in machine tools. In: *Wissenschaftliche Scripten, Auerbach / Vogtl*, pp 127–139.
- [60] Wan M, Zhang WH, Qin GH, et al (2008) Strategies for error prediction and error control in peripheral milling of thin-walled workpiece. *International Journal of Machine Tools and Manufacture* 48(12):1366–1374. <https://doi.org/10.1016/j.ijmachtools.2008.05.005>
- [61] Ratchev S, Liu S, Huang W, et al (2004) Milling error prediction and compensation in machining of low-rigidity parts. *International Journal of Machine Tools and Manufacture* 44(15):1629–1641. <https://doi.org/10.1016/j.ijmachtools.2004.06.001>
- [62] Del Sol I, Rivero A, López de Lacalle LN, et al (2019) Thin-Wall Machining of Light Alloys: A Review of Models and Industrial Approaches. *Materials* 12(12):2012. <https://doi.org/10.3390/ma12122012>

- [63] Li ZL, Tuysuz O, Zhu LM, et al (2018) Surface form error prediction in five-axis flank milling of thin-walled parts. *International Journal of Machine Tools and Manufacture* 128:21–32. <https://doi.org/10.1016/j.ijmachtools.2018.01.005>
- [64] Ma Jw, He Gz, Liu Z, et al (2018) Instantaneous cutting-amount planning for machining deformation homogenization based on position-dependent rigidity of thin-walled surface parts. *Journal of Manufacturing Processes* 34:401–411. <https://doi.org/10.1016/j.jmapro.2018.05.027>
- [65] Sridhar G, Ramesh Babu P (2015) Effect of a milling cutter diameter on distortion due to the machining of thin wall thin floor components. *Advances in Production Engineering & Management* 10(3):140–152. <https://doi.org/10.14743/apem2015.3.198>
- [66] Segurajauregui U, Masset L, Arrazola PJ (2007) Improving Quality in Machined Automotive Parts with the Finite Element Method. In: *AIP Conference Proceedings*, vol 907. AIP, Zaragoza (Spain), pp 769–774, <https://doi.org/10.1063/1.2729606>
- [67] Masoudi S, Amini S, Saeidi E, et al (2015) Effect of machining-induced residual stress on the distortion of thin-walled parts. *The International Journal of Advanced Manufacturing Technology* 76(1-4):597–608. <https://doi.org/10.1007/s00170-014-6281-x>
- [68] Cherif I, Outeiro J, Cotton D, et al (2019) Effects of toolpath and clamping strategies in machining distortion of stainless-steel parts. *Procedia CIRP* 82:427–431. <https://doi.org/10.1016/j.procir.2019.04.065>
- [69] Rai JK, Xirouchakis P (2008) Finite element method based machining simulation environment for analyzing part errors induced during milling of thin-walled components. *International Journal of Machine Tools and Manufacture* 48(6):629–643. <https://doi.org/10.1016/j.ijmachtools.2007.11.004>
- [70] Cerutti X, Mocellin K, Hassini S, et al (2017) Methodology for aluminium part machining quality improvement considering mechanical properties and process conditions. *CIRP Journal of Manufacturing Science and Technology* 18:18–38. <https://doi.org/10.1016/j.cirpj.2016.07.004>
- [71] Rambaud P (2019) Computational modelling of post machining distortion of aluminium aeronautical parts. Doctoral dissertation, PSL Université Paris
- [72] Volk W, Groche P, Brosius A, et al (2019) Models and modelling for process limits in metal forming. *CIRP Annals* 68(2):775–798. <https://doi.org/10.1016/j.cirp.2019.05.007>

- [73] Chantzis D, Van-der Veen S, J.Zettler, et al (2013) An Industrial Workflow to Minimise Part Distortion for Machining of Large Monolithic Components in Aerospace Industry. *Procedia CIRP* 8:281–286. <https://doi.org/10.1016/j.procir.2013.06.103>
- [74] Sim WM (2010) Challenges of residual stress and part distortion in the civil airframe industry. *International Journal of Microstructure and Materials Properties* 5(4/5):446. <https://doi.org/10.1504/IJMMP.2010.037621>
- [75] Cerutti X (2014) Numerical modelling and mechanical analysis of the machining of large aeronautical parts: Machining quality improvement. Doctoral dissertation, MINES ParisTech
- [76] Saleem W, Ijaz H, Zain-ul Abdein M, et al (2017) Studying control strategies for dimensional precision in aerospace parts machining. *International Journal of Precision Engineering and Manufacturing* 18(1):39–47. <https://doi.org/10.1007/s12541-017-0005-8>
- [77] Marusich TD, Usui S, Marusich KJ (2008) Finite Element Modeling of Part Distortion. In: Xiong C, Liu H, Huang Y, et al (eds) *Intelligent Robotics and Applications*, vol 5315. Springer Berlin Heidelberg, Berlin, Heidelberg, p 329–338, https://doi.org/10.1007/978-3-540-88518-4_36
- [78] Izamshah R, Mo JPT, Ding S (2012) Hybrid deflection prediction on machining thin-wall monolithic aerospace components. *Proceedings of the Institution of Mechanical Engineers, Part B: Journal of Engineering Manufacture* 226(4):592–605. <https://doi.org/10.1177/0954405411425443>
- [79] Bilkhu R (2020) Machining strategies for distortion control during high speed machining.pdf. PhD thesis, The University of Sheffield
- [80] Benzley SE, Perry E, Merkley K, et al (1995) A comparison of all hexagonal and all tetrahedral finite element meshes for elastic and elasto-plastic analysis. In: *Proceedings of 4th International Meshing Roundtable*, pp 179–191
- [81] Landwehr M, Schmid S, Holla V, et al (2021) The finite cell method for the prediction of machining distortion caused by initial residual stresses in milling. *Procedia CIRP* 102:144–149. <https://doi.org/10.1016/j.procir.2021.09.025>
- [82] Shen CQ, Jiao L, Dong ZH, et al (2014) Experimental Investigation and Simulation of Machining Thin-Walled Aluminum Alloy Workpiece Center. *Applied Mechanics and Materials* 543-547:370–373. <https://doi.org/10.4028/www.scientific.net/AMM.543-547.370>

- [83] Albino J, Gonçalves Junior L, Beal V (2019) On the convergence of solid meshes for the prediction of part distortions due to residual stresses. *Proceedings of the Institution of Mechanical Engineers, Part C: Journal of Mechanical Engineering Science* p 095440621986140. <https://doi.org/10.1177/0954406219861405>
- [84] Young KA, Nervi S, Szabo B (2005) Machining-Induced Residual Stress and Distortion. *SAE International* pp 2005-01-3317. <https://doi.org/10.4271/2005-01-3317>
- [85] Denkena B, de León-García L, Köhler J (2006) Influence of high performance cutting operations on the residual stresses of aluminium structural workpieces. In: *International Congress of the Aeronautical Sciences*, p 7
- [86] Schindler S, Zimmermann M, Aurich JC, et al (2014) Thermo-elastic deformations of the workpiece when dry turning aluminum alloys - A finite element model to predict thermal effects in the workpiece. *CIRP Journal of Manufacturing Science and Technology* 7(3):233-245. <https://doi.org/10.1016/j.cirpj.2014.04.006>
- [87] Yang Y, Li M, Li KR (2014) Comparison and analysis of main effect elements of machining distortion for aluminum alloy and titanium alloy aircraft monolithic component. *The International Journal of Advanced Manufacturing Technology* 70(9-12):1803-1811. <https://doi.org/10.1007/s00170-013-5431-x>
- [88] Prete AD, Franchi R, Antermite F, et al (2018) Numerical simulation of machining distortions on a forged aerospace component following a one and a multi-step approaches. *AIP Conference Proceedings* 1960(1):070,009. <https://doi.org/10.1063/1.5034905>, publisher: American Institute of Physics
- [89] Pierard O, Barboza J, Duflot M, et al (2008) Distortions prediction during multi-pass machining simulations by using the level-set method. *International Journal of Material Forming* 1(S1):563-565. <https://doi.org/10.1007/s12289-008-0318-3>
- [90] Svanberg J, Holmberg J (2004) Prediction of shape distortions. Part II. Experimental validation and analysis of boundary conditions. *Composites Part A: Applied Science and Manufacturing* 35(6):723-734. <https://doi.org/10.1016/j.compositesa.2004.02.006>
- [91] Tekkaya A, Martins P (2009) Accuracy, reliability and validity of finite element analysis in metal forming: a user's perspective. *Engineering Computations* 26(8):1026-1055. <https://doi.org/10.1108/02644400910996880>
- [92] Cerutti X, Mocellin K (2015) Parallel finite element tool to predict distortion induced by initial residual stresses during machining of aeronautical parts. *International Journal of Material Forming* 8(2):255-268. <https://doi.org/10.1007/s12289-014-1164-0>

- [93] Hussain A, Lazoglu I (2019) Distortion in milling of structural parts. *CIRP Annals* 68(1):105–108. <https://doi.org/10.1016/j.cirp.2019.04.053>
- [94] Nervi S, Szabó BA, Young KA (2009) Prediction of Distortion of Airframe Components Made from Aluminum Plates. *AIAA Journal* 47(7):1635–1641. <https://doi.org/10.2514/1.37233>
- [95] Carlisle OJ (2012) Modelling the effects of residual stress and material removal in sheet metal forming. PhD thesis, University of Ulster
- [96] Jiang Z, Liu Y, Li L, et al (2014) A novel prediction model for thin plate deflections considering milling residual stresses. *The International Journal of Advanced Manufacturing Technology* 74(1-4):37–45. <https://doi.org/10.1007/s00170-014-5952-y>
- [97] Zhu Y, Mao K, Yu X (2020) A general model for prediction of deformation from initial residual stress. *The International Journal of Advanced Manufacturing Technology* 109(3-4):1093–1101. <https://doi.org/10.1007/s00170-020-05683-2>
- [98] Shin SH (1995) Prediction of the dimensional instability resulting from machining residually stressed components. Doctoral dissertation, Texas Tech University, Lubbock, Texas, US
- [99] Timoshenko S, Woinowsky-Krieger S (1940) *Theory of Plates and Shells*. Engineering mechanics series, McGraw-Hill
- [100] Timoshenko S, Goodier J (1934) *Theory of Elasticity*. Engineering mechanics series, McGraw-Hill
- [101] Gao H, Zhang Y, Wu Q, et al (2017) An analytical model for predicting the machining deformation of a plate blank considers biaxial initial residual stresses. *The International Journal of Advanced Manufacturing Technology* 93(1-4):1473–1486. <https://doi.org/10.1007/s00170-017-0528-2>
- [102] Heinzl C, Sölter J, Gulpak M, et al (2017) An analytical multilayer source stress approach for the modelling of material modifications in machining. *CIRP Annals* 66(1):531–534. <https://doi.org/10.1016/j.cirp.2017.04.073>
- [103] Llanos I, Lanzagorta JL, Beristain A (2017) Part Distortion Modeling on Aluminum Slender Structural Components for Aeronautical Industry. *Procedia CIRP* 58:158–162. <https://doi.org/10.1016/j.procir.2017.03.213>
- [104] Jiang X, Wang Y, Ding Z, et al (2017) An approach to predict the distortion of thin-walled parts affected by residual stress during the milling process. *The International Journal of Advanced Manufacturing Technology* 93(9-12):4203–4216. <https://doi.org/10.1007/s00170-017-0811-2>

- [105] Rice JR (2010) *Solid Mechanics*. Harvard University, Cambridge
- [106] Pidaparti RM (2017) Engineering Finite Element Analysis. *Synthesis Lectures on Mechanical Engineering* 1(1):1–267. <https://doi.org/10.2200/S00761ED1V01Y201703MEC001>
- [107] Fan L, Tian H, Li L, et al (2020) Machining Distortion Minimization of Monolithic Aircraft Parts Based on the Energy Principle. *Metals* 10(12):1586. <https://doi.org/10.3390/met10121586>
- [108] Schultz R, Karabin M (2002) Characterization of Machining Distortion by Strain Energy Density and Stress Range. *Materials Science Forum* 404-407:61–68. <https://doi.org/10.4028/www.scientific.net/MSF.404-407.61>
- [109] Heymes F, Commet B, Du Bost B, et al (1997) Development of New Al Alloys for Distortion Free Machined Aluminium Aircraft Components. In: 1st International non-ferrous processing and technology conference. ASM International, Materials Park, pp 249–258
- [110] Nurhaniza M, Ariffin MKA, Ali A, et al (2013) Development of genetic algorithm toolbox using MATLAB in cutting tool path optimization. *Academic Journals* 8(38):1848–1857. <https://doi.org/10.5897/SRE10.550>
- [111] Wang Q, Hu XD, Li W, et al (2006) Numerical Simulation of Machining Distortion of Residually Stressed Aircraft Aluminum Components. *Key Engineering Materials* 315-316:235–238. <https://doi.org/10.4028/www.scientific.net/KEM.315-316.235>
- [112] Robinson JS, Tanner DA, Truman CE, et al (2011) Measurement and Prediction of Machining Induced Redistribution of Residual Stress in the Aluminium Alloy 7449. *Experimental Mechanics* 51(6):981–993. <https://doi.org/10.1007/s11340-010-9389-4>
- [113] Veubeke BMF (1979) The Equations Of Linear Elasticity. In: *A Course in Elasticity, Applied Mathematical Sciences*, vol 29. Springer, New York, NY, p 81–134
- [114] Guang-yao L, Han-bin Z (1993) A finite difference method at arbitrary meshes for the bending of plates with variable thickness. *Applied Mathematics and Mechanics* 14(3):299–304. <https://doi.org/10.1007/BF02451414>
- [115] Schillinger D, Ruess M (2015) The Finite Cell Method: A Review in the Context of Higher-Order Structural Analysis of CAD and Image-Based Geometric Models. *Archives of Computational Methods in Engineering* 22(3):391–455. <https://doi.org/10.1007/s11831-014-9115-y>

- [116] Wang J, Quan L, Tang K (2020) A prediction method based on the voxel model and the finite cell method for cutting force-induced deformation in the five-axis milling process. *Computer Methods in Applied Mechanics and Engineering* 367:113,110. <https://doi.org/10.1016/j.cma.2020.113110>
- [117] Li X, Venuvinod PK, Djorjevich A, et al (2001) Predicting Machining Errors in Turning Using Hybrid Learning. *International Journal of Advanced Manufacturing Technology* 18(12):863–872. <https://doi.org/10.1007/PL00003954>
- [118] Rodríguez-Sánchez AE, Ledesma-Orozco E, Ledesma S (2020) Part distortion optimization of aluminum-based aircraft structures using finite element modeling and artificial neural networks. *CIRP Journal of Manufacturing Science and Technology* pp 1230–1234. <https://doi.org/10.1016/j.cirpj.2020.08.011>
- [119] Zhao Z, Li Y, Liu C, et al (2020) On-line part deformation prediction based on deep learning. *Journal of Intelligent Manufacturing* 31(3):561–574. <https://doi.org/10.1007/s10845-019-01465-0>
- [120] Gulpak M, Sölter J, Brinksmeier E (2013) Prediction of Shape Deviations in Face Milling of Steel. *Procedia CIRP* 8:15–20. <https://doi.org/10.1016/j.procir.2013.06.058>
- [121] Li B, Gao H, Deng H, et al (2019) Investigation on the influence of the equivalent bending stiffness of the thin-walled parts on the machining deformation. *The International Journal of Advanced Manufacturing Technology* 101(5-8):1171–1182. <https://doi.org/10.1007/s00170-018-2987-5>
- [122] Li B, Deng H, Hui D, et al (2020) A semi-analytical model for predicting the machining deformation of thin-walled parts considering machining-induced and blank initial residual stress. *The International Journal of Advanced Manufacturing Technology* 110(1-2):139–161. <https://doi.org/10.1007/s00170-020-05862-1>
- [123] Madariaga A, Perez I, Arrazola PJ, et al (2018) Reduction of distortions in large aluminium parts by controlling machining-induced residual stresses. *The International Journal of Advanced Manufacturing Technology* 97(1-4):967–978. <https://doi.org/10.1007/s00170-018-1965-2>
- [124] Li W, Ma L, Wan M, et al (2018) Modeling and simulation of machining distortion of pre-bent aluminum alloy plate. *Journal of Materials Processing Technology* 258:189–199. <https://doi.org/10.1016/j.jmatprotec.2018.03.019>
- [125] Wang Z, Sun J, Chen W, et al (2018) Machining Distortion of Titanium Alloys Aero Engine Case Based on the Energy Principles. *Metals* 8(6):464. <https://doi.org/10.3390/met8060464>

- [126] Toubhans B, Viprey F, Fromentin G, et al (2021) Study of phenomena responsible for part distortions when turning thin Inconel 718 workpieces. *Journal of Manufacturing Processes* 61:46–55. <https://doi.org/10.1016/j.jmapro.2020.11.007>
- [127] Zhan C, Yang W (2016) A high efficient surface-based method for predicting part distortions in machining and shot peening. *International Journal of Mechanical Sciences* 119:125–143. <https://doi.org/10.1016/j.ijmecsci.2016.09.032>
- [128] Wang J, Zhang D, Wu B, et al (2018) Prediction of distortion induced by machining residual stresses in thin-walled components. *The International Journal of Advanced Manufacturing Technology* 95(9-12):4153–4162. <https://doi.org/10.1007/s00170-017-1358-y>
- [129] Yao C, Zhang J, Cui M, et al (2020) Machining deformation prediction of large fan blades based on loading uneven residual stress. *The International Journal of Advanced Manufacturing Technology* 107(9):4345–4356. <https://doi.org/10.1007/s00170-020-05316-8>
- [130] Jiang X, Zhang Z, Ding Z, et al (2017) Tool overlap effect on redistributed residual stress and shape distortion produced by the machining of thin-walled aluminum parts. *The International Journal of Advanced Manufacturing Technology* 93(5-8):2227–2242. <https://doi.org/10.1007/s00170-017-0693-3>
- [131] Böß V, Rust F, Denkena B, et al (2020) Prediction of part distortion in re-contouring processes. *CIRP Journal of Manufacturing Science and Technology* 29(A):25–35. <https://doi.org/10.1016/j.cirpj.2020.01.006>
- [132] Han S, Faverjon P, Valiorgue F, et al (2018) Prediction and modeling of thermal distortion in sequential MQL drilling of AlSi7 cylindrical parts. *Procedia CIRP* 77:336–339. <https://doi.org/10.1016/j.procir.2018.09.029>
- [133] Zhang FP, Yan Y, Butt SI (2016) Integrated model based thin-walled part machining precision control for the workpiece-fixture system. *The International Journal of Advanced Manufacturing Technology* 85(5-8):1745–1758. <https://doi.org/10.1007/s00170-015-8036-8>
- [134] Zhou H, Wang C, Jing X, et al (2018) Influence of cutting and clamping forces on machining distortion of diesel engine connecting rod. *The International Journal of Advanced Manufacturing Technology* 99(1-4):897–910. <https://doi.org/10.1007/s00170-018-2436-5>
- [135] Dreier S, Brüning J, Denkena B (2016) Simulation based reduction of residual stress related part distortion: Simulationsbasierte Reduzierung eigenspannungsbedingten

- Bauteilverzugs. *Materialwissenschaft und Werkstofftechnik* 47(8):710–717. <https://doi.org/10.1002/mawe.201600604>
- [136] Weber D, Kirsch B, Chighizola CR, et al (2021) Investigation on the scale effects of initial bulk and machining induced residual stresses of thin walled milled monolithic aluminum workpieces on part distortions: experiments and finite element prediction model. *Procedia CIRP* 102:337–342. <https://doi.org/10.1016/j.procir.2021.09.058>
- [137] Denkena B, Schmidt C, Krüger M (2010) Experimental investigation and modeling of thermal and mechanical influences on shape deviations in machining structural parts. *International Journal of Machine Tools and Manufacture* 50(11):1015–1021. <https://doi.org/10.1016/j.ijmachtools.2010.06.006>
- [138] Zhang Y, Zhang H (2009) Finite element simulation of machining deformation for aeronautical monolithic component. *Beijing Hangkong Hangtian Daxue Xuebao/Journal of Beijing University of Aeronautics and Astronautics* 35(2):188–192
- [139] Wang H, Wang H (2019) Numerical and experimental investigation of bulk stress distribution in edge under different clamping sequence. *Assembly Automation* 39(4):523–531. <https://doi.org/10.1108/AA-10-2017-131>
- [140] Jayanti S, Ren D, Erickson E, et al (2013) Predictive Modeling for Tool Deflection and Part Distortion of Large Machined Components. *Procedia CIRP* 12:37–42. <https://doi.org/10.1016/j.procir.2013.09.008>
- [141] Tang ZT, Yu T, Xu LQ, et al (2013) Machining deformation prediction for frame components considering multifactor coupling effects. *The International Journal of Advanced Manufacturing Technology* 68(1-4):187–196. <https://doi.org/10.1007/s00170-012-4718-7>
- [142] Ball D, Ryan M, Yurko J, et al (2019) Quantification of Uncertainty in Forging Process Induced Residual Stress and Associated Fatigue Life. San Antonio TX
- [143] Aksel B, Arthur WR, Mukherjee S (1992) A Study of Quenching: Experiment and Modelling. *Journal of Engineering for Industry* 114(3):309–316. <https://doi.org/10.1115/1.2899797>
- [144] Koç M, Culp J, Altan T (2006) Prediction of residual stresses in quenched aluminum blocks and their reduction through cold working processes. *Journal of Materials Processing Technology* 174(1-3):342–354. <https://doi.org/10.1016/j.jmatprotec.2006.02.007>

- [145] Awan WS, Mabrouki T (2017) Numerical and experimental investigations of post-machining distortions in thin machined structures considering material-induced residual stress. *Journal of the Brazilian Society of Mechanical Sciences and Engineering* 39(2):509–521. <https://doi.org/10.1007/s40430-015-0386-5>
- [146] Hosseinzadeh F, Mahmoudi AH, Truman CE, et al (2009) Prediction and Measurement of Through Thickness Residual stresses in Large Quenched Components. In: *Proceedings of the World Congress on Engineering, London, U.K.*, pp 978–988
- [147] Weiss M, Rolfe B, Hodgson PD, et al (2012) Effect of residual stress on the bending of aluminium. *Journal of Materials Processing Technology* 212(4):877–883. <https://doi.org/10.1016/j.jmatprotec.2011.11.008>
- [148] Rae W, Rahimi S (2018) Evolution of Microstructure and Residual Stress in Hot Rolled Ti-6Al-4V Plates Subjected to Different Heat Treatment Conditions. *Residual Stresses* pp 171–176. <https://doi.org/10.21741/9781945291890-27>
- [149] Lin K, Wang W, Jiang R, et al (2017) A Numerical Study on the Redistribution of Residual Stress After Machining. In: *Advanced Manufacturing*, vol 2. ASME, Tampa, Florida, USA, <https://doi.org/10.1115/IMECE2017-71199>
- [150] Carpenter K, Tabei A (2020) On Residual Stress Development, Prevention, and Compensation in Metal Additive Manufacturing. *Materials* 13(2):255. <https://doi.org/10.3390/ma13020255>
- [151] Yaghi A, Ayvar-Soberanis S, Moturu S, et al (2019) Design against distortion for additive manufacturing. *Additive Manufacturing* 27:224–235. <https://doi.org/10.1016/j.addma.2019.03.010>
- [152] Treuting RG, Jr WTR (1951) A Mechanical Determination of Biaxial Residual Stress in Sheet Materials. *Journal of Applied Physics* 22(2):130–133. <https://doi.org/10.1063/1.1699913>
- [153] Chobaut N, Wagner J, Carron D, et al (2017) Stress generation during the quenching of large AA2618 forgings: Finite element computations and validation against neutron diffraction measurements. *Finite Elements in Analysis and Design* 131:17–24. <https://doi.org/10.1016/j.finel.2017.03.004>
- [154] Mo F, Sun G, Li J, et al (2018) Recent Progress of Residual Stress Distribution and Structural Evolution in Materials and Components by Neutron Diffraction Measurement at RSND. *Quantum Beam Science* 2(3):15. <https://doi.org/10.3390/qubs2030015>

- [155] Reimers W, Pyzalla A, Broda M, et al (1999) The use of high-energy synchrotron diffraction for residual stress analyses. *Journal of Materials Science Letters* 18(7):581–583. <https://doi.org/10.1023/A:1006651217517>
- [156] Reyes-Ruiz C, Figueroa I, Braham C, et al (2016) Residual stress distribution of a 6061-T6 aluminum alloy under shear deformation. *Materials Science and Engineering: A* 670:227–232. <https://doi.org/10.1016/j.msea.2016.06.016>
- [157] Schajer GS, Prime MB (2006) Use of Inverse Solutions for Residual Stress Measurements. *Journal of Engineering Materials and Technology* 128(3):375. <https://doi.org/10.1115/1.2204952>
- [158] Schajer GS (2010) Relaxation Methods for Measuring Residual Stresses: Techniques and Opportunities. *Experimental Mechanics* 50(8):1117–1127. <https://doi.org/10.1007/s11340-010-9386-7>
- [159] Prime MB (1999) Residual Stress Measurement by Successive Extension of a Slot: The Crack Compliance Method. *Applied Mechanics Reviews* 52(2):75. <https://doi.org/10.1115/1.3098926>
- [160] Nervi S, Szabó BA (2007) On the estimation of residual stresses by the crack compliance method. *Computer Methods in Applied Mechanics and Engineering* 196(37–40):3577–3584. <https://doi.org/10.1016/j.cma.2006.10.037>
- [161] Prime MB, Hill MR (2006) Uncertainty, Model Error, and Order Selection for Series-Expanded, Residual-Stress Inverse Solutions. *Journal of Engineering Materials and Technology* 128(2):175–185. <https://doi.org/10.1115/1.2172278>
- [162] Fu S, Feng P, Ma Y, et al (2020) Initial residual stress measurement based on piecewise calculation methods for predicting machining deformation of aeronautical monolithic components. *The International Journal of Advanced Manufacturing Technology* 108(7–8):2063–2078. <https://doi.org/10.1007/s00170-020-05493-6>
- [163] Zhang Z, Yang Y, Li L, et al (2015) Assessment of residual stress of 7050-T7452 aluminum alloy forging using the contour method. *Materials Science and Engineering: A* 644:61–68. <https://doi.org/10.1016/j.msea.2015.07.018>
- [164] Sun YL, Roy MJ, Vasileiou AN, et al (2017) Evaluation of Errors Associated with Cutting-Induced Plasticity in Residual Stress Measurements Using the Contour Method. *Experimental Mechanics* 57(5):719–734. <https://doi.org/10.1007/s11340-017-0255-5>

- [165] Masoudi S, Amirian G, Saeedi E, et al (2015) The Effect of Quench-Induced Residual Stresses on the Distortion of Machined Thin-Walled Parts. *Journal of Materials Engineering and Performance* 24(10):3933–3941. <https://doi.org/10.1007/s11665-015-1695-7>
- [166] Prime MB (2000) The Contour Method: Simple 2-D Mapping of Residual Stresses. In: *Recent Advances in Solids and Structures*. American Society of Mechanical Engineers, Orlando, Florida, USA, pp 121–127, <https://doi.org/10.1115/IMECE2000-1262>
- [167] Zhang Z, Li L, Yang Y, et al (2016) Residual Stress Calculation by Measuring Deformation After a Diagonal Cut. *Experimental Techniques* 40(2):583–595. <https://doi.org/10.1007/s40799-016-0059-z>
- [168] Ekmekci B, Ekmekci N, Tekkaya A, et al (2004) Residual stresses measurement with layer removal method. *Meas Tech* 1(3):9
- [169] Dreier S, Denkena B (2014) Determination of Residual Stresses in Plate Material by Layer Removal with Machine-integrated Measurement. *Procedia CIRP* 24:103–107. <https://doi.org/10.1016/j.procir.2014.07.137>
- [170] Liu L, Sun J, Chen W, et al (2015) Modified layer-removal method for measurement of residual stress in pre-stretched aluminium alloy plate. *Journal of Harbin Institute of Technology (New Series)* 22:34–40. <https://doi.org/10.11916/j.issn.1005-9113.2015.02.005>
- [171] Cerutti X, Arsene S, Mocellin K (2016) Prediction of machining quality due to the initial residual stress redistribution of aerospace structural parts made of low-density aluminium alloy rolled plates. *International Journal of Material Forming* 9(5):677–690. <https://doi.org/10.1007/s12289-015-1254-7>
- [172] Cerutti X, Mocellin K (2016) Influence of the machining sequence on the residual stress redistribution and machining quality: analysis and improvement using numerical simulations. *The International Journal of Advanced Manufacturing Technology* 83(1-4):489–503. <https://doi.org/10.1007/s00170-015-7521-4>
- [173] Taraphdar P, Thakare J, Pandey C, et al (2020) Novel residual stress measurement technique to evaluate through thickness residual stress fields. *Materials Letters* 277:128,347. <https://doi.org/10.1016/j.matlet.2020.128347>
- [174] Sim WM (2010) Residual Stress Engineering in Manufacture of Aerospace Structural Parts. In: Zoch HW, Lübben T (eds) *Proceedings of the 3rd Conference on Distortion Engineering*, Bremen, Germany, pp 187–194

- [175] Prime MB, Gnaupelherold T, Baumann J, et al (2006) Residual stress measurements in a thick, dissimilar aluminum alloy friction stir weld. *Acta Materialia* 54(15):4013–4021. <https://doi.org/10.1016/j.actamat.2006.04.034>
- [176] Cherif I, Cotton D, Poulachon G, et al (2019) Instrumented clamping device and numerical simulations to study machining distortion. *The International Journal of Advanced Manufacturing Technology* 105(7-8):3093–3103. <https://doi.org/10.1007/s00170-019-04510-7>
- [177] Pagliaro P, Prime MB, Swenson H, et al (2010) Measuring Multiple Residual-Stress Components using the Contour Method and Multiple Cuts. *Experimental Mechanics* 50(2):187–194. <https://doi.org/10.1007/s11340-009-9280-3>
- [178] Stoney GG (1909) The tension of metallic films deposited by electrolysis. *Proc R Soc Lond* 82:172–175. <https://doi.org/10.1098/rspa.1909.0021>
- [179] Jawahir I, Brinksmeier E, M'Saoubi R, et al (2011) Surface integrity in material removal processes: Recent advances. *CIRP Annals* 60(2):603–626. <https://doi.org/10.1016/j.cirp.2011.05.002>
- [180] Arrazola P, Özel T, Umbrello D, et al (2013) Recent advances in modelling of metal machining processes. *CIRP Annals* 62(2):695–718. <https://doi.org/10.1016/j.cirp.2013.05.006>
- [181] Ulutan D, Ozel T (2011) Machining induced surface integrity in titanium and nickel alloys: A review. *International Journal of Machine Tools and Manufacture* 51(3):250–280. <https://doi.org/10.1016/j.ijmachtools.2010.11.003>
- [182] Wang B, Liu Z (2018) Influences of tool structure, tool material and tool wear on machined surface integrity during turning and milling of titanium and nickel alloys: a review. *The International Journal of Advanced Manufacturing Technology* 98(5-8):1925–1975. <https://doi.org/10.1007/s00170-018-2314-1>
- [183] Wan M, Ye XY, Wen DY, et al (2019) Modeling of machining-induced residual stresses. *Journal of Materials Science* 54(1):1–35. <https://doi.org/10.1007/s10853-018-2808-0>
- [184] Ulutan D, Erdem Alaca B, Lazoglu I (2007) Analytical modelling of residual stresses in machining. *Journal of Materials Processing Technology* 183(1):77–87. <https://doi.org/10.1016/j.jmatprotec.2006.09.032>
- [185] Yan L, Yang W, Jin H, et al (2012) Analytical modeling of the effect of the tool flank wear width on the residual stress distribution. *Machining Science and Technology* 16:265–286. <https://doi.org/10.1080/10910344.2012.673973>

- [186] Chen L, El-Wardany T, Harris W (2004) Modelling the Effects of Flank Wear Land and Chip Formation on Residual Stresses. *CIRP Annals* 53(1):95–98. [https://doi.org/10.1016/S0007-8506\(07\)60653-2](https://doi.org/10.1016/S0007-8506(07)60653-2)
- [187] Ulutan D, Arisoy Y, Özel T, et al (2014) Empirical Modeling of Residual Stress Profile in Machining Nickel-based Superalloys Using the Sinusoidal Decay Function. *Procedia CIRP* 13:365–370. <https://doi.org/10.1016/j.procir.2014.04.062>
- [188] ASTM (2008) Standard Test Method for Determining Residual Stresses by the Hole-Drilling Strain-Gage Method, Standard Test Method E837-08. Tech. rep., American Society for Testing and Materials, West Conshohocken, PA.
- [189] Grant PV, Lord JD, Whitehead PS (2002) The Measurement of Residual Stresses by the Incremental Hole Drilling Technique. Tech. rep., National Physical Laboratory, UK.
- [190] BSI (2008) BS EN 15305:2008 Non-destructive testing. Test method for residual stress analysis by X-ray diffraction. European Standard
- [191] Prevey PS (1986) X-Ray Diffraction Residual Stress Techniques. In: *Materials Characterization*. ASM International, <https://doi.org/10.31399/asm.hb.v10.a0001761>, <https://dl.asminternational.org/book/chapter-pdf/481788/a0001761.pdf>
- [192] (2022) Xstress G2R X-Ray Diffractometer. URL <https://www.stresstech.com/products/xstress/xstress-g2r/>
- [193] Guo J, Fu H, Pan B, et al (2021) Recent progress of residual stress measurement methods: A review. *Chinese Journal of Aeronautics* 34(2):54–78. <https://doi.org/https://doi.org/10.1016/j.cja.2019.10.010>
- [194] Lu J, Reira D (1998) A review of recent developments and applications in the field of X-ray diffraction for residual stress studies. *Journal of Strain Analysis for Engineering Design* 33(2):127–136. <https://doi.org/10.1243/0309324981512869>, publisher: Sage Publications Ltd.
- [195] Prime MB (2013) Residual Stress Measurement Methods : Making an Informed Choice LA-UR-13-27700. URL https://www.researchgate.net/profile/Michael-Prime/publication/320881590_Residual_Stress_Measurement_Methods_Making_an_Informed_Choice/links/5a00e4ae4585159634c0de8d/Residual-Stress-Measurement-Methods-Making-an-Informed-Choice.pdf
- [196] Fontanari V, Frenzo F, Bortolamedi T, et al (2005) Comparison of the hole-drilling and X-ray diffraction methods for measuring the residual stresses in shot-peened

- aluminium alloys. *The Journal of Strain Analysis for Engineering Design* 40(2):199–209. <https://doi.org/10.1243/030932405X7791>
- [197] Fitzpatrick ME, Fry AT, Holdway P, et al (2002) Measurement Good Practice Guide No. 52 p 77
- [198] Ceglias RB, Alves JM, Botelho RA, et al (2016) Residual Stress Evaluation by X-Ray Diffraction and Hole-Drilling in an API 5L X70 Steel Pipe Bent by Hot Induction. *Materials Research* 19(5):1176–1179. <https://doi.org/10.1590/1980-5373-MR-2016-0012>
- [199] Bobzin K, Wietheger W, Knoch MA, et al (2020) Comparison of Residual Stress Measurements Conducted by X-ray Stress Analysis and Incremental Hole Drilling Method. *Journal of Thermal Spray Technology* 29(6):1218–1228. <https://doi.org/10.1007/s11666-020-01056-z>
- [200] Akhtar W, Lazoglu I, Liang SY (2022) Prediction and control of residual stress-based distortions in the machining of aerospace parts: A review. *Journal of Manufacturing Processes* 76:106–122. <https://doi.org/10.1016/j.jmapro.2022.02.005>
- [201] Munthe M (2011) The Method Of Corrective Shot Peening : How To Correct The Distortion On The Machined Parts. In: *Conf Proc 2011: ICSP-11*, South Bend, IN USA, pp 377–382
- [202] Dearden G, Edwardson SP, Abed E, et al (2006) Correction of distortion and design shape in aluminium structures using laser forming. In: *International Congress on Applications of Lasers & Electro-Optics*, <https://doi.org/10.2351/1.5060920>
- [203] Volk G, Leacock AG, Brown D (2013) Profile Correction of a Stretch Formed Aluminium Alloy during Artificial Ageing. *Key Engineering Materials* 549:213–219. <https://doi.org/10.4028/www.scientific.net/KEM.549.213>
- [204] Gao H, Zhang Y, Wu Q, et al (2018) Fatigue life of 7075-T651 aluminium alloy treated with vibratory stress relief. *International Journal of Fatigue* 108:62–67. <https://doi.org/10.1016/j.ijfatigue.2017.11.011>
- [205] Johnson G (2008) Residual stress measurements using the contour method. Doctoral dissertation, University of Manchester
- [206] Zhang Z, Li L, Yang Y, et al (2014) Machining distortion minimization for the manufacturing of aeronautical structure. *The International Journal of Advanced Manufacturing Technology* 73(9-12):1765–1773. <https://doi.org/10.1007/s00170-014-5994-1>

- [207] Haichao Y, Guohua Q, Huamin W, et al (2020) A machining position optimization approach to workpiece deformation control for aeronautical monolithic components. *The International Journal of Advanced Manufacturing Technology* 109(1-2):299–313. <https://doi.org/10.1007/s00170-020-05588-0>
- [208] Huang X (2017) Effects of milling process sequence on the residual stress related monolithic components deformation. In: 2nd International Conference on Mechanics and Information Technology (ICMIT 2017), p 6
- [209] Fan L, Li L, Yang Y, et al (2021) Control of machining distortion stability in machining of monolithic aircraft parts. *The International Journal of Advanced Manufacturing Technology* 112(11):3189–3199. <https://doi.org/10.1007/s00170-021-06605-6>
- [210] Wang H, Zhou MX, Zheng WZ, et al (2017) 3D machining allowance analysis method for the large thin-walled aerospace component. *International Journal of Precision Engineering and Manufacturing* 18(3):399–406. <https://doi.org/10.1007/s12541-017-0048-x>
- [211] Chen YZ, Chen WF, Liang RJ, et al (2017) Machining Allowance Optimal Distribution of Thin-Walled Structure Based on Deformation Control. *Applied Mechanics and Materials* 868:158–165. <https://doi.org/10.4028/www.scientific.net/AMM.868.158>
- [212] Wang MH, Sun Y (2014) Error prediction and compensation based on interference-free tool paths in blade milling. *The International Journal of Advanced Manufacturing Technology* 71(5-8):1309–1318. <https://doi.org/10.1007/s00170-013-5535-3>
- [213] Gao Yy, Ma Jw, Jia Zy, et al (2016) Tool path planning and machining deformation compensation in high-speed milling for difficult-to-machine material thin-walled parts with curved surface. *The International Journal of Advanced Manufacturing Technology* 84(9-12):1757–1767. <https://doi.org/10.1007/s00170-015-7825-4>
- [214] Javidikia M, Sadeghifar M, Songmene V, et al (2020) Effect of turning environments and parameters on surface integrity of AA6061-T6: experimental analysis, predictive modeling, and multi-criteria optimization. *The International Journal of Advanced Manufacturing Technology* 110(9-10):2669–2683. <https://doi.org/10.1007/s00170-020-06027-w>
- [215] Cheng DJ, Xu F, Xu SH, et al (2020) Minimization of Surface Roughness and Machining Deformation in Milling of Al Alloy Thin-Walled Parts. *International Journal of Precision Engineering and Manufacturing* 21:1597–1613. <https://doi.org/10.1007/s12541-020-00366-0>

- [216] Smith S, Wilhelm R, Dutterer B, et al (2012) Sacrificial structure preforms for thin part machining. *CIRP Annals* 61(1):379–382. <https://doi.org/10.1016/j.cirp.2012.03.142>
- [217] Li B, Gao H, Deng H, et al (2020) A machining deformation control method of thin-walled part based on enhancing the equivalent bending stiffness. *The International Journal of Advanced Manufacturing Technology* 108(9-10):2775–2790. <https://doi.org/10.1007/s00170-020-05585-3>
- [218] Denkena B, Fischer R, Dege JH, et al (2013) Precise Compensation of Component Distortion by an Adaptive Clamping System. In: *Proceedings of the 13th euspen International Conference, Berlin, Germany*
- [219] Li Y, Liu C, Hao X, et al (2015) Responsive fixture design using dynamic product inspection and monitoring technologies for the precision machining of large-scale aerospace parts. *CIRP Annals* 64(1):173–176. <https://doi.org/10.1016/j.cirp.2015.04.025>
- [220] Li H, Chen W, Shi S (2016) Design and Application of Flexible Fixture. *Procedia CIRP* 56:528–532. <https://doi.org/10.1016/j.procir.2016.10.104>
- [221] Xiong L, Molfino R, Zoppi M (2013) Fixture layout optimization for flexible aerospace parts based on self-reconfigurable swarm intelligent fixture system. *The International Journal of Advanced Manufacturing Technology* 66(9-12):1305–1313. <https://doi.org/10.1007/s00170-012-4408-5>
- [222] Chen C, Sun Y, Ni J (2018) Optimization of flexible fixture layout using N-M principle. *The International Journal of Advanced Manufacturing Technology* 96(9-12):4303–4311. <https://doi.org/10.1007/s00170-018-1907-z>
- [223] Yu JH, Chen ZT, Jiang ZP (2016) A control process for machining distortion by using an adaptive dual-sphere fixture. *The International Journal of Advanced Manufacturing Technology* 86(9-12):3463–3470. <https://doi.org/10.1007/s00170-016-8470-2>
- [224] Hao X, Li Y, Chen G, et al (2018) 6+X locating principle based on dynamic mass centers of structural parts machined by responsive fixtures. *International Journal of Machine Tools and Manufacture* 125:112–122. <https://doi.org/10.1016/j.ijmachtools.2017.11.006>
- [225] Abellan-Nebot JV, Liu J, Romero Subirón F (2012) Quality prediction and compensation in multi-station machining processes using sensor-based fixtures. *Robotics and Computer-Integrated Manufacturing* 28(2):208–219. <https://doi.org/10.1016/j.rcim.2011.09.001>

- [226] Denkena B, Möhring HC, Litwinski KM (2008) Design of dynamic multi sensor systems. *Production Engineering* 2(3):327–331. <https://doi.org/10.1007/s11740-008-0102-8>
- [227] Möhring HC, Litwinski K, Gümmer O (2010) Process monitoring with sensory machine tool components. *CIRP Annals* 59(1):383–386. <https://doi.org/10.1016/j.cirp.2010.03.087>
- [228] Gonzalo O, Seara JM, Guruceta E, et al (2017) A method to minimize the workpiece deformation using a concept of intelligent fixture. *Robotics and Computer-Integrated Manufacturing* 48:209–218. <https://doi.org/10.1016/j.rcim.2017.04.005>
- [229] Zhang Z, Luo M, Tang K, et al (2020) A new in-processes active control method for reducing the residual stresses induced deformation of thin-walled parts. *Journal of Manufacturing Processes* 59:316–325. <https://doi.org/10.1016/j.jmapro.2020.09.079>
- [230] Huang N, Bi Q, Wang Y, et al (2014) 5-Axis adaptive flank milling of flexible thin-walled parts based on the on-machine measurement. *International Journal of Machine Tools and Manufacture* 84:1–8. <https://doi.org/10.1016/j.ijmachtools.2014.04.004>
- [231] Yuan Y, Bi Q, Zhu L, et al (2017) Real-Time Normal Measurement and Error Compensation of Curved Aircraft Surface Based on On-line Thickness Measurement. In: *Intelligent Robotics and Applications*. Springer International Publishing, Cham, Lecture Notes in Computer Science, pp 157–170, https://doi.org/10.1007/978-3-319-65292-4_15
- [232] Wang X, Bi Q, Zhu L, et al (2018) Improved forecasting compensatory control to guarantee the remaining wall thickness for pocket milling of a large thin-walled part. *The International Journal of Advanced Manufacturing Technology* 94(5-8):1677–1688. <https://doi.org/10.1007/s00170-016-9785-8>
- [233] Zhao Z, Ding D, Fu Y, et al (2019) Measured data-driven shape-adaptive machining via spatial deformation of tool cutter positions. *Measurement* 135:244–251. <https://doi.org/10.1016/j.measurement.2018.11.051>
- [234] Liu C, Li Y, Shen W (2018) A real time machining error compensation method based on dynamic features for cutting force induced elastic deformation in flank milling. *Machining Science and Technology* 22(5):766–786. <https://doi.org/10.1080/10910344.2017.1402933>
- [235] Hao X, Li Y, Zhao Z, et al (2018) Dynamic machining process planning incorporating in-process workpiece deformation data for large-size aircraft structural

- parts. *International Journal of Computer Integrated Manufacturing* 32(2):136–147. <https://doi.org/10.1080/0951192X.2018.1529431>
- [236] Hao X, Li Y, Huang C, et al (2020) An allowance allocation method based on dynamic approximation via online inspection data for deformation control of structural parts. *Chinese Journal of Aeronautics* 33(12):3495–3508. <https://doi.org/10.1016/j.cja.2020.03.038>
- [237] Rego RR (2016) Residual stress interaction in-between processes of the gear manufacturing chain. Doctoral dissertation, Instituto Tecnológico de Aeronáutica, Brasil
- [238] Mirkoohi E, Bocchini P, Liang SY (2019) Inverse analysis of residual stress in orthogonal cutting. *Journal of Manufacturing Processes* 38:462–471. <https://doi.org/10.1016/j.jmapro.2019.01.033>
- [239] Wang Zj, Chen Wy, Zhang Yd, et al (2005) Study on the Machining Distortion of Thin-walled Part Caused by Redistribution of Residual Stress. *Chinese Journal of Aeronautics* 18(2):175–179. [https://doi.org/10.1016/S1000-9361\(11\)60325-7](https://doi.org/10.1016/S1000-9361(11)60325-7)
- [240] Wei Y, Wang XW (2007) Computer simulation and experimental study of machining deflection due to original residual stress of aerospace thin-walled parts. *The International Journal of Advanced Manufacturing Technology* 33(3-4):260–265. <https://doi.org/10.1007/s00170-006-0470-1>
- [241] Zheng Z, Li L, Yang YF, et al (2014) Prediction and Measurement of Machining Distortion in Aluminium Alloy 7085. *Advanced Materials Research* 996:640–645. <https://doi.org/10.4028/www.scientific.net/AMR.996.640>
- [242] Liu L, Sun J, Chen W, et al (2015) Study on the machining distortion of aluminum alloy parts induced by forging residual stresses. *Proceedings of the Institution of Mechanical Engineers, Part B: Journal of Engineering Manufacture* 231(4):618–627. <https://doi.org/10.1177/0954405415583805>
- [243] Pan R, Zheng J, Zhang Z, et al (2019) Cold rolling influence on residual stresses evolution in heat-treated AA7xxx T-section panels. *Materials and Manufacturing Processes* 34(4):431–446. <https://doi.org/10.1080/10426914.2018.1512121>
- [244] Rafey Khan A, Nisar S, Shah A, et al (2017) Reducing machining distortion in AA 6061 alloy through re-heating technique. *Materials Science and Technology* 33(6):731–737. <https://doi.org/10.1080/02670836.2016.1243335>
- [245] Wang YQ, Mei ZY, Fan YQ (2012) Research on Machining Distortion due to Residual Stresses of Large Monolithic Beam. *Advanced Materials Research* 433-440:530–537. <https://doi.org/10.4028/www.scientific.net/AMR.433-440.530>

- [246] Lv T, Zhang Y (2015) A combined method of thermal and vibratory stress relief. *Journal of Vibroengineering* 17(6):2837–2845
- [247] Hill MR, Olson MD (2014) Repeatability of the Contour Method for Residual Stress Measurement. *Experimental Mechanics* 54(7):1269–1277. <https://doi.org/10.1007/s11340-014-9867-1>
- [248] Prime MB, Sebring RJ, Edwards JM, et al (2004) Laser surface-contouring and spline data-smoothing for residual stress measurement. *Experimental Mechanics* 44(2):176–184. <https://doi.org/10.1007/BF02428177>
- [249] Gulpak M, Sölter J (2016) Development of a hybrid model for the prediction of shape deviations in milling: Entwicklung eines Hybridmodells für die Vorhersage von Formabweichungen beim Fräsen. *Materialwissenschaft und Werkstofftechnik* 47(8):718–725. <https://doi.org/10.1002/mawe.201600605>
- [250] Aurrekoetxea M, López de Lacalle LN, Llanos I (2020) Machining Stresses and Initial Geometry on Bulk Residual Stresses Characterization by On-Machine Layer Removal. *Materials* 13(6):1445. <https://doi.org/10.3390/ma13061445>
- [251] Peral Jiménez D (2017) Desarrollo de métodos para la acotación de la incertidumbre en medidas de tensiones residuales en materiales metálicos tratados por LSP. Doctoral dissertation, E.T.S.I. Industriales (UPM)
- [252] Schajer GS (1988) Measurement of Non-Uniform Residual Stresses Using the Hole-Drilling Method. Part I—Stress Calculation Procedures. *Journal of Engineering Materials and Technology* 110(4):338–343. <https://doi.org/10.1115/1.3226059>
- [253] Schajer GS (1988) Measurement of Non-Uniform Residual Stresses Using the Hole-Drilling Method. Part II—Practical Application of the Integral Method. *Journal of Engineering Materials and Technology* 110(4):344–349. <https://doi.org/10.1115/1.3226060>
- [254] He BB (2018) Two-Dimensional X-ray diffraction, 2nd edn. WILEY, URL <https://www.wiley.com/en-us/Two+dimensional+X+ray+Diffraction%2C+2nd+Edition-p-9781119356103>
- [255] Gnäupel-Herold T, Creuziger AA, Iadicola M (2012) A model for calculating diffraction elastic constants. *Journal of Applied Crystallography* 45(2):197–206. <https://doi.org/10.1107/S0021889812002221>
- [256] Yang D, Xiao X, Liu Y, et al (2019) Peripheral milling-induced residual stress and its effect on tensile–tensile fatigue life of aeronautic titanium alloy Ti–6Al–4V. *The Aeronautical Journal* 123(1260):212–229. <https://doi.org/10.1017/aer.2018.151>

- [257] Group S (2020) XTronic - Software User's Guide, V1.14
- [258] Suominen L, Carr D (2000) Selected methods of evaluating residual stress gradients measured by x-ray diffraction traditional, full tensor, and wavelet. *JCPDS-International Centre for Diffraction Advances in X-ray Analysis* 43:78–82
- [259] Sagrado S, Asociación Española de Normalización y Certificación. (2004) Manual práctico de calidad en los laboratorios: enfoque ISO 17025
- [260] Jiang X, Li B, Yang J, et al (2013) Effects of tool diameters on the residual stress and distortion induced by milling of thin-walled part. *The International Journal of Advanced Manufacturing Technology* 68(1-4):175–186. <https://doi.org/10.1007/s00170-012-4717-8>
- [261] Jiang X, Li B, Yang J, et al (2013) An approach for analyzing and controlling residual stress generation during high-speed circular milling. *The International Journal of Advanced Manufacturing Technology* 66(9-12):1439–1448. <https://doi.org/10.1007/s00170-012-4421-8>
- [262] Grant PV, Lord JD, Whitehead PS (2002) The Measurement of Residual Stresses by the Incremental Hole Drilling Technique p 49
- [263] Fuht KH, Wu CF (1995) A Proposed statistical model for surface quality prediction in end-milling of Al alloy. *International Journal of Machine Tools and Manufacture* 35(8):1187–1200. [https://doi.org/10.1016/0890-6955\(95\)90408-E](https://doi.org/10.1016/0890-6955(95)90408-E)
- [264] Tan L, Zhang D, Yao C, et al (2017) Evolution and empirical modeling of compressive residual stress profile after milling, polishing and shot peening for TC17 alloy. *Journal of Manufacturing Processes* 26:155–165. <https://doi.org/10.1016/j.jmapro.2017.02.002>
- [265] Organización Internacional de Normalización, Organización Internacional de Normalización. (1989) ISO 8688-1: Tool life testing in milling. Part 1, Face milling. Section: 27 p
- [266] Caldeirani J, Diniz A (2002) Influence of Cutting Conditions on Tool Life, Tool Wear and Surface Finish in the Face Milling Process. *Journal of the Brazilian Society of Mechanical Sciences* 24. <https://doi.org/10.1590/S0100-73862002000100002>
- [267] Huang X, Zhang X, Ding H (2015) An Analytical Model of Residual Stress for Flank Milling of Ti-6Al-4V. *Procedia CIRP* 31:287–292. <https://doi.org/10.1016/j.procir.2015.03.061>
- [268] James GM, Witten D, Hastie TJ, et al (2013) An introduction to statistical learning: with applications in R, corrected at 6th printing 2015 edn. No. 103 in Springer texts in statistics, Springer Springer Science and Business Media, New York